

8-16-2024

New Techniques for Studying Ocean Eddy Dynamics in the Arabian Sea and the Gulf of Mexico

Paul Andrew Ernst
University of South Carolina

Follow this and additional works at: <https://scholarcommons.sc.edu/etd>



Part of the [Earth Sciences Commons](#)

Recommended Citation

Ernst, P. A.(2024). *New Techniques for Studying Ocean Eddy Dynamics in the Arabian Sea and the Gulf of Mexico*. (Doctoral dissertation). Retrieved from <https://scholarcommons.sc.edu/etd/7773>

This Open Access Dissertation is brought to you by Scholar Commons. It has been accepted for inclusion in Theses and Dissertations by an authorized administrator of Scholar Commons. For more information, please contact digres@mailbox.sc.edu.

NEW TECHNIQUES FOR STUDYING OCEAN EDDY DYNAMICS IN THE
ARABIAN SEA AND THE GULF OF MEXICO

by

Paul Andrew Ernst

Bachelor of Science
University of Delaware, 2020

Submitted in Partial Fulfillment of the Requirements

For the Degree of Doctor of Philosophy in

Marine Science

College of Arts and Sciences

University of South Carolina

2024

Accepted by:

Michael Bizimis, Major Professor

James Pinckney, Committee Member

George Voulgaris, Committee Member

Jean Ellis, Outside Committee Member

Ann Vail, Dean of the Graduate School

© Copyright by Paul Andrew Ernst, 2024
All Rights Reserved.

DEDICATION

This dissertation is dedicated to my family for their ceaseless support, to my friends both in the U.S. and abroad for their commitments to the stories we tell together, and to Megan, the light of my life.

ACKNOWLEDGEMENTS

I would first like to acknowledge my coauthors: Dr. Subrahmanyam Bulusu, Dr. Corinne B. Trott, Dr. Alexis Chaigneau, and Dr. Yves Morel, for their patience and assistance throughout the construction of this work. I would also like to acknowledge Dr. Jean Taylor Ellis, who has helped me through a difficult time. Thanks is also due to the former members of the Satellite Oceanography Lab: Emily Eley, Dr. Sarah Hall, Lydia Sims, Autumn Toms, Susan Harrison, and Emma Hoffman. Thank you all for your comradery.

As for my funding, this work was supported primarily by the University of South Carolina's Presidential Fellowship and the Science Mathematics and Research for Transformation (SMART) Scholarship. My SMART sponsoring facility is the Naval Undersea Warfare Center and I thank my supervisor, Dr. Joy Lapseritis, as well as my mentor, Dr. Lauren Freeman, for their continued support.

Lastly, a special thanks to the SEOE as a whole and to my committee members: Dr. Michael Bizimis, Dr. James L. Pinckney, Dr. George Voulgaris, and Dr. Jean Taylor Ellis (again!).

ABSTRACT

Coherent vortices known as eddies are ubiquitous throughout the world's oceans and are responsible for modulating regional climates via the transfer of heat, momentum, and salt. Two regions where eddies are particularly prominent are the Arabian Sea (AS) and the Gulf of Mexico (GoM). This dissertation advances the study of eddies in these regions by developing and employing new techniques in conjunction with remotely sensed data and high-resolution ocean models. These models focus particularly on lesser-studied eddy components at the subsurface and the submesoscale (below 25 km in radius).

The first component of this dissertation focuses on the Lakshadweep High (LH), a climatological eddy in the AS. Using an automatic eddy tracking algorithm, the entire life cycle of the LH is described for the first time, including its previously unresolved propagation to the Somali Current. There, the LH negatively influences the eddy kinetic energy of the current by inhibiting the formation of a cyclonic eddy after the onset of the southwest monsoon.

Refocusing on the subsurface component of the eddy field in the AS, the second part of this work is the development of a novel eddy tracking algorithm using the rescaled Potential Vorticity (PV) to detect eddies in ocean models. Compared to its alternatives, the PV algorithm provides superior performance in terms of eddy detection. This algorithm illuminates a previously unknown eddy in the southern AS near the Chagos Archipelago that mixes Red Sea Water with Antarctic Intermediate Water and downwells the result.

The final component of this dissertation moves to the GoM, where a $1/48^\circ$ grid resolution simulation is used with a custom-designed spatial filtering process to isolate the small-scale component of the eddy field. This submesoscale eddy field induces variability in temperature, salinity, and eddy kinetic energy in the overlying mesoscale eddy field. Additionally, the presence of submesoscale eddy-like features predicts eddy dissipation and Loop Current Eddy (LCE) separation.

The techniques and results presented in this dissertation combine to elucidate previously unresolved eddy dynamics in culturally important regions, providing the tools for researchers to do the same in other regions in the future.

TABLE OF CONTENTS

Dedication	iii
Acknowledgements	iv
Abstract	v
List of Tables	viii
List of Figures	ix
Chapter 1: Introduction	1
Chapter 2: Lakshadweep High Propagation and Impacts on the Somali Current and Eddies During the Southwest Monsoon	7
Chapter 3: Subsurface Eddy Detection Optimized with Potential Vorticity from Models in the Arabian Sea	69
Chapter 4: Characteristics of Submesoscale Eddy Structures within Mesoscale Eddies in the Gulf of Mexico from 1/48° ECCO Estimates	124
Chapter 5: Conclusions	165
References	169
Appendix A: Copyright Permissions	189
Appendix B: Calculation of Averaged PV in the Surface Layer	191

LIST OF TABLES

Table 2.1 Year-Wise Southwest Monsoon Strength (2nd column), Occurrences of ENSO Phase (3rd column), IOD Phase (4th column), and LH type of propagation (5th column) from 1993 to 2019. Example years are highlighted. Table entries without an explicit designation are neutral in their respective indices. Columns 2, 3, and 4 are adapted from Roman-Stork et al. (2020).....	43
Table 3.1 The summary of final parameters for all tested detection methods as individually noted in Figures 1-5. Kilometer values for optimal smoothing are approximate, rounded values given the variation of longitude with latitude and are intended primarily for reference within our specified domain.....	106
Table 4.1 The arithmetic means and standard deviations of Internal SEV lifetimes (column 1), radii (column 2), amplitudes (column 3), and EKE (column 4) for SEV-AEs internal to mesoscale AEs (row 1), SEV-CEs internal to mesoscale AEs (row 2), SEV-AEs internal to mesoscale CEs (row 3) and SEV-CEs internal to mesoscale CEs (row 4).	151

LIST OF FIGURES

- Figure 2.1 Mean absolute dynamic topography (ADT) (cm) during Winter (mean of November, December, January, and February) (a), March (c), Summer (mean of May, June, July, August, and September) (e), and October (g), averaged from 1993 to 2019. (b), (d), (f), and (h): Same as (a), (c), (e), and (g) but for eddy kinetic energy (EKE) ($\text{cm}^2 \text{s}^{-2}$). The locations of the LH, the GW, and the Somali Current (SC) are annotated.44
- Figure 2.2 The original (filled triangles) and final (filled circles) locations tracked for each LH, 1993-2019. The lines indicate an average of all trajectories of a given type based off of the average origin point through the final recorded location at the mean lifetime of the propagation type. Blue objects and lines in (a) indicate trajectories that do not pass 70°E . Red objects and lines in (b) indicate trajectories that are recorded passing 70°E , but dissipating before passing 60°E . Black objects and lines in (c) indicate trajectories that are recorded passing 60°E . (d) displays all trajectory clusters on the same panel for comparison.45
- Figure 2.3 ADT (cm) of the AS in 2006, 1994, and 1998. Arrows depict geostrophic current vectors (m s^{-1}) from altimetry data. Black pinwheels mark locations of the tracked LH at the given times. (a)-(c) 15 January, 16 March, and 21 July 2006. (d)-(f) Same as (a)-(c) but for 1994. (m)-(r) Same as (a)-(c) but for 1998.46
- Figure 2.4 Trajectories of the tracked LH in 2006 (a), 1994 (b), and 1998 (c). Solid black lines indicate LH trajectories, while black pinwheels indicate LH origin location. Thinner colored lines each correspond to a unique GDP drifter that overlapped with the radius of LH for at least a week at some point in its life. Smaller colored pinwheels represent the origin points of the respective colored drifter.47
- Figure 2.5 SLA (cm) depicting CKW propagation between 13 October and 26 January averaged from 1993 to 2019. Arrows depict geostrophic current vectors (m s^{-1}) from altimetry data. Green pinwheels mark the average locations of the tracked LH at the given times. (a)-(f) Average for full years. (g)-(i) Average for half years. (m)-(r) Average for local years. The black box is the zone within which all LHs form.48

Figure 2.6 Mean SLA Anomaly (cm) for all years (a) and example years (b); areas of elevated SLA (> 10 cm, km^2) for all years (c) and example years (d). Means are performed over the boxed area in Figure 2.5 (9.5°N , 5°S , 80°E , 72°E) and anomalies are calculated for each location in regard to a 27-year mean.49

Figure 2.7 Mean wind stress (N m^{-2}) and SLA contours over the STIP area between the beginning of October and the end of December for full (a-f), half (g-l), and local (m-r) years. Each date represents the beginning of a two week period over which the wind stresses and SLAs are averaged.50

Figure 2.8 The 3-dimensional profiles of the location and date marked by the black pinwheel in Figure 2.3a for the full example year (15 January, 2006). These are as follows: (a) measured ADT (cm), (b) GLORYS12v1 sea surface salinity (SSS) (PSU), (c) GLORYS12v1 SST ($^\circ\text{C}$), and (d) Spiciness with geostrophic current vectors overlaid. The white dashed line depicts the cross sections of the following properties: (e) Potential density (kg m^{-3}) with isopycnals overlaid. (f) Absolute salinity (PSU) and (g) conservative temperature ($^\circ\text{C}$) with contours of swirl velocity (m s^{-1} , meridional components) overlaid. (h) Vertical velocity (m s^{-1}) with its own contours overlaid. White squares represent regions of no GLORYS12v1 data, in this case representing the Lakshadweep islands.51

Figure 2.9 Same as Figure 2.8 but for the location marked in Figure 2.3d for the half example year (15 January, 1994).....52

Figure 2.10 Same as Figure 2.8 but for the location marked in Figure 2.3g for the local example year (15 January, 1998).53

Figure 2.11 WSC (N m^{-3}) for the first week in each month between January and June averaged from 1993 to 2019 in the AS. Contours depict areas of elevated ADT in intervals of 5 cm. Green pinwheels mark the average locations of the tracked LH following the trajectories marked in Figure 2.2. (a)-(f) Average for full years. (g)-(i) Average for half years. (m)-(r) Average for local years.54

Figure 2.12 Same as Figure 2.11, but displaying the normalized spatial covariance between the WSC and the ADT. Areas of significant correlation ($p < .05$) are shaded.55

Figure 2.13 The characteristics of the LH and the wind over the radius of the LH for the first 90 days of its lifespan for each year type (left) and example years (right): (a) is the mean WW ($\text{m}^3 \text{s}^{-3}$) for all propagation

types; (b) is as in (a) but for example years. (c) is the mean WSC (N m^{-2}) for all propagation types; (d) is as in (c) but for example years. (e) is the radius (km) of the LH for all propagation types; (f) is as in (e) but for example years. Lastly, (g) is the mean EKE ($\text{m}^2 \text{s}^{-2}$) of the LH for all propagation types; (h) is as in (g) but for example years. Black lines display the average for all years and are the same across both columns.....56

Figure 2.14 Hovmöller longitude-time diagram of SLA (cm) contours for a spatial average of 7°N - 9°N and a temporal average for 1993-2019 between January and the end of July. Green lines depict average LH propagation (see Figure 2.2) along this longitude. (a) Average for full years. (b) Average for half years. (c) Average for local years.....57

Figure 2.15 Radon transforms of the L-T plots shown in Figure 2.14. (a) Transform for full years. (b) Transform for half years. (c) Transform for local years. (d) is the standard deviation of the SLA in (a)-(c) on blue, green, and red lines respectively. Colored pinwheels mark the maximum in the curve. (e) plots the gradient of (d).58

Figure 2.16 Same as Figure 2.8 but for the location marked in Figure 2.3b for the full example year (March 26th, 2006).59

Figure 2.17 Same as Figure 2.8 but for the location marked in Figure 2.3e for the half example year (March 26th, 1994).....60

Figure 2.18 Same as Figure 2.8 but for the location marked in Figure 2.3h for the local example year (March 26th, 1998). As before, white squares mark the locations of the Lakshadweep islands, which are not painted over in the GLORYS12v1 dataset as they are in the CMEMS altimetry interpolations.61

Figure 2.19 Yearlong characteristics of eddies in the Somali Current (the area between the Equator, 11°N , 40°E , and 58°E) for 2006, 1994, and 1998. Characteristics include the spatial median SC eddy (a) amplitude in cm, (b) radius in km, and (c) EKE in $\text{cm}^2 \text{s}^{-2}$. (d) Mean EKE of the SC from geostrophic current observations. (e) EKE in $\text{cm}^2 \text{s}^{-2}$ of the LH (solid lines) and GW (dotted lines) of each year. The GW is tracked in the same way that the LH is as set out in section 2.4.1, but for the SC region and April through June.....62

Figure 2.20 Same as Figure 2.19 but averaged across all years 1993-2019. (e-h) boxplots with the mean, upper and

lower quartiles, and minimum and maximum of the characteristics shown.....	63
Figure 2.21 Wind stress curl ($N\ m^{-3}$) differences between full, half, and local years for the first week in each month between April and September averaged across 1993-2019 in the SC region. Contours depict ADT (cm). Black pinwheels mark the average locations of the tracked LH. (a)-(f) Average for full years. (g)-(i) Average for full years minus the average for half years. (m)-(r) Average for full years minus the average for local years.	64
Figure 2.22 The same spatiotemporal area as Figure 2.22, but plotting the normalized covariance (color) and significant correlations (shading) between the WSC and the ADT (as in Figure 2.12.) Contours are ADT, the same as Figure 2.21.	65
Figure 2.23 Yearlong characteristics of eddies in the Somali Current averaged between 1993 and 2019 (as in Figure 2.20) but separated between AEs and CEs. Blue lines depict full years, green lines depict half years, and red lines depict local years. (a) Median AE amplitude (cm). (b) same as (a) but for CEs. (c) Median AE radius (km). (d) same as (c) but for CEs. (e) Median average AE EKE ($cm^2\ s^{-2}$). (f) same as (e) but for CEs. Note that there is a difference in the y-axis scales between AEs and CEs.	66
Figure 2.24 The average ADT (cm) of the SC region between 1993 and 2019 per type of LH propagation year. Full years: (a) July 22 nd , (b) July 29 th , (c) August 5 th , (d) August 12 th , and (e) August 19 th . (f-j) same as (a-e) but for half years. (k-o) same as (a-e) but for local years.	67
Figure 2.25 Same as Figure 2.8 but for the location marked in Figure 2.3c for the full example year (July 21 st , 2006).	68
Figure 3.1 Optimizations of the center threshold parameters of $VORT_T$ (a), OW_T (b), and $LNAM$ (c) with each type of error and score. The STD factor for OW_T is considered to be always negative, as only a negative OW is associated with eddy centers.	107
Figure 3.2 Smoothing factors optimized for the center components of $VORT_T$ (a), $VORT_{WA}$ (b), OW_T (c), OW_{WA}	

	(d), and PV_{ISO} (e) for each type of error and score. STD factors are the optimized values in Figure 3.1.	108
Figure 3.3	Optimizations of the edge threshold parameters of $VORT_T$ (a) and OW_T (b) with each type of error and score. The STD factor for OW_T is always negative.	109
Figure 3.4	Aggregate similarity score of the edge components of $VORT_T$ (a), $VORT_{WA}$ (b), OW_T (c), OW_{WA} (d), and PV_{ISO} (e) for the optimization of both smoothing factor and minimum centroid ratio using SSH centers. Black Xs mark the combination of smoothing factor and centroid ratio that result in the best similarity score for each edge method tested.	110
Figure 3.5	Hybrid method optimization using all center and edge method combinations. Shown are the number error Err_{Num} (a), centroid ratio error Err_{Ratio} (b), spatial correct error Err_{Pos} (c), spatial incorrect error Err_{Neg} (d), and aggregate similarity score (e). Black Xs mark optimal combinations of methods per error and score. Errors are considered optimal when minimized, and similarity score is considered optimal when maximized.	111
Figure 3.6	Detected contours (black lines) and centers (+s for AE centers, Xs for CE centers) on January 1 st , 2016 in the GoA for the following center/edge hybrid methods: SSH/SSH (a), OW_T/OW_{WA} (b), $VORT_{WA}/VORT_{WA}$ (c), LNAM/ OW_{WA} (d), $VORT_{WA}/PV_{ISO}$ (e), and PV_{ISO}/PV_{ISO} (f). Color is given by the edge fields and are shown without low pass filtering. Current vectors are overlaid.	112
Figure 3.7	As in Figure 3.6, but for the Gulf of Oman on July 28 th , 2017.	113
Figure 3.8	As in Figure 3.6, but for the Laccadive Sea and West India Coastal Current region on January 1 st , 2016.	114
Figure 3.9	As in Figure 3.6, but for the Somali Current region on August 28 th , 2019.	115
Figure 3.10	The isopycnal limits of RSW. (a) T-S diagram for the GoA with the median profile \pm one standard deviation; the boundary isopycnals ($kg\ m^{-3}$) defined by L'Hégaret et al. (2021) are bolded. (b) The L'Hégaret et al. (2021) algorithm for RSW water mass detection on a vertical profile located at 55°E, 13°N on July 7 th , 2018. The vertical spiciness trend to be removed is the dotted blue line. The bolded portion of	

the profile lies between the bolded isopycnals in (a) and below 600 m; the red circle denotes the maximum of the RSW while the red crosses represent the upper and lower minimums.116

Figure 3.11 (a) The maximum densities (kg m^{-3}) within the RSW isopycnal bounds in our model. (b) the range width between the upper minimum and lower minimum bounds of RSW density within the isopycnal bounds defined above (kg m^{-3}).....117

Figure 3.12 The properties of each type of RSW eddy separated by monsoon in $2^\circ \times 2^\circ$ bins: Winter CEs (a-d), Winter AEs (e-h), Summer CEs (i-l), and Summer AEs (m-p). Gen. Num. refers to where eddies are first detected. Radius and Amplitude (absolute value) are average values.118

Figure 3.13 The three dimensional structure of a Chagos eddy on May 29th, 2019 with NEMO levels 2, 29, 35, 38, 40, and 42 displayed. Column 1: the potential density (kg m^{-3}) and current vectors on each level, with mesh grids marking the upper ($1026.95 \text{ kg m}^{-3}$) and lower (1027.4 kg m^{-3}) isopycnal bounds within which the eddy is defined in our algorithm. Column 2: the salinity (psu) and current vectors of the column. Column 3: The PV anomaly (s^{-1}) and current vectors of the column with a mesh contour defining the algorithmically defined boundaries of the eddy within the layers of Column 1. A black line marks the center point of the eddy, with a solid line marking the target density layer and spaced triangles marking depths outside of the target density layer.119

Figure 3.14 (a) The beginning (February 18th, 2019, colored) and end (May 29th, 2019, black) locations of each type of particle as described in the text (red cross = high PV, blue triangle = low PV, green diamond = medium PV). The Chagos Archipelago is greyed out to the eddy's northwest. (b) A T/S diagram of the initial (colored) and final (black) particles. (c) a density/PV diagram of the initial (colored) and final (black) particles. (d) the depth evolution of each type of particle by date with colors as in (a). (e) as in (d), but with PV.120

Figure 3.15 The trajectories of eastern low PV particles, colored by PV anomaly (a), the density evolution of eastern low PV particles by date (b), and the Richardson numbers below 1 over time for eastern high PV particles (c). (d), (e), and (f) are as in (a), (b), and (c) but for western high PV particles.121

Figure 3.16 As in Figure 3.15, but for medium PV particles.....122

Figure 3.17 As in Figure 3.15, but for high PV particles defined in Figure 3.14.123

Figure 4.1 The SSH fields (m) in the central Gulf of Mexico for Nov. 3rd, 2012, showcasing the filtering process and eddy detection methodologies. (A) The total scale model outputs; (B) the large scale filtered SSH after convolution with the Dolph-Chebyshev window and corresponding mesoscale eddy edge detections (black lines); (C) the small scale filtered SSH after subtracting (B) from (A) along with both detections of large and small scale eddies (black lines). (D) The normalized power spectrum for the large scale field (in blue) and the small scale field (in red) demonstrating a crossover point near 25 km.152

Figure 4.2 The properties of all mesoscale eddies and SEVs broken down geographically by eddy center location and binned into $\frac{1}{2}^\circ$ pixels. (A)-(E) The generation number, i.e. number of eddies the originated in the pixel, the number of all eddy detections, the mean eddy radius (km), the mean eddy amplitude (cm), and the mean EKE ($\text{m}^2 \text{s}^{-2}$) for all mesoscale AEs. (F)-(J) As in (A)-(E) but for mesoscale CEs. (K)-(O) As in (A)-(E) but for SEV-AEs. (P)-(T) As in (A)-(E) but for SEV-CEs. The black box in (T) denotes the Loop Current region.153

Figure 4.3 The properties of all SEVs over time from the beginning of the model simulation to its end, separated into AEs and CEs and binned into 12-hour increments. (A) The number of eddies per increment; (B) the median eddy amplitude (cm); (C) the median eddy radius (km); (D) the median eddy EKE ($\text{m}^2 \text{s}^{-2}$). (E) The EKE for the Loop Current region as defined by Brokaw et al. (2020): $21.5^\circ\text{N} - 28^\circ\text{N}$ and $81^\circ\text{W}-90^\circ\text{W}$, both with and without tidal variability (as removed by a low-pass Gaussian filter with a half-window of 28 days). (F)-(J) As in (A)-(E) but using a box plot to show the median, quartiles, and extremes of the data upon which the time series is constructed.154

Figure 4.4 The magnitude-squared wavelet coherence computed using the analytic Morlet wavelet between each of the time series in Figure 4.3A-D and Figure 4.3E. The white dashed line shows the cone of influence, after which edge effects dominate, while the black arrows show the direction of phase for coherence > 0.5 . Rightward-facing arrows indicate the time series are in-phase, leftward facing arrows indicate the time series are anti-phase,

downward facing arrows generally indicate that the first time series leads the second by 90 degrees, and upward facing arrows generally indicate that the second time series leads the first by 90 degrees. (A)-(D) The coherence between SEV-AEs number, amplitude, radius, and EKE time series and the Loop Current time series. (E)-(H) As in (A)-(D) but for SEV-CEs.155

Figure 4.5 The geographic properties, as in Figure 4.2, for each type of internal SEV-outer mesoscale eddy combination pair. (A)-(E) The generation number, the mean eddy radius (km), the mean eddy amplitude (cm), and the mean EKE ($m^2 s^{-2}$) for all SEV-AEs internal to mesoscale AEs. (F)-(J) As in (A)-(E) but for SEV-CEs internal to mesoscale AEs. (K)-(O) As in (A)-(E) but for SEV-AEs internal to mesoscale CEs. (P)-(T) As in (A)-(E) but for SEV-CEs internal to mesoscale CEs. The black box in (T) denotes the Loop Current region.....156

Figure 4.6 The time series of SEV properties, exactly as in Figure 4.3, but for only internal SEVs. Loop Current EKE is repeated without alterations. (A) The number of eddies per increment; (B) the median eddy amplitude (cm); (C) the median eddy radius (km); (D) the median eddy EKE ($m^2 s^{-2}$). (E) The EKE for the Loop Current region both with and without tidal variability. (F)-(J) As in (A)-(E) but using a box plot to show the median, quartiles, and extremes of the data upon which the time series is constructed.157

Figure 4.7 The Morlet wavelet coherence, exactly as in Figure 4.4, but for the internal SEV time series in Figure 4.6. The white dashed line shows the cone of influence, after which edge effects dominate, while the black arrows show the direction of phase for coherence > 0.5 . (A)-(D) The coherence between internal SEV-AEs number, amplitude, radius, and EKE time series and the Loop Current time series. (E)-(H) As in (A)-(D) but for internal SEV-CEs.158

Figure 4.8 The binned histograms, in number of eddies, between the coincident properties of parent mesoscale eddies (x-axes) and their internal SEVs (y-axes) for each type of internal SEV-outer mesoscale eddy combination pair (columns 1-4). (A)-(D) The lifespans (days) of SEVs versus their parent mesoscale eddy lifespans. (E)-(H) The radii (km) of SEVs versus their parent mesoscale eddy radii. (I)-(L) The amplitudes (cm) of SEVs versus their parent mesoscale eddy amplitudes. (M)-(P) The EKEs ($m^2 s^{-2}$) of SEVs versus their parent

mesoscale eddy EKEs. Linear regressions are shown as black lines with R^2 values annotated.159

Figure 4.9 The numbers, fractions of parent eddy area, and fractions of parent eddy EKE taken up by internal SEVs over the normalized lifespan of their parent eddies. Number of parent eddies in each figure is shown. The left y-axes depict the percentage statistics, while the right y-axis depict the number of SEVs. (A) The statistics for parent AEs with a maximum trajectory radius of between 25 and 75 km. (B) As in (A) but for parent CEs. (C) As in (A) but for eddies whose maximum radius lies between 76 and 125 km. (D) As in (C) but for parent CEs. (E) As in (A) but for eddies whose maximum radius lies above 126 km. (F) As in (E) but for parent CEs.160

Figure 4.10 The locational composites for all instances of internal SEVs, showing the likelihood of a SEV covering a given pixel in a mesoscale eddy in percentage points for each type of internal SEV-outer mesoscale eddy combination pair. (A)-(D) The composites for eddies of maximum radius between 25 and 75 km. (E)-(H) As in (A)-(D) but for eddies of maximum radius between 76 and 125 km. (I)-(L) As in (A)-(D) but for eddies whose maximum radius lies above 126 km.161

Figure 4.11 The composites for all SST anomalies ($^{\circ}\text{C}$) associated with internal SEVs (difference between center SEV temperature and mean temperature computed up to 3 radii) for each type of internal SEV-outer mesoscale eddy combination pair. (A)-(D) The composites for eddies of maximum radius between 25 and 75 km. (E)-(H) As in (A)-(D) but for eddies of maximum radius between 76 and 125 km. (I)-(L) As in (A)-(D) but for eddies whose maximum radius lies above 126 km.162

Figure 4.12 The composites for all SSS anomalies (PSU) associated with internal SEVs (difference between center SEV salinity and mean salinity computed up to 3 radii) for each type of internal SEV-outer mesoscale eddy combination pair. (A)-(D) The composites for eddies of maximum radius between 25 and 75 km. (E)-(H) As in (A)-(D) but for eddies of maximum radius between 76 and 125 km. (I)-(L) As in (A)-(D) but for eddies whose maximum radius lies above 126 km.163

Figure 4.13 The separation of the Loop Current Eddy AE trajectory #4, or AE4. (A) The percent of AE4's area and EKE taken up by SEVs over its lifespan, with black dashed lines showing the dates of the following snapshots. (B) The

large-scale SSH (m) field associated with Jan. 4th, 2012
showing AE4 (dashed line) and its internal SEVs (solid lines).
(C) As in (B) but for Feb. 26th, 2012. (D) As in (B) but for
Mar. 28th, 2012. (E)-(G) As in (B)-(D) but showing the
small-scale SSH (m) field instead.....164

CHAPTER 1

INTRODUCTION

1.1 REVIEW OF SUBJECT, REGIONS, AND KNOWLEDGE GAPS

1.1.1 EDDIES

Ocean coherent vortices, also known as eddies, are ubiquitous throughout the world's oceans, transporting as much mass as the rest of the major ocean currents combined (Zhang et al., 2014). Modern satellite altimetric Sea Surface Height (SSH) products, combined with advances in automatic eddy tracking algorithms, have helped to clarify the roles that eddies play in influencing climate on both regional and global scales (Amores et al., 2018; Chaigneau et al., 2008; Chelton et al., 2011; Trott et al., 2018). High-resolution modelling simulations, numerous *in-situ* measurements, and deep Argo floats have also helped to extend studies of eddy dynamics into the submesoscale (<25 km scale) from the mesoscale (>25 km scale) and the subsurface from the surface, where their impacts on related processes, such as air-sea interactions and water mass spreading, have been partially quantified (D'Addezio et al., 2020; de Marez et al., 2019; de Marez et al., 2020; Peterson et al., 2013; Sun et al., 2022; Verzemskaya, et al., 2021). However, despite the proliferation of such data sources, several unanswered questions remain, partly due to a lack of purpose-designed methods with which to apply to them. These include the persistent identification of specific large eddy structures, detection of coherent subsurface eddies, and an ability to surveil the submesoscale eddy fields hidden beneath the mesoscale eddy field signature (Beal & Donohue, 2013; Gula et al., 2019; Ni et al., 2021; Xu et al.,

2019; Zachariah et al., 2019). The guiding purpose of this dissertation is to elucidate these physical processes and related eddy dynamics using novel methodologies.

1.1.2 THE ARABIAN SEA

The first major region of study is the Arabian Sea (AS), located in the northwest Indian Ocean and straddling the equator. The AS is dominated by the seasonally reversing monsoon circulation (Schott & McCreary, 2001). This process of prevailing landward winds in the summer, called the southwest monsoon, reversing to seaward winds in the winter, called the northeast monsoon, causes a complete reversal of the AS current patterns (Beal et al., 2013; Schott et al., 1994; Schott et al., 1997). This seasonal disturbance sets into motion four annual equatorial Kelvin waves, two upwelling and two downwelling, which propagate along the equator and split into coastal Kelvin waves that travel along the Bay of Bengal and into the AS from the east, radiating Rossby waves westward as they travel (Brandt et al., 2002 Chaudhuri et al., 2021; Rao et al., 2010; Tozuka et al., 2014).

From these annual wind and planetary wave cycles, several climatological, *i.e.* recurrent at the same time of year, mesoscale eddies form, including the anticyclonic Great Whirl in the Somali Current in the southwest monsoon and the anticyclonic Lakshadweep High (LH) in the Lakshadweep Sea, to the southwest of India's tip in the northeast monsoon (Akuetevi et al., 2016; Beal & Donohue, 2013; Shankar & Shetye, 1997; Vic et al., 2014). These mesoscale eddies are responsible for significant changes in local conditions, including vertical subsurface motions and air-sea interactions (Rao et al., 2008 Wang et al., 2019). As a result, their detection and tracking are necessary components for regional monitoring (Melzer et al., 2019; Seo, 2017). However, while the Great Whirl has been consistently studied over the past decades (*e.g.* Melzer et al., 2019), the LH has not been

studied with modern data and tracking techniques since the turn of the millennium (*e.g.* Shankar & Shetye, 1997), meaning that its influences on local processes remain unclarified, such as the Arabian Sea Mini Warm Pool that precedes the onset of the southwest monsoon or the Rossby waves that propagate westward and kickstart the Somali Current in spring and into summer (Bruce et al., 1994; Kurian & Vinayachandran, 2007; Roman-Stork et al., 2020; Vic et al., 2014).

In addition to the LH, many subsurface processes in the AS remain undocumented. It is within this region that many intermediate water masses converge, including the Red Sea Water, Persian Gulf Water, and Antarctic Intermediate Waters (L'Hégaret et al., 2021; Prasad et al., 2001; Shenoi et al., 2005; You, 1998). These water masses mix and, depending on the part of the AS, may sink into the deep-water masses, *i.e.* Antarctic Bottom Water, or even upwell into the near-surface layers (Fischer et al., 2002; Morrison et al., 1998). Given the potential of subsurface eddies to spread and modulate these processes and other surface or near-surface eddies, their examination is critical for understanding regional circulation patterns, yet they remain under-studied, partly due to a paucity of methods for doing so efficiently (de Marez et al., 2019; Izumo et al., 2008; L'Hégaret et al., 2016).

1.1.2 THE GULF OF MEXICO

The Gulf of Mexico (GoM) is, unlike the AS, dominated by a single circulation feature: the Loop Current (LC) and its Loop Current Eddies (LCEs) (Leben & Born, 1993). The LC varies between two distinct phases, the extended phase and the retracted phase, with the transition between the former and the latter being the shedding of a large LCE that then propagates westward over a period of months (Brokaw et al., 2020). Whether or not an LCE is present in the GoM at a given time is of critical regional importance, for LCEs

intensify hurricanes, induce and shear phytoplankton blooms, spread oil spills, and modify the extent and intensity of the GoM hypoxic “Dead Zone” (Jaimes et al., 2016; Liu et al., 2009; Özgökmen et al., 2016; Potter et al., 2021; Rabalais et al., 2002; Toner et al., 2003). Modern forecasting of the LC and the formation of an LCE has reached an advanced state, with positional forecasting available weeks in advance courtesy of modern machine learning methods (Wang et al., 2019).

However, such prediction methods only consider mesoscale fields for lack of submesoscale data that might otherwise improve prediction quality. Recent studies suggest that the seasonal changes between the forward and inverse energy cascades between the mesoscale and submesoscale and their associated instabilities may play critical parts in the state of the LC (Bracco et al., 2019; Yang et al., 2021; Yang et al., 2020). With the advent of the Surface Water Ocean Topography (SWOT) mission in 2022 and data to be released later in 2024, wide-scale observational submesoscale SSH fields will become available for the first time (Chelton et al., 2019; Durand et al., 2020). It therefore becomes necessary for the submesoscale eddy field of the GoM to be surveyed using high resolution models, such that predictions of the effects of submesoscale eddies on mesoscale features like the LC can be made and validated against observational data. However, few methods exist for the algorithmic study of submesoscale eddies, particularly within mesoscale features whose signatures drown out the submesoscale (D’Addezio et al., 2020).

1.2 DISSERTATION OUTLINE

There are five chapters in this dissertation, including this introduction. Chapter 2 was published in the *Journal of Geophysical Research: Oceans* in 2022 and is titled “Lakshadweep High Propagation and Impacts on the Somali Current and Eddies During

the Southwest Monsoon.” Its focus is on the surface mesoscale eddy field of the AS, particularly the Lakshadweep Sea off the southwest coast of India. It explores the LH from 1993-2019 using a combination of remotely sensed observations, *in-situ* measurements from drifters, and high-resolution model data. These data are fed through an augmented automatic eddy tracking algorithm that is used to track the LH across the AS and ensure that its impacts on the surrounding waters are documented.

After Chapter 2 details one component of the surface eddy field of the AS, Chapter 3 investigates the subsurface eddy field. Titled “Subsurface Eddy Detection Optimized with Potential Vorticity from Models in the Arabian Sea,” this work was originally published in the *Journal of Atmospheric and Oceanic Technology* in 2023. Through it, the entire development of a novel subsurface eddy detection algorithm using the rescaled PV, including its optimization in comparison to other competing algorithms, is documented. The algorithm is utilized to effect in a high-resolution model in the southern AS near the Chagos Archipelago, and it is released to the public.

The last of the published papers that comprise this dissertation, Chapter 4, entitled “Characteristics of Submesoscale Eddy Structures within Mesoscale Eddies in the Gulf of Mexico from $1/48^\circ$ ECCO Estimates,” was published in *Frontiers in Marine Science* in 2023. This work focuses on the smaller scale eddy interactions that comprise the submesoscale in the GoM with a focus on internal eddy dynamics and eddy life cycles. The technique developed in this work utilizes the Dolph-Chebyshev window to design a custom spatial filter that separates the small scale from the large scale. A tracking procedure is applied to both scales, co-locating submesoscale eddies within mesoscale eddies. Through

this, the properties of the internal eddies are estimated and their impacts on upper-ocean properties in the GoM quantified.

Finally, the major conclusions of this dissertation are contained within Chapter 5, which also provides suggestions and directions for future studies using the methodologies developed in this work.

CHAPTER 2
LAKSHADWEEP HIGH PROPAGATION AND IMPACTS ON THE
SOMALI CURRENT AND EDDIES DURING THE SOUTHWEST
MONSOON¹

¹ Ernst, P. A., Subrahmanyam, B., & Trott, C. B. (2022). Lakshadweep High Propagation and Impacts on the Somali Current and Eddies During the Southwest Monsoon. *Journal of Geophysical Research: Oceans*, 127(3), e2021JC018089. <https://doi.org/10.1029/2021JC018089>

Reprinted here with permission from publisher.

2.1 ABSTRACT

Climatological eddies in the Arabian Sea (AS), including the Lakshadweep High (LH) and the Great Whirl (GW), play major roles in the regional fluxes of upper ocean properties. For the first time, we apply an eddy tracking algorithm to the LH using altimetric sea surface height observations from 1993 through 2019. We additionally analyze the LH's water mass composition throughout its life cycle using the 1/12° Global eddy resolving physical ocean and sea ice reanalysis (GLORYS12). We observe that the second annual downwelling coastal Kelvin wave's (CKW) arrival during the winter monsoon is primarily responsible for generating the LH. In March, Rossby waves propagate along 8°N at the same speed of that of the LH. In 17 of 27 years, the LH maintains coherence across the AS. The LH sustains a shallow lens of lower salinity Bay of Bengal water up to 68°E in these years. In the remaining 10 years, the LH dissipates between 60°E-70°E or fails to propagate beyond the southwest Indian coast. We attribute the differences between propagation types to fluctuations in the CKW strength, differences in wind stress between the southern tip of India and Sri Lanka, and the variable distribution of wind stress curl around the LH. We also find that longer propagating LH types negatively correlate with the eddy kinetic energy of the Somali Current region during the summer monsoon. We conclude that, upon its arrival in late July, the LH either merges with or replaces the GW, disrupting the cyclone that normally orbits the GW

2.2 INTRODUCTION

Oceanic mesoscale eddies are circulation features that contribute significantly to fluxes across the air-sea interface and transport seawater properties throughout the global oceans (Ma et al., 2016; Zhang et al., 2014). Previous studies have indicated the relative

importance of eddy dynamics to broader circulation patterns and the distribution of physical parameters, such as temperature and salinity, in the Arabian Sea (AS) (Fischer et al., 2002, Trott et al., 2018; Trott et al., 2019; Zhan et al., 2020). The AS is additionally characterized by seasonal variability due to the reversal of winds associated with the northeastern monsoon in the boreal winter and the southwestern monsoon in the boreal summer (Schott & McCreary, 2001; Beal et al. 2013). This circulation reversal results in the recurring development of several distinct, quasi permanent eddies that form and dissipate within the AS each year (Akuetevi et al., 2016). These include the Lakshadweep (sometimes named Laccadive) High (LH) and the Great Whirl (GW), among others (Figure 2.2.1). Each of these features has been subjected to observational and numerical model investigations that have shed light on their respective formation mechanisms and interannual variability (Beal & Donohue, 2013; Bruce, 1983; Bruce et al., 1994; Bruce et al., 1998, Vic et al. 2014). However, while the spatial variability of the GW has been extensively described both manually (Beal et al. 2013) and algorithmically (Melzer et al. 2019; Wang et al. 2019), the LH's complete life cycle has yet to be rigorously classified and tracked in the context of an eddy tracking algorithm, leaving questions regarding the interannual variability of the LH, including its propagation mechanism, its characteristics while propagating, and its ultimate fate in the AS basin.

The LH is an anticyclonic eddy that forms during the northeast monsoon off the west coast of India and to the east of the Lakshadweep islands (Figure 2.2.1a). It was first identified by Bruce et al. (1994), and later more specifically characterized in terms of linear planetary wave dynamics by Shankar and Shetye (1997). The formation mechanism of the LH put forward by these initial studies and later supported by a numerical study by Kurian

and Vinayachandran (2007) is that the LH is a result of the second annual downwelling coastal Kelvin wave (CKW) arriving from the Bay of Bengal in the late boreal fall and early winter (Rao et al. 2010), travelling northward along the western coast of India and radiating westward-propagating Rossby waves. It is worth noting that this same CKW is associated with the transport of low-salinity Bay of Bengal (BoB) waters around the tip of Sri Lanka and into the southeastern Arabian Sea (Shenoi et al., 2005). Therefore, eddies produced along these CKWs are more likely to have a fresher core water mass than the surrounding AS waters. After forming in late December or early January, the LH detaches from the coast and propagates westward across the Arabian Sea, most likely as a part of a Rossby wave, before appearing to become indistinct in mid basin by March (Bruce et al., 1998; Prasad and Ikeda, 2001). Although the Lakshadweep Low (the LH's summertime component) has been recently observationally and dynamically described (Zachariah et al. 2019), no study has specifically examined the LH's interannual variability, its observed life cycle over recent years, or its impacts on the rest of the AS circulation, such as the Somali Current (SC).

As the LH's dynamics can be largely explained in terms of planetary waves, it is important to understand the role Rossby waves play in the AS basin. The propagation of Rossby waves westward across the AS has been well documented (Brandt et al. 2002; Heffner et al. 2008; Subrahmanyam et al. 2001; Subrahmanyam et al. 2009; Tozuka et al. 2014). The Rossby waves radiated by the second annual downwelling CKW in particular have been demonstrated in a modelling study by Vic et al. (2014) to significantly alter the characteristics of the GW. In their "NO-RW" experiment, they modelled a situation wherein the Rossby waves from the west coast of India are blocked from propagating

across the AS basin. They found that the development of the GW was delayed by nearly two months as compared to the same model run with the Rossby waves allowed to propagate. Furthermore, they observe that the location of the GW is shifted 250 km to the southeast. This study provides compelling evidence towards the hypothesis of Beal & Donohue (2013) that the arrival of first- and second-baroclinic mode Rossby waves kickstart the formation of the GW and help determine its final location in the SC. Due in part to the size of the GW and its cold filament, as well as the intensity of the SC, there is a stable correlation between the sea surface temperature (SST) of the western AS, the strength of the atmospheric Findlater Jet that overlies the SC, and the quantity of summer monsoon precipitation over India (Findlater, 1969; Izumo et al. 2008; Murtugudde and Busalacchi, 1999; Seo 2017; Shukla, 1975; Vecchi et al. 2004; Wang et al. 2019). This sequence of correlations between the development of the GW and the SC and the summer monsoon as a whole highlights the importance of understanding the factors that influence the GW and the SC, as well as documenting the effects and variability of Rossby waves in the region.

Advances in satellite altimetry have yielded global observations with resolutions sufficiently high to track mesoscale eddies. Many authors have since developed automated eddy-tracking algorithms based on various physical properties, such as sea surface height anomaly (SSHA, used interchangeably sea level anomaly, or SLA), absolute dynamic topography (ADT), the Okubo-Weiss parameter, and others (Chaigneau et al., 2008; Chelton et al., 2011, Franz et al., 2018, Le Vu et al., 2018, Williams et al., 2011). Previous studies have since improved the accuracy of these algorithms (Pegliasco et al., 2015; Trott et al., 2018) and have used them to track merging eddies (Cui et al., 2019; de Marez et al.,

2020), as well as the life cycles of specific large eddies, such as the GW (Melzer et al. 2019). Thanks to advances in the number of floats and drifters available through initiatives such as Argo and the Global Drifter Program (GDP) as well as the accuracy of ocean circulation model and reanalysis products, these eddy tracking algorithms can even be used to provide estimates of the 3D structure of eddies over time, including in the AS (de Marez et al. 2019, Greaser et al. 2020; L'Hégaret et al. 2016; Trott et al. 2018).

In this study, we apply an automatic eddy tracking algorithm to 27 years of ADT satellite data from 1993 to 2019 in the AS. In doing so, we analyze the life cycles, trajectories, and properties of the LH in order to better understand it and the ways it may influence the interannual variability of the monsoon phenomenon. We provide the first 3D analysis of the LH and shed light on its subsurface profiles, interannual variability, and impacts on the rest of the AS, including the SC region and the GW within. The rest of the paper will be organized as follows. Section 2 describes our data and methodology. Section 3 presents our results, while Section 4 summarizes and concludes our findings.

2.3 DATA AND METHODS

2.3.1 DATA USED

ADT, SLA, and derived surface geostrophic currents used in this work are provided by the Copernicus Marine and Environmental Monitoring Service (CMEMS). This product is currently available daily from 1993 through June 2020 at a 0.25° global grid spacing resolution and is an optimal interpolation of altimetry satellites, merging observations from TOPEX/POSEIDON, HY-2A, JASON-1, JASON-2, JASON-3, ENVISAT, Saral/AltiKa, ERS1/2, Sentinel-3A, and GFO. The dataset is computed with respect to a twenty-year mean (Ducet et al., 2000; Le Traon et al., 1998) and has been recently used to track eddies

in the Arabian Sea (Trott et al., 2018). This dataset is available online from CMEMS at <https://marine.copernicus.eu>.

To obtain wind stress and compute wind stress curl (WSC), we use the U.S. National Oceanic and Atmospheric Administration (NOAA) Blended Winds Dataset, a 0.25° global grid resolution dataset daily from 1987 to 2021. The winds from this dataset are combined from all available satellite wind measurements, scaling from a single satellite in 1987 to more than 5 after 2000, including SSMI F13, SSMI F14, SSMI F15, TMI, QuikSCAT, and AMSR-E. This product is available from NOAA at <https://www.ncei.noaa.gov/products/blended-sea-winds> and has similarly been used in studies of the Indian Ocean and its monsoons (Liu et al., 2014).

We use ocean drifter surface location and current velocity data from the NOAA Global Drifter Program (GDP) to illustrate and validate the trajectories of our tracked eddies. This data is available at six-hourly intervals basis from 1979 through 2020, and provides an *in situ* method for measuring surface currents around and within eddies in the AS (de Marez et al. 2019). This product is available at <http://osmc.noaa.gov/>.

To obtain estimates for subsurface data, including temperature, salinity, and currents, we use the CMEMS $1/12^\circ$ Global eddy resolving physical ocean and sea ice reanalysis (GLORYS) 12v1 reanalysis, the next generation product with respect to the GLORYS2v4 dataset (Lellouche et al. 2018). This is a $1/12^\circ$ spatial resolution global dataset available daily for the altimetry era (1993 to 2021). It assimilates observational data from satellite and *in situ* datasets while its model component is based off of the Nucleus for European Modelling of the Ocean (NEMO) model 3.1 driven at the surface by European Centre for Medium-Range Weather Forecasts (ECMWF) ERA-interim analysis. It additionally

incorporates climatological runoff from Dai et al. (2009). This dataset was chosen due to its high spatiotemporal resolution and focus on accurate comparisons to observational CMEMS datasets of SSH, freshwater content, and EKE. Additionally, Verezemskaya et al. (2021) found GLORYS12v1 was the most accurate reanalysis dataset of the datasets they studied when used to study the variability of various ocean characteristics along a section of latitude in the ocean, an ultimately similar task to our study. GLORYS12v1 is available online at <https://marine.copernicus.eu>.

2.3.2 METHODOLOGY

2.3.2.1 EDDY TRACKING

In order to sufficiently describe the LH and its impacts on the GW and the SC, we must first be able to identify it discretely and track it over time and space. In order to classify eddies and map their trajectories, we apply the closed-contour eddy tracking algorithm developed by Chaigneu et al. (2008), upgraded by Pegliasco et al. (2015), and used throughout the Indian Ocean by Trott et al. (2018), Trott et al. (2019), Roman-Stork et al. (2020), and Greaser et al. (2020). As compared to other eddy methods, this method is threshold-free, detects a fewer number of false eddies, and allows for a more exact eddy shape. A complete explanation of the algorithm as applied here, including the cost function used for tracking eddy centers, can be found in Trott et al. (2018).

2.3.2.2 LH & GW CLASSIFICATION

The first step in tracking the impacts of the LH is correctly classifying the characteristic LH. While a previous study by Bruce et al. (1998) has correctly identified that the LH region generates multiple eddies, there is typically a single eddy that consistently dominates the circulation of the region after late December. It is this eddy that we examine

here and refer to as “LH.” To this end, after we applied the eddy tracking algorithm to the altimetry dataset, we filtered for all eddy trajectories that passed within the zone between 5°N-15°N and 71°E-80°E. We then additionally filtered for eddies that originated between the beginning of November and the end of January of each year. This spatiotemporal area was chosen based upon an evaluation of the preceding research (Bruce et al. 1998; Shankar & Shetye, 1997), the internationally recognized boundaries of the Laccadive Sea, and our own observations made in the ADT of the region over our 27 year timespan (Figure 2.2.1a). Once all eddies outside of this area were excluded, the eddies that passed inside the area were ranked from greatest to least in terms of their lifespan and maximum radius. The minimums of the sums of these rankings (*e.g.* the longest lived trajectory, ranked 1st, with the second highest maximum radius, ranked 2nd, is equal to a sum of $1 + 2 = 3$) were classified as major eddies within the region. This radius-ranking procedure is similar to the criteria used by Trott et al. (2018) to identify the GW, although we add the lifetime ranking to reduce the weight given to short-lived, large-radius outliers. This allowed us to narrow down the 108,883 individual trajectories down to a ranked list of the largest, longest lived eddies each year.

After this initial automatic classification, a manual examination was conducted on ADT maps of the region over all years, and the automatic trajectories were checked against the LH region. In 18 of the 27 years, the primary candidate identified by the automatic classification was correct in identifying the LH. However, the remaining 9 years, our initial algorithm falsely identified a signature corresponding to a characteristic eddy of the Southern Arabian High (SAH) as defined by Prasad and Ikeda (2001). This signal was initially difficult to differentiate from the LH automatically due to their near-identical

origin points off the southern tip of India and similar eventual large size. However, our manual reevaluation allowed a correction of these trajectories, as the SAH eddies propagate along 6°N beginning in December and January, while the LH eddies propagate along 8°N beginning in February and March. Adjusting the initial automatic selection criteria for eddies that remain in close proximity to 8°N for most of their lives results in a correct automatic identification of the LH 95% of the time. The outlier in this case is the year 2000, where manual examination reveals an LH that proceeds to join the SAH along 6°N.

We conducted the same ranking analysis followed by manual confirmation in order to identify the GW. In this case, the ranking algorithm’s initial eddy selection was correct in all years as confirmed by previous studies of the GW (Beal & Donohue, 2013; Melzer et al. 2019). It is worth noting that in ten of the 27 years studied, the SAH was directly identified as the GW with the same tracking number, indicating a persistent closed contour of ADT through the entire period. In 15 of the remaining years, the tracking number assigned to the GW was one of the SAH’s direct descendants (*i.e.* an eddy that split off from the SAH) as identified by our tracking algorithm. However, an analysis of the linkage between the SAH and the GW is outside of the scope of the present study.

2.3.2.3 VERTICAL VELOCITY

As in Greaser et al. (2020), we calculate the vertical velocity (w) using the zonal (u) and meridional (v) components of ocean currents from GLORYS12v1 by integrating the continuity equation:

$$\frac{\partial w}{\partial z} = -\left(\frac{\partial u}{\partial x} + \frac{\partial v}{\partial y}\right). \quad (1)$$

2.3.2.4 SPICINESS

The definition of spiciness used in our eddy analysis is the same one described by McDougall and Krzysik (2015) and implemented in the TEOS-10 Gibbs SeaWater (GSW) Oceanographic Toolbox. We use spiciness referenced to the surface as demonstrated in the AS by Echols and Riser (2020).

2.3.2.5 WIND WORK

Our definition and application of wind work to our analysis is defined in the same way as in Zhang et al. (2017):

$$WW = \overline{\tau_w \cdot v_0'}, \quad (2)$$

where τ_w denotes the wind stress and v_0 is the surface horizontal velocity. As in Zhang et al. (2017), the overbar reflects a time mean, while the prime denotes anomalies from that time mean.

2.3.2.6 RADON TRANSFORM

We use a two-dimensional Radon Transform (RT) to calculate Rossby wave speed in the AS. The use of the RT in regards to Rossby waves is the same as Deans (2007) and Challenor et al. (2001). We begin with a longitude-time (L/T) plot, in our case, a Hovmöller diagram of SLA. Then, the RT projects the diagram onto a line at an angle, θ , to the x-axis. The values along this line are taken with the angle varied from 0° to 180° . The standard deviation of the values on this line will be at its maximum when the line is perpendicular to the propagation direction of the Rossby wave, and, as such, the speed of the wave can be obtained by taking the tangent of θ at the angle of maximum standard deviation:

$$c_{RW} = \tan(\theta) \cdot \cos(\varphi), \quad (3)$$

where φ is the degree of latitude of the L/T plot. In this study, we plot both the cumulative intensity image directly output by the RT as well as the standard deviation of the SLA in the cumulative intensity image.

2.4 RESULTS

2.4.1 OVERVIEW OF LH TRAJECTORY TYPES BY YEAR

Upon identifying the trajectories corresponding to the LHs, we proceed to map out their origin points, the points at which their trajectories terminate, and the average trajectories of the LH propagation (Figure 2.2.2).

The end behavior of the LH is classifiable into three distinct groups depending upon the termination point of the eddy track (the point at which the closed contour breaks and the eddy ceases being a closed, coherent whirl). The most numerous, occurring in 17 out of the 27 years, is the propagation type in which the LH is able to remain coherent past 60°E, most often reaching the outermost contour of the GW before dissipating. For the rest of this study, we refer to this type of propagation as “full” and the years in which this type occurs as “full years.” The second most common, occurring in 6 of the remaining years, is a type in which the LH begins propagating across the AS basin but loses coherence between 60°E and 70°E, roughly the halfway point between Somalia in the west and India in the east. It is for this reason that we will refer to this type of propagation and its years as “half” and “half years” respectively. Finally, in the remaining four years, the LH may move slightly off the west coast of India, but never propagates west of the Lakshadweep islands. Due to its lack of movement away from its origin, we deem this type the “local” type and

its years “local years.” The total list of year wise classification, along with relevant climatic phenomena, such as the El Niño Southern Oscillation (ENSO) and the Indian Ocean Dipole (IOD) is in Table 2.1.

It is worth noting in Table 2.1 that, as the LH forms late in the previous year, the formation circumstances of each year’s LH are owed primarily to the previous year. In Table 2.1, strong (weak) monsoons are defined by total monsoon rainfall that is 10% above (below) the long term mean (Subrahmanyam et al., 2020). We note that both strong monsoons are half years, while every local year occurs either on or after an El Niño event. However, other El Niño years precede full years (*e.g.* 2015). Based on this distribution, we conclude that the full propagation type represents a relatively normal state for the LH and that specific changes to the generation and development of the LH are necessary to explain the difference between these typical years and the atypical half and local years. We further discuss the connection between El Niño, IOD, and half/local years in section 2.4.2.

We display years that best illustrate the notable features of LH's type of propagation. As the development and propagation of LH occurs on slightly different timescales and in slightly different locations each year, choosing example years allows us to highlight common features that geographic composites may disperse due to the averaging process over both time and space. We choose 2006 for full propagation, 1994 for half propagation, and 1998 for local propagation. These years in particular are chosen because these years’ LHs develop and propagate on similar timescales (*i.e.* Figure 2.2.3) and demonstrate most of the unique features of their respective propagation types. As a result, their development can be compared to each other at the same time in their respective years. Additionally, the

1994 LH is the LH analyzed by Bruce et al. (1998), allowing us to highlight differences between studies.

We observe that the high encompassing the LH in the winter monsoon is greater in extent in 2006 (470,000 km², Figure 2.3a) than in 1994 (384,000 km², Figure 2.3d), and that the same region in 1994 is larger than in 1998 (110,000 km², Figure 2.2.3g). This high is determined via a 10 cm SLA threshold; this was chosen to align with Rao et al., (2010), where the 10 cm threshold is used to define a “strong” equatorial Kelvin wave in the Indian Ocean. Here, we use the threshold in much the same way, using it to define the extent of strongest CKW influence, both here and in Section 3.2. Upon an examination of the GW in the summer monsoon, we find that the 2006 LH is directly influencing the GW in July (3c) while the 1998 GW is much larger and more coherent at the same time of the year (Figure 2.2.3i). As noted by Beal and Donohue (2013), the 1998 GW remains the largest GW on record.

To further examine the LH trajectories of these years, we collocate each LH with drifters from the GDP (Figure 2.4). We find that the 2006 LH influenced two drifters in its early lifetime while trapping four more much later in its life. We attribute this latter phenomenon to the fact that the LH enters the SC region as the GW shifts towards the island of Socotra (Figure 2.3c), growing and remaining in place in the SC for the rest of the calendar year. As a result, the 2006 LH spends the last months of its life largely stationary and thereby with more capacity for the recirculation of an individual drifter (Figure 2.4a). This stationary aspect is the same for the 1998 LH, as it captures a single drifter, which circulates about the LH for 50 days (Figure 2.4c). The 1994 LH did not capture any drifters, likely due to the paucity of drifters in the AS as compared to later

years, as well as the fact that it does not remain stationary for a long period of time, as the 2006 and 1998 LHs do (Figure 2.4b).

Here, we compute the error between the geostrophic currents derived from altimetric observations and the surface currents measured by drifters. Across all LH trajectories, this error averages 43%, while the error for the specific trajectories in Figure 2.4 is 57%. This average error is plausible for eddies within the AS (de Marez et al., 2019), as the expected range of errors varies from negligible error at the edges of eddies to 500% at the center. It is worth noting that the average error present in the zonal (u) components of drifter-measured velocity is just 10% of the meridional (v) components on average, indicating that the ageostrophic components of the flow in the LH are generally far more meridional than they are zonal when being measured by drifters. This is likely due to the times of year that the LH traps drifters, as the LH traps drifters primarily while it circulates in place in either the SC (Figure 2.4a) or off the southwest Indian coast (Figure 2.4c). These stationary periods coincide with the most intense periods of the summer and winter monsoons, respectively. During these times, the meridional winds are at their zenith, and, as such, the ageostrophic components of the flow will likewise be more meridional than zonal in nature.

2.4.2 LH FORMATION & POST-FORMATION CHARACTERISTICS

Similarly to the conclusions presented by Shankar and Shetye (1997) and Bruce et al. (1998), we find that the initial formation of the LH can be attributed to remote forcing, specifically the arrival of the second annual downwelling CKW in late November and early December (Figure 2.5). The composites clearly demonstrate the propagation of a high in SLA propagating around the Bay of Bengal (BoB), past Sri Lanka, and arriving in the Laccadive Sea in mid-November. Of particular note is the difference in the average

strength of the arriving high in late November and early December. This high extends between the southern tip of India and Sri Lanka first in full years (Figure 2.5c) and then in half years (Figure 2.5j), but is never fully formed in local years (Figure 2.5o, p). It is at this time in early to mid-December that the LH typically forms (Figure 2.5d, j, p). The full year CKW continues to extend further to the northwest than half or local years' CKWs through January (Figure 2.5e), before expanding slightly westward towards the end of January (Figure 2.5f). While this extended area is present in half years as well (Figure 2.5 k-l), it is nearly entirely absent in local years (Figure 2.5 q-r). Instead, the SAH is elevated in January of local years. Statistically, the correlation between the yearly date of maximum SLA at the entrance to the Laccadive Sea at 80°E (the right side of the box in Figure 2.5) and the formation date of LH is significant ($p < .05$). This in conjunction with the appearance of the LH in early December (Figure 2.5d, j, p) supports the hypothesis that the timing of the onset of the second annual downwelling CKW is intrinsically related to the formation date of the LH.

To quantify the relationship between the extent and strength of the CKW and the formation of the LH, we have extracted the anomalies of SLA and elevated SLA area within the LH formation area, *i.e.* the black boxes annotated in Figure 2.5 (shown in Figure 2.6). We find that the early November amplitude of the area is roughly equivalent between full and local years before diverging in mid-December (Figure 2.6a). After early December, full years are always greater in amplitude and extent than local years (Figure 2.6a-d). This represents the strongest section of the CKW (Figure 2.5d, j, p), and reflects the results in Figure 2.5. Half years, however, are more variable, with peaks and troughs that can bring half years above full years (late January of Figure 2.6a, December through January of

Figure 2.6d) or below local years (February of Figure 2.5b, Figure 2.5d). That said, half years typically remain above local years and are generally similar to full years. Due to the consistently below-mean amplitudes and extents of local CKWs, we suggest that the less intense CKW is a major factor leading to the differentiation between full/half years and local LH propagation types.

Our assessment of the CKW in the Laccadive Sea both mirrors and contrasts other studies of CKWs in the Indian Ocean. For example, Rao et al. (2010), the study from which the 10 cm SLA threshold is taken, classifies 1997 as one of the weakest years in terms of equatorial Kelvin wave strength. As the CKW in Figure 2.5 originates in the previous year, their 1997 equatorial Kelvin wave is the wave that splits into the CKW that generates 1998 LH here, and so it follows that a weaker equatorial Kelvin wave produces a weaker CKW and weaker LH. Similarly, they classify several of our other local and half years as ‘weak’ (*e.g.* 1994 and 2004) and several of our full years as ‘strong’ (*e.g.* 1996 and 2000). However, for each year classification that is in agreement, there is another classification that is not in agreement (*e.g.* our 2005-2007 years are all full years, while their 2005-2007 years are all either ‘weak’ or ‘IOD’, *i.e.* absent). Therefore, our results relating to the apparent strength of the second downwelling CKW in the Laccadive Sea require an additional analysis besides the original equatorial wind forcing of the Kelvin waves to explain their interannual variability.

For this additional analysis, we look to Suresh et al., (2016), who demonstrated the role of wind forcing over the southern tip of India and Sri Lanka (“STIP”) and hypothesized its role in the formation of the LH. We plot the wind stress and SLA in this region in Figure 2.7. We find that there is a general agreement between full and half years for the entire

period (Figure 2.7 a-f, g-l) in both wind stress and SLA. However, there is a notable difference between full/half years and local years (Figure 2.7m-r) especially in late November (Figure 2.7d, j, p) and late December (Figure 2.7f, l, r). This additionally manifests in the form to a higher SLA to the west of the STIP region.

We calculate in Figures S2 and S3 the lag correlation between the wind stress over the STIP region, both as in Suresh et al., (2016), and in the area between 5°N, 9°N, 76°E, and 80°E as in Figure 2.7. We find that the strongest correlations between wind stress in the latter region and SLA in the LH region occur at a 30-60 day lag (Figure 2.S3e-f), with significantly higher correlations in full years than in either half or local years (Figure 2.S3l-m, s-t). This suggests that the wind forcing in the STIP region contributes more heavily to the post-new-year phase of LH development in full years than in either other type of year. As a result, differences between full, half and local years lie not just in the amplitude of the CKW, as in Figure 2.5, but also in the wind stress in the STIP region prior to the new year.

We now examine the three-dimensional structure of the LH, beginning one month after its formation in 2006 (Figure 2.8). The 2006 full LH's core amplitude at this stage is 112 cm (Figure 2.8a), and it is entraining fresher BoB water into its core from the south, with a core sea surface salinity (SSS) that is 3.1 PSU fresher than the northwestern flank of AS water (Figure 2.8b). This entrainment is similarly visible in the surface temperature profile (Figure 2.8c). The difference in the surface spiciness of the two masses confirms that it is SSS and not sea surface temperature (SST) that is the dominant property separating BoB water from AS water (Figure 2.8d). The lens of BoB water extends to a depth of approximately 50 meters before the saltier AS water dominates below the halocline (Figure

2.8e, f). The vertical extent of the BoB water is consistent with studies of winter monsoon transports in the region, which confirm that BoB water transported around Sri Lanka is limited to the upper 100 meters of the ocean (Schott et al. 1994). The depth of the BoB water is also visible in the depth of the thermocline, as the temperature remains relatively uniform down to 90 meters (Figure 2.8g). There is strong upwelling on the eastern side of the eddy, with a region of subsurface downwelling to the west (Figure 2.8h). This pattern of western downwelling and eastern upwelling is consistent with the modelling of Rao et al. (2008), namely their Figure 2.12, which displays a similar region of downwelling corresponding to the western flank of the LH. As noted by Rao et al. (2008), this downwelling can be expected to move westward along with the LH in full and half years.

The center amplitude of the 1994 half LH is comparable to but less than the full LH at 106 cm (Figure 2.9a). The half LH is also further to the northwest as compared to the full LH and so the salinity and temperature signatures of the BoB water is shifted to the south relative to the center of the LH (Figure 2.9b, c, d). A filament of the AS water is pulled around the northern edge and into the core of the LH from the east, swirling and mixing together with the BoB water from the south and southeast. This results in a less pronounced fresh lens, with the lower density BoB water being shifted to the west of the center of the LH (Figure 2.9e, f). The temperature profile is similar to the full LH, with the exception of a small shallowing of the thermocline on the western edge. As with the full LH, positive vertical velocity dominates the center of the LH while a negative vertical velocity is seen below the surface to the west (Figure 2.9h).

Finally, the amplitude of the 1998 local LH is the smallest of the three LHs, achieving only 98 cm at the center (Figure 2.10a). Of particular note is the scale of the ADT (Figure

2.10a) and SSS (Figure 2.10b) as compared to its full and half counterparts. The entire region is nearly 10-20 cm lower in 1998 than in 2006. This is likely due to the CKW amplitude differences discussed in regards to Figure 2.6. The SSS minimum is only 32.9 PSU as compared to the 31.3 PSU of 2006, and the high surface temperature signature of AS water is more prominent to the northeast of the LH (Figure 2.10b, c). These comparisons indicate that the mean flow of BoB water into the region is substantially reduced between full and local years, confirmed by the spiciness of the region, which demonstrates only a small filament of BoB water on the west coast of India (Figure 2.10d). The isopycnals are more clustered and the thermo- and haloclines more condensed in the local LH, reflecting this comparative lack of mixing and shallowing of the mixed layer depth (Figure 2.10e, f, g). In the same way, the up- and downwelling of the LH are both less intense than in full or half years.

Contributing factors to the differences between this local LH and the full and half LHs before it include the combined 1997-98 El Niño and fall 1997 IOD event. Durand et al. (2009) find that the East India Coastal Current flows anomalously poleward prior to the 1998 winter monsoon, while Jensen (2007) models that BoB water penetration into the AS basin during the winter monsoon should be lowered during El Niño years and entirely absent during IOD years. In 1998, these factors occur at once, combining with the smaller CKW to possibly facilitate a lower-magnitude LH. It is worth noting that the 1993-1994 El Niño/IOD event is generally a less extreme version of the 1997-1998 event (Schott and McCreary, 2001), which matches well with our classification of those years as half and local years respectively. This analysis is complicated by the fact that ENSO/IOD modes manipulate each other and the monsoons in following years (Izumo et al. 2010, Yuan et al.

2008). Further research into the exact consequences of ENSO/IOD on the Laccadive Sea during the winter monsoons would be required to quantify the precise amount of variability in the LH due to these events.

2.4.3 LH DEVELOPMENT POST-FORMATION

As CKWs are transient (*i.e.* Figure 2.5) and are subject to substantial interannual variability, they may fail to provide the continual energy required for the maintenance and expansion of the LH. Furthermore, we find that the elevated SLA area calculated in section 2.4.2 more than doubles after the new year. In full years, this area reaches an average of 332,000 km², 12,000 km² larger than in half years and 77,000 km² larger than in local years. While this may be partially attributed to the wind stress in the STIP region (Figure 2.7), there may be other factors during this time that assist in forcing the growth of the LH. Specifically, we explore the hypothesis put forward by Bruce et al. (1998) that the expansion of the eddy field is due to strong negative WSC in the LH region over the course of the winter monsoon (Figure 2.11).

There is indeed a strong ($< -1 * 10^{-7} \text{ N m}^{-3}$) region of negative WSC in the average case of all modes of LH propagation in January and February (Figure 2.11a-b, g-h, m-n). In each type, the WSC weakens around the LH after February (Figure 2.11c-d, i-j, o-p) before increasing in magnitude dramatically with the onset of the summer monsoon in May and June (Figure 2.11e-f, k-l, q-r). It is worth noting that the full type of LH on average propagates into another region of negative WSC as the summer monsoon intensifies (Figure 2.11f). This may explain why the full LH deteriorates in the central AS before restrengthening as it enters the SC region, and why the half LH dissipates during the intermonsoon period (Figure 2.11k-l). In order to further provide evidence for this connection,

we examine the normalized point-by-point covariance for the average LH of each type during the same time period in Figure 2.11 (Figure 2.12).

We find that the normalized covariance supports the WSC hypothesis, as a negative covariance indicates that a negative WSC is forcing a more positive ADT throughout January and February (Figure 2.12a-b, g-h, m-n). The LH is constantly in a region of significant correlation in regards to local wind forcing the ADT field during this time. Furthermore, we see that the LH as it propagates in the full and half modes seems to ride a line of exactly 0 covariance with a non-significant correlation (Figure 2.12c-e, i-k) suggesting that the eventual dissipation of the half LH is likely not caused by any active effect of the wind, rather, due to a lack of wind. This lack of correlation with local wind suggests the ADT field is primarily due to by non-wind forcing, in this case a Rossby wave, which we expand upon in section 2.4.4.

We take a closer look at the effect of the wind on LH growth by quantifying WW and the WSC alongside the radius and EKE of each type of LH over their development periods (Figure 2.13). The largest quantity of wind work is done over the LH during the first months of the LH's life, consistent across all LH types (Figure 2.13a). The effect of wind reduces over time in most cases so that the third month's wind is generally less intense than the first month's wind. We find that the full LH experiences above-average WW in the first two weeks of its lifespan and again around 35 days after formation (Figure 2.13b). We also find a strong spike in WW centered around 60 days post-formation. With these spikes aside, there is little average deviation across year types. We also find that WW varies considerably within an individual year (Figure 2.13b). Overall, we do not find any significant correlation between amounts of wind work done and mode of the LH. By

contrast, the WSC manifests a very particular pattern, as negative WSCs correlate with local LHs (Figure 2.13c). Additionally, the net WSC over the 2006 and 1994 LHs is positive for the first two months of their lives (Figure 2.13d). Regardless of the sign of the WSC, the LH grows substantially between the first and second months before typically plateauing or diminishing slightly after its third month (Figure 2.13e, f). This decline is more sharply pronounced in the radius of half and local LHs than in full LHs. The end result is that the radii of full LHs are generally comparable with the radii of half LHs and significantly larger than the radii of local LHs at the end of the growth period. This mirrors the end state of EKE (Figure 2.13g, h), where both the full LH and the 2006 LH lie substantially above the average as compared to the below-average performance of half (1994) and local (1998) LHs. If the LH were being directly grown through the negative WSC, then the opposite would be expected, as the local/half LHs receive a more negative WSC and a similar amount of WW to full LHs.

A possible explanation for this lies in the recent work by Rai et al. (2021) that demonstrates that the wind extracts more energy than it inputs into the small scale circulations across the global oceans, a phenomenon dubbed “eddy killing.” As the individual LH eddy is rarely larger than their threshold for small-scale circulations (260 km), it would follow that the wind is actually “killing” the LH, rather than enhancing it as expected. Even with this eddy killing effect, the wind would still be simultaneously energizing the large-scale circulation of the Laccadive Sea, forcing Rossby waves within the region as concluded by Brandt et al. (2002). These large-scale Rossby waves would then explain the growth of maintenance of LH, as we demonstrate in Section 3.4 that the LH is carried along them. However, the relative amount of energy taken from the LH by

eddy killing as compared to the energy entered into LH by the forcing of Rossby waves remains unclear. This warrants further research into how eddy killing changes over the course of the monsoons, but this is outside the scope of the present study.

We also find that, both in the average (Figure 2.S1a) and the example years (Figure 2.S1b), the LH experiences frequent spikes and average higher values in terms of nearby mesoscale eddies over the first three months of its life. This, combined with observations of the half and local LHs, indicates that these propagation types undergo more extensive splitting events during their growth periods. This provides another way for the half and local LHs to diminish by transferring energy from the mesoscale to the submesoscale. Algorithms specifically tailored to the splitting and merging of eddies, *e.g.* Tian et al.'s (2021) *EddyGraph*, are currently being developed and may be used to more specifically quantify the effects of these processes on the LH. Additional submesoscale measurements, such as those collected from the NASA Surface Water and Ocean Topography (SWOT) mission, will also help elucidate this process of energy transfer.

We close this section by suggesting that local years are the minority of total years because they require both a weak CKW (Figure 2.5) and a greater diminishing of the LH specifically due to the effect of the wind (Figure 2.13) and by eddy splitting (Figure 2.S1) as compared to full years, which represent a relatively normal or strong state of CKW propagation and normal or weak WSC in the eastern AS.

2.4.4 LH PROPAGATION

While we have since investigated both the formation and developmental mechanisms and the variability of those mechanisms with respect to the LH, we still need to address its

westward propagation using a Hovmöller diagram (Figure 2.14). The propagation of the LH is, on average, latitude restricted between the bounds of 7°N-9°N (Figure 2.2.2).

The typical propagation of LHs is restricted to a band of high SLA, rarely leaving the 10 cm contour defined in Section 3.2. Even in half and local years, this contour extends across the basin (Figure 2.14b, c). We also note that the width of this contour is narrower around March in local years (Figure 2.14c), as it diverges from the average path of the LH. These two factors together demonstrate that this westward propagating high is independent of the participation of LH, but increases in magnitude when the LH propagates with it.

In order to confirm whether or not the propagation of LH is a fundamental aspect of the first downwelling Rossby wave, we perform a Radon transform (RT) on the L/T plot in Figure 2.14 (Figure 2.15).

According to the maximums in the standard deviations of the transform, we find that the corresponding degree of rotation is between 6° and 7° (Figure 2.15d) and that the resulting Rossby wave phase speed is between 11.13 and 13.37 cm s⁻¹ (per Equation 3). This reasonably matches the observations and theoretical calculations of previous studies along this same latitude band (see Subrahmanyam et al., (2001) Table 4). Furthermore, upon taking the location of the average full LH on March 1st and its eventual destination when it terminates in late July (Figure 2.14a) and calculating the distance it travels divided by the time it takes to propagate, we find an average propagation speed of around 12.1 cm s⁻¹. Given that the two speeds align, we suggest that the LH's propagation across the AS basin is due primarily to a Rossby wave bound to 8°N. The mechanism for this propagation may be as presented by Polito & Sato (2015), who demonstrated that the phase speeds of eddies and Rossby waves will tend to align such that an eddy “rides” Rossby waves. This

speed alignment occurs due to an out-of-phase eddy being forced by an asymmetric divergence field towards the Rossby wave crest, and functions primarily in situations where an eddy and a Rossby wave are locked in phase for large durations, such as the LH transiting across the AS.

As noted earlier, the strength of this Rossby wave is largely attributable to the same factors as LH, *i.e.* the initial CKW and the subsequent WSC over the region (Brandt et al., 2002). Due to this, it would follow that a weaker LH would be less likely to accompany a weaker Rossby wave. A smaller LH in local years may also fail to propagate due to needing to pass through the Lakshadweep islands and over the Chagos-Laccadive Ridge. The LH may then remain trapped behind the ridge. The exact effects of the Lakshadweep islands on the eddy field around them is unstudied, but, as the LH is in the lee of the islands during the winter monsoon, it is possible that their presence enhances the EKE of the LH in a similar manner to that demonstrated by Calil et al. (2008). This could bolster the local LH until the end of the winter monsoon, which is indeed what we observe, as the local LH in 1998 persists into March.

We continue our examination of the LH structure over time in each of its modes, beginning with a snapshot of the full type in late March of 2006 as it propagates (Figure 2.16). At this point in time, the full LH has travelled 780 km west and 190 km north from its position in Figure 2.8. We find that, even as the full LH is no longer affected by the local WSC (Figure 2.12c), the LH remains remarkably coherent after it passes 70°E with an amplitude of 103 cm (Figure 2.16a). Its low-salinity lens has been carried with it but is less than 40 meters deep and has been eroded at its minimum from 31.5 PSU to 33.5 PSU (Figure 2.16b, f). This is reflected in the difference between the low core density of the LH

and the high density of surrounding AS water (Figure 2.16e). The spiciness profile confirms that this is still an exchange of water masses dominated by differences in salinity (Figure 2.16d) as temperature is still largely comparable across the eddy (Figure 2.16c, g). Lastly, the vertical velocity profile is similarly eroded and not nearly as pronounced near the surface as earlier in its life cycle (Figure 2.8h). Regardless, at this point, the 2006 LH is still strongly defined in relation to its surroundings.

This may be contrasted with the profiles of the 1994 LH (Figure 2.17), which present an eddy close to decoherence. The half LH here has travelled slightly further westward as compared to the full LH (890 km vs. 780 km) and instead of propagating northward, it has instead moved southward by 140 km. The ADT amplitude of the half LH is still pronounced, achieving over 90 cm at its center, but this high is shared with smaller eddies to the southeast and southwest (Figure 2.17a). The geostrophic current vectors around the LH are already flowing into these eddies, facilitating an exchange that is visible in the SSS profile (Figure 2.17b) and the SST profile (Figure 2.17c). Here, relatively low salinity water is transported from the southwest into the center of the LH before being carried around the eddy center and into the southeast eddy. For the first time, the spiciness profile displays characteristics of both the mixing of salinity and temperature, though the salinity profile still dominates (Figure 2.17d). The LH eddy center has been meridionally compressed, and carries only a very shallow, less than 30-m deep contour of approximately 34 PSU water that is similarly visible in the density profile (Figure 2.17e, f). While there is still a column of positive vertical motion to the eastern side of the LH (Figure 2.17g, h), this eddy is otherwise close to splitting. In fact, a week after this snapshot, it will splinter into the eddies around it, although its core maintains coherence as a substantially smaller

eddy for several months. This core, now with less than 50 km in radius, repropagates eastward and then northward before finally dissipating on June 10th (Figure 2.4b).

Lastly, we examine the fate of the 1998 local LH, which has only shifted 110 km south and 55 km east since it was last examined in Figure 2.10 (Figure 2.18). As with the half LH, the local LH is beginning to lose coherence amidst other eddies (Figure 2.18a). Its geostrophic current vectors also begin to flow into these competing eddies to the north and northeast. However, due to its proximity to the west coast of India, it still maintains a relatively fresh core of under 33 PSU that is prominent in the near-surface density profile (Figure 2.18b, e, f). This fresher water is being supplied from the east along a relatively strong current, a remnant of the winter monsoon current. Beyond this fresh core, the temperature across the LH is near-uniform, with only minor differences about a mean of 31 °C (Figure 2.18c, g). As a result, the spiciness profile again reflects salinity primarily (Figure 2.18d). The vertical profile lacks any kind of centrally occurring pattern, with a negative column overlying a positive column to the west (Figure 2.18h). As with the half LH of 1994, this eddy will dissipate soon, merging with the northern eddies and losing coherence in its core on April 11th.

2.4.5 EFFECT ON SOMALI CURRENT

Even after the half and local LHs have decohered, the full LHs continue to approach the SC region, possibly bolstered by the WSC prior to and during the onset of the summer monsoon (Figure 2.11f). Therefore, we next examine the changes in the SC region that result from the different modes of propagation of LH (Figure 2.19).

Here, the SC region is defined as the area between the Equator, 11°N, 40°E, and 58°E (similar to de Marez et al. 2019, Figure 2.5a, area B). We immediately find that there is a

large spike in all median eddy characteristics at the end of August in 1998, followed by a sharp decline, then another spike (Figure 2.19c). Due to the median being used for this analysis, this indicates that there is a merging of eddies (the first spike), followed by a major splitting event (the dip), concluded by another major eddy merger (the second spike). This hypothesis is supported by the abrupt apparent dissipation of the original tracked GW at the beginning of July, simultaneously with the dip in median eddy characteristics. In effect, the GW undergoes a rapid series of splittings and mergers, with the resulting GW emerging even stronger for the first weeks of August. However, these August spikes are almost entirely absent in 2006 and 1994, and the high in the SC EKE continues after the GW has reached its zenith (Figure 2.19d). The only other major spikes are those in the properties of the SC eddies in mid-June of 2006 and in the SC EKE in mid-early July (Figure 2.19d). An examination of the ADT of the region over time reveals that this first spike is largely attributable to the arrival of the forward elements of the 8°N Rossby wave, while the second spike is the arrival of LH itself. The dip shortly afterwards is due in part to the ejection of the GW from the defined SC region.

In regards to the full-lifetime LH EKE profiles (Figure 2.19e), we find that the main divergence between 2006, 1994, and 1998 occurs in early March, with the full LH emerging as more than twice as energetic as the half or local LH. In addition, the 2006 LH is the only LH of the three here that begins a second period of growth, as it enters the SC region in July. It is worth noting here that the dissipation dates of all half LHs are clustered around a mean of May 23rd, with the latest date being June 23rd and the earliest date being May 5th. In all circumstances, the half LH dissipates either by merging (splitting) with (into) several nearby eddies, as in 1994 (Figure 2.16), or by slowly reducing in size until it

is no longer defined, as in the year 1999. In each case, the LH dissipates before the maximum of the southwest monsoon is reached (Figure 2.11k, l). Given the matter of a month until the southwest monsoon peak revitalizes the full LH (Figure 2.19e) as noted above, the difference in strength between the full and half LHs is just enough to fail to sustain the half LH until this latter period of growth.

Of additional interest in Figure 2.19e is the decline of the GW in late August of 2006. This occurs due to the GW travelling northward at the same time as the LH enters the SC from the east. The LH then remains stationary in the SC in the GW's previous location until it dissipates. After one last spike in EKE in mid-August, the GW rapidly diminishes and dissipates by September, while the LH slowly decreases in EKE until the end of October. Although not the usual case for LH across all years surveyed, this type of event where the GW rapidly diminishes as the LH grows larger in the SC did occur five times over the period surveyed, in 2000, 2006, 2007, 2014, and 2017 (the eddy identified as the LH in 2000 is notable for being additionally identifiable as the SAH, GW, and Socotra Eddy (SE) at different points in its more-than-year long lifespan, a unique feat among all eddies surveyed).

In order to determine if the changes in the SC by type of LH are robust, we survey the average characteristics of the SC region over all years (Figure 2.20).

The results presented in Figure 2.20 demonstrate that the early-August peak in all eddy characteristics, as well as SC EKE, remains even when averaged across all years. It is worth noting, however, that these years only seem to affect maximums of these properties, less so the average values (Figure 2.20e-h). This indicates that it is the largest and most energetic eddies that are being altered, and that these eddies are in turn influencing the EKE

of the SC as a whole. Given the consistent spikes and implications on major eddies, we proceed to examine the differences in the dynamics of the SC region between each type of year to determine possible causes.

We begin with a look at the average WSC of the region over time (Figure 2.21) as well as the covariance between the WSC and ADT (Figure 2.22) as previously seen in Figures 11 and 12. Figure 2.21 is different than Figure 2.12 in that the second and third columns are the differences between full years and half years, and the differences between full and local years respectively. This is to visualize the changes from one year type to another.

Here, we can view the onset of the summer monsoon and the Findlater Jet between May and June (Figure 2.21b-c, h-i, n-o) and the subsequent swelling of the GW along the southern edge of the jet through the heavily negative covariance during the entire summer monsoon (Figure 2.22c-f, i-l, o-r). The most striking difference between the year modes is the region of much more negative WSC on the northern flank of the GW. There is also a more positive WSC on the eastern flank in July and August of both the half years (Figure 2.21j-k) and full years (Figure 2.21, p-q). This more positive WSC may help induce the slightly greater peaks in the half and local years' SC EKE as compared to the full years in Figures 19 and 20. Furthermore, we observe a positive WSC and covariance on the eastern flank of the GW in local years in August (Figure 2.22q). This indicates an enhanced development of the cyclone that often orbits the GW from northwest to southeast (Beal & Donohue, 2013). As noted in Section 3.3, the variability of eddy killing within monsoons in the AS has not been studied. However, recent measurements of the radius of the GW indicate an average radius above 300 km (Melzer et al. 2019). Therefore, the GW and its cyclone, which reaches a similar size, are above the most recent estimates for the global

eddy killing scale of 260 km (Rai et al. 2021). Together with Figure 2.22, this allows us to reasonably conclude the GW's growth and the growth of its orbiting cyclone are primarily due to the WSC over the region. The same conclusion applies to the LH as it typically grows in the SC in July (Figure 2.22d).

In order to assess the growth of the GW and its cyclone independently, we separate the amplitude, radius, and EKE of the SC between anticyclonic eddies (AEs) and cyclonic eddies (CEs) (Figure 2.23).

We find that the properties of the measured eddies match with previously established analyses in the region in all years (Trott et al. 2017; Trott et al. 2018). While the previous mid-August spikes are evident in all profiles, of specific note is the magnitude of the scales involved. The spikes in CE amplitude and EKE (Figure 2.23b, f) are twice those of their respective AE profiles (Figure 2.23a, e). Given that the circulation of the GW is always anticyclonic, this indicates that these spikes are present partially due to changes in the GW but more so due to the growth of a significantly larger cyclonic circulation. As seen in the average ADT of the SC region in local years in the first week of August (Figure 2.22q), the cyclone that orbits around the GW is the most likely culprit for this spike, as no other CE approaches its size in the region.

We test this hypothesis by inspecting the ADT of the region per year during this spiking time period (Figure 2.24). We observe that the average case of the late July to early August cyclone is relatively indistinct in full and half years (Figure 2.24a-e, f-j) but is particularly well-pronounced during local years (Figure 2.24k-o). The ADT profile moving into August shows an elongated GW and a large, circular orbiting cyclone (Figure 2.24i) which corresponds to the time period during which the EKE of the region is increasing. This

culminates in the early August spike (Figure 2.24m) where the orbiting cyclone has moved to the south of the GW and is at its maximum extent. The decrease in the region's EKE continues as the cyclone diminishes into mid-August (Figure 2.24n) before becoming indistinct in late August (Figure 2.24o). This larger GW-related cyclone in the local years is also partially seen in Beal and Donohue (2013)'s Figure 2.10.

Besides the WSC facilitating the growth of the cyclone, we hypothesize that the arrival of the stronger Rossby wave carrying LH in full and half years (Figure 2.14) may be inhibiting its development. To explore this possibility, we again look at the 3D profile of the 2006 LH, this time as it arrives in the SC region, 1,845 km westward and only 10 km southward of its original position in Figure 2.8 (Figure 2.25).

We see in the ADT profile the previous GW orbiting cyclone to the southwest and the next orbiting cyclone to the northwest (Figure 2.25a), with a GW that is at this point smaller in amplitude and radius than the LH itself. The geostrophic currents still show a strong circulation around the LH, but with contours that stretch around the GW system. However, unlike in the previous profiles where currents flowed between eddies (Figures 17, 18), this LH is more distinct in terms of its SSS and SST as compared to the GW (Figure 2.25b, c). We observe a warm core to the LH as compared to the cold frontal zone of the GW, a sign of the AS water that now forms the entirety of the LH clashing with some of the more equatorial waters of the GW and SC as a whole (Figure 2.25c, g). In this stage of its life, the LH's BoB water lens of fresher water has been entirely obliterated in the subsurface profile (Figure 2.25b, f), and the spiciness provides evidence to suggest that the water masses in the region are now more heavily temperature-controlled than salinity-controlled (Figure 2.25d). These properties combine to form a relatively deep mixed layer

(Figure 2.25d). Lastly, the vertical velocity profile is similarly distinct, with a positive column to the east of the LH and a negative layer beneath 100 meters to the west (Figure 2.25h). The future of this LH is, as visualized in its trajectory (Figure 2.4a), to shift westward as the GW shifts to the northeast, reaching a maximum radius of 375 km. As it moves into position and grows, the GW cyclone can no longer form, and so it prevents the spike seen in the SC EKE (Figure 2.21d). The 2006 full LH finally loses coherence on October 26th, achieving a total lifespan of 319 days.

2.5 CONCLUSIONS

The variability of the eddy field in the AS plays a critical role in the modulation of air-sea fluxes and the transport of water masses across the basin. However, little attention has been given in recent years to the LH and none of the current high-resolution altimetric datasets or reanalysis products have been used to analyze its interannual variability and the possible consequences therein. In this study, we have used the closed-contour eddy tracking algorithm previously used by Trott et al. (2018) in the AS to track the LH through the course of the year. We examined the different processes that contribute to the phases of the LH's life cycle, and provided observational evidence that supports past hypotheses regarding the LH, such as those by Shankar and Shetye (1997) and Bruce et al. (1998), while arriving at new findings regarding the LH's impact on the GW and the SC region.

We began with a full-life trajectory analysis of the LH, categorizing it into three distinct types of propagation (full, half, and local) based on its eventual location of decoherence. We correlated drifter trajectories with that of LH, determining the error of the altimetric geostrophic currents. The dynamics of the origin of the LH are then considered, with a conclusion that the second annual downwelling CKW is the major phenomenon

responsible, though the forcing of this wave by wind stress in the STIP region is another likely factor. We identify that different strengths of CKW correlate with the type of propagation of LH. At this stage and each step thereafter, we provide 3D profiles of the LH, allowing for a more in-depth analysis of the water masses involved in the LH over its life. We continued with an inspection of the WSC over the LH, demonstrating that it is both a complex factor that may detract from the initial growth and maintenance of the LH and a differentiator that separates the modes of LH propagation. After the LH's growth, we further inspect the primary westward propagation mechanism of the LH, the Rossby wave along 8°N, and find that its speed and the speed of the LH both agree with each other and the theoretical speeds of the region. It is at this point that we note that in full years, fresher BoB water is pulled by the LH past 70°N, into the center of the AS. With the coherent propagation of LH thus established, we study its effects on the SC, its eventual destination. We hypothesize that the WSC of the region fuels a larger GW in most local years, while the arrival of the LH in full years may inhibit the growth of a larger cyclone in the beginning of August. This causes a steeper peak to occur in the outlier local years, and to a lesser extent in the half years.

Our new evaluation of the LH indicates that it is a more long-lived and far-reaching phenomenon than previously considered. We also demonstrate that there are a myriad of ill-studied factors and limitations to this study that must be addressed in order to complete a total understanding of the LH phenomenon. We acknowledge that the resolution of current altimetry products is insufficient to capture the totality of the eddy field, and may be falsely aggregating smaller eddies into larger formations (Amores et al. 2018). Likewise, there remain questions regarding the linkage between ENSO and IOD, as well as their exact

effects on the winter monsoon and CKW propagation (*e.g.* McKenna et al. 2020). With these factors in mind, we formulate a few lingering questions beyond the scope of our study. These include the effect of eddy killing throughout the AS, the effects of submesoscale energy transfer via eddy splitting/merging events in the AS, and the variability of these factors by monsoon. When these questions and those following them are answered, whether by further investigation using existing techniques (*e.g.* Rai et al. 2021), new algorithms (*e.g.* Tian et al. 2021), and/or improved observations, such as from the upcoming National Aeronautics and Space Administration (NASA) Surface Water and Ocean Topography (SWOT) mission, we will understand the LH phenomenon.

Table 2.1. Year-Wise Southwest Monsoon Strength (2nd column), Occurrences of ENSO Phase (3rd column), IOD Phase (4th column), and LH type of propagation (5th column) from 1993 to 2019. Example years are highlighted. Table entries without an explicit designation are neutral in their respective indices. Columns 2, 3, and 4 are adapted from Roman-Stork et al. (2020).

Year	Monsoon	ENSO	IOD	LH
1993				Full
1994	Strong	El Niño	Positive	Half
1995		La Niña		Full
1996			Negative	Full
1997		El Niño	Positive	Local
1998		La Niña	Negative	Local
1999		La Niña		Half
2000		La Niña		Full
2001				Full
2002	Weak	El Niño		Full
2003				Half
2004	Weak	El Niño		Local
2005		La Niña		Full
2006		El Niño	Positive	Full
2007		La Niña		Full
2008		La Niña		Full
2009	Weak	El Niño		Full
2010		La Niña	Negative	Local
2011		La Niña		Half
2012			Positive	Full
2013				Half
2014	Weak	El Niño	Negative	Full
2015	Weak	El Niño	Positive	Full
2016	Weak	La Niña	Negative	Full
2017				Full
2018		La Niña		Full
2019	Strong		Positive	Half

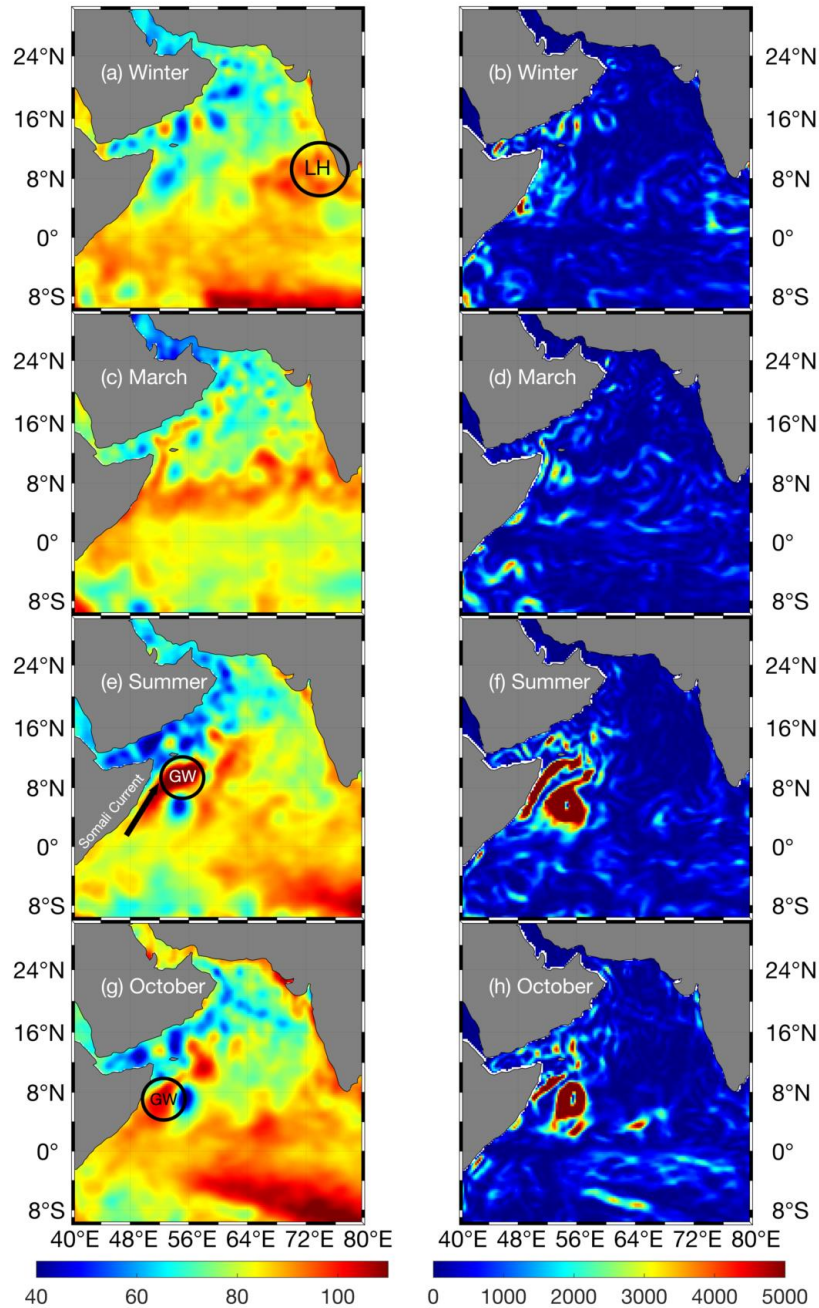


Figure 2.1. Mean absolute dynamic topography (ADT) (cm) during Winter (mean of November, December, January, and February) (a), March (c), Summer (mean of May, June, July, August, and September) (e), and October (g), averaged from 1993 to 2019. (b), (d), (f), and (h): Same as (a), (c), (e), and (g) but for eddy kinetic energy (EKE) ($\text{cm}^2 \text{s}^{-2}$). The locations of the LH, the GW, and the Somali Current (SC) are annotated.

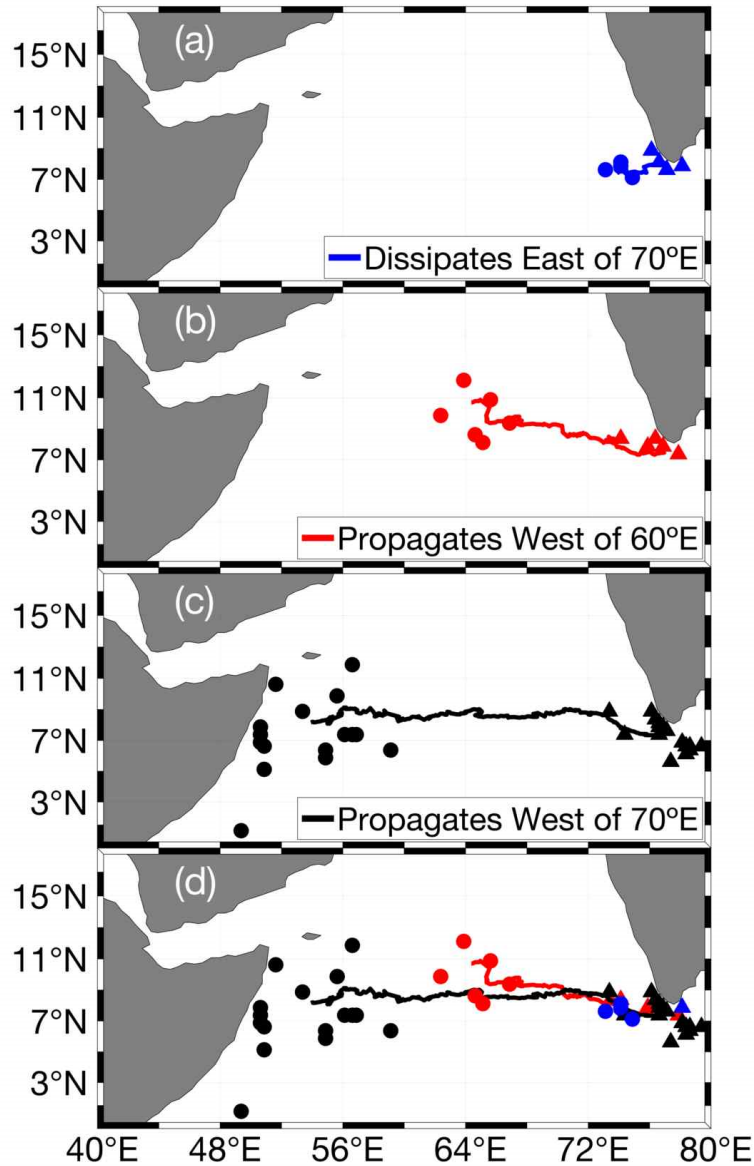


Figure 2.2. The original (filled triangles) and final (filled circles) locations tracked for each LH, 1993-2019. The lines indicate an average of all trajectories of a given type based off of the average origin point through the final recorded location at the mean lifetime of the propagation type. Blue objects and lines in (a) indicate trajectories that do not pass 70°E. Red objects and lines in (b) indicate trajectories that are recorded passing 70°E, but dissipating before passing 60°E. Black objects and lines in (c) indicate trajectories that are recorded passing 60°E. (d) displays all trajectory clusters on the same panel for comparison.

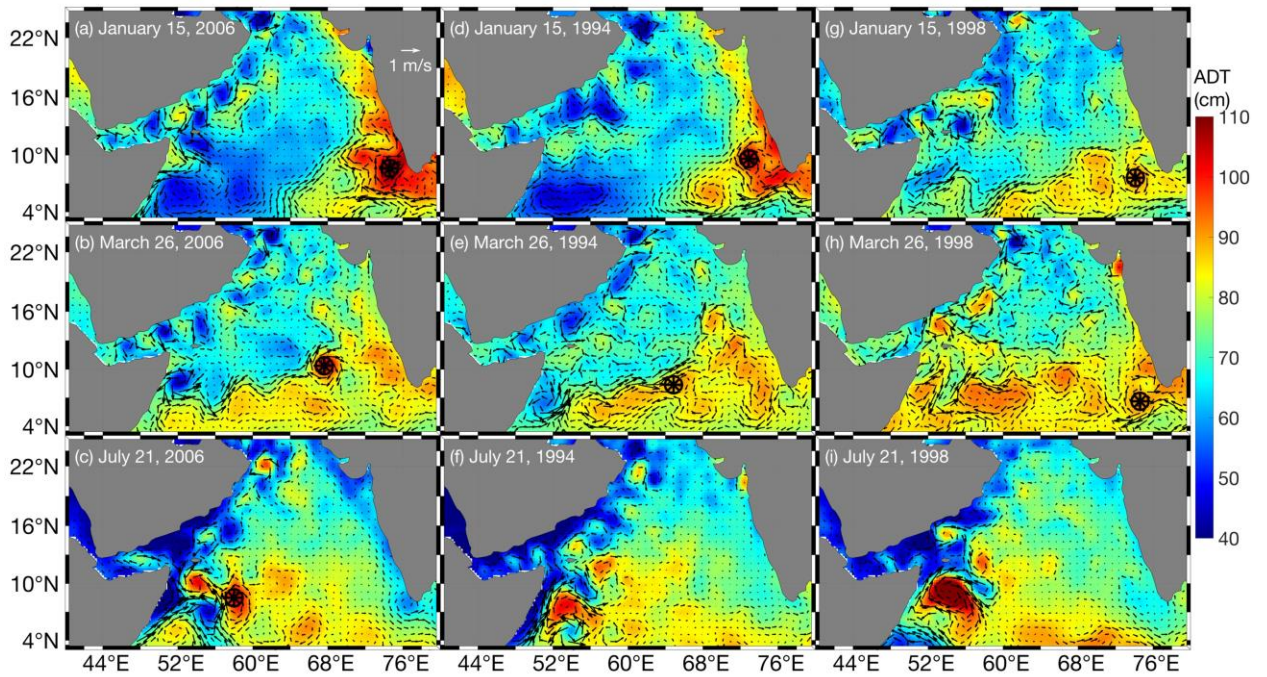


Figure 2.3. ADT (cm) of the AS in 2006, 1994, and 1998. Arrows depict geostrophic current vectors (m s^{-1}) from altimetry data. Black pinwheels mark locations of the tracked LH at the given times. (a)-(c) 15 January, 16 March, and 21 July 2006. (d)-(f) Same as (a)-(c) but for 1994. (m)-(r) Same as (a)-(c) but for 1998.

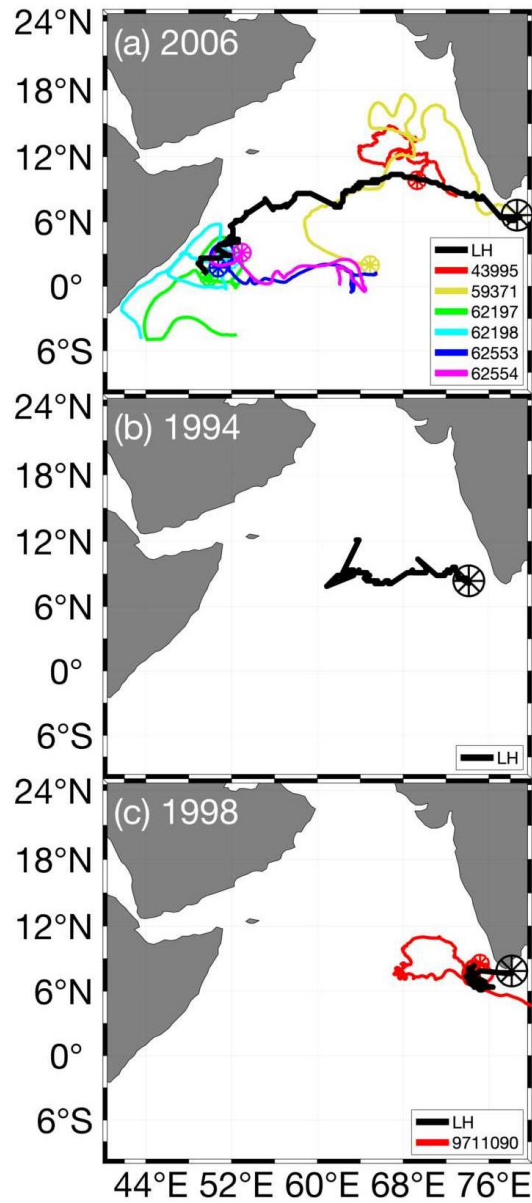


Figure 2.4. Trajectories of the tracked LH in 2006 (a), 1994 (b), and 1998 (c). Solid black lines indicate LH trajectories, while black pinwheels indicate LH origin location. Thinner colored lines each correspond to a unique GDP drifter that overlapped with the radius of LH for at least a week at some point in its life. Smaller colored pinwheels represent the origin points of the respective colored drifter.

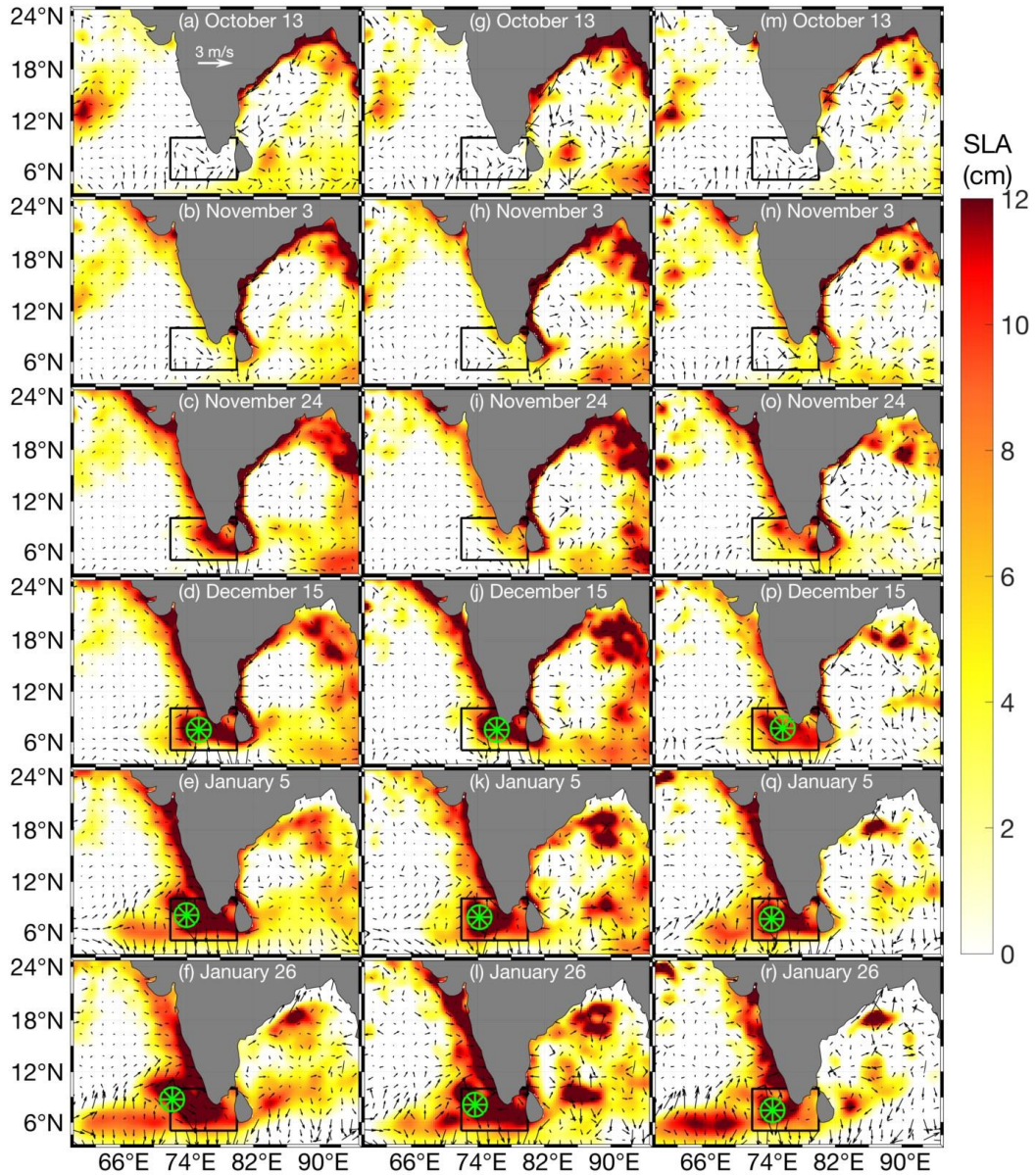


Figure 2.5. SLA (cm) depicting CKW propagation between 13 October and 26 January averaged from 1993 to 2019. Arrows depict geostrophic current vectors (m s^{-1}) from altimetry data. Green pinwheels mark the average locations of the tracked LH at the given times. (a)-(f) Average for full years. (g)-(i) Average for half years. (m)-(r) Average for local years. The black box is the zone within which all LHs form.

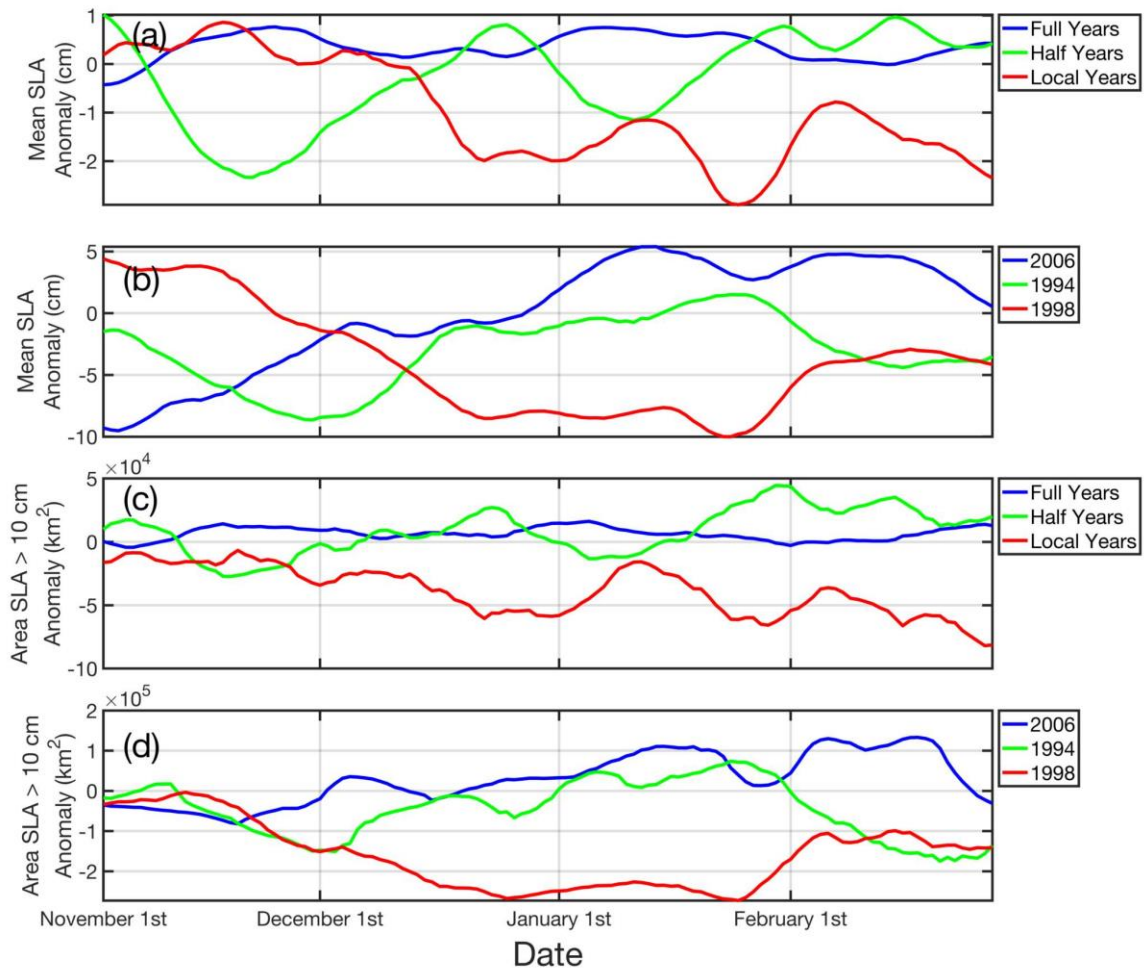


Figure 2.6. Mean SLA Anomaly (cm) for all years (a) and example years (b); areas of elevated SLA (> 10 cm, km^2) for all years (c) and example years (d). Means are performed over the boxed area in Figure 2.5 (9.5°N , 5°S , 80°E , 72°E) and anomalies are calculated for each location in regard to a 27-year mean.

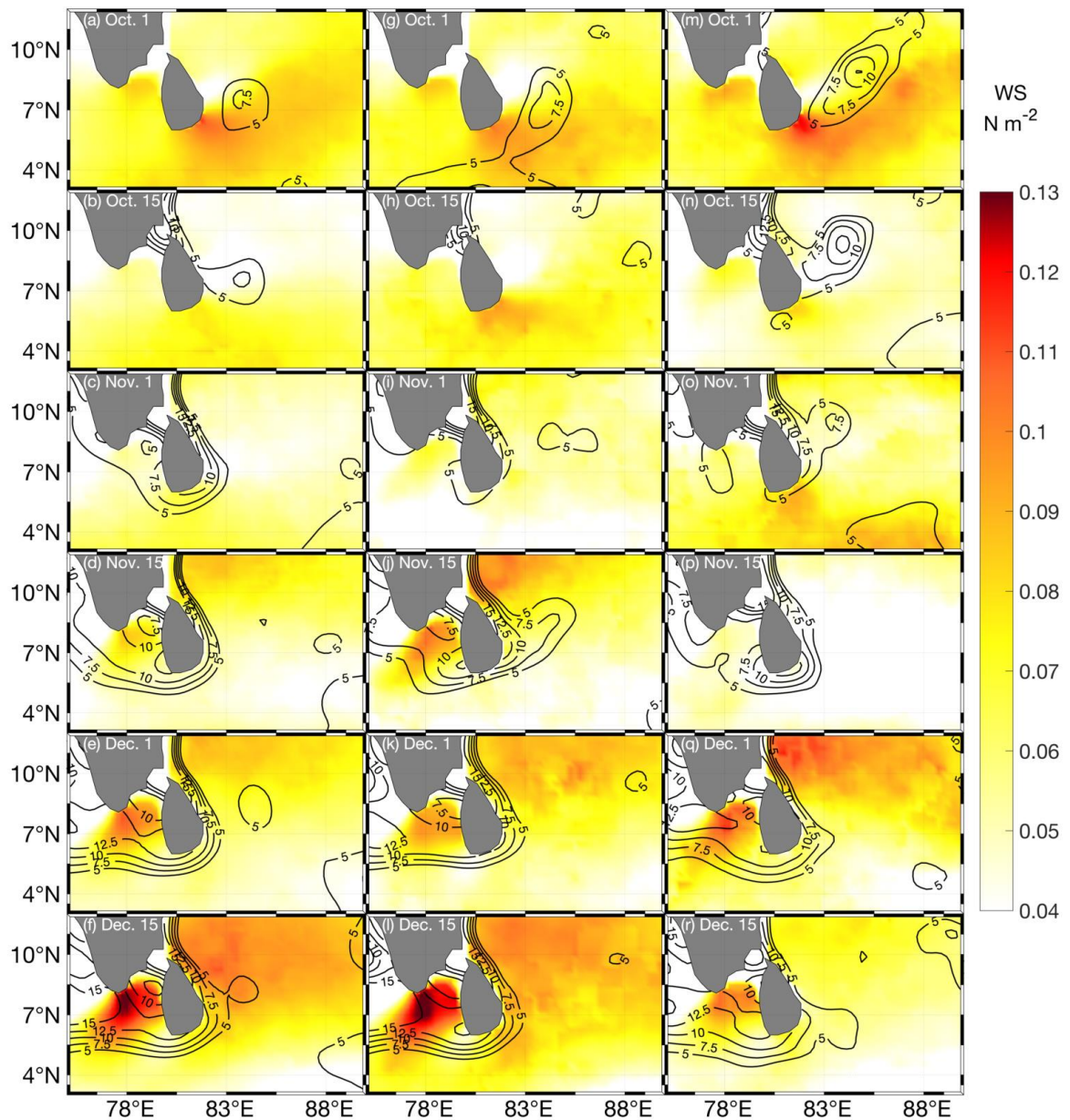


Figure 2.7. Mean wind stress (N m^{-2}) and SLA contours over the STIP area between the beginning of October and the end of December for full (a-f), half (g-l), and local (m-r) years. Each date represents the beginning of a two week period over which the wind stresses and SLAs are averaged.

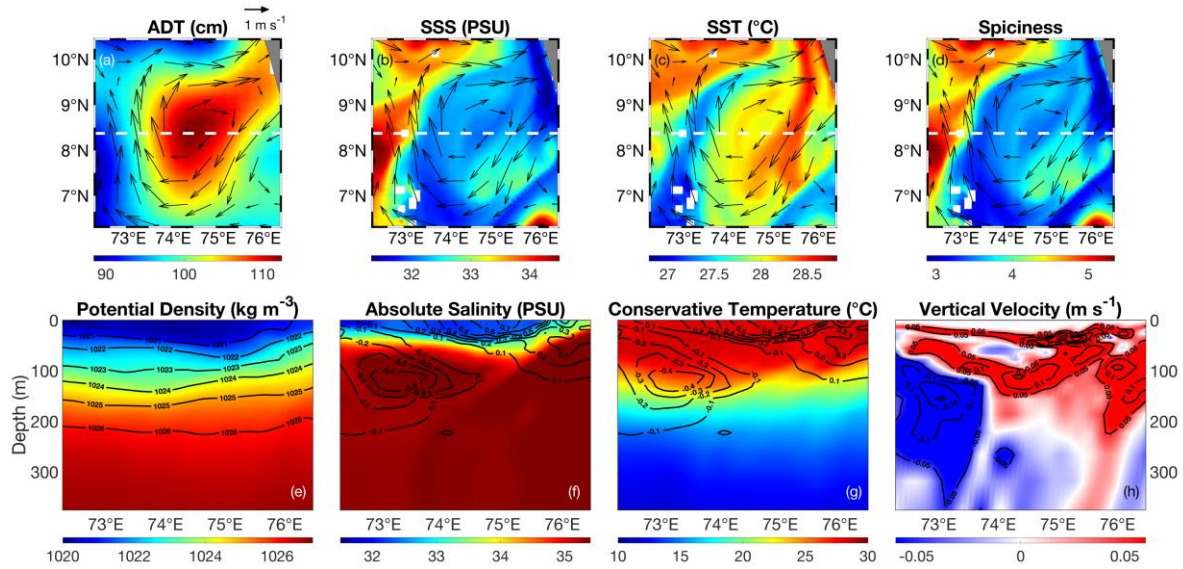


Figure 2.8. The 3-dimensional profiles of the location and date marked by the black pinwheel in Figure 2.3a for the full example year (15 January, 2006). These are as follows: (a) measured ADT (cm), (b) GLORYS12v1 sea surface salinity (SSS) (PSU), (c) GLORYS12v1 SST ($^{\circ}\text{C}$), and (d) Spiciness with geostrophic current vectors overlaid. The white dashed line depicts the cross sections of the following properties: (e) Potential density (kg m^{-3}) with isopycnals overlaid. (f) Absolute salinity (PSU) and (g) conservative temperature ($^{\circ}\text{C}$) with contours of swirl velocity (m s^{-1} , meridional components) overlaid. (h) Vertical velocity (m s^{-1}) with its own contours overlaid. White squares represent regions of no GLORYS12v1 data, in this case representing the Lakshadweep islands.

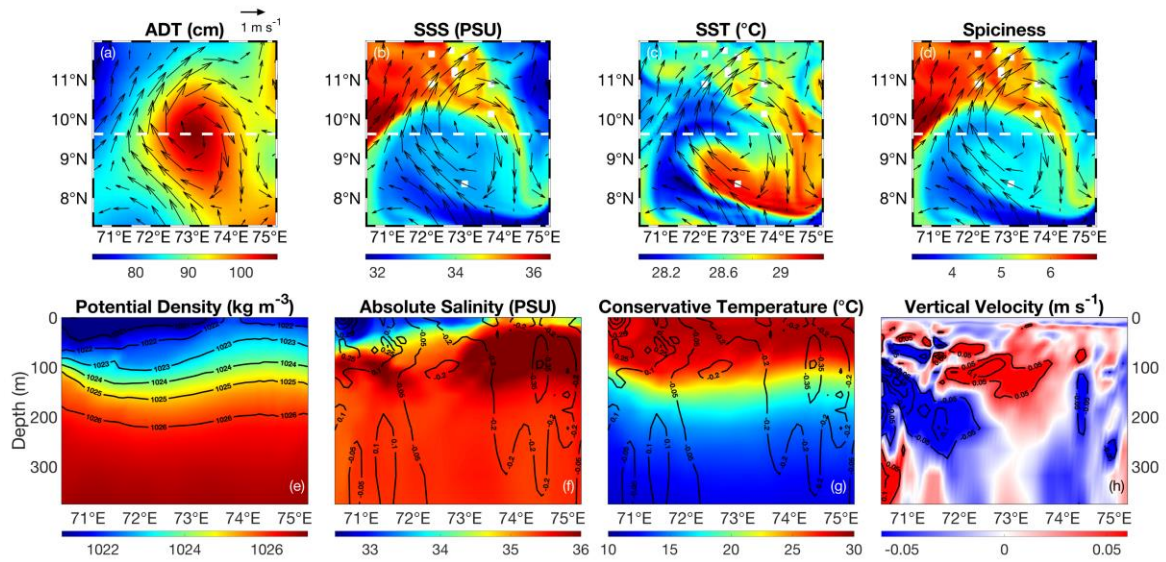


Figure 2.9. Same as Figure 2.8 but for the location marked in Figure 2.3d for the half example year (15 January, 1994).

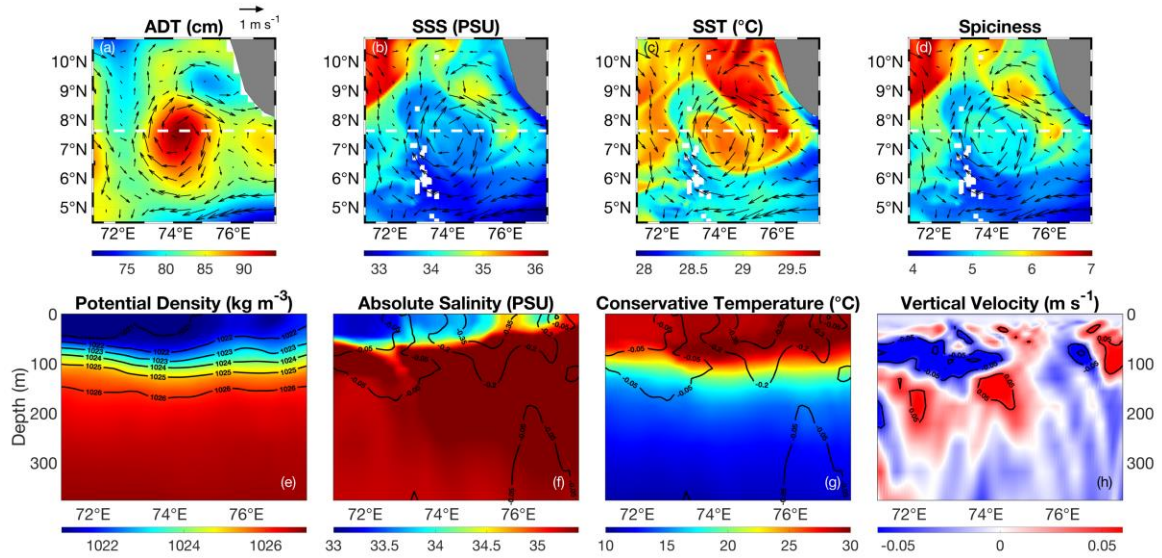


Figure 2.10. Same as Figure 2.8 but for the location marked in Figure 2.3g for the local example year (15 January, 1998).

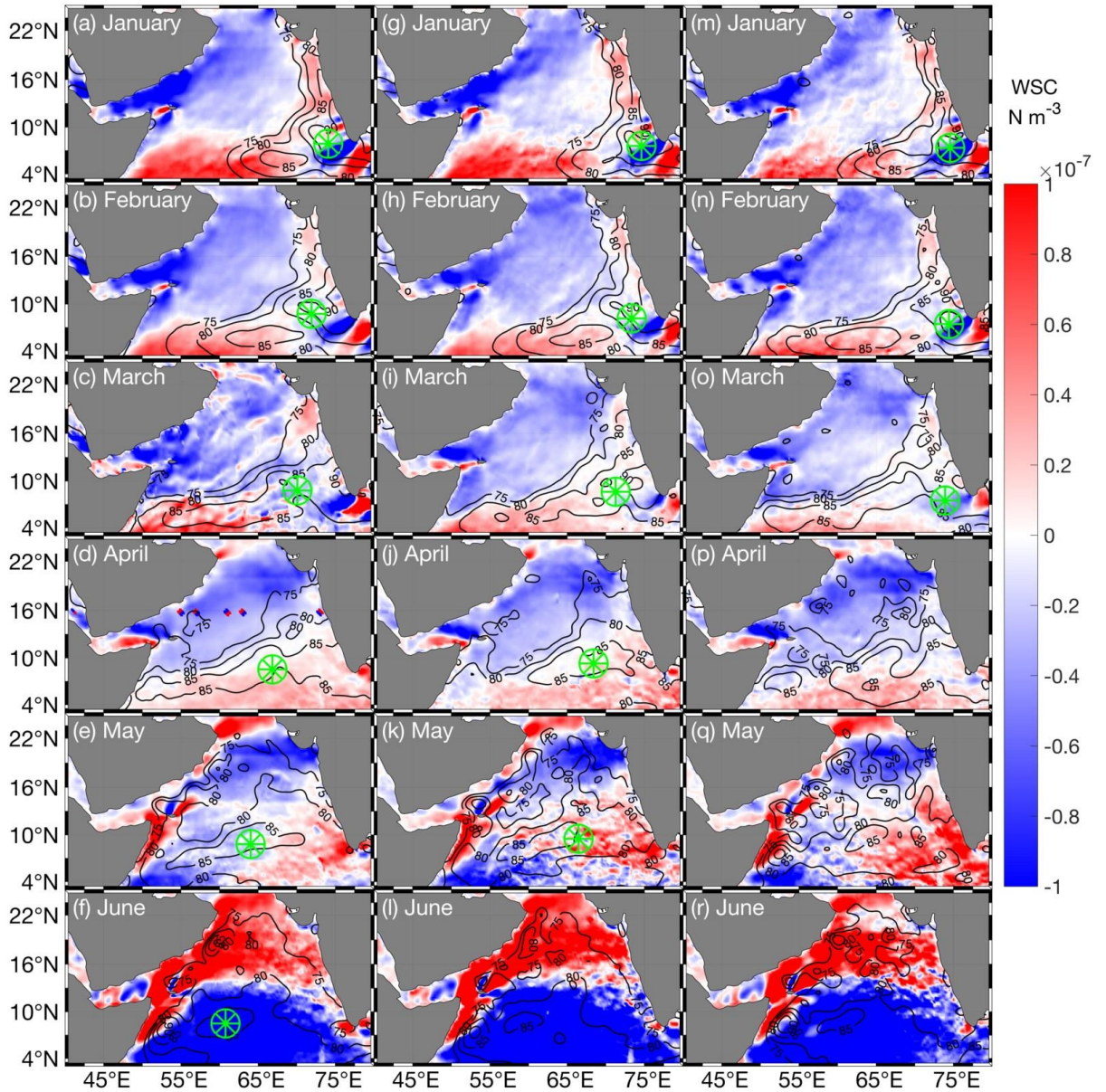


Figure 2.11. WSC (N m^{-3}) for the first week in each month between January and June averaged from 1993 to 2019 in the AS. Contours depict areas of elevated ADT in intervals of 5 cm. Green pinwheels mark the average locations of the tracked LH following the trajectories marked in Figure 2.2. (a)-(f) Average for full years. (g)-(i) Average for half years. (m)-(r) Average for local years.

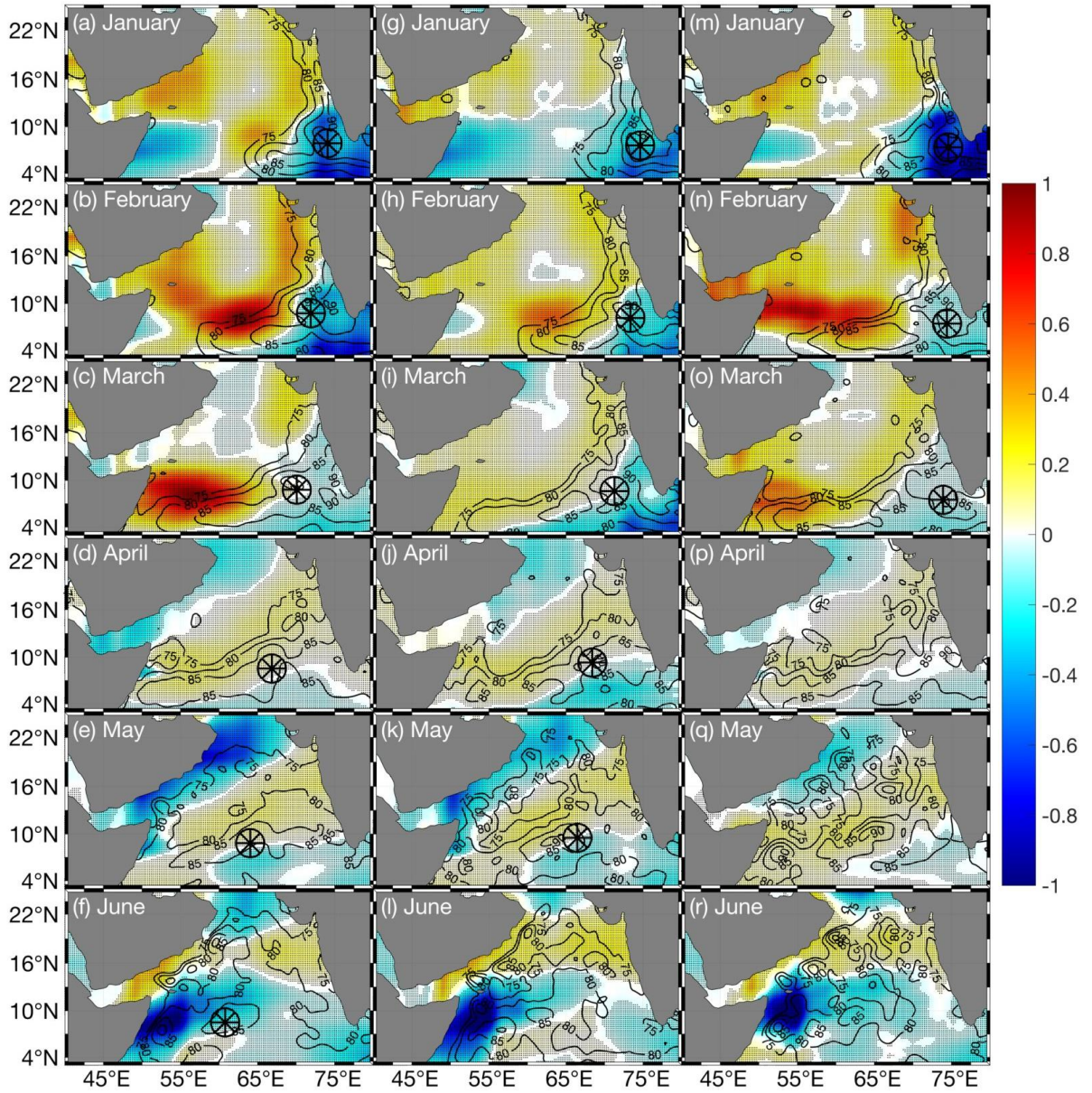


Figure 2.12. Same as Figure 2.11, but displaying the normalized spatial covariance between the WSC and the ADT. Areas of significant correlation ($p < .05$) are shaded.

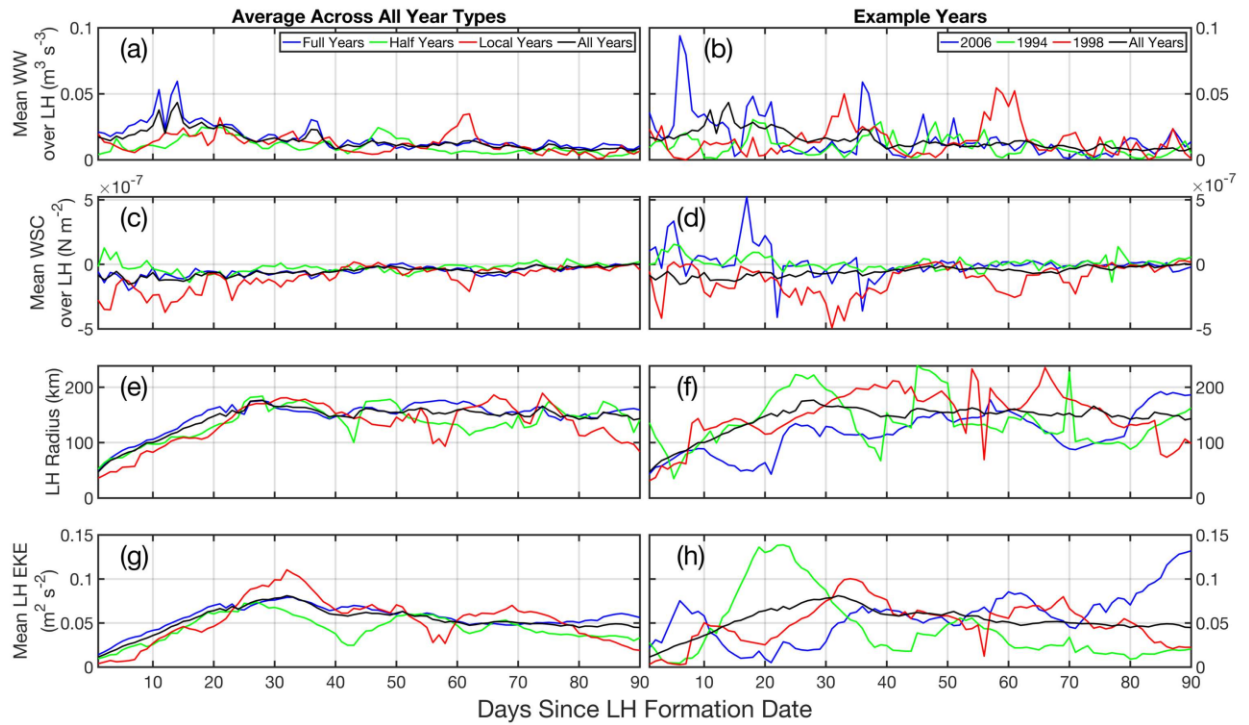


Figure 2.13. The characteristics of the LH and the wind over the radius of the LH for the first 90 days of its lifespan for each year type (left) and example years (right): (a) is the mean WW ($\text{m}^3 \text{s}^{-3}$) for all propagation types; (b) is as in (a) but for example years. (c) is the mean WSC (N m^{-2}) for all propagation types; (d) is as in (c) but for example years. (e) is the radius (km) of the LH for all propagation types; (f) is as in (e) but for example years. Lastly, (g) is the mean EKE ($\text{m}^2 \text{s}^{-2}$) of the LH for all propagation types; (h) is as in (g) but for example years. Black lines display the average for all years and are the same across both columns.

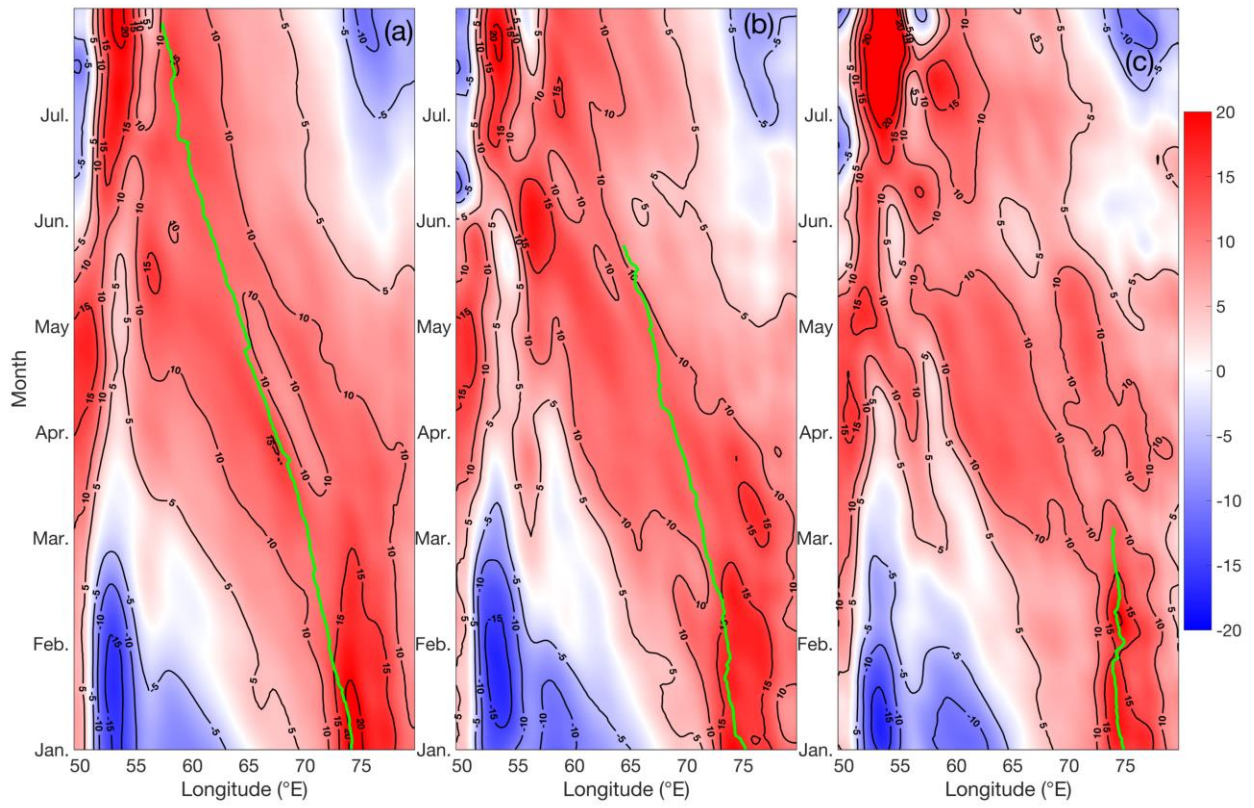


Figure 2.14. Hovmöller longitude-time diagram of SLA (cm) contours for a spatial average of 7°N-9°N and a temporal average for 1993-2019 between January and the end of July. Green lines depict average LH propagation (see Figure 2.2) along this longitude. (a) Average for full years. (b) Average for half years. (c) Average for local years.

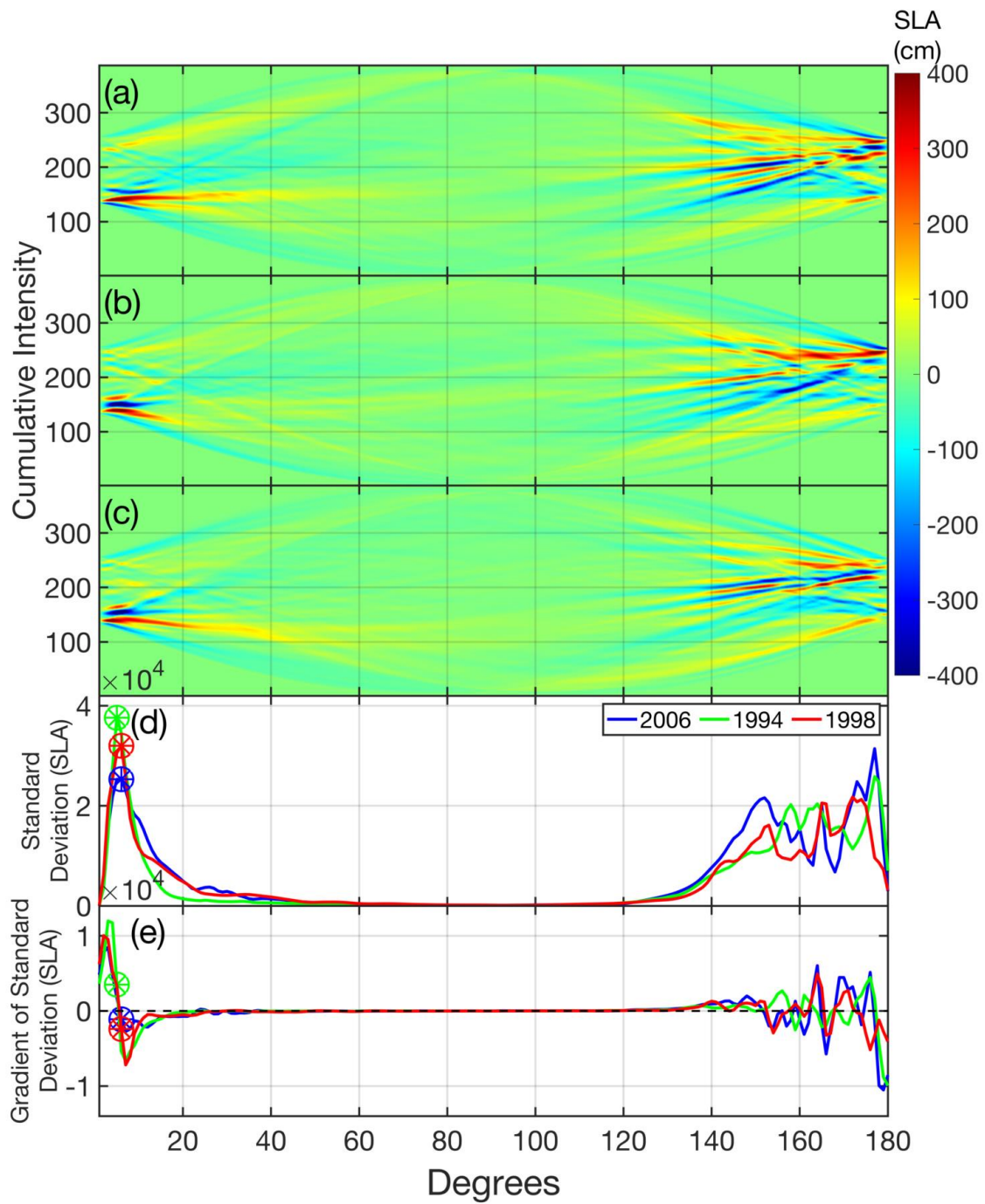


Figure 2.15. Radon transforms of the L-T plots shown in Figure 2.14. (a) Transform for full years. (b) Transform for half years. (c) Transform for local years. (d) is the standard deviation of the SLA in (a)-(c) on blue, green, and red lines respectively. Colored pinwheels mark the maximum in the curve. (e) plots the gradient of (d).

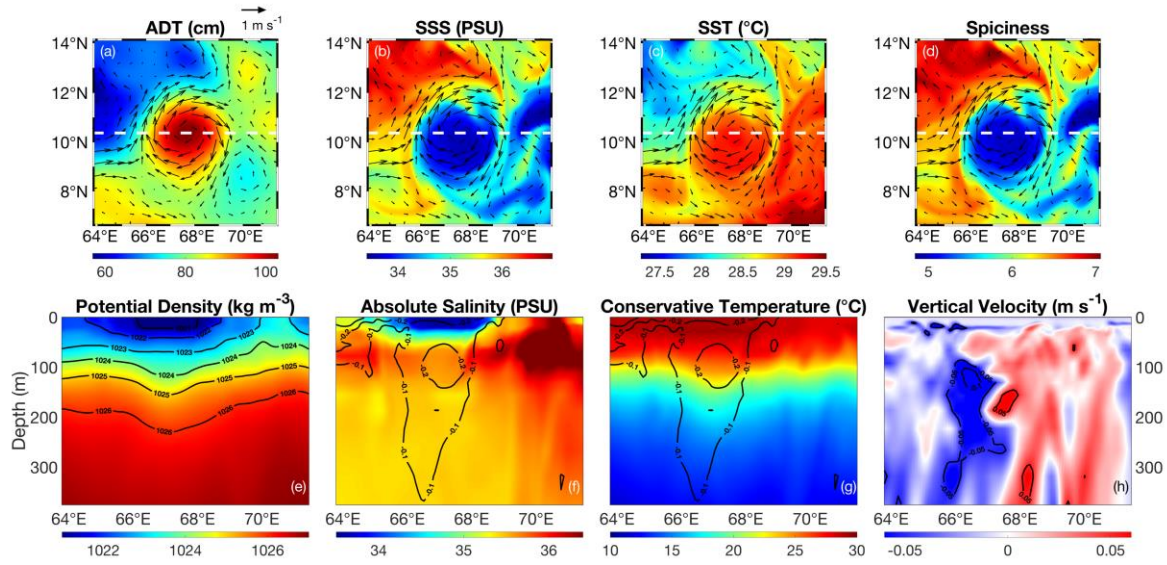


Figure 2.16. Same as Figure 2.8 but for the location marked in Figure 2.3b for the full example year (March 26th, 2006).

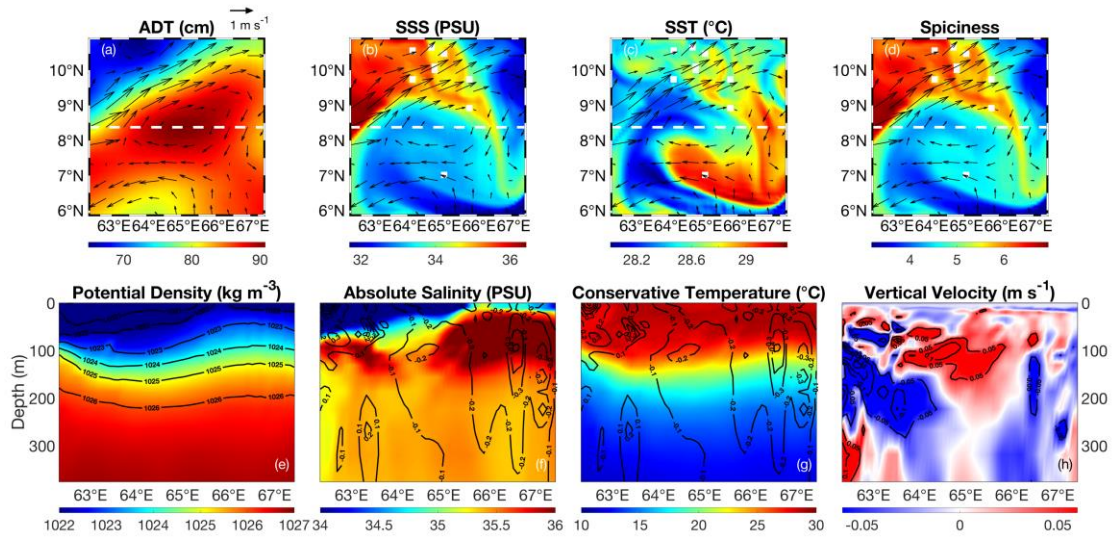


Figure 2.17. Same as Figure 2.8 but for the location marked in Figure 2.3e for the half example year (March 26th, 1994).

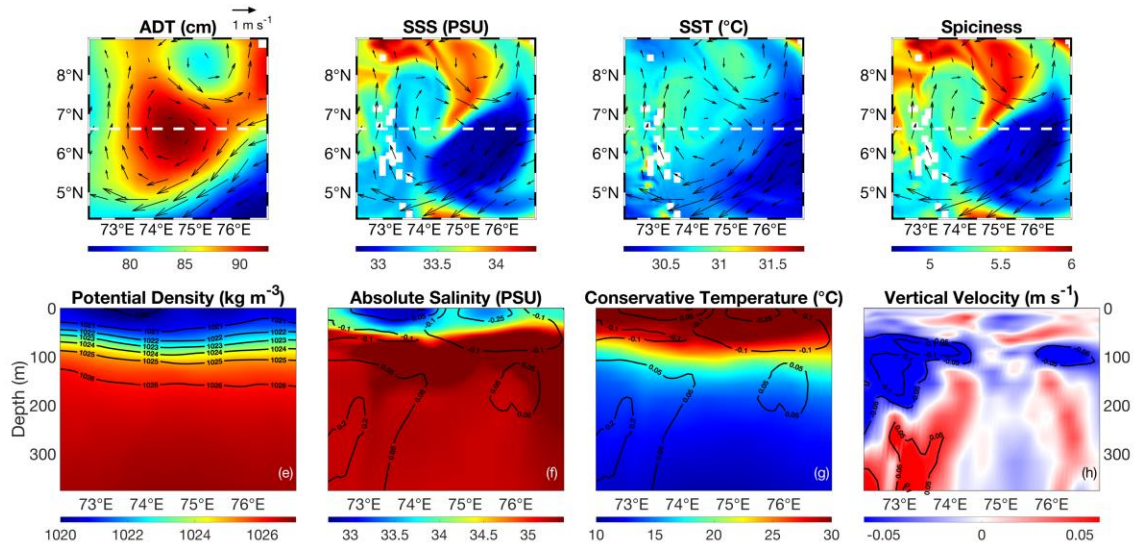


Figure 2.18. Same as Figure 2.8 but for the location marked in Figure 2.3h for the local example year (March 26th, 1998). As before, white squares mark the locations of the Lakshadweep islands, which are not painted over in the GLORYS12v1 dataset as they are in the CMEMS altimetry interpolations.

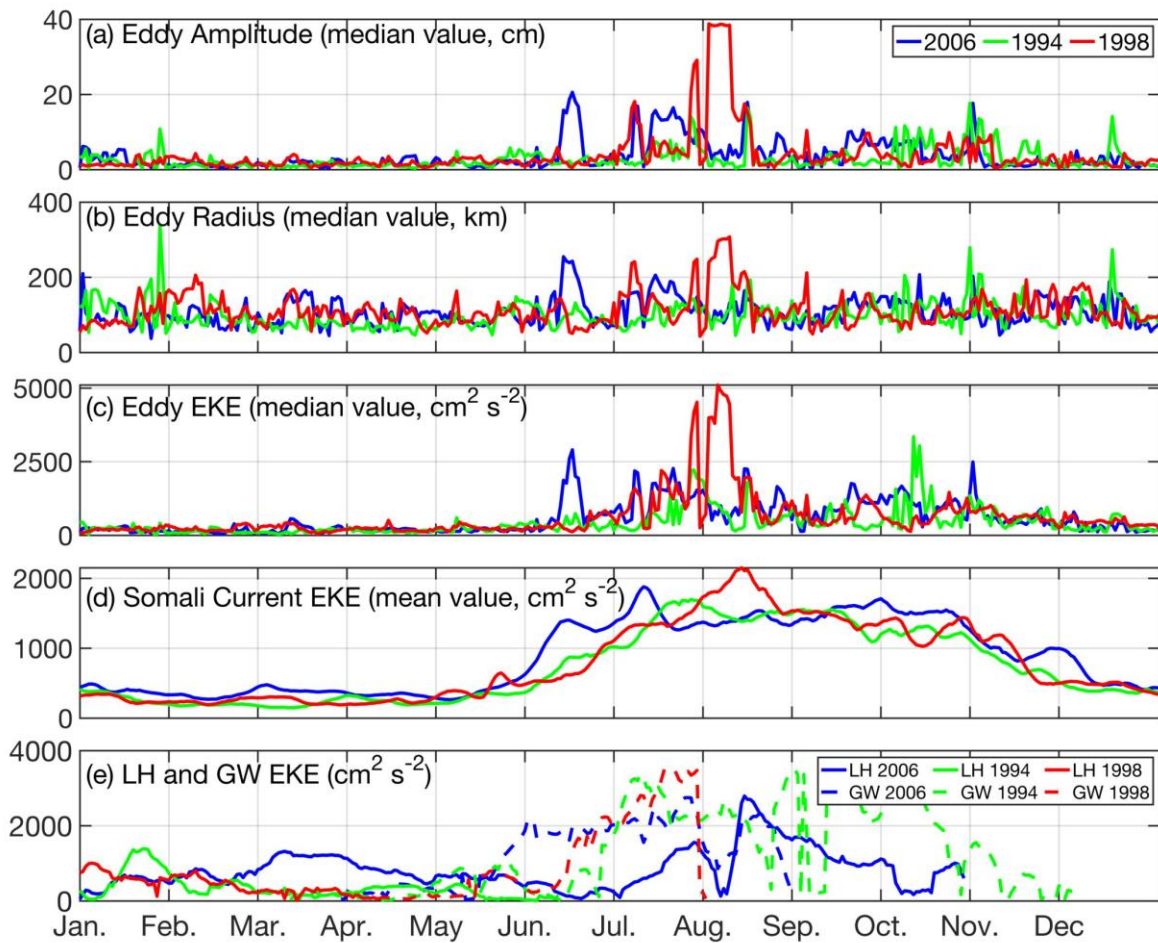


Figure 2.19. Yearlong characteristics of eddies in the Somali Current (the area between the Equator, 11°N, 40°E, and 58°E) for 2006, 1994, and 1998. Characteristics include the spatial median SC eddy (a) amplitude in cm, (b) radius in km, and (c) EKE in $\text{cm}^2 \text{s}^{-2}$. (d) Mean EKE of the SC from geostrophic current observations. (e) EKE in $\text{cm}^2 \text{s}^{-2}$ of the LH (solid lines) and GW (dotted lines) of each year. The GW is tracked in the same way that the LH is as set out in section 2.4.1, but for the SC region and April through June.

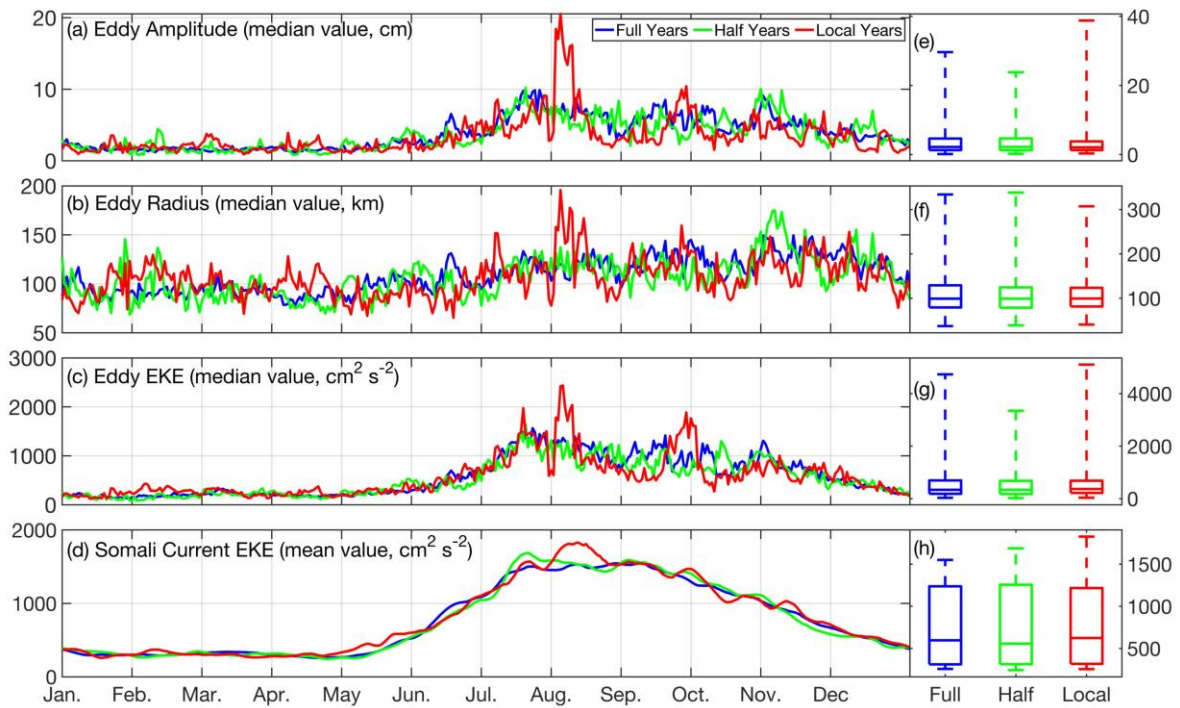


Figure 2.20. Same as Figure 2.19 but averaged across all years 1993-2019. (e-h) boxplots with the mean, upper and lower quartiles, and minimum and maximum of the characteristics shown.

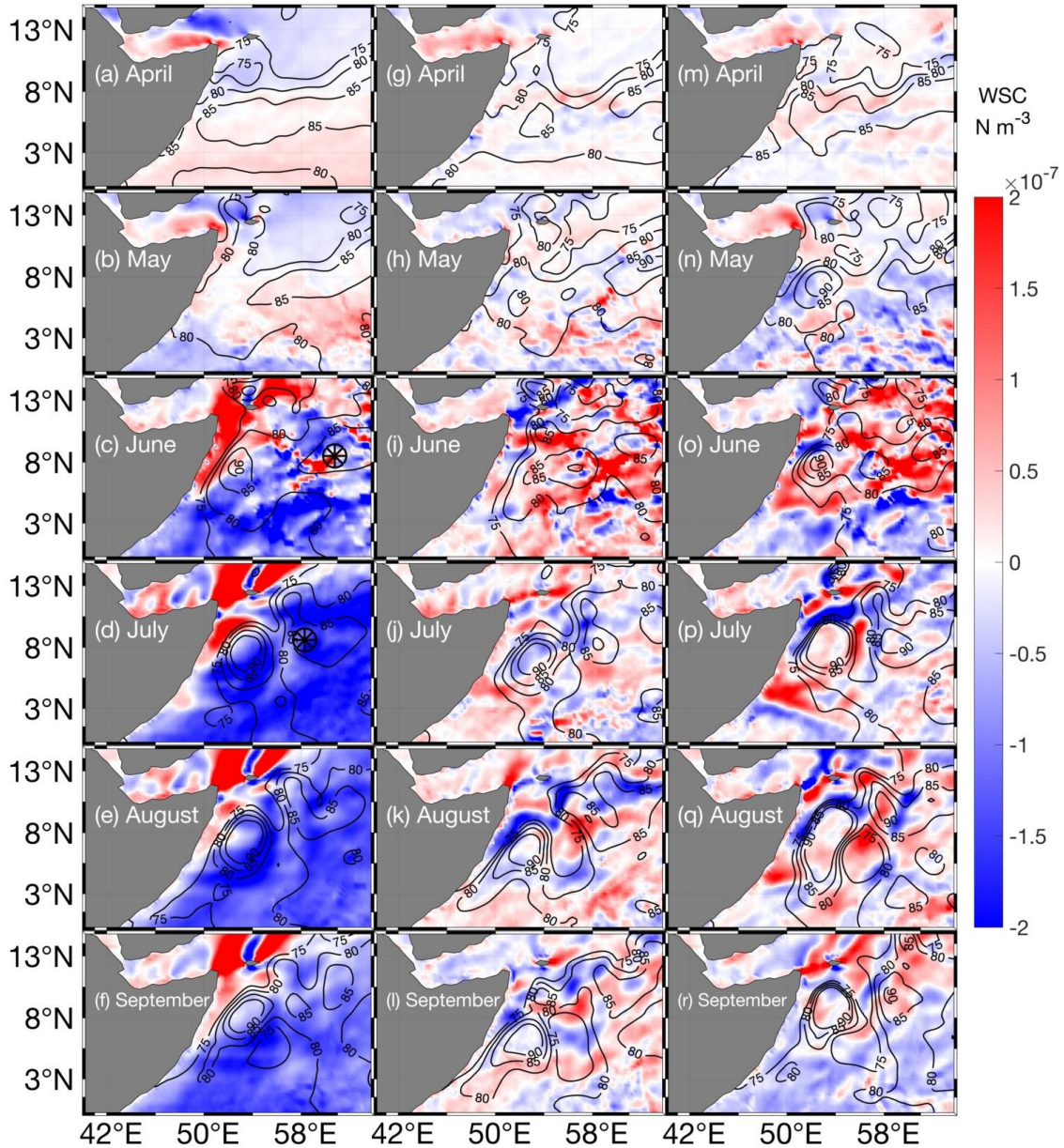


Figure 2.21. Wind stress curl (N m^{-3}) differences between full, half, and local years for the first week in each month between April and September averaged across 1993-2019 in the SC region. Contours depict ADT (cm). Black pinwheels mark the average locations of the tracked LH. (a)-(f) Average for full years. (g)-(i) Average for full years minus the average for half years. (m)-(r) Average for full years minus the average for local years.

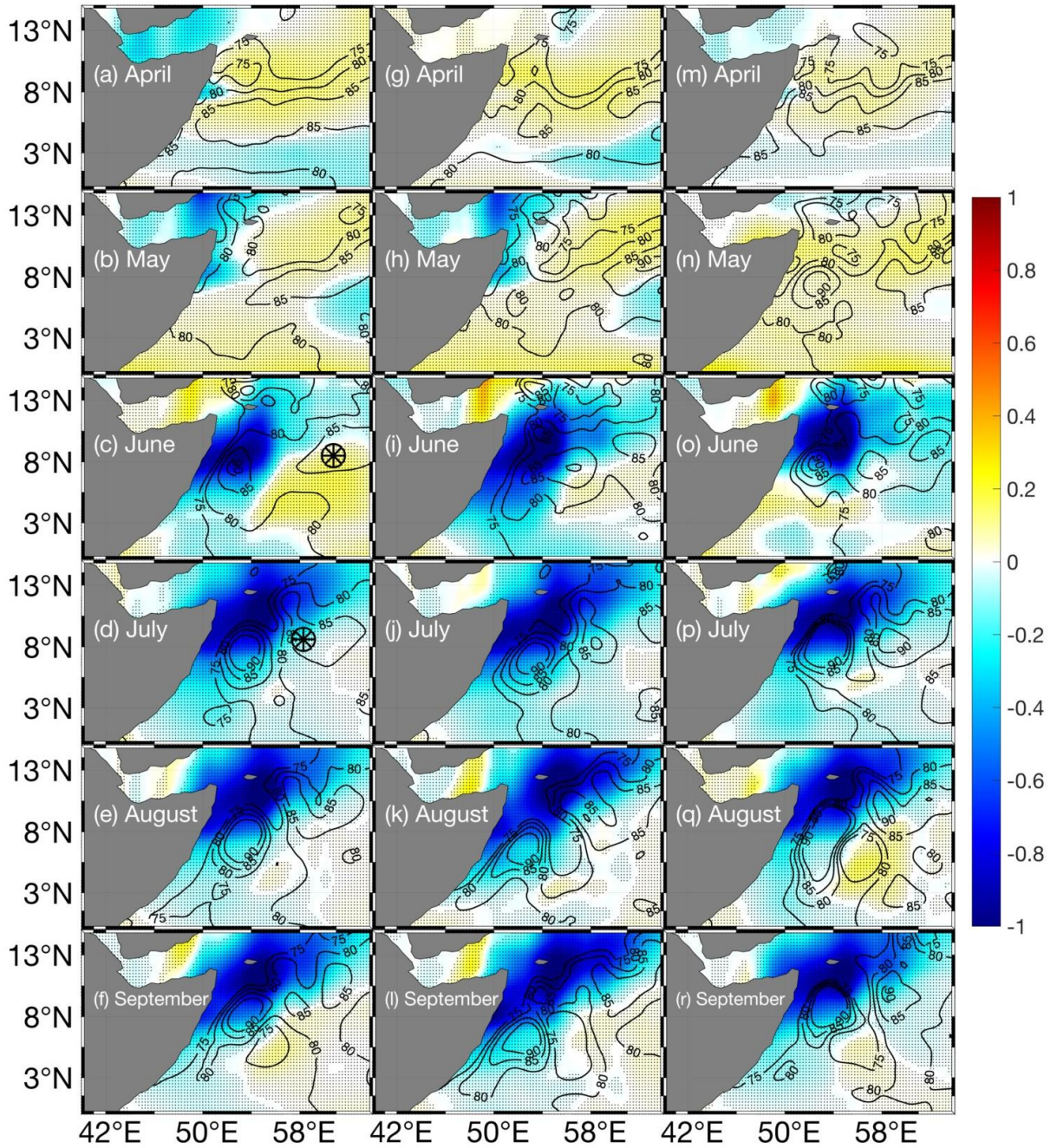


Figure 2.22. The same spatiotemporal area as Figure 2.22, but plotting the normalized covariance (color) and significant correlations (shading) between the WSC and the ADT (as in Figure 2.12.) Contours are ADT, the same as Figure 2.21.

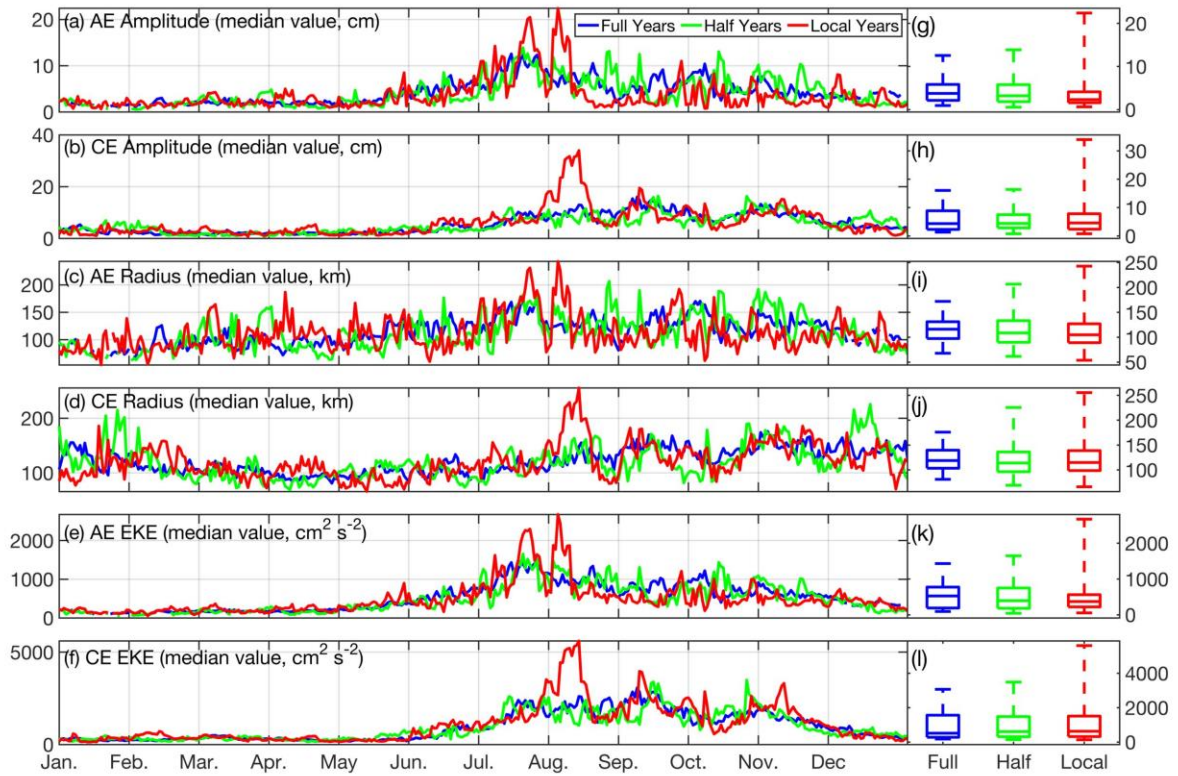


Figure 2.23. Yearlong characteristics of eddies in the Somali Current averaged between 1993 and 2019 (as in Figure 2.20) but separated between AEs and CEs. Blue lines depict full years, green lines depict half years, and red lines depict local years. (a) Median AE amplitude (cm). (b) same as (a) but for CEs. (c) Median AE radius (km). (d) same as (c) but for CEs. (e) Median average AE EKE ($\text{cm}^2 \text{s}^{-2}$). (f) same as (e) but for CEs. Note that there is a difference in the y-axis scales between AEs and CEs.

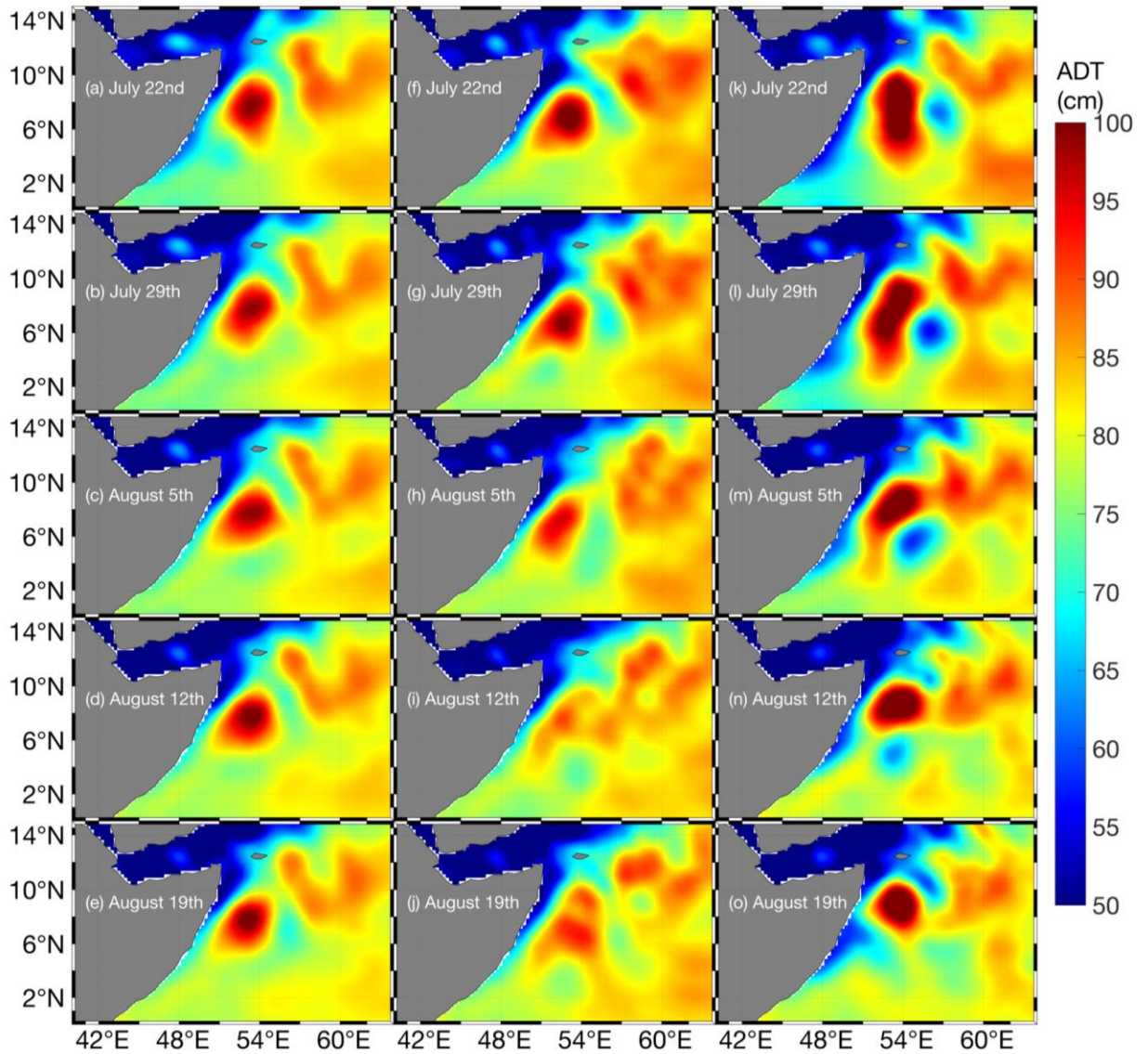


Figure 2.24. The average ADT (cm) of the SC region between 1993 and 2019 per type of LH propagation year. Full years: (a) July 22nd, (b) July 29th, (c) August 5th, (d) August 12th, and (e) August 19th. (f-j) same as (a-e) but for half years. (k-o) same as (a-e) but for local years.

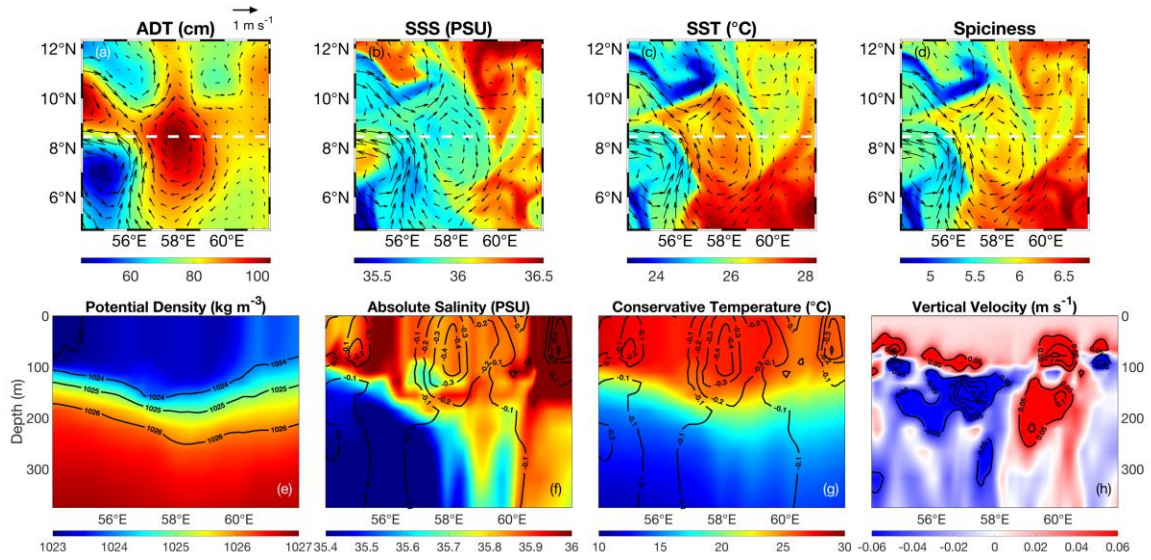


Figure 2.25. Same as Figure 2.8 but for the location marked in Figure 2.3c for the full example year (July 21st, 2006).

CHAPTER 3

SUBSURFACE EDDY DETECTION OPTIMIZED WITH POTENTIAL
VORTICITY FROM MODELS IN THE ARABIAN SEA²

² Ernst, P. A., Subrahmanyam, B., Morel, Y., Trott, C. B., & Chaigneau, A. (2023). Subsurface Eddy Detection Optimized with Potential Vorticity from Models in the Arabian Sea. *Journal of Atmospheric and Oceanic Technology*, 1(aop). <https://doi.org/10.1175/JTECH-D-22-0121.1>

© American Meteorological Society. Used with permission.

3.1 ABSTRACT

Coherent ocean vortices, or eddies, are usually tracked on the surface of the ocean. However, tracking subsurface eddies is important for a complete understanding of deep ocean circulation. In this study, we develop an algorithm designed for the detection of subsurface eddies in the Arabian Sea using Nucleus for European Modelling of the Ocean (NEMO) model simulations. We optimize each parameter of our algorithm to achieve favorable results when compared with an algorithm using sea surface height (SSH). When compared to similar methods, we find that using the rescaled isopycnal potential vorticity (PV) is best for subsurface eddy detection. We proceed to demonstrate that our new algorithm can detect eddies successfully between specific isopycnals, such as those that define the Red Sea Water (RSW). In doing so, we showcase how our method can be used to describe the properties of eddies within the RSW and even identify specific long-lived subsurface eddies. We conduct one such case study by discerning the structure of a completely subsurface RSW eddy near the Chagos Archipelago using Lagrangian particle tracking and PV diagnostics. We conclude that our rescaled PV method is an efficient tool for investigating eddy dynamics within the ocean's interior, and publicly provide our optimization methodology as a way for other researchers to develop their own subsurface detection algorithms with optimized parameters for any spatiotemporal model domain.

3.2 INTRODUCTION

Coherent ocean vortices known as eddies are ubiquitous throughout the world's oceans (Chelton et al., 2011). Mesoscale (50-300 km) eddies contribute as much to global mass transport as the mean flow (Zhang et al., 2014). In the Arabian Sea, the variability of the surface mesoscale eddy field is primarily driven by instability generated via the

seasonal reversal of monsoon winds, producing the southwest monsoon in the summer and northeast monsoon in the winter (Trott et al., 2018). As a result of the reversing winds and their associated planetary wave dynamics, several climatological eddies consistently form in the same regions every year, including the Great Whirl and the Socotra Eddy in the Somali Current region, as well as the Lakshadweep High in the Laccadive Sea (Beal and Donohue, 2013; Ernst et al., 2022; Shankar and Shetye, 1997). These named eddies and the mesoscale eddy field as a whole modulate changes in upper ocean stratification, air-sea interactions, and transport of heat and salt across the Arabian Sea (Trott et al., 2019; Wang et al., 2019; Zhan et al., 2020).

Oceanic eddies and their impacts are often studied with the aid of automated eddy detection and tracking algorithms due to their transience, ubiquity, and the increasing number of observations (Lian et al., 2019). At the surface, the most widely used detection methods utilize quantities derived from sea surface height (SSH), including sea level anomaly (SLA), absolute dynamic topography (ADT), and geostrophic currents (Chaigneau et al., 2008; Pegliasco et al., 2021; Nencioli et al., 2010). Currents in particular may be further processed to derive other fields through which eddies can be identified, including relative vorticity, the Okubo-Weiss (OW) parameter, and the local normalized angular momentum (LNAM) (Isern-Fontanet et al., 2003; Le Vu et al., 2018; Souza et al., 2011). Conventional Eulerian algorithms use these fields to identify local extremes that correspond with eddy centers, as well as numerical or geometric criteria that define eddy edges (Sadarjoen and Post, 2000). By contrast, Lagrangian methods, including the Lagrangian averaged vorticity deviation and the modulus of vorticity, define Lagrangian coherent structures (LCS) associated with the attraction or repulsion of particles (Haller et

al., 2019; Vortmeyer-Kley et al., 2016, 2019). Generally, Lagrangian methods tend to detect fewer total eddies with smaller eddy radii, being highly sensitive to the time integration parameter while adhering to a stricter definition of particle interactions (Vortmeyer-Kley et al., 2019). Both Eulerian and Lagrangian methods have been compared for surface mesoscale eddy detection, with the prevailing conclusion that different algorithms are suitable for different purposes, although some methods conclusively perform better than others at specific tasks (Lian et al., 2019; Souza et al., 2011; Vortmeyer-Kley et al., 2019).

While eddy detection and tracking at the surface has been extensively developed, subsurface eddy detection in both observations and models is less mature. High resolution satellite data are only available at the surface, meaning that subsurface data must be derived from numerical models, synthetic profiles, or sparse *in-situ* observations (Petersen et al., 2013). In the first two cases, verification of completely subsurface findings is scarce; while in the third case, observations can provide a limited picture of eddy three-dimensional structure and occasionally identify individual subsurface eddies, but ultimately cannot provide a comprehensive overview of subsurface eddying (Assassi et al., 2016; de Marez et al., 2019; de Marez et al., 2020; Sun et al., 2022). Regardless, models have been used for subsurface eddy surveys in the past, albeit using methodologies and thresholds developed for surface eddy detection or using algorithms that compare unfavorably with more recently developed methodologies (Doglioli et al., 2007; Petersen et al., 2013; Lian et al., 2019; Xu et al., 2019). Due to the lack of SSH and corresponding geostrophic current measurements found beneath the surface, methodologies need to be adapted and optimized for a subsurface ageostrophic environment. Many of the best-performing methodologies

were designed using criteria derived for geostrophic regimes, such as edge detection methods that require finding closed streamlines (Le Vu et al., 2018; Nencioli et al., 2010). Therefore, there is a current lack of synchronicity between existing surface and potential subsurface eddy detection algorithms.

Successful subsurface tracking methodologies, properly implemented, may be used for multiple purposes, including the study of the spread of distinct water masses. In the Arabian Sea, there are several high-salinity water masses that typically exist in the range between 0 and 1000 meters: the Arabian Sea high salinity water (ASHSW), Persian Gulf water (PGW), and Red Sea water (RSW) (Prasad et al., 2001). These water masses each impact the physical structure of the Arabian Sea with implications for oxygen and nutrient concentrations both above and below the pycnocline (Morrison et al., 1998; Queste et al., 2018). Recent modelling and observational studies have indicated the role that subsurface eddies might play in the spreading and mixing of these water masses (L'Hégaret et al., 2015, 2016, 2021; Morvan et al., 2020). L'Hégaret et al. (2021) specifically suggest that mesoscale eddies have a major impact on the distribution and spreading of outflows from the Gulf of Oman and Gulf of Aden (GoA) through the rest of the Arabian Sea. Through the development of a specialized eddy tracking algorithm, we aim to distribute a tool that can efficiently detect eddies that lie specifically within important subsurface water masses. Here, we choose RSW as an example due to its identifiable presence at depths greater than 600 meters (L'Hégaret et al. 2021).

Eddy detection algorithms aimed at detecting purely subsurface eddies must perform well independently from surface-derived measurements. The main remaining model-derived fields for use are current velocities, temperature, and salinity. From these,

vorticity, the OW parameter, and LNAM are all viable derived fields. PV is another useful field for use in subsurface eddy detection, and has been used to success observationally but is more complex for surface eddy tracking due to the effect of outcropping (Bretherton, 1966; Morel et al., 2019; Pelland et al., 2013; Schneider et al., 2003). In this study, we will perform the first comparison and optimization of Eulerian subsurface eddy detection algorithms derived from these fields against an established winding angle algorithm using SSH at the surface (Chaigneau et al., 2008). We will then demonstrate our resulting optimized algorithm by characterizing the dynamics of a large, previously undiscovered subsurface eddy that forms semi-regularly to the east of the Chagos Archipelago. The remainder of our study is organized as follows: section 3.3 details the data, fields, and tracking algorithm used in this study, section 3.4 describes the optimization of our algorithms, section 3.5 is a case study of a subsurface eddy that highlights the effectiveness of our optimized algorithm, and section 3.6 presents a summary and the conclusions of our work.

3.3 DATA & METHODOLOGY

3.3.1 MODEL SIMULATIONS

In this study, we use model simulations from the Nucleus for the European Modelling of the Ocean (NEMOv3.1) maintained by the Copernicus Marine Environmental Service (CMEMS), available online at <https://resources.marine.copernicus.eu/> with a product ID of GLOBAL_ANALYSIS_FORECAST_PHY_001_024. Variables used include potential temperature and salinity from which we derive potential density, SSH, and zonal and meridional velocities. This is a daily gridded $1/12^\circ$ horizontal resolution dataset with 50

vertical levels between 0 meters and 5500 meters. Output is generated in 10-day forecast segments beginning on January 1st, 2016 and extending into 2022. We choose this model simulations given its eddy-resolving high resolution and the fact that it has been successfully used in studies of Indian Ocean dynamics, notably in the Bay of Bengal (Roman-Stork and Subrahmanyam, 2020). As these are publicly available model outputs, the use of this product in this study allows for reproduction of our results and calibration of other subsurface eddy detection methodologies in the future.

3.3.2 FIELD CALCULATIONS

3.3.2.1 VORTICITY

We calculate relative vorticity, ω , as the curl of the total velocity field:

$$\omega = \frac{\partial v}{\partial x} - \frac{\partial u}{\partial y}, \quad (1)$$

where v and u are the magnitudes of the meridional and zonal currents respectively. In the northern hemisphere, a high-magnitude positive vorticity indicates a maximum of cyclonic rotation, while a high-magnitude negative vorticity indicates a maximum of anticyclonic rotation. Vorticity typically decreases from a maximum at the eddy center to zero in the area of maximum velocity of an isolated eddy, then often reverses sign towards its outer edge (Aouni, 2021).

3.3.2.2 OKUBO-WEISS PARAMETER

The Okubo-Weiss (OW) parameter, W , is a combination of vorticity as well as the normal (s_n) and shear (s_s) components of the strain as follows (Okubo, 1970; Weiss, 1991):

$$s_n = \frac{\partial u}{\partial x} - \frac{\partial v}{\partial y}, \quad (2)$$

$$s_s = \frac{\partial v}{\partial x} + \frac{\partial u}{\partial y}, \quad (3)$$

and

$$W = s_n^2 + s_s^2 - \omega^2. \quad (4)$$

A highly negative W signifies a vorticity dominated environment, indicating a likely eddy center, and W increases towards the edge of an eddy. The sign of the relative vorticity in the eddy center is used to determine the sense of rotation of an eddy detected using the OW parameter.

3.3.2.3 LOCAL NORMALIZED ANGULAR MOMENTUM

The local normalized angular momentum (LNAM) is defined identically to Le Vu et al. (2018)'s Eq. (2) as implemented in their Angular Momentum Eddy Detection Algorithm (AMEDA):

$$\text{LNAM}(G_i) = \frac{\sum_j \mathbf{G}_i \mathbf{X}_j \times \mathbf{V}_j}{\sum_j \mathbf{G}_i \mathbf{X}_j \cdot \mathbf{V}_j + \sum_j |\mathbf{G}_i \mathbf{X}_j| |\mathbf{V}_j|} = \frac{L_i}{S_i + \text{BL}_i}, \quad (5)$$

Where G_i is a grid point and X_j and V_j are the position and velocity vector of a neighboring point; L_i is therefore the local angular momentum at G_i while S_i , the sum of the scalar products, is added to the renormalization term BL_i . The summed area is a square domain whose exact size depends upon the first baroclinic deformation radius. LNAM is especially useful for detecting eddies whose size lies closely to this radius; as the Arabian Sea lies at low latitudes, this varies from more than 200 km towards the equator to 80 km or less towards the northern terrestrial boundaries (Chelton et al., 1998). The only difference between our formulation of LNAM here and LNAM as defined in Le Vu et al. (2018) is that we use ageostrophic currents in this analysis. A full description of LNAM can be found in Le Vu et al. (2018).

3.3.2.4 RESCALED POTENTIAL VORTICITY

We calculate the rescaled potential vorticity (PV) as designed by Morel et al. (2019) and demonstrated by Assene et al. (2020). The rescaled PV is defined as

$$\begin{aligned} \mathbf{PV}_{\text{rescaled}} &= (\nabla \times \mathbf{U} + f) \cdot \nabla Z(\rho) \\ &= \mathbf{div} [(\nabla \times \mathbf{U} + f) \nabla Z(\rho)] \end{aligned} \quad (6)$$

where U is the velocity field, f defines the Coriolis parameter, and $Z(\rho)$ is a function of potential density. In practice, this function is a reference density profile chosen to represent the stratification of an area such that the typically overwhelming signature of the pycnocline in the traditional Ertel PV can be minimized or eliminated. Therefore the choice of this profile depends upon the spatiotemporal study area. While the rescaled PV (hereafter PV) is highly sensitive to the choice of reference profile in the surface layers, it becomes less important the further away the calculation is made from the pycnocline. For this study, we choose a new reference profile located at 72°E, 0°N on a particular day for each monsoon for each year: July 1st for the summer monsoon, and January 1st for the winter monsoon. This location on these dates often displays stratification typical of the open ocean Arabian Sea and rarely contains either eddies or a distinct signature of RSW, making it ideal for the elimination of near-surface stratification without interfering with subsurface water mass signatures.

The rescaled PV bears the same conservation properties as the traditional Ertel PV and is also closely related to the quasigeostrophic PV. As a result, it is more closely related to other dynamical fields, such as vorticity. Indeed, at rest, the rescaled PV is close to f , the local Coriolis parameter, and an eddy can be identified by its PV anomaly (*i.e.* $PV_a = PV - f$) within a layer bounded by two isopycnals, determining its dynamical core. Similarly to quasigeostrophic eddies, the vertical integration of the rescaled PV within this layer is then

representative of the eddy strength. Finally, in numerical configurations where tides are simulated, internal gravity waves are generated and they can have a strong mesoscale signature in all dynamical fields (pressure, stratification, velocity, vorticity) that can spoil detection and tracking of eddies. PV filters out the signature of gravity waves, which, even though the present simulation results used here do not represent tides, is another argument for the use of PV for the detection of eddies.

This makes the rescaled PV a powerful tool for interpreting the dynamics of subsurface eddies in numerical models, though some considerations must be noted. Firstly, the necessary use of isopycnic layers separates the calculation of the PV field from the other fields noted here, which are typically calculated at static depths. Secondly, the dynamics associated with PV anomalies are non-local, such that the velocity or vorticity fields associated with a PV anomaly extend outside the layer. The choice of the isopycnal layers is thus crucial and vertical sections can be used to make sure the layer is associated with specific PV signature of water masses and eddies. Finally, when considering the surface layer, the previous arguments are still valid replacing the upper isopycnic surface bounding the layer with the ocean surface. But an additional effect, representing the dynamical effect of outcropping in terms of a PV Dirac sheet, has to be calculated (Bretherton, 1966; Schneider, 2003; Morel et al, 2019). The calculation of the mean isopycnal PV proposed in Assene et al (2020) has here been extended to take this term into account (Bretherton, 1966; Schneider, 2003; Morel et al, 2019). For the optimization component of this study, we calculate the surface layer of the PV between 1000 kg m^{-3} and 1025.5 kg m^{-3} , accounting for this outcropping at the surface (see Appendix B). The 1025.5 kg m^{-3} boundary corresponds to the upper edge of the PGW mass as defined by L'Hégaret

et al. (2021). As a result, this isopycnal is effective at capturing the surface water mass dynamics in the Arabian Sea without being contaminated by subsurface dynamics as a denser isopycnal might. Less dense bounding isopycnals reduce the viable study areas around the Gulfs of Aden and Oman due to the highly dense surface water in these locations.

3.3.2.5 VERTICAL VELOCITY

We obtain estimates of vertical velocity (w) using the zonal (u) and meridional (v) components of velocity where appropriate through the integration of the continuity equation:

$$\frac{\partial w}{\partial z} = -\left(\frac{\partial u}{\partial x} + \frac{\partial v}{\partial y}\right) \quad (7)$$

3.3.3 EDDY DETECTION METHODS

3.3.3.1 THRESHOLDED METHODS

Thresholded methods search for an area with only one local extreme where the largest enclosing contour is at (or sometimes above, depending on the exact formulation) a threshold defined by the field in question. These thresholds can be determined at a fixed value arbitrarily, or as a result of some other calculation. The most common calculation performed to obtain a threshold for OW is as a multiplicative factor of the standard deviation of the field. Hereafter, this multiplier is called the STD factor (*e.g.* Henson & Thomas, 2008; Lian et al., 2019). We will use the standard deviation method, but optimize the STD factor for both OW and vorticity, with the ensuing methods of center and edge detection being labelled hereafter as OW_T and $VORT_T$ respectively. The STD factors of each will differ between center detection and edge detection, as the center factor will be stricter than the edge factor to ensure a local extreme is properly identified. It is worth

noting that threshold methods necessarily may not need to obtain centers before enclosing contours. In this study, we separate both in order to determine if different center and edge detection fields or methods are more efficient than a single field center-and-edge detection method.

LNAM as defined by Le Vu et al. (2018) is also a thresholded method with a static parameter K that is specified as $|\text{LNAM}(\text{LOW} < 0)| = K$, where LOW is the Local Okubo Weiss parameter, calculated in the same domain as LNAM. As with the OW_T and VORT_T methods' thresholds, we will optimize K . LNAM is designed and calculated as a center detection method, not as an edge detection method, and so we only use LNAM for obtaining eddy centers.

3.3.3.2 WINDING ANGLE METHODS

Winding angle methods are those that do not set a threshold for obtaining eddy centers or edges, instead obtaining these features by searching for the largest closed contour around a single local extreme with at least 4×4 grid points enclosed. This is the original methodology used by Chaigneau et al. (2008) with SLA (hereafter referred to as the SSH method, as SSH is the field available in the NEMO model simulations used). We use the winding angle methodology for OW, hereafter OW_{WA} , vorticity, hereafter VORT_{WA} , and PV averaged within a layer bounded by two isopycnals, hereafter PV_{ISO} . The only parameter that must be set for winding angle methods is the search increment, which we set as a value lower than the typical absolute minimum value for each respective parameter: 10^{-4} m for SSH, 10^{-7} s^{-1} for VORT_{WA} , 10^{-14} s^{-1} for OW_{WA} , and 10^{-7} s^{-1} for PV_{ISO} . As Lian et al., (2019) demonstrate, winding angle methods are weakly sensitive to adjustments in this parameter. Our chosen values, at the expense of longer computation times, ensure that

the closed contours we obtain are accurate and do not stop short of the largest closed contour. The winding angle contour edge can be discarded to isolate the winding angle center, allowing for a hybridization of different center and edge detection methodologies as we detail in Section 3.

3.3.4 ERROR-DERIVED SIMILARITY SCORE

In order to numerically optimize the performance of each prospective subsurface eddy detection method, we employ a metric that we will attempt to maximize as we vary each detection method's parameters. We first recognize that we must perform this optimization at the surface, given the lack of observation-based subsurface eddy identification algorithms. Due to the success of the SSH method in previous studies specifically in the Arabian Sea, we first analyze surface eddies and use this method's output as our benchmark (Ernst et al., 2022; Trott et al., 2018, 2019). Given that our goal is to obtain an algorithm with the best possible similarity to a proven surface detection method at depth, we can compare the output of our methods to the SSH method in several ways. We have selected four axes along which to measure error, selected to reflect the critical components of an eddy tracking algorithm: number of eddies, shape of eddies, and area covered by eddies (positive and negative error). For each of the following calculations, the label AE refers to anticyclonic eddies (AEs) while the label CE refers to cyclonic eddies (CEs).

3.3.4.1 NUMBER ERROR

The percentage error between the number of eddies identified by the SSH algorithm (N_{SSH}) and the algorithm to be tested (N_{Test}) was used to eliminate algorithms that over-

identify eddies in situations where they should be identifying a fewer eddies and vice versa.

It is calculated as:

$$\mathbf{Err}_{\text{Num}} = \left| \frac{\mathbf{N}_{\text{Test}} - \mathbf{N}_{\text{SSH}}}{\mathbf{N}_{\text{SSH}}} \right| \quad (8)$$

3.3.4.2 RATIO ERROR

Some eddy detection schemes will frequently falsely classify currents, front, filaments, and other elongated structures as eddies. In order to reduce these false classifications, we can take the ratio of the longest and shortest distances between the eddy edge and the geometric eddy centroid. Therefore, the ratio error is calculated as the percentage error between the average of the ratio in both the SSH algorithm ($\mathbf{Ratio}_{\text{SSH}}$) and the algorithm to be tested ($\mathbf{Ratio}_{\text{Test}}$). A ratio closer to 1 reflects a perfectly circular eddy, while a lower ratio reflects an eddy that is either overly elongated or possesses some anomalously extending element such as a filament. This is functionally very similar to the classic circularity test but is much more computationally efficient. We calculate the ratio error as:

$$\mathbf{Err}_{\text{Ratio}} = \left| \frac{\mathbf{Ratio}_{\text{Test}} - \mathbf{Ratio}_{\text{SSH}}}{\mathbf{Ratio}_{\text{SSH}}} \right| \quad (9)$$

3.3.4.3 SPATIAL POSITIVE ERROR

This is the percentage error between the area correctly identified as an eddy, either AE or CE, in the SSH algorithm and the algorithm to be tested. This is assessed pixel by pixel using a classification scheme where a pixel labelled 0 is considered to be not an eddy, 1 is considered to be within an AE, and 2 is considered to be within a CE. Any pixels labelled AE or CE are considered to be part of an eddy, or positively detected. This error is calculated as:

$$\mathbf{Err}_{\text{Pos}} = \frac{1}{2} \left(\left| \frac{\mathbf{FN}_{\text{AE}}}{\mathbf{TP}_{\text{AE}} + \mathbf{FN}_{\text{AE}}} \right| + \left| \frac{\mathbf{FN}_{\text{CE}}}{\mathbf{TP}_{\text{CE}} + \mathbf{FN}_{\text{CE}}} \right| \right) \quad (10)$$

Where TP is the number of true positive pixel identifications, and FN is the number of false negative pixel identifications.

3.3.4.4 SPATIAL NEGATIVE ERROR

This is the percentage error between the area correctly identified as not containing an eddy in the SSH algorithm and the algorithm to be tested, using the same pixel by pixel classification as per the spatial positive error. It is therefore calculated as:

$$\mathbf{Err}_{\text{Neg}} = \frac{1}{2} \left(\left| \frac{\mathbf{FP}_{\text{AE}}}{\mathbf{TN}_{\text{AE}} + \mathbf{FP}_{\text{AE}}} \right| + \left| \frac{\mathbf{FP}_{\text{CE}}}{\mathbf{TN}_{\text{CE}} + \mathbf{FP}_{\text{CE}}} \right| \right) \quad (11)$$

where TN is the number of true negative pixel identifications with the SSH algorithm considered to be the truth, and FP is the number of false positive pixel identifications.

3.3.4.5 AGGREGATE SIMILARITY SCORE

This is the aggregate score, S , used to optimize eddy detection methods. It is calculated using an arithmetic mean of the above errors:

$$S = \left[1 - \frac{1}{4} (\mathbf{Err}_{\text{Num}} + \mathbf{Err}_{\text{Ratio}} + \mathbf{Err}_{\text{Pos}} + \mathbf{Err}_{\text{Neg}}) \right] * 100 \quad (12)$$

A perfect similarity score of 100 indicates that the test and SSH methods result in the exact same eddy detection scheme with the same number of eddies, in the same shapes, covering all of the same pixels. We therefore attempt to maximize the similarity score of an algorithm in the ensuing analysis, although each individual error is considered in the performance of the results. In our analysis below, there is no weighting given to each of the scores. However, the reader is invited to use arbitrary weighting of the scores in their own applications for their own purposes.

3.3.5 TRACKING

An eddy tracking methodology is required to verify the identification of specific eddies over multiple time steps. In this study, we use the eddy tracking algorithm developed by Chaigneau et al. (2008) and Pegliasco et al. (2015). This algorithm has since been used in the Arabian Sea to describe the nature and variability of both the eddy field as a whole and to characterize specific climatological eddies (Ernst et al., 2022; Trott et al., 2018). This algorithm compares eddies with overlapping areas between subsequent time steps using a cost function based upon the differences in radii, amplitudes, and EKE of each eddy. A minimum of this cost function represents the most statistically similar and thus likely eddy trajectory to continue tracking. A comprehensive description of this tracking algorithm can be found in Trott et al. (2018). It is worth noting that any other tracking algorithms may be used in conjunction with our detection scheme.

3.3.6 OPTIMIZATION DOMAIN

All optimizations are performed between 10°S and 30°N, 40°E and 80°E, and over the winter (November, December, January, February) and summer (May, June, July, August, September) monsoons of 2016, 2017, and 2019 to encompass the Arabian Sea. These years were chosen as their monsoons cover each classification of monsoon from weak (2016) to normal (2017) to strong (2019) and so provide variation of the Arabian Sea eddy field to fully test each parameter (Ernst et al., 2022; Greaser et al., 2020). All eddies with a radius smaller than 25 km are eliminated from our results, as these eddies are below the mesoscale (defined here as smaller than the first baroclinic deformation radius, approximately 50 km in the central Arabian Sea) and currently lack altimetric verification for the SSH method in the Arabian Sea (Le Vu et al., 2018). The total number of eddy maps

(days) across all tested monsoons is 837, with the SSH method at the surface finding a total number of 24,681 CEs and 23,532 AEs before individual detections are collated into trajectories.

3.4 EDDY TRACKING OPTIMIZATION

3.4.1 CENTER THRESHOLDS

To begin our search for an optimized detection method, we separate the center- and edge-finding components and test their parameters separately. First, we optimize the thresholds of the methods that require them, namely $VORT_T$, OW_T , and LNAM. We do this by using the SSH edge component, ensuring that the edge-finding method is the same for each center method tested (Figure 3.1).

We find that the optimized center threshold values of 0.85 for $VORT_T$ (Figure 3.1a), 0.15 for OW_T (Figure 3.1b), and 0.65 for LNAM (Figure 3.1c). We note that the optimum threshold parameter is most heavily determined by the number and the spatial positive errors, with only a slight variation in ratio error and very little change in spatial negative errors. We find that these thresholds lie closely to values found in the literature, *i.e.* 0.2 for OW_T 's STD factor and 0.7 for LNAM's K (Isern-Fontanet et al., 2003; Le Vu et al., 2018; Xu et al., 2019). However, our optimal values are smaller by 0.05 in both cases, reflecting a very slightly more lenient threshold. Overall, only OW_T favors a single optimum value based upon its aggregate score, while $VORT_T$ and OW_T each have a wide range of similar values higher than 0.7; $VORT_T$ scores are similar between a STD factor of 0.5 and 1, while LNAM scores have the largest range of comparable values between 0.1 and 0.8, which also matches the findings of Le Vu et al. (2018). All further analysis with these methods is hereafter performed with the optimized values determined above.

3.4.2 CENTER FILTERING

Given the high resolution of the model used and the noise often contained within the non-normalized vorticity derived fields, a simple low-pass moving average filter may be applied to the data to enhance detectability of mesoscale features (Souza et al., 2011). The size of this filter, if it should be applied at all, may also be optimized, with the number of pixels on each side of the center pixel (the half window) denoting the smoothing factor (Figure 3.2). In this case, an increase in smoothing factor by 1 increases the size of the low-pass filter by $1/12^\circ$ on all sides, such that a maximum tested smoothing factor of 15 is a filter of 31 pixels by 31 pixels (including the center pixel), or approximately a 280 km low-pass filter depending on latitude.

We find that the optimal smoothing factors for each field are 2 for $VORT_T$ (Figure 3.2a), 7 for $VORT_{WA}$ (Figure 3.2b), 0 (no smoothing) for OW_T (Figure 3.2c), 3 for OW_{WA} (Figure 3.2d), and 3 for PV_{ISO} (Figure 3.2e). Of these optimizations, $VORT_T$ and OW_T are the most sensitive, with higher smoothing factors drastically increasing both number and spatial correct errors. OW_{WA} and PV_{ISO} are only slightly less sensitive, with increasing number and spatial correct errors on either side of the optimized value. Lastly, $VORT_{WA}$ is relatively stable, with little difference between high and low smoothing factors. As with the threshold values obtained in section 3.4.1, we continue with the optimized smoothing factors above.

3.4.3 EDGE THRESHOLDS

$VORT_T$ and OW_T can be decomposed into center and edge thresholds which may be considered separately (Figure 3.3). For this purpose and for other edge method optimizations, the center method is set to SSH to remain constant.

We find that $VORT_T$ has an edge STD factor threshold optimized at 0.6 (Figure 3.3a) while OW_T is optimized at 0.1 (Figure 3.3b). Both STD factors are smaller than their respective center STD factors (Figure 3.1), reflecting the need for a more restrictive STD factor to determine the center versus the edge of an eddy. Neither $VORT_T$ nor OW_T compare well to SSH as edge methods, with minimal spatial correct errors of 0.91 and 0.84 respectively, meaning that more than 4 out of every 5 eddy-containing pixels in the SSH method were identified as non-eddies with these methods. This is consistent with previous comparisons that have demonstrated that the OW_T method identifies smaller eddy contours than other methods as compared to the SSH method, which tends to result in relatively large eddy contours (Lian et al., 2019; Souza et al., 2011). We would logically expect that if our ‘truth’ method were, *e.g.*, a variant of the OW_T method, the spatial positive error would be considerably less for OW_T given the method’s resemblance.

3.4.4 EDGE FILTERING AND RATIOS

As with center methods, we can determine what degree of low-pass filtering might benefit eddy edge detection. We can also filter out elongated fronts and other non-eddy structures using the same axis ratio used for the calculation of the ratio error metric (Section 2, d, 2). In other words, all eddies with a ratio of longest to shortest edge away from the centroid less than a certain threshold are eliminated. In this regard, we vary both the spatial smoothing and minimum ratio together to obtain an optimal result (Figure 3.4).

We find that both thresholded methods perform best when relatively unprocessed: $VORT_T$ (Figure 3.4a) is optimized at a smoothing factor of 2 with no minimum centroid ratio, while OW_T (Figure 3.4c) is optimized without smoothing or a minimum ratio. OW_{WA} follows $VORT_T$ in benefiting from a small smoothing factor of 1 and no minimum centroid

ratio (Figure 3.4d). $VORT_{WA}$ (Figure 3.4b) benefits from moderate smoothing factor of 5 and a minimum ratio of 0.12 and PV_{ISO} (Figure 3.4e) benefits from a similar smoothing factor of 4 as well as a small minimum centroid ratio of 0.08. We proceed to the final step of method hybridization with these parameters set exactly as in Figure 3.3.4.

3.4.5 HYBRID METHOD EVALUATION

Hybrid center and edge detection methods can leverage the strengths of two separate fields or sets of restrictions to produce a superior detection algorithm; AMEDA is one such example, using LNAM for center detection with SSH or geostrophic currents used for edge detection (Le Vu et al., 2018). As a result, we can combine the optimized center and edge methods independently produced by the above analysis to determine if using separate center and edge detection methods creates the optimal hybrid method for subsurface eddy detection when compared to the traditional SSH method (Figure 3.5).

We find that the overall best algorithm is one that utilizes PV_{ISO} for both center and edge detection with a similarity score of 74.65 (Figure 3.5e); this algorithm performs best for both number errors (Figure 3.5a) and ratio errors (Figure 3.5b) as well, with optimal errors of 12.16% and 5.07% respectively. However, both spatial errors have separate optimal algorithms, as Err_{Pos} is optimized with $VORT_{WA}$ centers and $VORT_{WA}$ edges with an error of 71.66% (Figure 3.5c) and Err_{Neg} is optimized with LNAM centers and OW_{WA} edges with an error of 1.27% (Figure 3.5d). We do note, however, that there is relatively little difference between the best and worst performing Err_{Neg} algorithms versus other error types and that Err_{Pos} is relatively large for all methods, underlining the fact that eddies delimited by SSH have larger contours than any other method. Overall, the best performing edge methods are $VORT_{WA}$ and PV_{ISO} regardless of center methods, while the best overall

center method varies by edge method (Figure 3.5e). That the winding angle edge algorithms perform better in this analysis is unsurprising, given the winding angle nature of the original SSH algorithm. We would expect that any such comparison would favor similarly constructed algorithms. However, this comparison process is applicable for any original eddy tracking methodology, and so the desirable traits of any other algorithm can be potentially replicated using our overall optimization approach.

Before using any of these hybrid algorithms, we must verify their performance visually to ensure they are detecting eddies sensibly. For this, we select 6 of our algorithms. We first display the SSH algorithm to provide a baseline, then follow with OW_T centers and OW_{WA} edges, as this algorithm is the best performing algorithm using only OW . Then, we demonstrate $VORT_{WA}$ centers and $VORT_{WA}$ edges as the best performing Err_{Pos} algorithm, $LNAM$ centers and OW_{WA} edges as the best performing Err_{Neg} algorithm, $VORT_T$ centers and PV_{ISO} edges as the runner up to the best algorithm, and PV_{ISO} centers and PV_{ISO} edges as the best overall algorithm. We demonstrate each of these algorithms in several times and locations, beginning in the GoA on January 1st, 2017 (Figure 3.6).

In this snapshot, we find 4 major eddies: an elongated CE in the GoA, two cyclones to the north and south of Socotra, and a large AE partially out of frame to the east (Figure 3.6a). All algorithms detect the eddies to the north and south of Socotra, with the PV_{ISO} algorithms achieving the most accurate shapes (Figure 3.6e, f). By contrast, only the $VORT_{WA}/VORT_{WA}$ and PV_{ISO}/PV_{ISO} algorithms properly detect the large eastern AE (Figure 3.6c, f). The middle CE is partially detected in two parts by the OW_{WA} edge algorithms and the $VORT_{WA}/VORT_{WA}$ algorithm, while only the PV_{ISO}/PV_{ISO} algorithm identifies it as a single eddy (Figure 3.6b, c, d, f). In terms of smaller eddies, the possible

AE to the west of Socotra seen in the SSH method is only identified by the $VORT_{WA}/VORT_{WA}$ algorithm, while the cyclone alone $8^{\circ}N$ is detected by all algorithms except the PV_{ISO}/PV_{ISO} one. Overall, this figure demonstrates that all methods are capable of detecting eddies within the GoA and around Socotra, but that PV_{ISO} algorithms achieve the most desirable eddy shapes. We continue to see if this is the case using an image of the Gulf of Oman on July 28th, 2017 (Figure 3.7).

At this point in time, we observe two major eddies in the region, an AE along the southeastern coast of the Arabian Peninsula and exiting the Gulf of Oman (Figure 3.7a). These eddies are once again detected by all algorithms, although the PV_{ISO} edge methods additionally identify an elongated section to the east (Figure 3.7e; Figure 3.7f). Besides these two large eddies, there are a handful of smaller cyclones and anticyclones centered around $64^{\circ}E$, $20^{\circ}N$ that are partially detected by all methods except $LNAM/OW_{WA}$. This makes sense, as every other algorithm over-detects smaller eddies in the region, while $LNAM/OW_{WA}$ is optimized for reducing false detections. The OW_T/OW_{WA} and $VORT_{WA}/VORT_{WA}$ methods are especially prone to false detections to the northeast. This is reflective of the broader trend of $VORT_{WA}/VORT_{WA}$ as seen in Figure 3.5c and 5d: this algorithm consistently detects almost every eddy in any given image as it optimizes spatial positive errors, but consistently over-detects, as it has the greatest spatial negative error. This is especially seen in the next series of images of climatological eddies, beginning with the Lakshadweep High (LH) during the northeast monsoon in 2016 (Figure 3.8).

Here, the LH is centered around $75.8^{\circ}E$, $7.5^{\circ}N$, with smattering of less intense AEs and CEs to the west and northwest (Figure 3.8a). As before, all algorithms detect the LH, though the PV_{ISO}/PV_{ISO} algorithm makes a curious detection of the LH as an AE, rather

than a CE, with a core of positive PV (Figure 3.8f). This is only possible due to the isopycnal averaging process detecting a cyclonic core underlying the LH as more powerful than the anticyclonic anomaly at the surface. Misdetections of this manner are not normally the case with this algorithm's performance, but it indicates a reason why its spatial positive error would be higher at the surface, as deeper features can confuse the algorithm. Logically, this would not be an issue in deeper isopycnal layers. Besides the LH, the smaller eddies are best represented by the PV_{ISO}/PV_{ISO} algorithm, with the other algorithms displaying their common traits as previously highlighted: an over detection of eddies by $VORT_{WA}/VORT_{WA}$, an under detection of eddies by $LNAM/OW_{WA}$, a balanced performance by OW_T/OW_{WA} that tends towards under detection, and a similar performance by $VORT_{WA}/PV_{ISO}$ that tends towards over detection (Figure 3.8b, c, d, e). To complement this analysis of the LH region and conclude our visual tests, we present a similar snapshot of the Great Whirl (GW) during the strong southwest monsoon of 2019 (Figure 3.9).

The GW is evidently the massive AE centered on $53.3^{\circ}E, 7.9^{\circ}N$ (Figure 3.9a). At this point in time, only $VORT_{WA}/VORT_{WA}$ and PV_{ISO}/PV_{ISO} algorithms properly detect it (Figure 3.9c; Figure 3.9e). By contrast, although centers are identified in every other algorithm, internal variation within the GW prevents a detection. The orbiting cyclone to the GW's east is detected by all algorithms except $LNAM/OW_{WA}$, a rare failing for this algorithm, while the OW algorithms falsely detect filaments along the southern edge of the GW (Figure 3.9b, d). The surrounding energetic eddy field is best represented by PV_{ISO}/PV_{ISO} , although no algorithm perfectly detects every eddy. Every algorithm in this snapshot falsely detects at least one eddy, *e.g.* the possible cyclone to the southwest of the GW that is detected by every algorithm except OW_T/OW_{WA} (Figure 3.9b). It is reasonable

to conclude that many of these less pronounced detections could be false detections or non-detections by the SSH algorithm. However, as previous studies have concluded, no single algorithm is perfect at detecting all types of eddies, and there is a lack of a unified eddy definition, so our analysis above includes all of the SSH algorithm's features and biases, by nature integrating some of them into our resulting algorithms that emulate it (Lian et al., 2019; Souza et al., 2011).

With all of the above analyses considered, we conclude that the best algorithm for use both along isopycnals and in the general sense is PV_{ISO}/PV_{ISO} , specifically with the smoothing factors and centroid ratios we have optimized. By contrast, algorithms that utilize the OW are prone to detecting much smaller eddy contours, often missing eddies entirely and often missing large circulations. Algorithms based around the relative vorticity are functional, but with a tendency to massively over identify eddies.

To summarize our final PV_{ISO}/PV_{ISO} optimized method: we first begin with the horizontal velocity fields, temperature, and salinity from our model. We calculate potential density and then rescale the density profile for each vertical column using a representative reference profile defined at a certain location and time (here, 72°E, 0°N, recalculated for each monsoon season). This rescaling reduces the effect of the pycnocline on the resultant PV profile. The PV field is averaged between two bounding isopycnals as in Assene et al. (2020). In the figures above, this is done for the surface waters of the Arabian Sea down to 1025.5 kg m⁻³. This rescaled PV is passed through a simple moving average low pass filter with a half-window of 3 pixels to slightly reduce noise (Figure 3.2). Then, we extract local extremes with closed contours of smoothed PV around them and label them as tentative eddy centers. Prior to edge detection, we again smooth the original rescaled PV field in a

similar manner with a half-window of 4 pixels (Figure 3.3). We then find the largest enclosing contour of PV around each previously identified extreme in the winding angle method style described by previous studies (Chaigneau et al., 2008). Finally, we eliminate all instances of contours with a longest-to-shortest centroid-to-edge distance ratio of less than 0.08, excluding overly elongated, front-like features from the final results (Figure 3.3).

To summarize, the final optimized parameters for PV_{ISO}/PV_{ISO} and all other algorithms are placed in Table 3.1.

3.5 CASE STUDY: RED SEA WATER

3.5.1 ISOPYCNAL EVALUATION

In this section, we demonstrate the procedure by which eddies within a water mass can be tracked using our method. We begin with a brief case study of RSW, using our diagnostics to pinpoint a new large eddy identifiable exclusively in the subsurface. However, we must begin this demonstration by defining the RSW domain in our model. Previous studies have determined several isopycnals along which the RSW water mass lies based upon observations (L'Hégaret et al., 2021; Prasad & Ikeda, 2001). Although exact ranges vary depending on the distance from the strait of Bab-el-Mandeb, strict definitions of RSW might choose isopycnals of 1027 kg m^{-3} and 1027.4 kg m^{-3} , while more loose boundaries might define isopycnals of 1026.5 kg m^{-3} and 1028 kg m^{-3} . In order to determine the isopycnals along which we determine the RSW water mass to be for our model, we must validate it against observations. In this case, we use the methodology of L'Hégaret et al., 2021 to determine our isopycnals (Figure 3.10).

Comparing to L'Hégaret et al. (2021) Figures 3b and 4b, we find that the NEMOv3.1 model results in the GoA are on average 0.5 kg m^{-3} less dense at the peak

density at depth (Figure 3.10a) with a much wider spread of salinity values in the intermediate layers. Regardless, the peak of the RSW still is encapsulated broadly by the 1026 kg m^{-3} and 1028 kg m^{-3} bounding isopycnals in the GoA. We use these values to repeat the L'Hégaret et al. (2021) water mass detection algorithm at each vertical profile. First each T-S profile is converted into spiciness following the Gibbs SeaWater (GSW) Oceanographic Toolbox of TEOS-10; this uses the McDougall and Krzysik (2015) formulation of spiciness. Then, the spiciness profiles are vertically detrended, and the previously defined isopycnals, combined with a minimum upper depth of 600 m, are used to define the range of possible depths within which we locate RSW. Within this range of values, a maximum, upper minimum, and lower minimum spiciness are defined (Figure 3.10b). We therefore calculate the temporal averages of these values and determine the basin-wide maxima and minima (Figure 3.11).

We find that the average RSW maximum decreases away from the strait of Bab-el-Mandeb, scaling from 1027.2 kg m^{-3} at the strait to 1027.1 kg m^{-3} at the edge of the GoA and out to $1027.05 \text{ kg m}^{-3}$ in the central and northern Arabian Sea (Figure 3.11a). Overall, the vast majority of the RSW maximums (within 2 standard deviations) in our model are found between 1026.95 and 1027.3 kg m^{-3} . The opposite trend is seen in the density ranges, as the density ranges are most constrained closer to Bab-el-Mandeb at 0.2 kg m^{-3} , increasing rapidly to the edge of the Gulf and out to 0.6 and 0.7 kg m^{-3} in the northern and southern Arabian Sea respectively (Figure 3.11b). We find that the density range width often follows bathymetry, with the shoaling of the Central Indian Ridge clearly visible as a decrease in density range. This reflects the propensity for the bottom minimum to lie literally on the bottom of the bathymetric model mesh throughout this region. The majority

of the density range is the difference between the maximum and the bottom minimum, rather than the top minimum; the average difference between the top minimum and the maximum is 0.037 kg m^{-3} , while the difference between the bottom minimum and the maximum averages 0.6 kg m^{-3} . With these numbers in mind, we aim to capture eddy dynamics in the maximum of RSW, constricting our depth range enough that we do not average over too many layers. We therefore choose an isopycnal range between $1026.95 \text{ kg m}^{-3}$ and 1027.4 kg m^{-3} for the following analysis. This contains all RSW maxima to within 3 standard deviations, with an upper bound adhering to the findings of Prasanna Kumar & Prasad (1999). Across the Arabian Sea in the model domain and time period studied, the average depth of the former isopycnal is 633 m and the average depth of the latter isopycnal is 1034 m, encompassed by NEMO model levels 32 through 36. As our reference profile location typically does not display a major signature of RSW, we maintain its use for our results as described in Section 2f.

We will now proceed to provide a brief overview of the results of our methodology. The total results as summarized below are best interpreted using our Movies S1 and S2 that present the PV and Spiciness of the Arabian Sea in conjunction with our detected eddies and their respective tracking numbers over time. We encourage the reader to examine these movies and note that, while many eddies are correctly identified, as noted by the spatial positive error from Figure 3.5, our method is not perfect, but can, as demonstrated below, still provide a useful tool for characterizing subsurface eddies that exist within specific water masses.

3.5.2 RED SEA WATER EDDY TRACKING

We find that the largest number of eddies by category are CEs produced in the summer monsoons (Figure 3.12i-j), with the largest generation sites at the mouth of the Gulf of Oman and along the Somali Current. By contrast, the winter monsoon CEs are detected most frequently along the West Indian Coastal Current (WICC) (Figure 3.12a-b). While the summer monsoon CE distribution is consistent with previous studies of surface eddies, such as Zhan et al. (2020), the winter CE distribution is unanticipated. The most likely explanation is Rossby wave activity radiating from the second annual downwelling coastal Kelvin wave each year, as the westward trajectories and phase speeds of these eddies suggest this origin (Brandt et al., 2002; Subrahmanyam et al., 2009). Additionally, Wang et al. (2021) demonstrate that the signals of baroclinic Rossby waves are visible in the vorticity balance even past 1000 meters, albeit weakly. Another reasonable source of these eddies might be a long-lasting meander in the RSW outflow tongue, as documented observationally by Meschanov & Shapiro (1998). AEs in the winter also are mainly found along the axes of what could be either Rossby waves or the RSW outflow tongue (Figure 3.12f). AEs during the summers are more scattered, with a large number of AEs detected around both in the WICC region and around Socotra (Figure 3.12 m-n). The prevalence of AEs in the eastern Arabian Sea during the summer is less supported by surface observations and may be assisted due to the deepening of the WICC undercurrent during the summer (Chaudhuri et al., 2021; Trott et al., 2018). If this is the case, then we will expect large levels of interannual variability in this region (as observed by Chaudhuri et al., 2021).

Regardless of the season, the largest and most intense eddies are detected in the Somali Current and the GoA (Figure 3.12c-d, g-h, k-l, o-p). Intense RSW eddies are

expected in the GoA, as RSW both lies along the bottom and encounters waters from the south, subjecting it to mixing and bottom friction simultaneously (Al Saafani & Shenoi, 2007; de Marez et al., 2020). This spreading also corresponds to previous observations of eddies in the RSW, where instabilities in the spreading out of the GoA is indicated as the primary eddy formation mechanism (Shapiro & Meschanov, 1991). This may help explain the relative deficit of eddies directly in the mouth of the GoA versus the proliferation of eddies further east. Unusually, there is a small region where an above-average number of large, very intense Antarctic Intermediate Water (AAIW) eddies are detected around 8°S, 73°E. This corresponds to the region around the Chagos Archipelago and has not been documented to this point (Trott et al., 2017; Trott et al., 2019; de Marez et al., 2019).

3.5.3 A CHAGOS EDDY AND ITS POTENTIAL VORTICITY EVOLUTION.

To demonstrate the dynamical analysis that is more easily enabled with the PV_{ISO}/PV_{ISO} method, we investigate the anomalously intense AEs that form near the Chagos Archipelago as identified in Figure 3.12, hereafter referred to as the Chagos eddies. These eddies form frequently around the Chagos Archipelago during the southwest monsoon, and select one such eddy on May 29th, 2019 (eddy ID 998 in Movie S1 and Movie S2), which had first been identified 16 days earlier and would continue to remain identifiable as a high PV core until late July, although our algorithm loses track of it after mid-June due to edge interference with the Chagos Archipelago (Figure 3.13).

We observe the deformation of the isopycnals downward in the water column (Figure 3.13, Col. 1) between 600 and 1200 meters. This is accompanied by an anticyclonic vortex that is positioned between a high salinity water mass to the north and a low salinity water mass to the south, with a peak salinity at approximately 700 meters' depth (Figure

3.13, Col. 2). This is almost the exact depth of the identified eddy (743 meters maximum PV anomaly), which at this time possesses an average radius of 112 km (Figure 3.13, Col. 3). As this lies in the southern hemisphere, this counterclockwise circulation is associated with the downwelling of water in the intermediate ocean. Furthermore, there is no sign of an eddy at the surface, indicating that this eddy is fully subsurface with a signature visible down to 2000 meters.

To determine how this eddy may have formed, we perform Lagrangian particle tracking as described by Assene et al. (2020). This takes 500 particles randomly seeded within the eddy radius and vertically within 100 meters of the maximum PV anomaly depth of the eddy core (Figure 3.13, Col. 3) in regions with a vorticity greater than $1 \times 10^{-6} \text{ s}^{-1}$. We calculate the particle's position, PV, and Richardson number (Ri) backwards in time to determine an initial position 100 days prior. Since isopycnal PV is conserved adiabatically, the particles that have experienced the largest changes in PV have therefore undergone mixing, friction, or some other diabatic process. We use the same scheme as Assene et al. (2020) to classify particles as high (initial PV greater than 2 standard deviations above final PV), low (initial PV less than 2 standard deviations above final PV), or medium (initial PV within 2 standard deviations of final PV) starting PV particles, where the standard deviations are calculated using all particles' final PV. These are displayed as red crosses, blue triangles, and green diamonds, respectively. We begin by displaying all 500 particles' evolution and general characteristics through time (Figure 3.14).

We find that 56.4%, or 282 of the particles that formed the Chagos eddy were initially low PV, with only 28.6%, or 153 of the particles possessing moderate PV and the remaining 15%, or 75 particles, having high in PV (Figure 3.14a). 80.6%, or 403 of the

particles originate to the east of the Chagos Archipelago, while the remaining 97 particles originate to the west. Low PV particles are the most clustered, found primarily in an eastern grouping centered on 6°S, 77°E and a western grouping around 7°S, 70°E. By contrast, moderate PV particles are found throughout the entire domain where particles are found, though with the smallest average movement from starting position to ending position, as a large number of moderate PV particles are scattered to the north of the eddy. Finally, the high PV particles are found both in the eastern cluster where the low PV particles are found, as well as the eastern edge of the Chagos Archipelago and the far western edge of the domain around 64.5°E. The particles' temperatures and salinities display two groupings roughly above and below 7.8°C, with a notable scattering of low PV particles being the warmest around 9°C and a tight grouping of high PV particles being the coldest at or below 6°C (Figure 3.14b). As seen by the highly concentrated final positions, particles remain grouped into two halves by temperature, with a range of salinities from 34.8 psu to 34.87 psu. The density groupings in Figure 3.14c further make apparent that there are two distinct clusters of density for all particles, regardless of initial PV. The original depths of the particles range from 450 meters to 1100 meters, with low PV particles dominating the layer closer to the surface and high PV particles being the most prevalent in the deepest layer (Figure 3.14d). The low PV particles sink by 200 meters around late April, while the high PV particles rise to 900 meters or above by early April. We observe that most particles are clustered around a PV of $-1 \times 10^{-5} \text{ s}^{-1}$ for most of their lifetime (Figure 3.14e). Many of the high PV particles are seen to rapidly vary PV up until the eddy formation in mid-May, while a distinct arc of low PV particles is seen between the end of February and early April;

as discussed below, this follows the evolution of another eddy in the region. Overall, PVs are constrained down to their final levels as of early May, just prior to the eddy formation.

First, we consider the evolution of the low PV particles specifically (Figure 3.15). We find that there are 226 low PV particles originating to the east of the Chagos Archipelago, and 56 particles originating to the west. The eastern particles mostly originate in the deeper layers around $1027.15 \text{ kg m}^{-3}$ (Figure 3.15a, b). These are seen to rotate anticyclonically inside another subsurface eddy centered around $8^{\circ}\text{S}, 77.5^{\circ}\text{E}$ before losing PV and mixing with less dense water as they are entrained within the identified Chagos eddy. In fact, this is the result of eddy number 995 in Movie S1 merging with a core of low PV water that is not identified as an eddy until eddy 995 merges with it. This merger is clearly visible in the low Ri numbers around early May, as the two main circulations that eventually become the Chagos eddy merge and mix together. Interestingly, strong PV variations are also associated with low Ri (Figure 3.15b, c) and occur at the same time of both the eddies merging and when the resulting structure interacts with the Chagos Archipelago. We observe another anticyclonic subsurface eddy originate in late February around 69°E to the west of the Archipelago (Figure 3.19d). In contrast to the eastern eddy, this western eddy is primarily composed of less dense water around 1026.8 kg m^{-3} (Figure 3.15e). This eddy impacts the Archipelago as it translates eastward, forcing its particles through a narrow channel that causes substantial mixing and a rapid increase in PV as the particles are forced along the southeastern edge of the Archipelago before finally being entrained in the Chagos eddy late in their lifetime. This mixing is clearly visible in the span

of low Ri numbers throughout all of April (Figure 3.15f). Overall, the particles that make up the western eddy are the same low PV particles that are warmest and shallowest in Figure 3.14.

We continue our analysis of the different types of particles with the particles that exhibit only a medium PV (Figure 3.16). As with low PV particles, the majority (112 of 143) of medium PV particles are found to the east of the Archipelago, with only 31 particles found to the west (Figure 3.16a). While around half of the eastern medium PV particles are found to be in the same eddy as identified in Figure 3.15 or from a westward current to its east, the other half originate from the north of the final eddy, and are mostly the particles that form the core of the Chagos eddy before it is fully identified as an eddy. This explains their moderate changes in PV and density, as well as only a small amount of mixing around the beginning of May (Figure 3.16b, c, d). By contrast, only 4 of the western medium PV particles follow the same path as the western low PV particles. The remaining 27 particles are advected outside of eddies along an eastward current that is eventually forced along the southern edge of the Archipelago (Figure 3.16d). These end up primarily on the southern extreme edge of the Chagos eddy, a delineation made clear from Figure 3.13, Column 2 as a fresher edge to the south of the eddy. These particles, advected and trapped along the edge of the eddy, most likely do not experience large amounts of mixing, with the exception of one particle in mid-May that experiences a rapid change in PV and density over the course of 3 days (Figure 3.16f).

We conclude this analysis with an examination of the high PV particles (Figure 3.17). The high PV particles lie almost exclusively to the east of the Archipelago, with 70 of 75 particles found eastward (Figure 3.17a). Of the only 5 particles to originate from the

west, every single one of them is found as a part of the eastward current identified previously from the medium PV particles in Figure 3.16, and so provide no new information (Figure 3.17d, e, f). By contrast, the high PV particles to the east of the Archipelago fall into three categories. First, there is a smooth procession of particles with a density of $1026.95 \text{ kg m}^{-3}$ from the far eastern edge of the domain that are eventually entrained within the Chagos eddy. These particles only gain PV as they enter the vortex at the end of May. The second group of particles is the same eastern merging AE identified previously; several dense, high PV particles are entrained in this vortex to dramatic effect in early April (Figure 3.17b). Finally, there is a grouping of particles that originate from the eastern coast of the Archipelago, many of which start with high PV but almost immediately spike to a PV of nearly $-2.5 \times 10^{-5} \text{ s}^{-1}$ before eventually joining the low PV particles advected along the edge of the Archipelago and falling in PV around early May. It is these particles that exhibited the most startling changes in PV in Figure 3.14e, as they are constantly experiencing friction with the bottom topography in this region until they are advected out of it (Figure 3.17c).

We combine our diagnostics above to provide a qualitative explanation of the likely processes that bring a Chagos eddy on the eastward side of the archipelago into being. First, in each southwest monsoon, the monsoonal winds and the Findlater Jet create the Somali Current and Southwest Monsoon Current (SMC), providing a strong eastward flow along the Equator and to its south (Schott & McCreary, 2001). At around 76°E , as seen in Schott & McCreary (2001), Figure 3.10, this flow encounters a westward current and bifurcates to the north and south. Part of this southern flow then bifurcates again to east and west, resulting in a clockwise loop around the Chagos Archipelago. When the currents to the

northeast of the archipelago meet in the wake of the Central Indian Ridge, they are seen to create anticyclonic eddies that then may follow the westward branch back towards the archipelago. At the same time, subsurface eddies and a deep current from the west encounter the geometry of the archipelago and are deflected northeastwards along its southern edge. Finally, as these eddies converge, they encounter the shallowing of the bathymetry, bringing them to the same depth. As a result, as seen in Figure 3.13, Column 2, there is a high salinity, warmer water mass from the north impacting a lower salinity, cooler water mass to the south: given the density surfaces that they lie upon and previous models of water mass mixing in Indian Ocean, we hypothesize that this is diluted RSW impacting AAIW and mixing and being downwelled further into the subsurface intermediate layer (Schott & McCreary, 2001; You, 1998).

3.6 CONCLUSIONS

In this study, we have demonstrated the feasibility of a novel optimization scheme for the development of subsurface eddy detection algorithms against existing surface tracking algorithms, in our case the widely-used winding angle SSH algorithm. We then present the favorable performance of the first eddy detection algorithm exclusively using the rescaled PV averaged across isopycnal layers in an operational forecast model. This detection scheme is tested using the RSW mass in the Arabian Sea and compared against surface and observational studies. We conclude with a Lagrangian analysis of an as of yet undescribed, completely subsurface, intense eddy that forms frequently around the Chagos Archipelago during the southwest monsoon. Through this analysis, we characterize its three dimensional structure, the water masses that form it, and the origin of the particles that comprise it, finding that a combination of instability driven mixing and bottom friction

is most likely responsible for the merging of diluted RSW and AAIW. Ultimately, we establish our optimization procedure and resulting rescaled PV algorithm as a new methodology that automatically identifies eddies in isopycnal layers whose dynamics may be efficiently analyzed through further PV diagnostics. Future studies may expand upon our results, using different score weightings, initial comparison algorithms, other tracking algorithms, and other water masses to develop their own version of our method that is optimal for their region of the globe.

Lastly, we would also like to acknowledge a few limitations of and questions raised by our results. Our chosen dataset contains data assimilation, which, when modifying the model fields, acts as a non-conservative process. The temporal continuity of the mesoscale circulation (vortex existence, position, shape and strength) can thus be spoiled. For the CMEMS fields used here, data assimilation is limited and, as shown by the process studies we presented, does not seem to be a strong problem. The approach proposed here presents an opportunity for a follow up study on the influence of data assimilation in terms of continuity of the PV dynamics and eddy detection algorithms.

Furthermore, our choices of isopycnal bounds for both the surface layer and for the RSW can, as remarked in Section 4a, be slightly altered and still be said to fit their respective water masses. While we have carefully chosen our bounds to align with certain previous observations, our results would change in both quantitative and physically descriptive senses if we aligned our bounds with other descriptions of the layer. Although both the surface layer and RSW layer that we describe are relatively sharply defined (*i.e.* Figure 3.10), such sensitivity to choice of bounds might need to be carefully evaluated for water masses with less distinct edges.

Finally, our definition of subsurface eddies is one in terms of PV and renders visible eddies that might be normally difficult to detect through existing methods. However, due to this definition and the paucity of both suitable observational data and previous studies that examine subsurface eddies through this lens, we acknowledge that some of our results as demonstrated above currently lack validation. Indeed, while subsurface dynamics are more conservative than those at the surface due to fluxes across of the ocean-atmosphere interface, implying that our detected eddies at depth might be more physically consistent than those made at the surface, our detections may still yet be improved through a comparison to extensive manual detections in models or detections from appropriate observations in the relevant regions. Regardless, our results above demonstrate the current utility of our method as presented in this work. Given the public repository linked in the Data Availability Statement below, we hope that other researchers will continue to improve upon the foundation we have developed here.

3.6.1 DATA AVAILABILITY STATEMENT

NEMOv3.1 data is available online at <https://resources.marine.copernicus.eu/> courtesy of CMEMS. Strong, weak, and normal monsoon delineation data were obtained from the Indian Institute of Tropical Meteorology at <https://www.tropmet.res.in/~kolli/MOL/Monsoon/Historical/air.html>. The codebase that comprises the optimization, eddy detection, eddy tracking, water mass tracking, and particle tracking scripts utilized in this work can be found at <https://github.com/ErnstPaul/PV-EDDIES-JTECH>.

Table 3.1. The summary of final parameters for all tested detection methods as individually noted in Figures 1-5. Kilometer values for optimal smoothing are approximate, rounded values given the variation of longitude with latitude and are intended primarily for reference within our specified domain.

Method	Optimal Smoothing (Pixels)	Optimal Smoothing (Kilometers)	Optimal Ratio	Optimal Threshold Parameter	Optimal Partner Method	Final Similarity Score
VORT_T, Center	2	19		0.85 * STD	OW _{WA}	69.18
VORT_T, Edge	2	19	0	0.6 * STD	VORT _T	58.98
OW_T, Center	0	0		0.15 * STD	OW _{WA}	67.86
OW_T, Edge	0	0	0	0.1 * STD	PV _{ISO}	58.48
VORT_{WA}, Center	7	65			PV _{ISO}	73.48
VORT_{WA}, Edge	5	46	0.12		VORT _{WA}	71.01
OW_{WA}, Center	3	28			VORT _{WA}	69.28
OW_{WA}, Edge	1	9	0		VORT _T	69.18
LNAM, Center				0.65 (K)	VORT _{WA}	65.90
PV_{ISO}, Center	3	28			PV _{ISO}	74.65
PV_{ISO}, Edge	4	37	0.08		PV _{ISO}	74.65

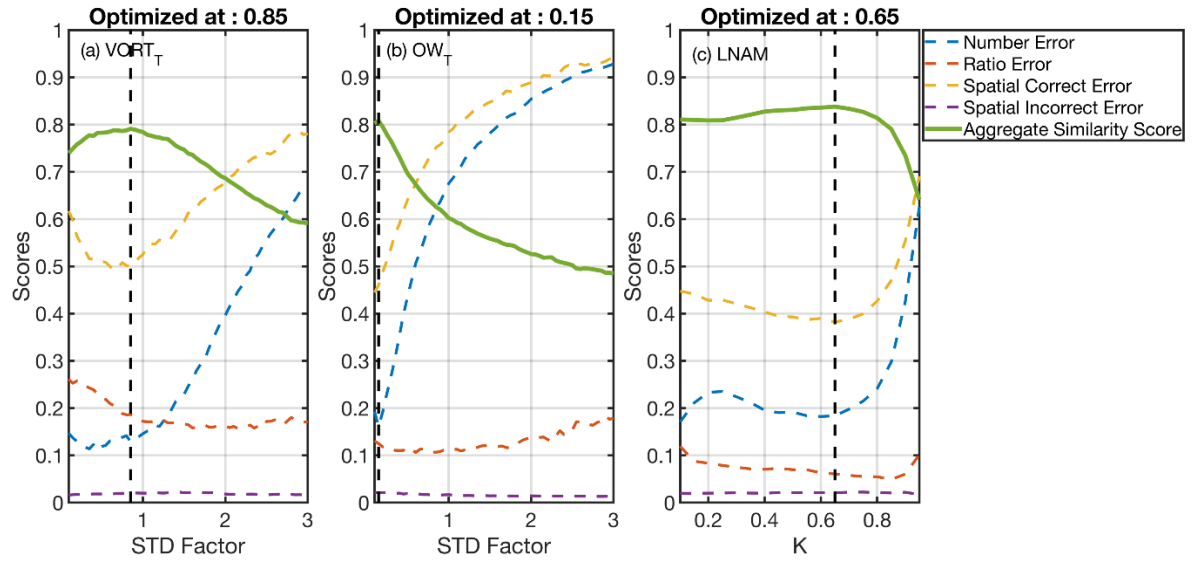


Figure 3.1. Optimizations of the center threshold parameters of $VORT_T$ (a), OW_T (b), and $LNAM$ (c) with each type of error and score. The STD factor for OW_T is considered to be always negative, as only a negative OW is associated with eddy centers.

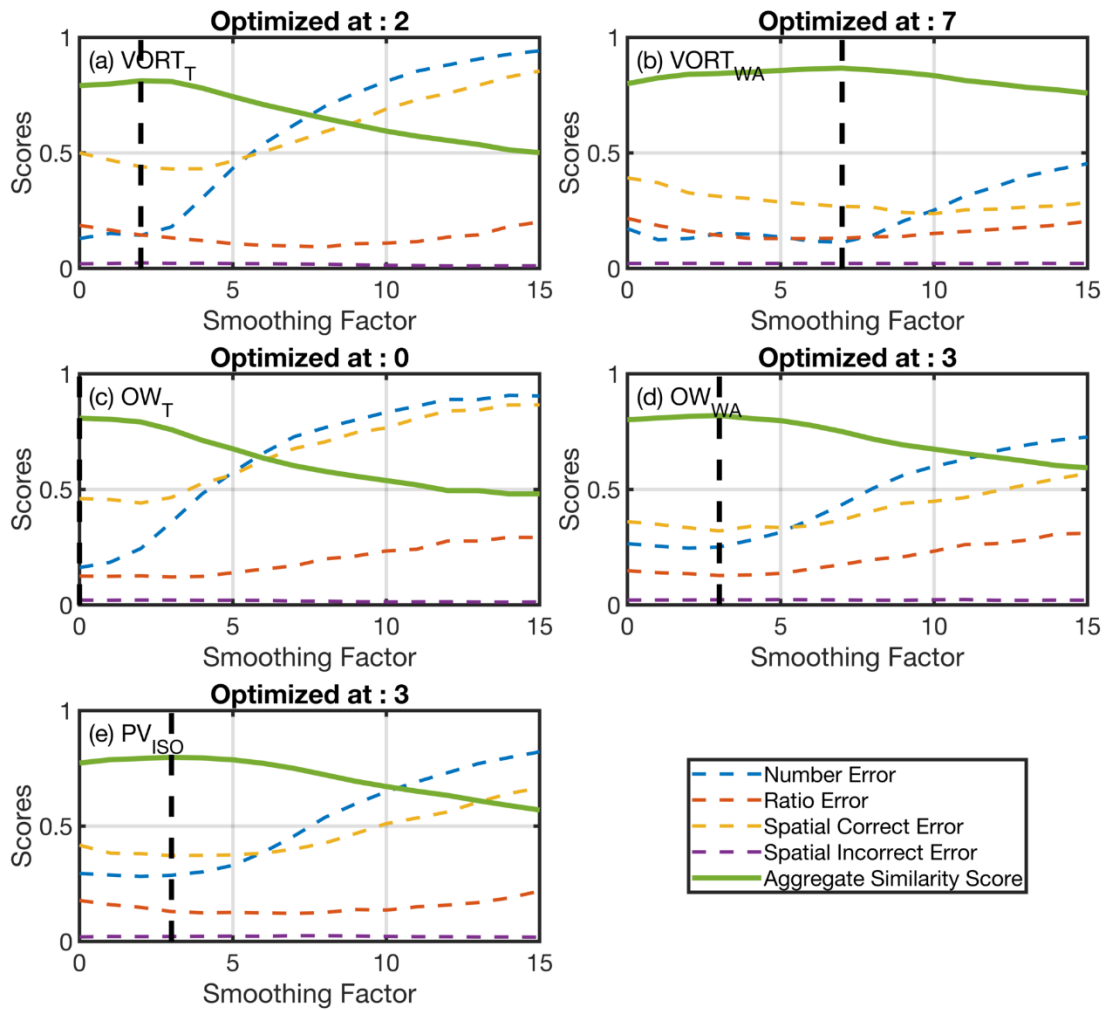


Figure 3.2. Smoothing factors optimized for the center components of $VORT_T$ (a), $VORT_{WA}$ (b), OW_T (c), OW_{WA} (d), and PV_{ISO} (e) for each type of error and score. STD factors are the optimized values in Figure 3.1.

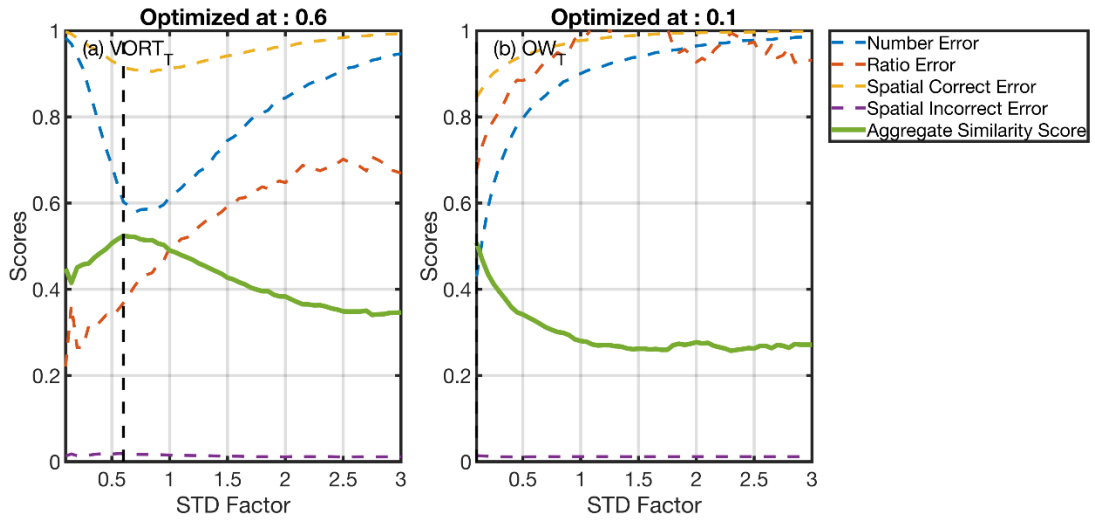


Figure 3.3. Optimizations of the edge threshold parameters of VORT_T (a) and OW_T (b) with each type of error and score. The STD factor for OW_T is always negative.

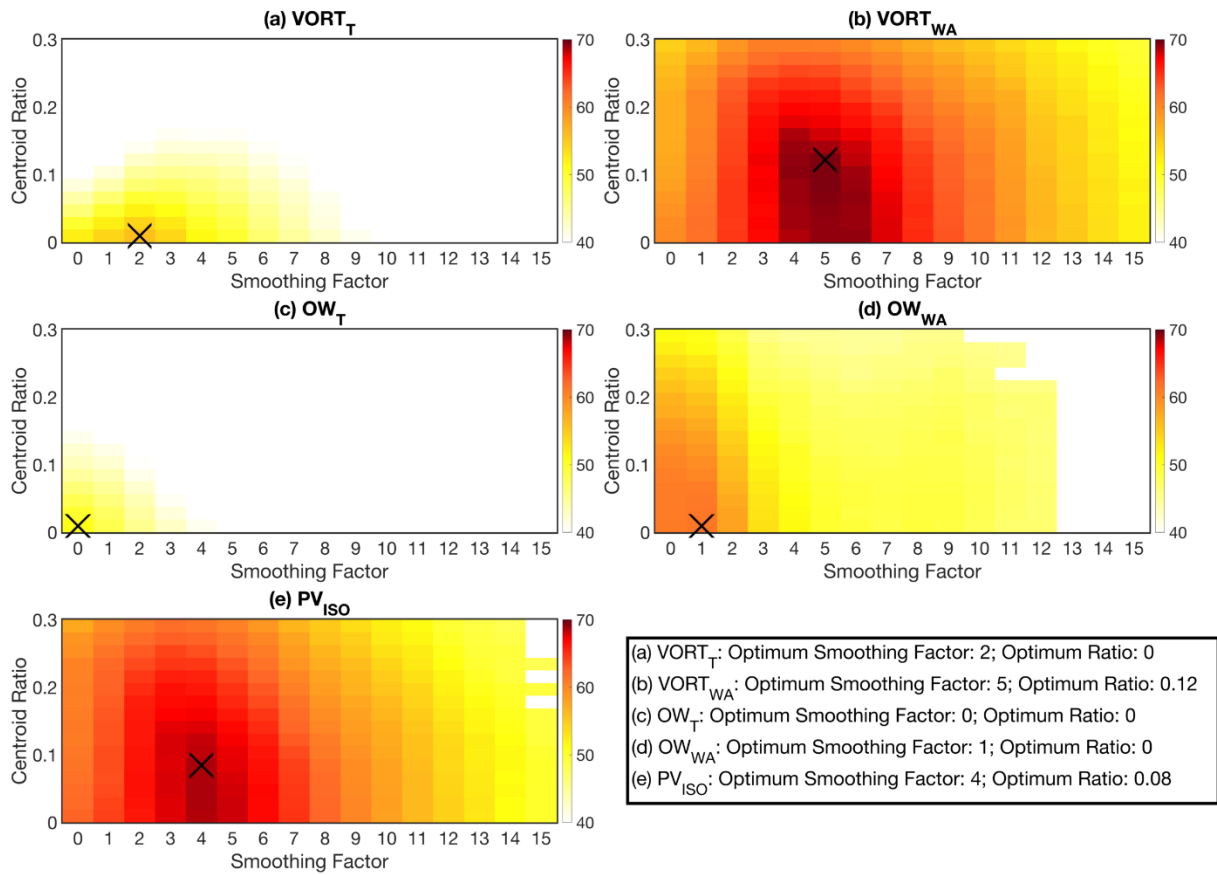


Figure 3.4. Aggregate similarity score of the edge components of $VORT_T$ (a), $VORT_{WA}$ (b), OW_T (c), OW_{WA} (d), and PV_{ISO} (e) for the optimization of both smoothing factor and minimum centroid ratio using SSH centers. Black Xs mark the combination of smoothing factor and centroid ratio that result in the best similarity score for each edge method tested.

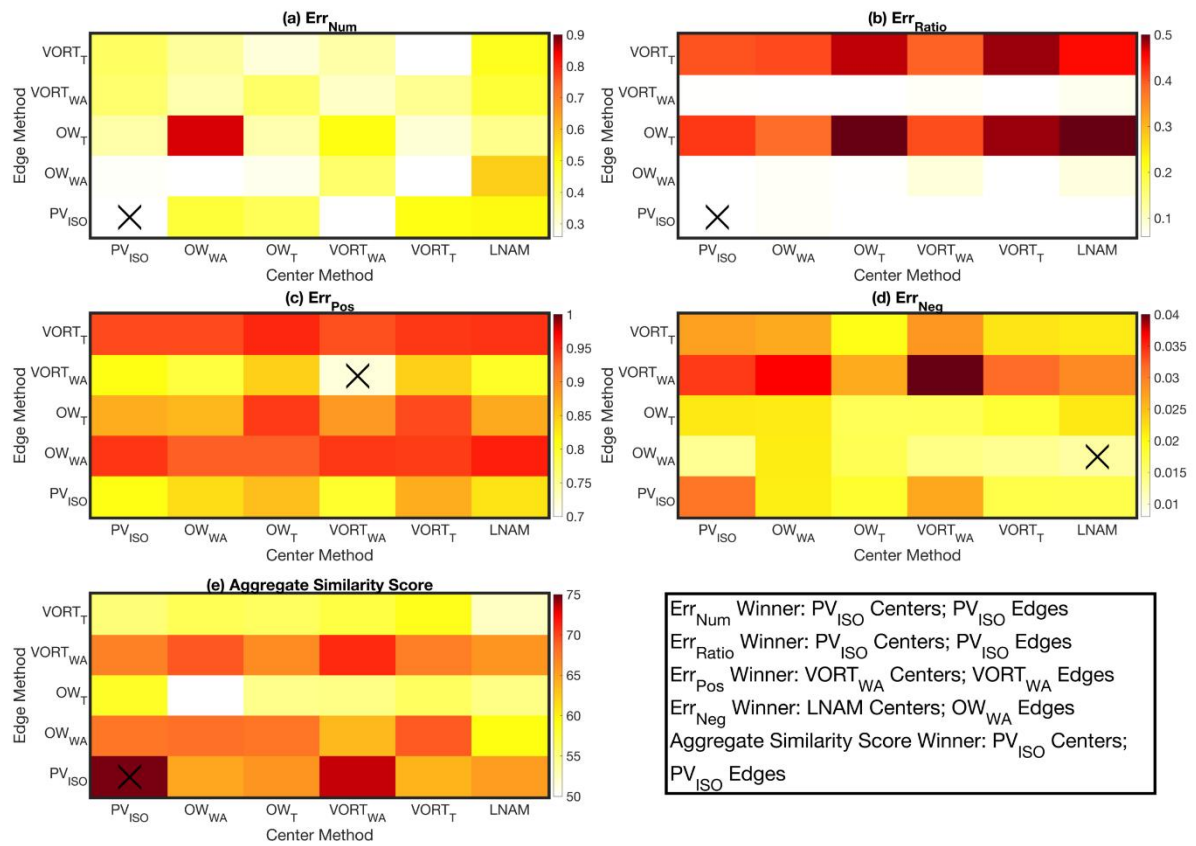


Figure 3.5. Hybrid method optimization using all center and edge method combinations. Shown are the number error Err_{Num} (a), centroid ratio error Err_{Ratio} (b), spatial correct error Err_{Pos} (c), spatial incorrect error Err_{Neg} (d), and aggregate similarity score (e). Black Xs mark optimal combinations of methods per error and score. Errors are considered optimal when minimized, and similarity score is considered optimal when maximized.

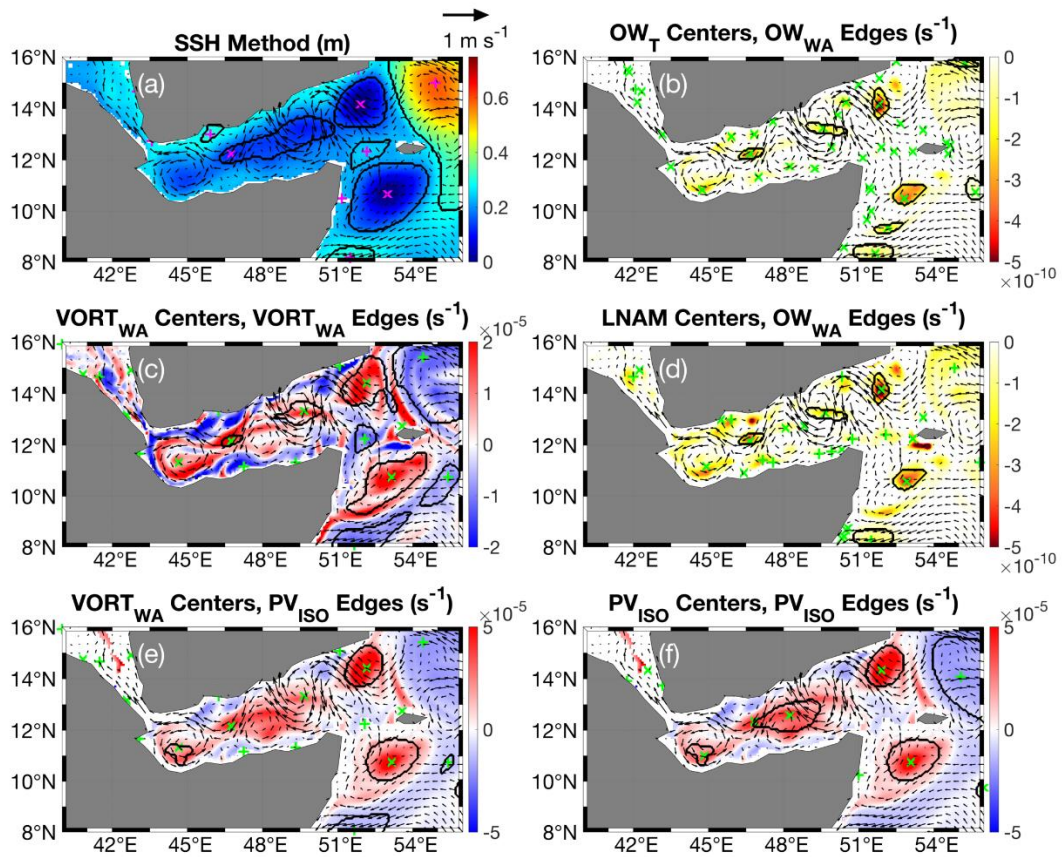


Figure 3.6. Detected contours (black lines) and centers (+s for AE centers, Xs for CE centers) on January 1st, 2016 in the GoA for the following center/edge hybrid methods: SSH/SSH (a), OW_T/OW_{WA} (b), $VORT_{WA}/VORT_{WA}$ (c), LNAM/ OW_{WA} (d), $VORT_{WA}/PV_{ISO}$ (e), and PV_{ISO}/PV_{ISO} (f). Color is given by the edge fields and are shown without low pass filtering. Current vectors are overlaid.

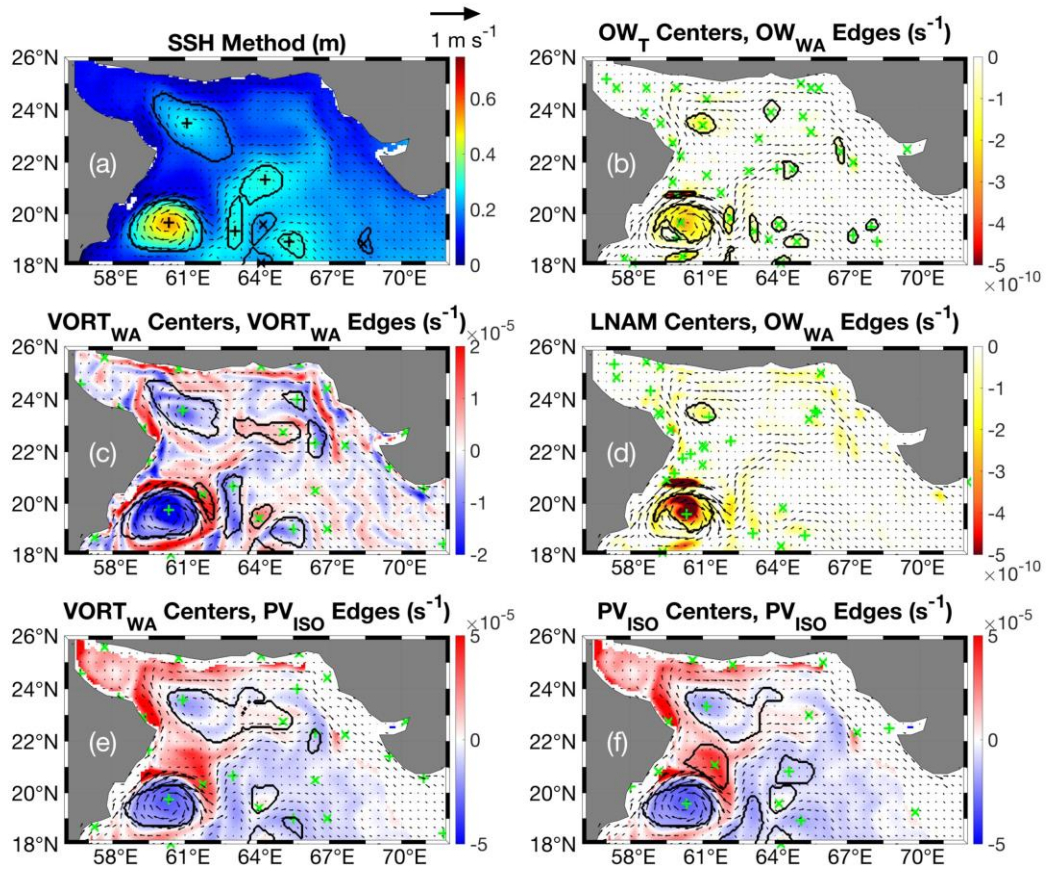


Figure 3.7. As in Figure 3.6, but for the Gulf of Oman on July 28th, 2017.

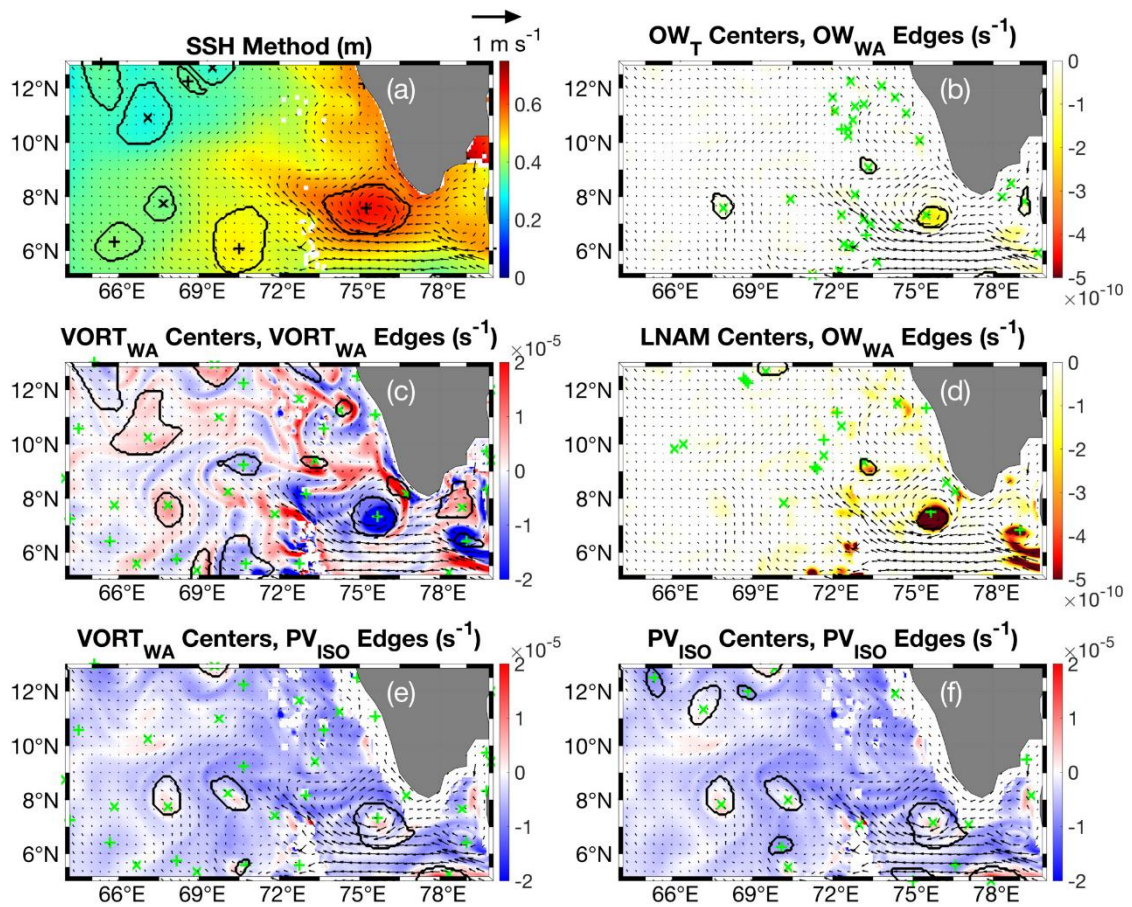


Figure 3.8. As in Figure 3.6, but for the Laccadive Sea and West India Coastal Current region on January 1st, 2016.

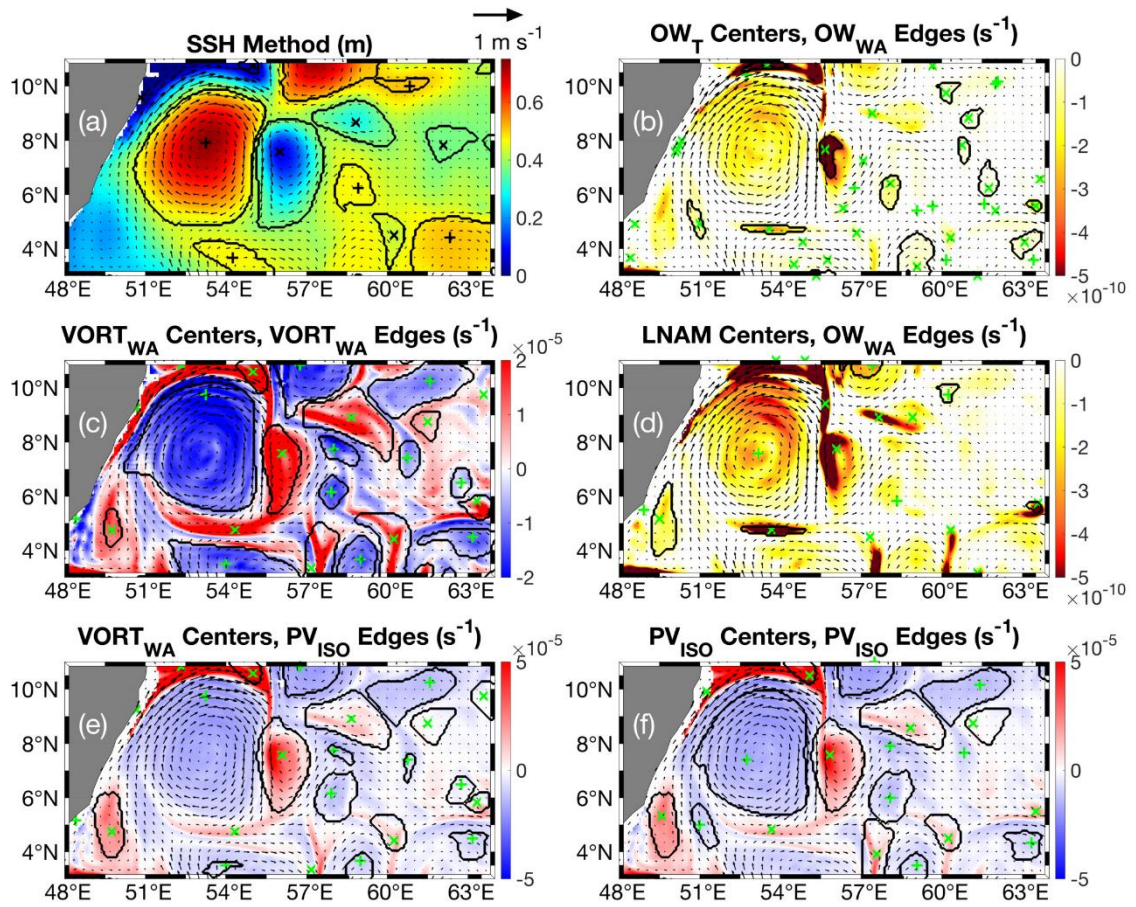


Figure 3.9. As in Figure 3.6, but for the Somali Current region on August 28th, 2019.

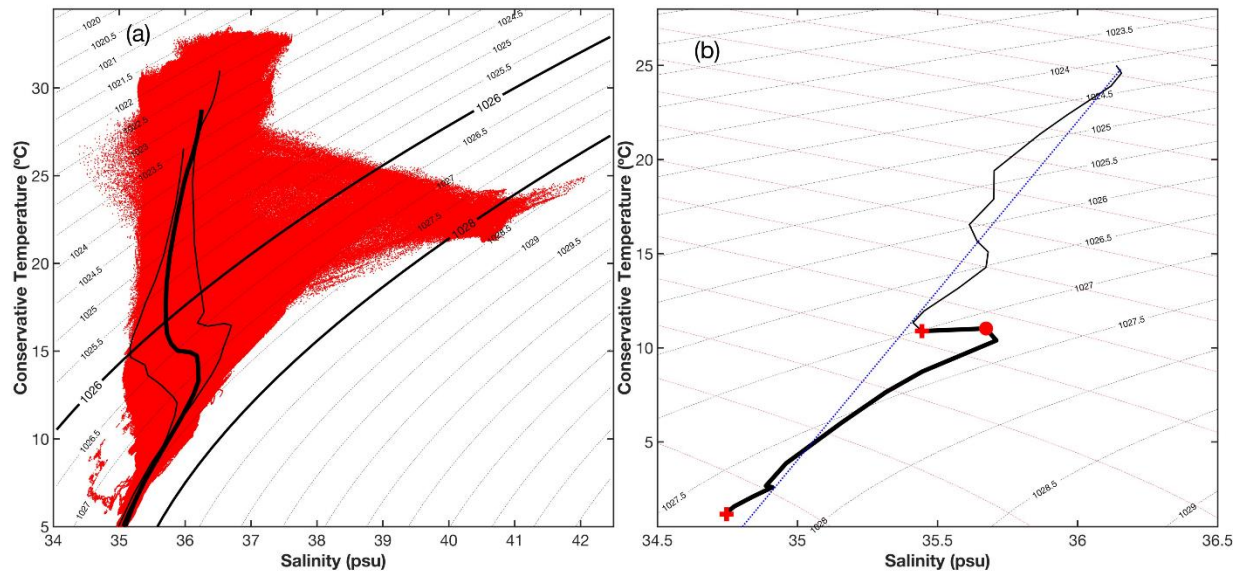


Figure 3.10. The isopycnal limits of RSW. (a) T-S diagram for the GoA with the median profile \pm one standard deviation; the boundary isopycnals (kg m^{-3}) defined by L'Hégaret et al. (2021) are bolded. (b) The L'Hégaret et al. (2021) algorithm for RSW water mass detection on a vertical profile located at 55°E , 13°N on July 7th, 2018. The vertical spiciness trend to be removed is the dotted blue line. The bolded portion of the profile lies between the bolded isopycnals in (a) and below 600 m; the red circle denotes the maximum of the RSW while the red crosses represent the upper and lower minima.

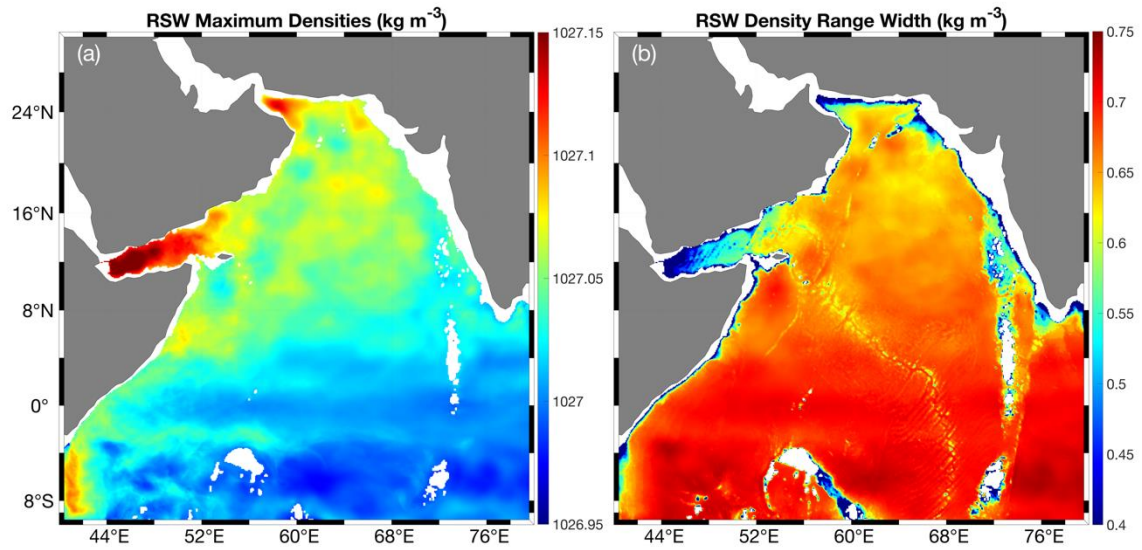


Figure 3.11. (a) The maximum densities (kg m^{-3}) within the RSW isopycnal bounds in our model. (b) the range width between the upper minimum and lower minimum bounds of RSW density within the isopycnal bounds defined above (kg m^{-3}).

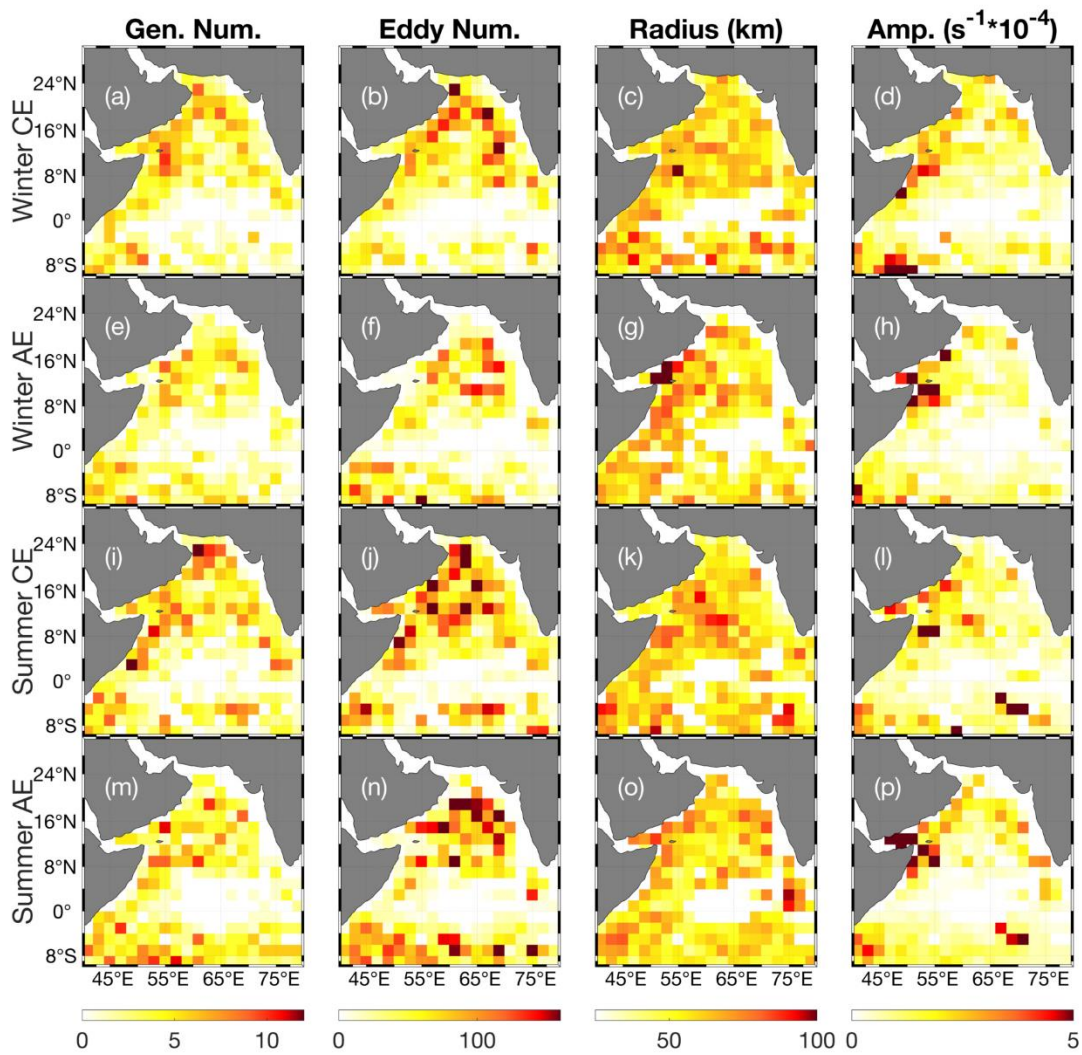


Figure 3.12. The properties of each type of RSW eddy separated by monsoon in $2^\circ \times 2^\circ$ bins: Winter CEs (a-d), Winter AEs (e-h), Summer CEs (i-l), and Summer AEs (m-p). Gen. Num. refers to where eddies are first detected. Radius and Amplitude (absolute value) are average values.

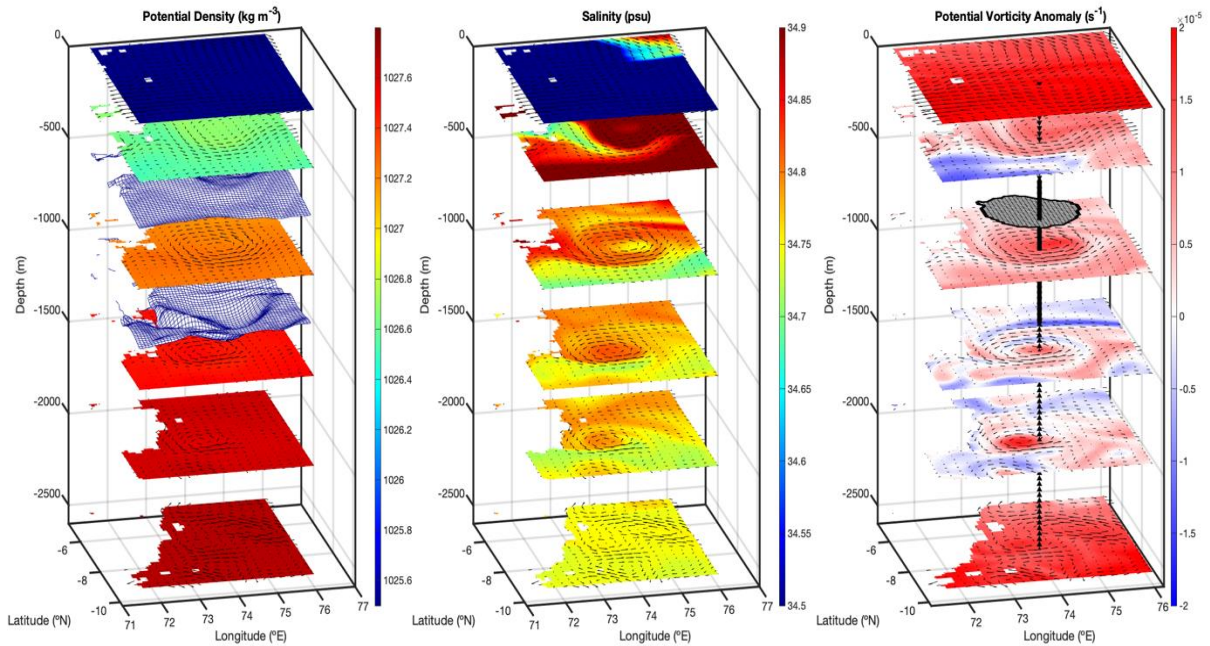


Figure 3.13. The three dimensional structure of a Chagos eddy on May 29th, 2019 with NEMO levels 2, 29, 35, 38, 40, and 42 displayed. Column 1: the potential density (kg m^{-3}) and current vectors on each level, with mesh grids marking the upper ($1026.95 \text{ kg m}^{-3}$) and lower (1027.4 kg m^{-3}) isopycnal bounds within which the eddy is defined in our algorithm. Column 2: the salinity (psu) and current vectors of the column. Column 3: The PV anomaly (s^{-1}) and current vectors of the column with a mesh contour defining the algorithmically defined boundaries of the eddy within the layers of Column 1. A black line marks the center point of the eddy, with a solid line marking the target density layer and spaced triangles marking depths outside of the target density layer.

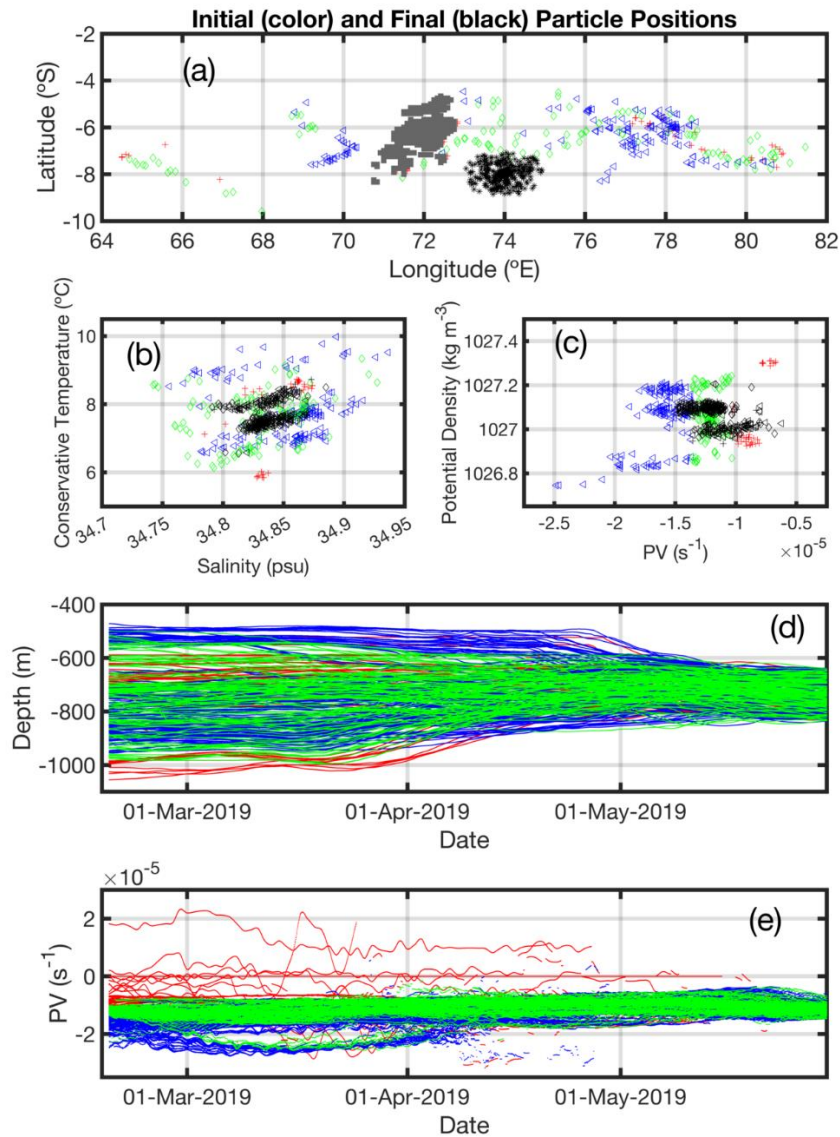


Figure 3.14. (a) The beginning (February 18th, 2019, colored) and end (May 29th, 2019, black) locations of each type of particle as described in the text (red cross = high PV, blue triangle = low PV, green diamond = medium PV). The Chagos Archipelago is greyed out to the eddy's northwest. (b) A T/S diagram of the initial (colored) and final (black) particles. (c) a density/PV diagram of the initial (colored) and final (black) particles. (d) the depth evolution of each type of particle by date with colors as in (a). (e) as in (d), but with PV.

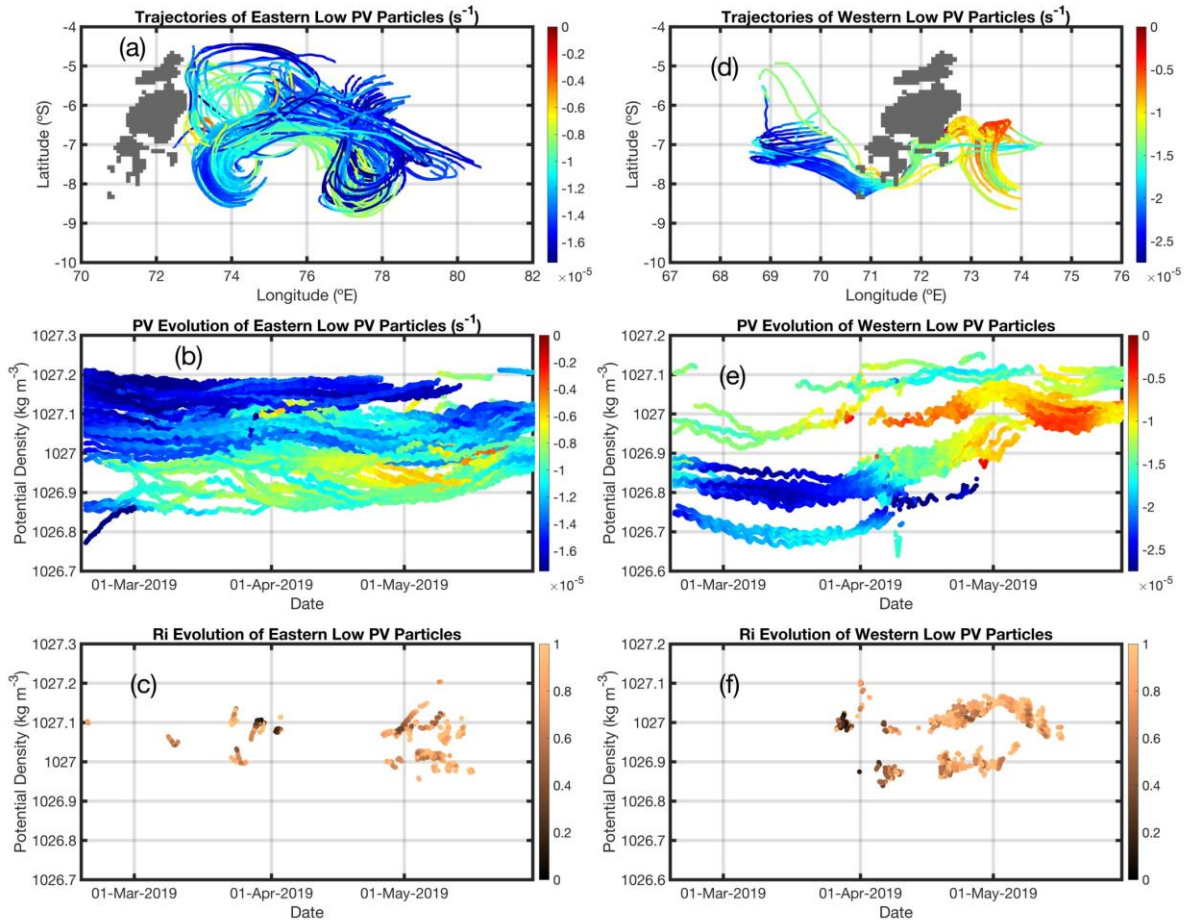


Figure 3.15. The trajectories of eastern low PV particles, colored by PV anomaly (a), the density evolution of eastern low PV particles by date (b), and the Richardson numbers below 1 over time for eastern high PV particles (c). (d), (e), and (f) are as in (a), (b), and (c) but for western high PV particles.

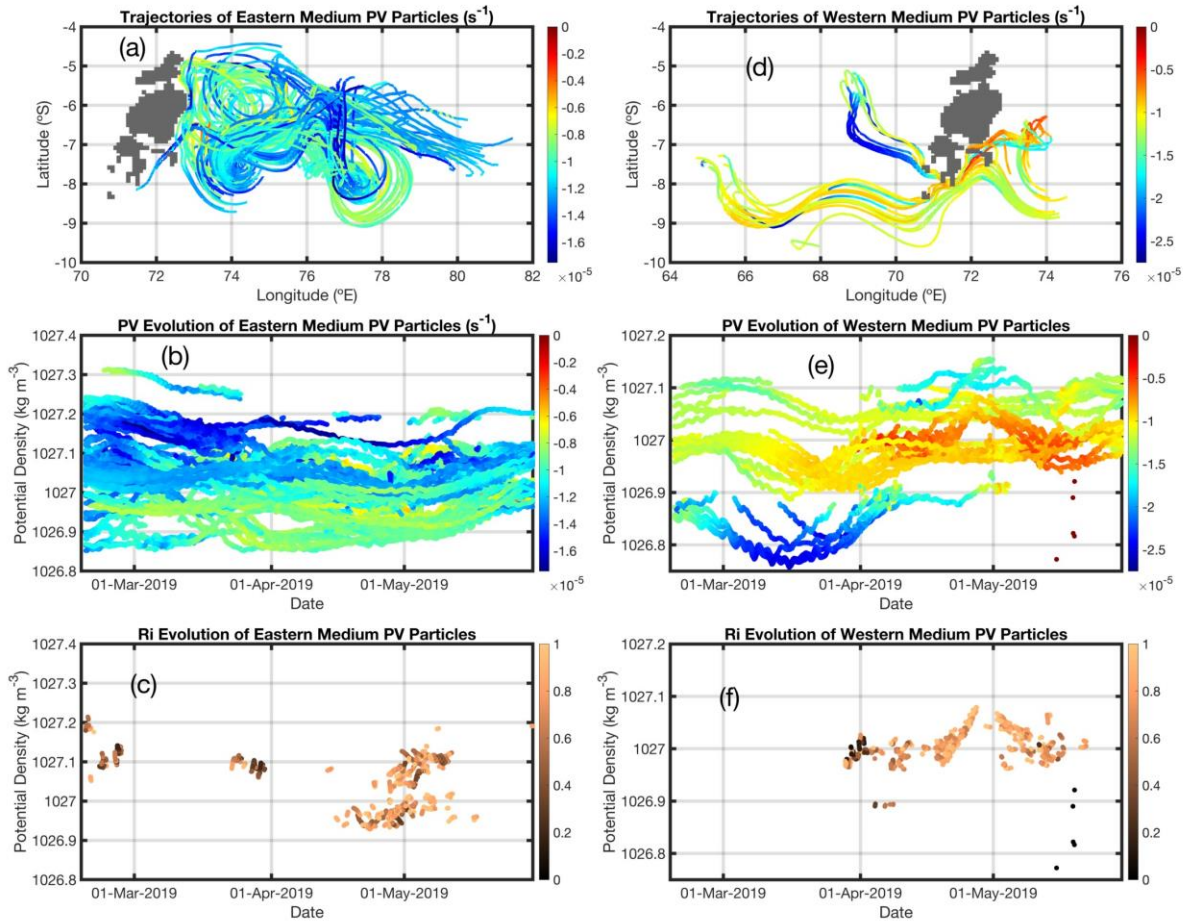


Figure 3.16. As in Figure 3.15, but for medium PV particles.

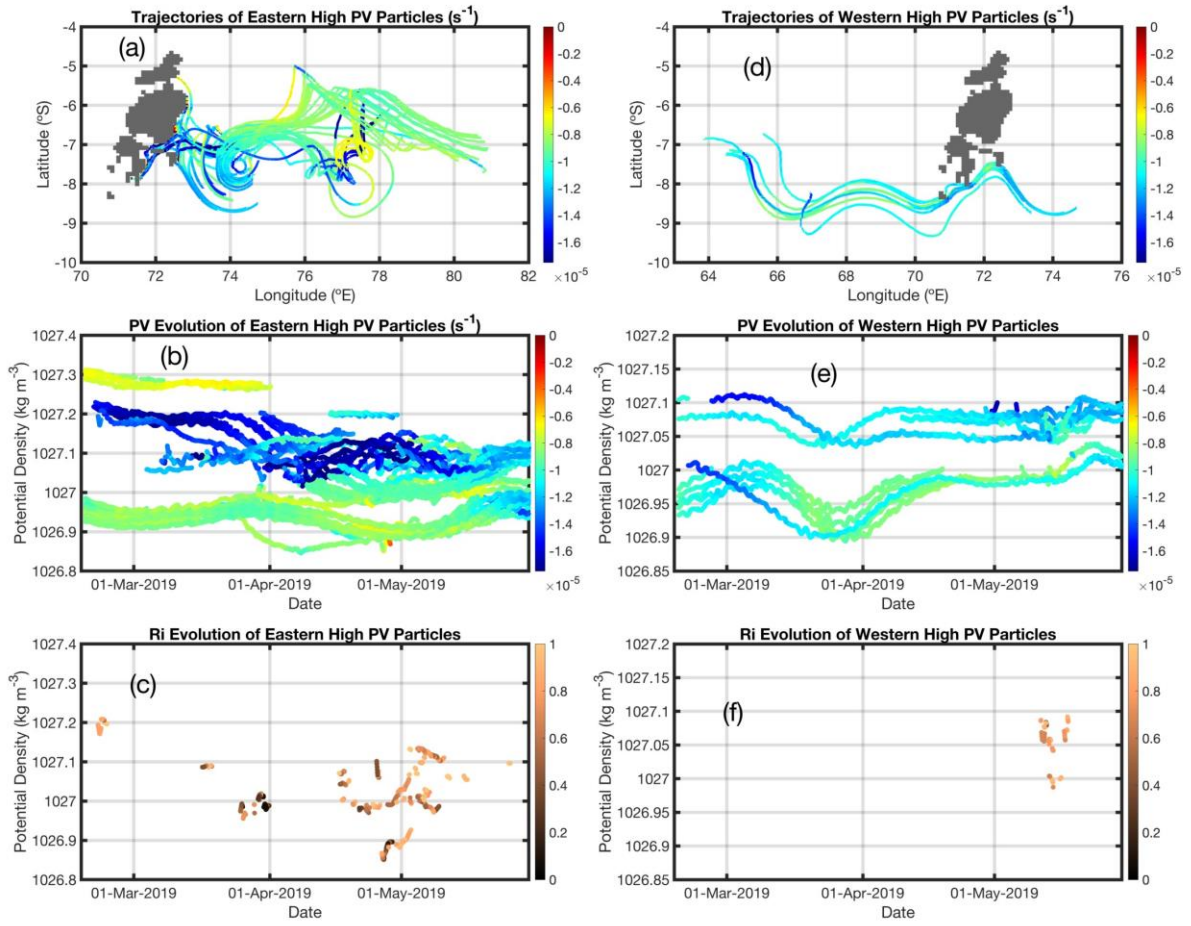


Figure 3.17. As in Figure 3.15, but for high PV particles defined in Figure 3.14.

CHAPTER 4
CHARACTERISTICS OF SUBMESOSCALE EDDY STRUCTURES
WITHIN MESOSCALE EDDIES IN THE GULF OF MEXICO FROM
1/48° ECCO ESTIMATES³

³ Ernst, P. A., Subrahmanyam, B., Trott, C. B., & Chaigneau, A. (2023). Characteristics of submesoscale eddy structures within mesoscale eddies in the Gulf of Mexico from 1/48° ECCO estimates. *Frontiers in Marine Science*, *10*. Retrieved from <https://www.frontiersin.org/articles/10.3389/fmars.2023.1181676>

Reprinted here with permission from publisher.

4.1 ABSTRACT

Submesoscale oceanic structures (<10-20 km) such as eddies and fronts are often difficult to describe given the influence of the mesoscale. In order to characterize the surface signatures of submesoscale structures, we utilize a custom spatial filtering function to separate the meso- and large-scale sea surface height (SSH) signal from the small scale SSH signal of $1/48^\circ$ high resolution estimates provided by NASA's Estimating the Circulation and Climate of the Oceans (ECCO) project. In this study, we use ECCO estimates from a 14-month global simulation between September 2011 and November 2012 with a 2 km horizontal grid spacing in the Gulf of Mexico. We then use an eddy detection and tracking algorithm to identify persistent circular features on both scales, giving rise to an atlas of submesoscale eddy-like variabilities (SEVs). We briefly investigate the geographic and temporal variability of SEVs as a whole before collocating SEVs inside mesoscale eddies, allowing us to evaluate the characteristics of internal SEVs and the impact of SEVs on mesoscale eddies. We find that SEVs, both anticyclonic and cyclonic, are ubiquitous inside mesoscale eddies with lifetimes longer than a week, accounting for an average of 10-20% of the spatial area and eddy kinetic energy of mesoscale eddies. We also show that internal SEVs are persistently associated with temperature and salinity anomalies in both eddy centers and edges of up to 0.1 °C and 0.05 psu, with anticyclonic internal SEVs being warmer and fresher while cyclonic internal SEVs are colder and saltier. Finally, we examine the life cycle of an anticyclonic Loop Current eddy, demonstrating that the number and intensity of internal SEVs within increases as the eddy approaches separation from the Loop Current until a maximum is obtained just after separation. In light of forthcoming submesoscale SSH observations from

NASA's Surface Water and Ocean Topography (SWOT) mission, our results showcase the variability of submesoscale eddy structures and their possible implications for biogeochemical cycling, the inverse energy cascade, and Loop Current prediction techniques.

4.2 INTRODUCTION

Mesoscale eddies are ubiquitous in the world's oceans, accounting for significant fractions of the total transport of upper ocean properties (Zhang et al., 2014; Xia et al., 2022). Much is known regarding mesoscale eddies thanks to the maturity of satellite altimetry, allowing global, daily measurements of sea surface height (SSH) at a $\frac{1}{4}^\circ$ spatial resolution since the launch of TOPEX/Poseidon in 1992 (Fu et al., 1994). Measurements of eddy behavior and fluxes on a global scale are therefore limited to this scale, leaving the smallest eddies defined by SSH to a radius of roughly 25 km. It is for this reason, and the fact that the diameter of these eddies often lies close to the baroclinic Rossby radius of deformation, that many recent publications choose 20-30 km as the cutoff point of the mesoscale and the beginning of the so-called submesoscale (Zhang & Qiu, 2018; Drushka et al., 2019; Gula et al., 2019; Y. Zhang et al., 2019; de Marez et al., 2020a; Morvan et al., 2020).

A variety of methods have been utilized to study eddy dynamics at the submesoscale, including using higher resolution observational ocean color, radar, gliders, drifters, and sea surface temperature (SST) datasets (Zamuda et al., 2016; Drushka et al., 2019; Y. Zhang et al., 2019; Ni et al., 2021). However, pending the first scientific data released to the public from the Surface Water and Ocean Topography mission, the main tool for studying submesoscale eddies on a regional scale remains the use of high resolution

model simulations (Durand et al., 2010). Such models, coupled with observations where possible, have been used to study several elements of submesoscale eddies, including their likely generation mechanisms, interactions with topography, roles in the energy budget, influence on vertical transports, and more (Morvan et al., 2019; Tedesco et al., 2019; D'Addezio et al., 2020; Cao et al., 2021).

Of particular interest is the behavior of submesoscale phenomena embedded into and around mesoscale eddies. These include filaments, fronts, and other instabilities, all of which alter the characteristics of the mesoscale (Brannigan et al., 2017). Such submesoscale alterations can contribute to mixing and energy dissipation within the overall mesoscale eddy, increasing vertical heat transport below the depth of the mixed layer (Bracco et al., 2019; Garabato et al., 2022; Wang et al., 2022). Given the importance of understanding mesoscale eddy dynamics, it is clear that a greater understanding of the possible submesoscale influences underlying currently visible mesoscale eddies is needed.

One region where submesoscale influences may play a major role in mesoscale dynamics is the Gulf of Mexico (GoM). The Loop Current and its associated eddies, termed Loop Current Eddies (LCEs) have significant implications for the circulation within the basin, with individual eddies lasting for months to years while interacting with, *e.g.*, hurricanes, oil spills, and phytoplankton blooms (Leben & Born, 1993; Liu et al., 2008; Liu et al., 2011; Jaimes et al., 2016; Wang et al., 2019). As a result, understanding the submesoscale structures present within mesoscale eddies in the GoM may lead to new insights into mesoscale processes. For example, Haza et al. (2016) demonstrate tracer leakage across mesoscale structures in the GoM due to submesoscale activity, while

Meunier et al. (2017) report observations of intrathermocline eddies (ITEs) within an LCE, likely formed through intense mixing and ensuing Rossby adjustment.

In this study, we aim to investigate the characteristics of submesoscale structures within mesoscale eddies in the GoM. We separate the spatial scales of a high-resolution model simulation provided by the Estimating the Circulation and Climate of the Oceans (ECCO) project using a purpose-designed filtering process. This provides us with the means to algorithmically detect persistent Eulerian structures on both the large- and small-scales of the GoM. By collocating small scale structures within mesoscale eddies, we are able to track small-scale structures with eddy-like characteristics over time, allowing us to ultimately characterize the impact that these small scale, eddy-like structures have on the surface signatures (dynamic height, temperature, salinity) of mesoscale eddies in the GoM.

4.2 MATERIALS AND METHODS

4.2.1 NUMERICAL SIMULATION AND DOMAIN

In this study, we use the ECCO project's (<https://ecco-group.org>) 1/48° run of the Massachusetts Institute of Technology general circulation model (MITgcm) on the Lat-Lon-Cap (LLC) 4320 grid (Marshall et al., 1997; Adcroft et al., 2004; Forget et al., 2015). The final product, often referred to by LLC4320, has hourly temporal resolution, 90 vertical levels, a nominal horizontal grid resolution in the Gulf of Mexico of roughly 2 km, and an effective resolution of roughly 8 km. This resolution was achieved through a series of progressively finer-scale models originally derived from an adjoint-method state estimate constrained to observations between 2009 and 2011 (Menemenlis et al., 2008). The forcings for this simulation were both atmospheric and tidal, including the 16 most significant tidal components, although this tidal forcing has been demonstrated to be

overestimated by a factor of 1.1121 (Arbic et al., 2022). The simulation is global, covering 14 months from September 13th, 2011 through November 15th, 2012. It has previously been used to study submesoscale dynamics throughout the world (*e.g.* Rocha et al., 2016; Qiu et al., 2018; Chereskin et al., 2019).

While we utilize the entire temporal domain, we constrain our spatial domain to the Gulf of Mexico (18°N - 32°N, 80°W - 100°W). As in Brokaw et al. (2020), we define the Loop Current region over which Eddy Kinetic Energy (EKE, calculated as $\frac{1}{2}(U^2 + V^2)$, where U and V are the zonal and meridional components of surface velocity) is calculated to be between 21.5°N - 28°N and 81°W-90°W.

4.2.2 SEPARATION OF SCALES

We separate the mesoscale (“large”) from the submesoscale (“small”) using a filtration and removal technique used to similar effect by Rosso et al. (2015) and D’Addezio et al. (2020). We first smooth the original simulation data (“total scale”) using a specific low-pass filter, then remove the low-pass output from the total scale to achieve the small scale. In this study, our focus is on the spatial scale of less than 25 km (below the current spatial scale resolved by satellite altimeters), and so we aim for a window design that can efficiently separate the large scale from the small scale with comparatively minimal large scale contamination. Given that contamination between scales will persist regardless of the filtering technique, we match D’Addezio et al. (2020) in referring to the filtered fields as “large” and “small” instead of “mesoscale” and “submesoscale” where appropriate.

While a perfectly clean separation is impossible due to the continuity of scales within oceanic power spectra, one must choose an appropriate window to smooth with, *i.e.*

one with sharper roll off at the filter transfer function. In this work, we utilize the Dolph–Chebyshev window (Lynch, 1997). This is a window with a steep roll off that guarantees minimal main lobe width for a given ripple ratio (Yao et al., 2014). As a result, it is theoretically more effective at achieving a separation of scales than a more gradually tapering window using a Parzen or Gaussian kernel. For our purposes, the Dolph–Chebyshev window is constructed with a filter size of 71 pixels (*i.e.* a half-power window of 30 pixels) and a sidelobe magnitude factor of 100. Our results are only weakly sensitive to the sidelobe magnitude factor, while a change in the filter size directly alters the frequency at which the filter operates. We also acknowledge that this is just one possible combination of parameters to achieve our desired result: a higher sidelobe magnitude factor could be used with a large filter size or vice versa and similar results may logically be obtained.

The operation of our filtering method as applied to our model’s SSH data is displayed in Figure 4.1: Figure 4.1A is an example of the unfiltered SSH data in a restricted region of the GoM, Figure 4.1B is the large-scale result after the convolution of SSH with the Dolph–Chebyshev window, Figure 4.1C is the small-scale result after subtracting Figure 4.1B from Figure 4.1A, and Figure 4.1D demonstrates the crossover point in the normalized power spectra between Figure 4.1B and Figure 4.1C. Given the crossover point near 25 km, we are confident that our procedure is effectively isolating the submesoscale and removing most mesoscale contamination. However, mesoscale energies do clearly still exist within our small-scale, so our results must be considered in this context.

4.2.3 EDDY DETECTION AND TRACKING

In order to detect eddy-like features, we employ an eddy detection and tracking algorithm first developed by Chaigneau et al. (2008; 2009), expanded by Pegliasco et al. (2015), and employed by Trott et al. (2018; 2019), Roman-Stork et al. (2021; 2023), and Ernst et al. (2022). Notably for our purposes, this algorithm was also successfully used by Brokaw et al. (2020) to examine mesoscale eddy characteristics in the GoM. This algorithm detects eddies using closed contours of SSH. We use SSH instead of other fields (*i.e.* Vorticity or the Okubo-Weiss parameter) as SSH will provide the best comparison to forthcoming SWOT data, which is limited by noise effects such that only SSH will be effective below a 25 km resolution (Chelton et al., 2019; 2022). Upon isolating local extrema in the SSH field (maxima for anticyclonic eddies and minima for cyclonic eddies), closed contours are drawn around them and expanded until the closed contour breaks, resulting in the final eddy edge detections laying upon the largest closed contours. This method does not require an arbitrary threshold for initial detection and results in a more accurate eddy shape than traditional thresholded methods.

Eddy trajectories over time are formed based upon a cost function that compares overlapping contours from adjacent time steps. Those overlapping closed contours that are minimally costed based upon radius, amplitude, and EKE are considered to be a part of the same trajectory. For more information on this cost function, see Pegliasco et al. (2015) or Trott et al. (2018). Given the hourly nature of the estimates used in this study, we discard any eddy trajectories that are not coherent over at least a 12 hour timespan. This helps reduce the likelihood of false instantaneous detections and retains features that are coherent in the Eulerian sense over at least this length of time.

For additional accuracy in the context of elongated false detections upon fronts, we apply a shape-constraining test that compares the length of the longest axis across the center (major axis) to the shortest axis across the center (minor axis) of each eddy. In this context, the ratio of the major axis to the minor axis determines the circularity of the eddy: a ratio of 1 indicates a perfect circle. We choose a cutoff ratio of 0.35, which helps eliminate most of the frontal structures and filaments within our results. This is broadly similar to the classic circularity test (see Kurian et al., 2011 for details) and achieves comparable results to their circularity threshold of 50% shape error, *e.g.* Figure 4.1C. The ratio test is significantly faster computationally than the circularity test over a high resolution domain given the simplicity of the calculation and the number of eddies detected versus the need to draw and compare a perfect circle to every contour.

Eddies are detected and tracked on both the large and small scale fields (see Figure 4.1B-C). Large scale eddies are hereafter referred to as ‘mesoscale’ eddies, while small scale eddy-like features are referred to as submesoscale eddy-like variabilities or SEVs. Large scale features are not tracked on the unfiltered field, as submesoscale variabilities can interrupt the formation of closed contours and falsely reduce or eliminate detections of eddy contours.

Given that these smaller scale features do not often have rotation velocities that exceed their translation velocities, it is unlikely that these can trap fluids for greater lengths of time. While they may still provide loci for particle attraction, deflection, and leakage, they are isolated through the filtering process, not prevalent in the total-scale, and as of yet lack observation from satellite altimetry, so we will not refer to SEVs as true coherent submesoscale vortices. In a physical sense, the process of SEV classification is meant to

extract eddies with a predominant submesoscale signature. However, this will also include other persistent submesoscale circular structures. We address the most likely causes and classifications of SEVs in Section 4.1.

4.3 RESULTS

4.3.1 MEAN CHARACTERISTICS OF SEVS

Before an understanding of the characteristics of SEVs internal to mesoscale eddies can be constructed, the general distributions of eddy properties must be noted. In this way, we may draw comparisons between the performance of the LLC4320 simulation and both observations and other operational models (Brokaw et al., 2020). In keeping with a comparison to established eddy characteristics in the GoM, we annotate the locations of eddy generation, called generation numbers, the locations of all eddy detections, eddy radius, eddy amplitude, and EKE (Figure 4.2).

We find that the characteristics of the mesoscale-filtered eddies closely match those of both altimetry and the Hybrid Coordinate Ocean Model (HYCOM) as reported by Brokaw et al. (2020). There is a locus of eddy generation for Anticyclonic Eddies (AEs) in the extended Loop Current region (Figure 4.2A); these eddies propagate westward, with large radii (> 125 km), amplitudes (> 25 cm), and EKEs ($> 0.2 \text{ m}^2 \text{ s}^{-2}$) reported in the central to western GoM (Figure 4.2B-E). CEs, meanwhile, are less frequent and more prevalent throughout the basin's edges (Figure 4.2F-G), with a notable persistently large CE in the southwest (Figure 4.2H). We find that our model does overestimate the EKE intensity of central GoM eddies as compared to observations, but that the relative distribution of properties is otherwise comparable.

The occurrences of SEVs, both AE and CE, are spread across the entire basin but are concentrated in the center and east with certain pixels of the Loop Current generating over 200 SEVs over the course of the 14-month simulation (Figure 4.2K-L, P-Q). SEV radii are near uniform, with the entire basin averaging 7-8 km (Figure 4.2M, R) while there is a trend for SEV amplitudes and EKEs to follow the path of the extended Loop Current and its LCEs (Figure 4.2N-O, S-T). High amplitudes and EKEs are also exhibited to the north of the LCE track and along the western coast of the GoM. It is worth noting that the areas of highest EKE intensity only outline the extended Loop Current and not its retracted state, mirroring the energy analysis of Loop Current instabilities conducted by Yang et al. (2020). Given that submesoscale eddies are often generated by such instabilities, it follows that SEVs would be observed along the Loop Current front (Buckingham et al., 2017). Beyond the geographic distribution of SEV characteristics, it is helpful to examine the timewise variability of SEVs over the 14-month duration of the simulation (Figure 4.3).

The number of SEVs across the basin is relatively consistent, with a grouping around 280 SEVs of each rotational tendency per day (Figure 4.3A, F). That stated, there is some degree of variability present, with the highest number of SEVs observed in January (~320) and the lowest number in April-June (~250) before rising slightly (~280) to the end of the simulation. SEV amplitudes are consistently lower than those of mesoscale eddies at around 2 cm (calculated between the eddy center and contour, Figure 4.3B, G) which follows from the magnitude of the submesoscale filtered SSH field being roughly an order of magnitude less than the large-scale field (Figure 4.1B-C). Between the middle of October and the end of March, the amplitude and EKE of SEV-CEs nearly double those of SEV-AEs even as SEV-AE amplitude increases, while median SEV-CE radius actually

declines below that of the median SEV-AE radius (Figure 4.3C-D, H-I). This is most likely due to the increase in instabilities caused during the generation and separation of a major LCE, as we discuss later.

Finally, we note that the EKE of the Loop Current itself follows a periodic pattern that matches with fortnightly tidal variability associated with neap and spring tides (Figure 4.3E, J). Once this variability is removed, it is clear that the EKE of the Loop Current reaches its greatest extents between February-May 2012 and September-November 2012. These coincide with the periods of greatest Loop Current extension during the simulation. To investigate how the intensity of the Loop Current and the tidal frequencies interact with the characteristics displayed in Figure 4.3, we perform a wavelet coherence analysis using the analytic Morlet wavelet (Figure 4.4).

The primary period of coherence between the energetics of the Loop Current and the characteristics of SEVs occurs in the 10-20 day range, with some degree of significant coherence across all properties at some point during the simulation. Among the characteristics highlighted, amplitude and EKE are most frequently significant, with the EKE of the Loop Current and the EKE of SEV-AEs being persistently in phase (rightward pointing phase arrows) throughout the entire simulation. By contrast, the amplitudes of most SEVs, where notable, lie either slightly against phase or lagged by 90 degrees (downward pointing arrows). In this context, the most important implication is that the fortnightly tidal cycle is immediately influencing the EKE of SEVs.

4.3.2 CHARACTERISTICS OF INTERNAL SEVS

With the general properties of SEVs laid out in the previous section, we may turn our attention to the prospect of SEVs internal to mesoscale eddies. In this analysis, we

collocate SEVs whose contours enclose an area that is within a ‘parent’ mesoscale eddy. There are therefore 4 combinations of SEVs and mesoscale eddies: SEV-AEs within mesoscale AEs (abbreviated M-AE where appropriate), SEV-CEs within M-AEs, SEV-AEs within mesoscale CEs (abbreviated M-CE where appropriate), and SEV-CEs within mesoscale CEs. Of the 54,330 SEV-AE trajectories identified, 8,958 (16.5%) contain at least one timestep where they are mostly within a mesoscale eddy; of the 54,951 SEV-CE trajectories identified, 7,346 (13.4%) contain at least one timestep where they are identified within a mesoscale eddy. Thus, around 85% of SEV trajectories belong outside mesoscale eddies. For mesoscale eddies, 1038 of the total 1266 (81.99%) of M-AEs contain at least one SEV internally during their lifetimes. For M-CEs, 622 of the 789 (78.83%) M-CEs identified contain at least one SEV internally. It is worth noting that of the ~20% of mesoscale eddies that do not contain an SEV at any point in their lifetimes, none of them have a lifetime of greater than 7 days, indicating that all long lived eddies are subject to SEV-based variability at some point in their lives. On average, internal SEV-AEs (CEs) live for 2.8 (2.5) days, spending an average of 1.8 (1.6) of those days within a mesoscale eddy and propagating an average of 14.3 (12.7) km away from their origin point. The longest lived internal SEV-AE (CE) lasts for 61.5 (96.0) days and propagates 245.6 (295.6) km away from its origin. The other mean characteristics of SEVs are given in Table 1.

Overall, while there is substantial variance in all parameters, SEVs within M-CEs have the longest lives, SEVs within M-AEs have the highest EKEs, and SEV-CEs have greatest amplitudes. We break these characteristics down geographically in the same manner as all SEVs (Figure 4.5).

We note that the geographic distribution of internal SEVs within M-AEs closely follows the track of LCEs (Figure 4.5A-B, F-G), with an additional increased concentration within the western Caribbean Sea. M-CE internal SEVs are most frequent within the southwestern corner of the GoM, corresponding to an intense, persistent M-CE (Figure 4.5K-L, P-Q). Three other loci of SEV-CE formation are notable: the eastern bend of the Loop Current, the tip of the extended Loop Current, and the northern Caribbean. As before, these all correspond to M-CE hotspots, both in our simulation (Figure 4.2) and in observations (Brokaw et al., 2020). Internal SEVs of all types on the boundaries are comparatively rare. This may be due in part to the filtering process, since results towards the boundaries are less reliable where there is insufficient data to fill the full filter window and so there are less mesoscale eddy detections. The distribution, then, of internal SEVs closely follows the areas of large parent eddy formation, an unsurprising result. The same trends are seen in the amplitude and EKE of internal SEVs, though it is notable that the most intense M-CE, SEV-CEs are found not in the extended Loop Current but at the base of the Loop Current, itself not a hotspot of M-CE EKE (Figure 4.5T). The properties of internal SEVs are further laid out over the duration of the dataset in Figure 4.6.

We note a much more intense variability in the characteristics of internal SEVs as opposed to all SEVs, with the number of daily internal SEVs at one point dropping to just 4, causing the median radius spike at the end of May (Figure 4.6A, C). In contrast to Figure 4.3, there is also a prolonged period of time where internal SEV-AE numbers exceed those of SEV-CEs between the beginning of January and mid-May. After this point, the number of all internal SEVs never exceeds 50 of either type, despite having regularly exceeded this value previously. During this second half of the simulation, internal SEV-AE EKE rises,

more often exceeding that of internal SEV-CEs. The increase in SEV-CE amplitude between December and March is also present here, though with more inherent variability (Figure 4.6B). As in Figure 4.4, we wish to determine whether there is significant coherence between the energy of the Loop Current and the energy of SEVs (Figure 4.7).

While there is significant coherence at the 32-day period near the beginning of the simulation for all non-EKE characteristics, there is a distinct lack of coherence at the 16-day period for EKE as there was in Figure 4.4 (Figure 4.7D, H). Interestingly, there is a particularly strong coherence between internal SEV-CE number and the 16 day period between February and April, with the phase arrows showing both the number of SEV-CEs leading Loop Current EKE (upwards arrows) and the two being anti-phase. This is the only relation of all those seen in Figures 4 and 7 that demonstrates a significant lead from SEV properties to Loop Current properties. This also partially coincides with the increase in SEV-CE amplitudes observed in Figures 3 and 6, indicating a possible relationship between the generation of instabilities in the Loop Current and its strength. However, there is no significant coherence between internal SEV-CE amplitudes and Loop Current EKE at this time. With the general characteristics of internal SEVs established, we turn our attention to the relationship between the properties of parent mesoscale eddies and their internal SEVs (Figure 4.8).

The lifespans of internal SEVs range between the minimum coherence interval (12 hours) and 80 days, with the longest-lived SEVs being those CEs internal to mesoscale CEs (Figure 4.8A-D). In particular, due to the length of the simulation, there are a handful of major mesoscale eddies that remain coherent for over half of the simulation, standing out clearly as sources of internal SEVs. There are in fact two mesoscale eddies whose

lifespans cover the entirety of the simulation, one AE and one CE. The CE in particular is clearly visible in Figure 4.8D, as it contains a large number of long-lived internal SEVs. While some longer lived SEVs are present in shorter lived mesoscale eddies, demonstrating the capability for submesoscale structures to persist through the dissipation of a mesoscale eddy, all longer lived (lifespan > 10 days) SEVs whose trajectories are over 50% internal to mesoscale eddies are logically only found in longer-lived mesoscale eddies. The overall correlation between SEV and mesoscale eddy lifetimes is not significant ($p < 0.05$).

The same relationship does not hold true for radius (Figure 4.8E-H) or amplitude (Figure 4.8I-L), with the mean radius of SEVs (~8 km) remaining relatively constant for all radii of parent eddy with very low R^2 values on a slightly negative trend; trends for radius and amplitude are also not statistically significant. Amplitude for SEVs internal to M-AEs follows a dipolar pattern, with a grouping of SEVs in low-amplitude M-AEs (~5 cm) and another in high-amplitude M-AEs (~23 cm). By contrast, SEVs internal to M-CEs mostly cluster around 10 cm in the parent eddy, without a spike in SEV number at lower amplitudes. Finally, the relationship between SEV and mesoscale eddy EKE is mostly focused around the origin, with lower EKE mesoscale eddies unable to host SEVs of higher EKE, and the number of high-EKE SEVs peaking around a parent eddy mean EKE of around $0.03 \text{ m}^2 \text{ s}^{-2}$ in all cases (Figure 4.8M-P). All correlations between SEV and mesoscale eddy EKEs are statistically significant. Another important element to examine in the relationship between mesoscale eddies and SEVs is how this relation changes over the course of the parent eddy lifetime (Figure 4.9).

Based upon the statistics of our mesoscale eddy detections, we separate the parent mesoscale eddies into classes based upon their maximum radii: 25-75 km covers eddies up

until roughly the mean, 76-125 km covers eddies between 1 and 2 standard deviations above the mean, and 126+ km covers eddies with maximum radii above 2 standard deviations above the mean. For all sizes of mesoscale eddies, we catalogue the number of internal SEV-AEs and SEV-CEs along with the percent of the parent eddy that is taken up by the internal SEVs in both spatial area and EKE. We find in all sizes of mesoscale eddies that the number of internal SEVs begins to rise at around 80% through the parent eddy's lifetime. Towards the end of an average large eddy lifetime, between 8 to 9 internal SEVs of each type are expected as the eddy decoheres (Figure 4.9E-F). The EKE and area shares only slightly increase during this time, without the same rapid increase. A notable exception is in mid-size M-CEs, where SEV-CE EKE share rises to 35% of the parent eddy total (Figure 4.9D).

In all cases, the same rotation direction between SEV and mesoscale eddy (CE-CE or AE-AE) is more likely to be found within an eddy, rather than the counterrotating opposite (CE-AE or AE-CE). Similarly, the EKE and area shares are dominated by same-direction rotating pairs, with an average value for same-direction pairs lying between 10 and 20% of the parent eddy, while opposite-direction pairs average between 0 and 10% for all eddy sizes. One last anomaly is in the lowest sample size category, large M-CEs: there are intense spikes in SEV-CE EKE share at the beginning and middle of the M-CE normalized lifetime (Figure 4.9F). Given that the figure shown is of an arithmetic mean, this is more likely to be contaminated by a handful of outliers; however, the values shown (76.7% at the beginning and 67.9% in the mid-life) are too high for a single outlier to be fully responsible. Additionally, we do see an early-life trend for higher SEV-CE EKE share in smaller M-CEs (Figure 4.9B, D). This indicates that there may be a relationship between

M-CE and SEV-CE EKE in the formation stages in addition to death stages; this relationship is not present in M-AEs and SEV-AEs. While the previous figures have indicated the characteristics of SEVs inside of parent eddies, the probabilities of the locations of the SEVs have yet to be interrogated. We examine this distribution in Figure 4.10.

The rows of Figure 4.10 are broken down as in Figure 4.9 for eddies of increasing maximum radii. The greatest probability of SEV occurrence is for M-CEs and SEV-CEs, where there is over a 25% chance of finding an SEV-CE at any given timestep in the center of any given M-CE (Figure 4.10D, H, L). This likelihood decreases away from the center of the eddy until a minimum is reached beyond 1 radius of the M-CE. Given that the size of SEVs is relatively consistent between 6 and 12 km, while the size of mesoscale eddies varies considerably, it follows that the probabilities of SEVs in larger mesoscale eddies would take up less of the overall eddy in the composite. However, the overall shape of the pattern is the same. A similar pattern is observed for M-AEs and SEV-AEs, although the likelihood is halved and the distribution is flattened longitudinally (Figure 4.10A, E, I). Furthermore, the pattern for M-AEs is more diffuse, reaching beyond the first radius of the M-AE for smaller eddies. It is also worth noting that some of the “SEVs” observed in the centers of same-type rotation pairs are actually the centers of the original mesoscale eddy leaking through the filter.

The more intriguing of the probability patterns are those found on opposite-type rotation pairs. While the most rare to find in one particular point in the eddy, M-AEs and SEV-CEs exhibit a ringed pattern focused on the edge of the first eddy radius, gradually shifting inside the radial edge as eddy size increases (Figure 4.10B, F, J). This is most

intense on the northern and southern edges. In a similar way, M-CEs and SEV-AEs exhibit a stricter dipolar pattern with two loci to the direct north and south of the eddy center and lying once again on or slightly in from the first eddy radius (Figure 4.10C, G, K). Interestingly, smaller M-CEs have a larger focus of SEV-AE activity on their southern edge; however, this reverses for larger eddies, with a more intense focus of SEV-AEs on the northern edge. In both opposite-type pairs, the center of the eddy is the least likely location for an SEV to occur, with a probability close to 0. The impacts of SEVs on mesoscale eddies may be evaluated not only through their location within mesoscale eddies, but also with their temperature and salinity signatures at the surface. We begin with sea surface temperature anomalies (SSTAs) of SEVs, computed as the difference between the center SST and the mean SST out to a distance of 3 radii (Figure 4.11).

The general trend of the anomalies of the SEVs are as expected: the cyclonic, upwelling motion of SEV-Ces in all cases create a negative SSTA versus the background, while the anticyclonic, downwelling motion of SEV-AEs create a positive SSTA. This is most intense in the case of M-CEs, where SEV-AEs are associated with an SSTA of up to 0.06 °C and SEV-CEs are associated with an SSTA of up to -0.07 °C (Figure 4.11C-D, G-H, K-L). By contrast, the anomalies associated with M-AE internal SEVs are less intense but still present (Figure 4.11A-B, E-F, I-J). For all combinations, the anomalies are generally an order of magnitude less than those SSTAs associated with mesoscale eddies from observations (Brokaw et al., 2020). The general shape of the background SST is also comparable to those from observations, with a cooler flank generally to the north and a warmer flank to the south, attributable to the warmer Loop Current bringing warmer water

to the south. As with SSTA, we compute the sea surface salinity anomalies (SSSAs) for SEVs of each type (Figure 4.12).

Interestingly, none of the SEVs exhibit a clear SSSA at their centers. Rather, each combination leads to a different arrangement of anomalies around the SEV center. In general, M-AEs and SEV-AEs lead to a negative SSSA to the direct east of the SEV center, being more intense with larger M-AEs (Figure 4.12A, E, I) while M-AEs and SEV-CEs demonstrate a positive SSSA to the east, with the most intense anomalies associated with mid-size eddies (Figure 4.12B, F, J). A similar set of patterns is exhibited for M-CEs and their constituent SEVs. However, the most intense SSSAs for M-CEs and both SEV-AEs and SEV-CEs is in smaller eddies rather than large ones (Figure 4.12C-D). While these patterns are similar in some respects to the patterns exhibited by observed mesoscale eddies in the GoM, such as the fact that the eddy center does not show a clear anomaly and that fresher water tends to originate to the north due to the Mississippi river outflow, the off-center anomaly is unusual (Brokaw et al., 2020).

As our results have indicated, internal SEVs are most often found within large eddies and induce anomalies in both SSTA and SSSA while they are present. Therefore, the last analysis we conduct is on the subject of the relationship between LCEs and SEVs using the major LCE of the simulation (Figure 4.13).

This LCE is noteworthy for being identifiable from the beginning of the simulation (as the Loop Current begins in an extended state) all the way through the end, not actually dissipating during the duration of the simulation. It separates fully from the Loop Current in early February before propagating westward and resting on the western boundary. This particular LCE was the fourth AE identified by the eddy detection algorithm, and so is

assigned the identifier AE4. Over the course of its life, AE4 always has at least 3 SEVs inside it, with at least 4% of its area and EKE devoted to these SEVs (Figure 4.13A). We showcase three snapshots of AE4 in relation to the Loop Current: one snapshot as the Loop Current is still extending in January (Figure 4.13B, E), one just after separation in late February (Figure 4.13C, F), and one a month after separating in late March (Figure 4.13D, G). As shown by the dashed lines in Figure 4.13A, these dates coincide with a middle, high, and low relative internal SEV composition respectively. We therefore observe that the SEVs reach a peak intensity inside AE4 just after separation from the Loop Current and rapidly fall thereafter as AE4 begins propagating westward.

4.4 DISCUSSION

In our results we have emphasized the characteristics of SEVs and their relationships with mesoscale eddies. Generally, SEVs are short-lived (on the order of a week lifetime) structures that are ubiquitous in long-lived (longer than a week lifetime) mesoscale eddies. They are most concentrated in the Loop Current and in the LCEs that spawn from it, but their general characteristics are similar across all types of eddies. SEVs increase in number both in the splitting of LCEs from the Loop Current as well as towards the end of the lifetimes of mesoscale eddies. The amplitude of SEV-CEs in particular is a strong signal produced by an extending Loop Current about to shed an LCE (Figure 4.3B, Figure 4.5B). The EKE of such SEVs strongly follows a fortnightly tidally induced signal apparent in the Loop Current. It is possible that, as suggested by previous literature, some of these SEVs are produced by barotropic tides near the coast (Nakamura et al., 2012). Regardless of when they appear, SEVs induce submesoscale temperature and salinity

variabilities in their parent mesoscale eddies. With this general breakdown, however, arises questions that we have not yet fully addressed in our analysis.

4.4.1 PROPOSED GENERATION MECHANISMS OF SEVS

We begin with an assessment of likely SEV generation mechanisms. One explanation particularly relevant for SEV-AEs, previously described by Brannigan (2016) and observed by Brannigan et al. (2017), is symmetric instabilities in the mixed layer. In this process, an instability is generated in the mixed layer, primarily driven by vertical buoyancy fluxes and vertical velocity shear, ultimately leading to a negative potential vorticity region at the surface. The number of filaments and structures generated through this process are shown to be highly resolution-dependent, first resolvable at the 2-km scale. As this is the scale resolved by our simulation, filaments, fronts, and eddy-like structures associated with symmetric instabilities may be associated with SEV-AEs found in the cores of M-AEs. Symmetric instabilities are also observed by de Marez et al. (2020b) to act at the northern edge of a simulated eddy, which then induces diapycnal mixing. Therefore, symmetric instabilities may explain the dipolar distribution of SEV-AEs within M-CEs. However, the coastal nature of the most numerous SEV-AEs within M-CEs (*i.e.* Figure 4.5K, L, P, Q) may also play a role in forcing this distribution. The intense vertical velocities associated with such structures, robust throughout studies of the submesoscale, may explain also the coherency of the SSTA observed in their cores (Figure 4.11).

Symmetric instabilities as a possible cause for SEV generation is also supported by the instability analysis of Lahaye and Zeitlin (2016), but alongside baroclinic and barotropic instabilities. The dominance of baroclinic and barotropic instabilities in the generation of submesoscale structures is likewise supported by the observations of

Buckingham et al. (2017). Similarly, Yang et al. (2020) report that baroclinic instabilities play a particular role in the genesis of eddies in the Loop Current region. They also observe a mechanical energy transfer between mesoscale eddies and high frequency frontal eddies as a part of an inverse energy cascade, an observation similarly reported by Lazaneo et al. (2022). The presence of SEVs, aligning with those frontal eddies described by Yang et al. (2020) correlates with the splitting of the LCE from the Loop Current as described previously (Figure 4.13). Therefore, through both baroclinic instabilities and the ensuing frontogenesis (*i.e.* Garabato et al., 2022), the generation of SEVs may indicate an intensification of the inverse energy cascade; this most likely varies in conjunction with the forward energy cascade on a seasonal basis, as highlighted by Yang et al. (2021). The concept that the inverse energy cascade might be uniquely prevalent for internal SEVs is supported by the findings in our Figure 4.9, as SEVs increase in number the closer a mesoscale eddy is to decoherence. These SEVs, particularly those of opposite sign that gather on eddy boundaries, may also play a role similar to the submesoscale structures noted by Haza et al. (2016), causing leakage across eddy boundaries. An eddy with more such SEVs, therefore, can be expected to fracture from within due to baroclinic and barotropic instabilities at and below the mixed layer expressed as a part of same-rotation type SEVs. At the same time, such an eddy might be leaking fluid to without due to symmetric instabilities and frontogenesis expressed by opposite-rotation type SEVs, possibly in a process similar to that described by Barkan et al. (2019) and Verma et al. (2019). The non-baroclinic processes are likely intensified as a mesoscale eddy approaches topographic features (Rosso et al., 2015; Morvan et al., 2019; Morvan et al., 2020). Lastly, it is worth noting that based upon the season and location of SEV formation the motions

and predominant EKE that characterize SEVs may be either primarily balanced or unbalanced in terms of dissipation vs. atmospheric forcings; the reader is referred to Cao et al. (2023) for a more complete discussion on the nature of such motions as manifested in our model simulations.

4.4.2 SSSA ANOMALY PATTERNS

While the SSTA patterns described in Figure 4.11 match those ascribed both to mesoscale eddies in the GoM and the dynamics of submesoscale vertical heat transport, the dynamical meaning behind the SSSA patterns of Figure 4.12 are less clear (Brokaw et al., 2020; Wang et al., 2022). As previously noted, in fact, the observed patterns are opposite of those expected in such structures from a theoretical standpoint. The SSSA signature associated with AEs is typically associated with an increased surface salinity, while the surface expression of CEs is more often associated with a decrease in surface salinity as described in mesoscale eddies throughout the world's oceans (Melnichenko et al., 2017). The patterns seen in Figure 4.12, however, show an opposite effect, as SEV-AEs are associated with more intense freshwater anomalies and SEV-CEs are associated with more intense salinity anomalies. In both cases, the dipolar structure is expected, but the intensity of the poles are reversed.

The answer may be found in the work of X. Zhang et al. (2019). In this study, the formation of a submesoscale eddy is observed as a result of baroclinic instability in a slumping salinity front. The authors find that, due to the fresher surface layer, upwelling induced by the eddy resulted in a more saline surface layer. In the same fashion, large submesoscale salinity variations on the order of 0.05 psu at the surface as observed by Drushka et al. (2019) might be expected in the GoM due to the river plume of the

Mississippi river. In effect, the decidedly fresher surface water of the GoM, especially towards its northern edge, is likely entrained by SEV-AEs, decreasing salinity adjacent to the SEV core. At the same time, SEV-CEs are responsible for upwelling through the surface layer, allowing for a more saline surface. This allows for frontal compensation across the GoM as described for freshwater-influenced regions by Spiro Jaeger and Mahadevan (2018). An intriguing connection here is made by Kobashi and Hetland (2020): the Mississippi river outflow is partially controlled by anthropogenic factors and remote interannual variabilities, *e.g.* the El Niño Southern Oscillation. As a result, SEVs and other structures often associated with salinity fronts may introduce an element of remote forcing into SEV variability. However, as the authors conclude, there is as of yet insufficient evidence to prove a significant link exists, especially at the under observed submesoscale.

4.4.3 BROADER IMPLICATIONS

The ubiquity of SEVs in the GoM and mesoscale eddies suggests that SEVs may play an important role in the biogeochemical cycling and chlorophyll dispersal within the Gulf. For example, frontal eddy structures have already been observed in the Florida Straits using ocean color data (Y. Zhang et al., 2019). At the same time, mesoscale eddies in the Gulf have been shown to aid in the dispersal of chlorophyll-a as eddies interact and break plumes apart (Toner et al., 2003). SEVs and the frontal dynamics associated with them likely play a role in the advection and vertical movement of nutrients into and away from the surface layer, influencing the distribution of phytoplankton blooms and hypoxic zones (Rabalais et al., 2002). Internal SEVs and leakage associated with them may also complicate the transport of freshwater away from the river plume with future implications for the spread of pollutants (Özgökmen et al., 2016).

Another implication of SEV-induced variability in the Gulf is that on tropical cyclone strength. Warm sea surface temperatures associated with mesoscale eddies have been observed to correlate with an increase in storm strength (Jaimes et al., 2016). LCEs have also been drained of heat and forcibly dissipated through air-sea interactions with hurricanes (Potter et al., 2021). As we demonstrate here, the submesoscale variability of both the Loop Current and LCEs changes dramatically depending on life cycle stage. Future observations will serve to clarify the role that submesoscale oceanic variability plays in the intensification and feedbacks associated with hurricane growth.

Finally, machine learning based approaches have already demonstrated skill in the prediction of the separation of LCEs (Wang et al. 2019). The most prevalent of these approaches utilizes high resolution SSH time series to extract hidden patterns that lead to LCE separation spatiotemporal predictions. Greater resolution data and an increased understanding of the submesoscale dynamics within that data may improve the accuracy and skill of future predictions, as the separation of an LCE from the Loop current involves interactions across both the mesoscale and submesoscale that cannot be properly discerned from previously available data (Yang et al., 2020).

4.5 CONCLUSIONS

In this study, we have used a tailor-made filtering approach to efficiently separate the spatial scales in a high resolution modelling simulation. Through the use of an automated eddy detection and tracking algorithm, we have identified regions that, through shape, persistence, and SSH anomalies, behave like eddies. These so-called SEVs were then evaluated both across the entire spatiotemporal domain and in the context of mesoscale eddies, where SEVs were collocated within mesoscale eddy contours. To our

knowledge, this is the first time this has been done algorithmically on a basin-wide scale. Through describing the characteristics of SEVs, particularly those internal to mesoscale eddies, we demonstrate that SEVs are typically responsible for up to 15% of the internal variability in terms of EKE, SSS, SST, and SSH in mesoscale eddies of all sizes throughout the GoM. We show that SEVs also correlate with the extensions of the Loop Current, with the number of SEVs internal to an LCE reaching a maximum just after separation from the loop current occurs. These findings have implications for biogeochemical processes in the Gulf, as well as Loop Current and LCE separation forecasting. Given our results' dependence on our model's resolution as demonstrated by previous studies, further observations are required to validate and confirm them. The SWOT mission, already in orbit and undergoing calibration and validation, promises to provide the first wide-scale SSH measurements of an effective resolution capable of resolving these SEVs.

Table 4.1. The arithmetic means and standard deviations of Internal SEV lifetimes (column 1), radii (column 2), amplitudes (column 3), and EKE (column 4) for SEV-AEs internal to mesoscale AEs (row 1), SEV-CEs internal to mesoscale AEs (row 2), SEV-AEs internal to mesoscale CEs (row 3) and SEV-CEs internal to mesoscale CEs (row 4).

	Lifetime (days)	Radius (km)	Amplitude (cm)	EKE ($\text{m}^2 \text{s}^{-2}$)
M-AE, SEV-AE	5.5 ± 7.3	9.2 ± 4.3	2.3 ± 1.8	0.10 ± 0.14
M-AE, SEV-CE	5.0 ± 8.0	8.2 ± 3.7	3.0 ± 2.5	0.073 ± 0.088
M-CE, SEV-AE	6.5 ± 8.5	9.4 ± 4.5	2.6 ± 2.0	0.033 ± 0.054
M-CE, SEV-CE	7.5 ± 12.8	9.8 ± 4.8	3.9 ± 3.1	0.055 ± 0.094

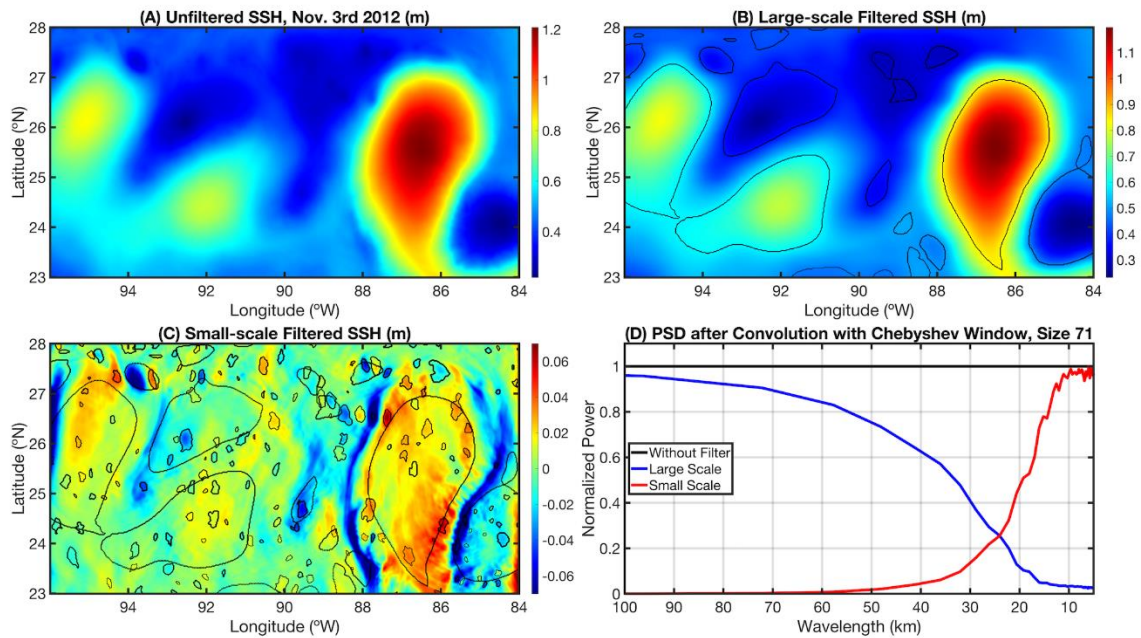


Figure 4.1. The SSH fields (m) in the central Gulf of Mexico for Nov. 3rd, 2012, showcasing the filtering process and eddy detection methodologies. (A) The total scale model outputs; (B) the large scale filtered SSH after convolution with the Dolph-Chebyshev window and corresponding mesoscale eddy edge detections (black lines); (C) the small scale filtered SSH after subtracting (B) from (A) along with both detections of large and small scale eddies (black lines). (D) The normalized power spectrum for the large scale field (in blue) and the small scale field (in red) demonstrating a crossover point near 25 km.

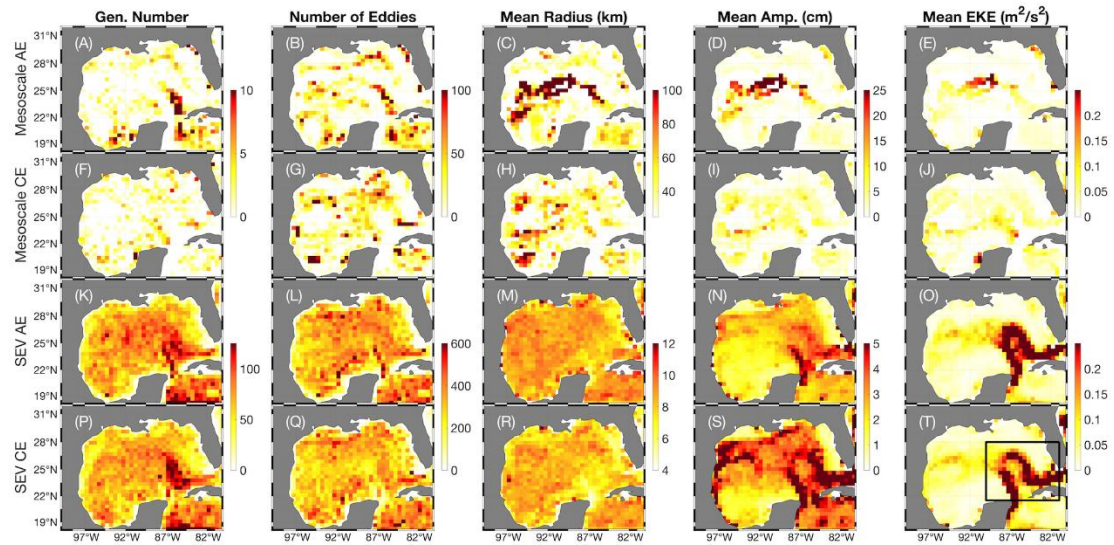


Figure 4.2. The properties of all mesoscale eddies and SEVs broken down geographically by eddy center location and binned into $\frac{1}{2}^\circ$ pixels. (A)-(E) The generation number, *i.e.* number of eddies the originated in the pixel, the number of all eddy detections, the mean eddy radius (km), the mean eddy amplitude (cm), and the mean EKE ($m^2 s^{-2}$) for all mesoscale AEs. (F)-(J) As in (A)-(E) but for mesoscale CEs. (K)-(O) As in (A)-(E) but for SEV-AEs. (P)-(T) As in (A)-(E) but for SEV-CEs. The black box in (T) denotes the Loop Current region.

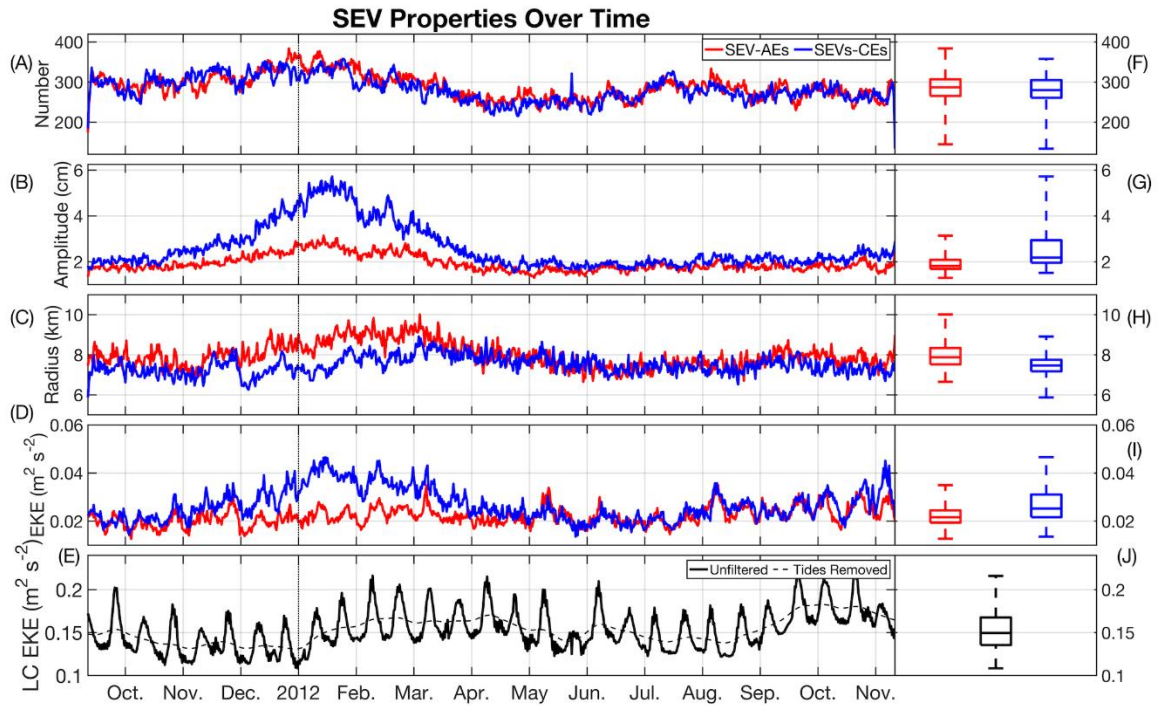


Figure 4.3. The properties of all SEVs over time from the beginning of the model simulation to its end, separated into AEs and CEs and binned into 12-hour increments. (A) The number of eddies per increment; (B) the median eddy amplitude (cm); (C) the median eddy radius (km); (D) the median eddy EKE ($m^2 s^{-2}$). (E) The EKE for the Loop Current region as defined by Brokaw et al. (2020): $21.5^{\circ}N - 28^{\circ}N$ and $81^{\circ}W - 90^{\circ}W$, both with and without tidal variability (as removed by a low-pass Gaussian filter with a half-window of 28 days). (F)-(J) As in (A)-(E) but using a box plot to show the median, quartiles, and extremes of the data upon which the time series is constructed.

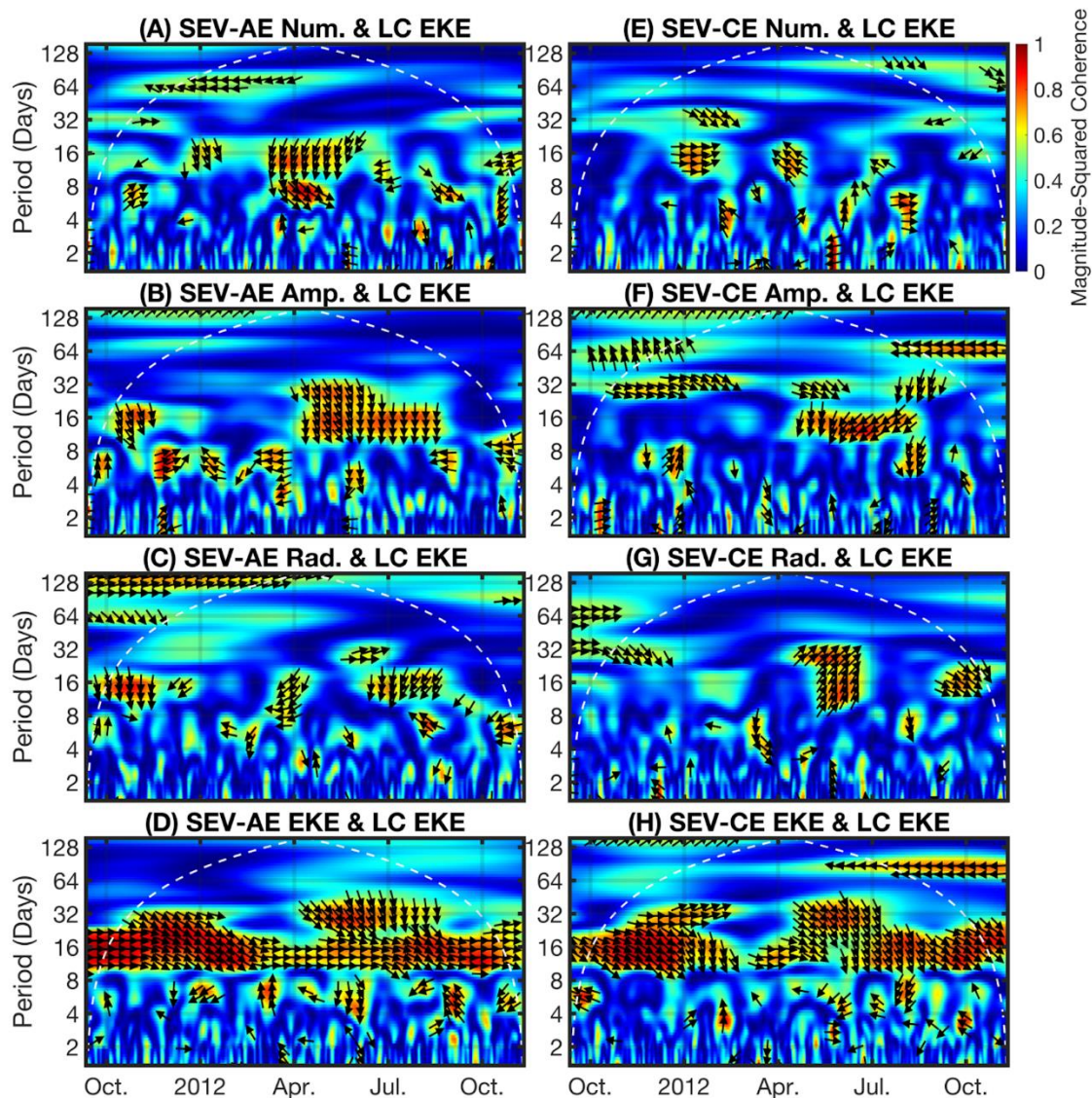


Figure 4.4. The magnitude-squared wavelet coherence computed using the analytic Morlet wavelet between each of the time series in Figure 4.3A-D and Figure 4.3E. The white dashed line shows the cone of influence, after which edge effects dominate, while the black arrows show the direction of phase for coherence > 0.5 . Rightward-facing arrows indicate the time series are in-phase, leftward facing arrows indicate the time series are anti-phase, downward facing arrows generally indicate that the first time series leads the second by 90 degrees, and upward facing arrows generally indicate that the second time series leads the first by 90 degrees. (A)-(D) The coherence between SEV-AEs number, amplitude, radius, and EKE time series and the Loop Current time series. (E)-(H) As in (A)-(D) but for SEV-CEs.

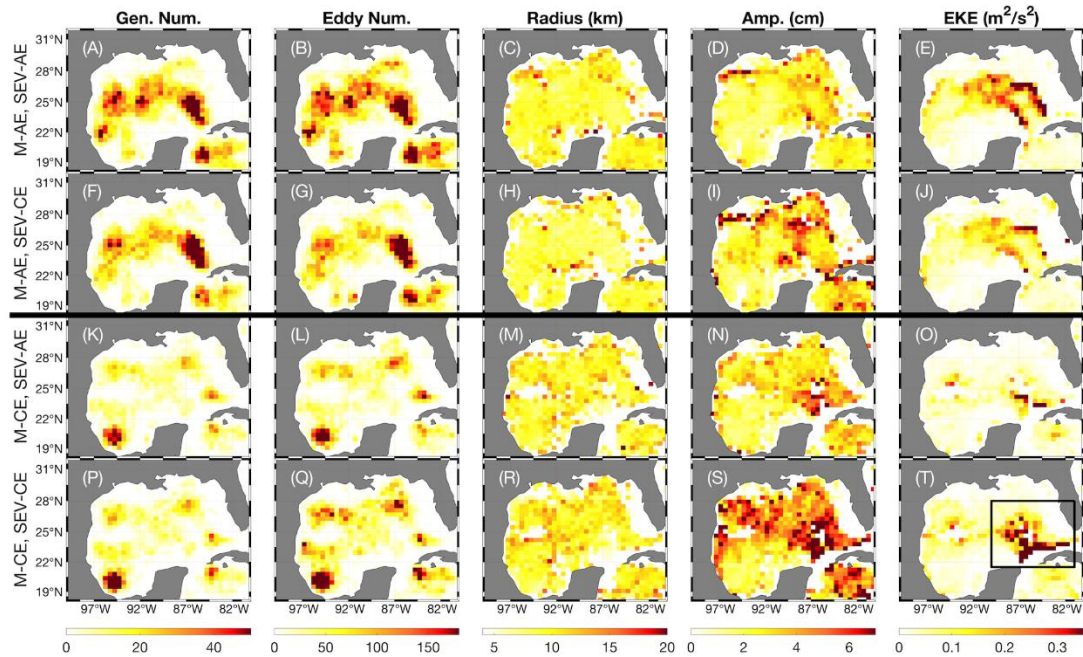


Figure 4.5. The geographic properties, as in Figure 4.2, for each type of internal SEV-outer mesoscale eddy combination pair. (A)-(E) The generation number, the mean eddy radius (km), the mean eddy amplitude (cm), and the mean EKE ($\text{m}^2 \text{s}^{-2}$) for all SEV-AEs internal to mesoscale AEs. (F)-(J) As in (A)-(E) but for SEV-CEs internal to mesoscale AEs. (K)-(O) As in (A)-(E) but for SEV-AEs internal to mesoscale CEs. (P)-(T) As in (A)-(E) but for SEV-CEs internal to mesoscale CEs. The black box in (T) denotes the Loop Current region.

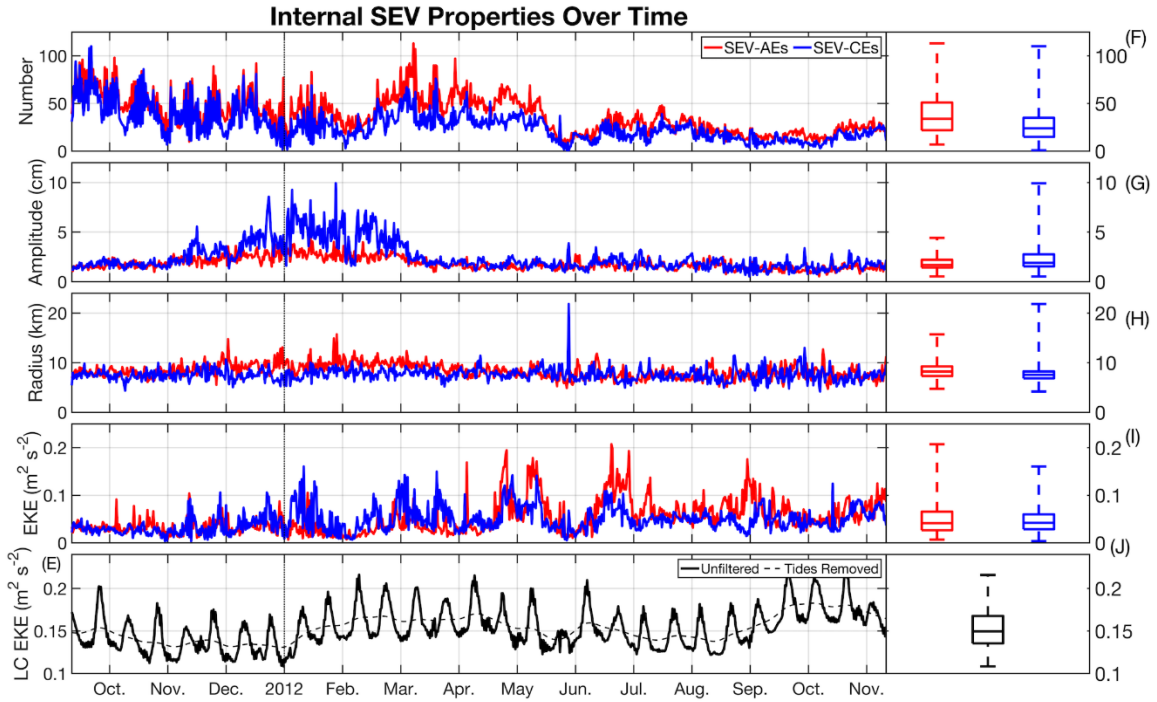


Figure 4.6. The time series of SEV properties, exactly as in Figure 4.3, but for only internal SEVs. Loop Current EKE is repeated without alterations. (A) The number of eddies per increment; (B) the median eddy amplitude (cm); (C) the median eddy radius (km); (D) the median eddy EKE ($\text{m}^2 \text{s}^{-2}$). (E) The EKE for the Loop Current region both with and without tidal variability. (F)-(J) As in (A)-(E) but using a box plot to show the median, quartiles, and extremes of the data upon which the time series is constructed.

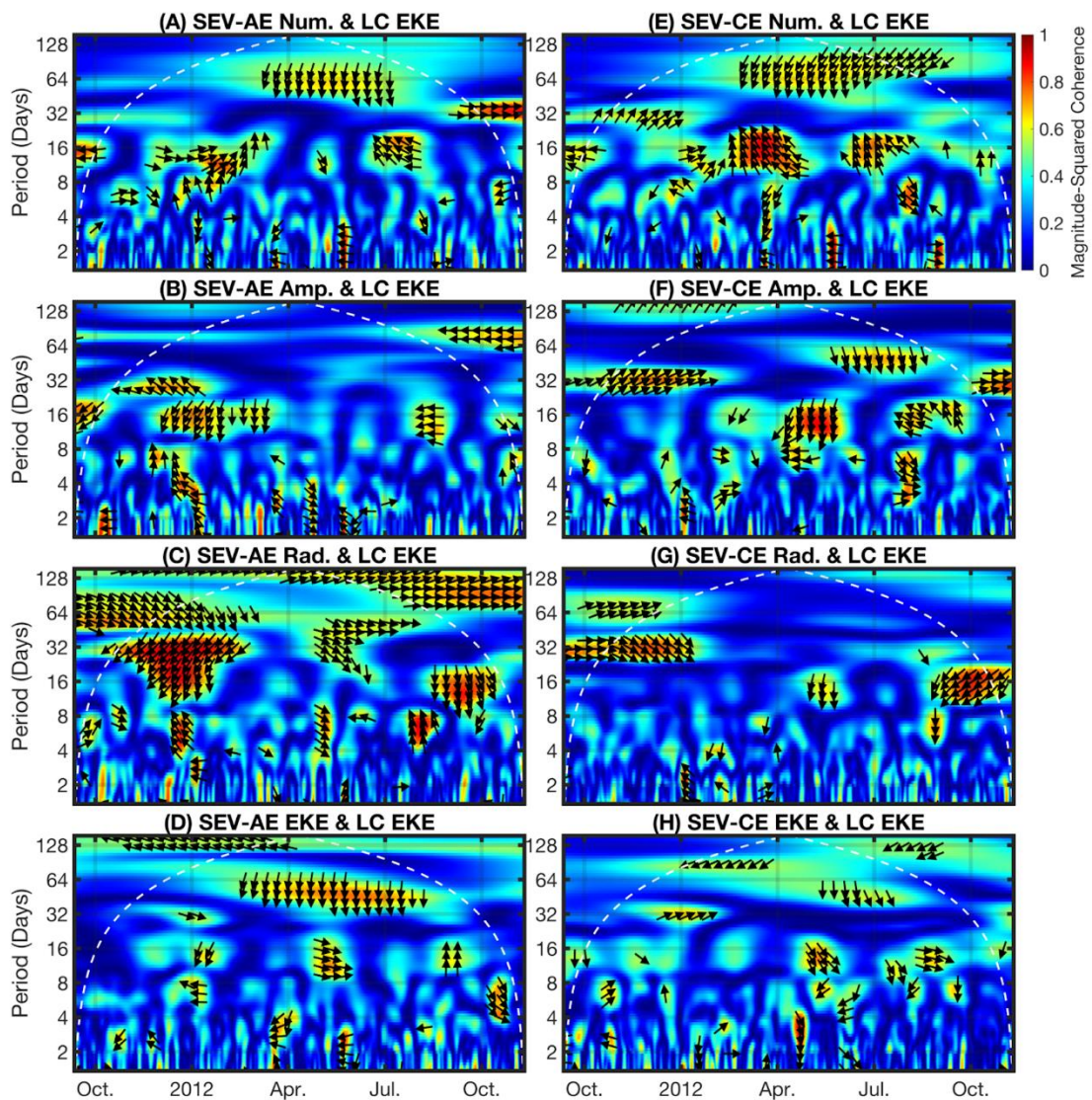


Figure 4.7. The Morlet wavelet coherence, exactly as in Figure 4.4, but for the internal SEV time series in Figure 4.6. The white dashed line shows the cone of influence, after which edge effects dominate, while the black arrows show the direction of phase for coherence > 0.5 . (A)-(D) The coherence between internal SEV-AEs number, amplitude, radius, and EKE time series and the Loop Current time series. (E)-(H) As in (A)-(D) but for internal SEV-CEs.

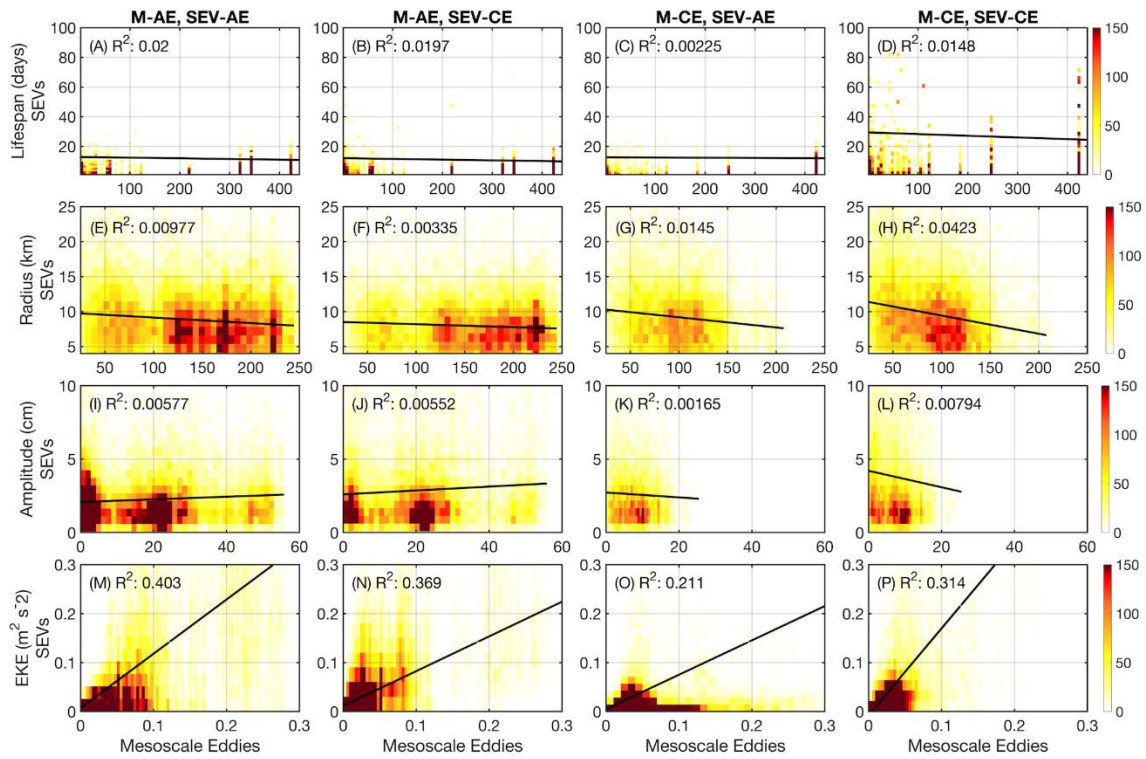


Figure 4.8. The binned histograms, in number of eddies, between the coincident properties of parent mesoscale eddies (x-axes) and their internal SEVs (y-axes) for each type of internal SEV-outer mesoscale eddy combination pair (columns 1-4). (A)-(D) The lifespans (days) of SEVs versus their parent mesoscale eddy lifespans. (E)-(H) The radii (km) of SEVs versus their parent mesoscale eddy radii. (I)-(L) The amplitudes (cm) of SEVs versus their parent mesoscale eddy amplitudes. (M)-(P) The EKEs ($m^2 s^{-2}$) of SEVs versus their parent mesoscale eddy EKEs. Linear regressions are shown as black lines with R^2 values annotated.

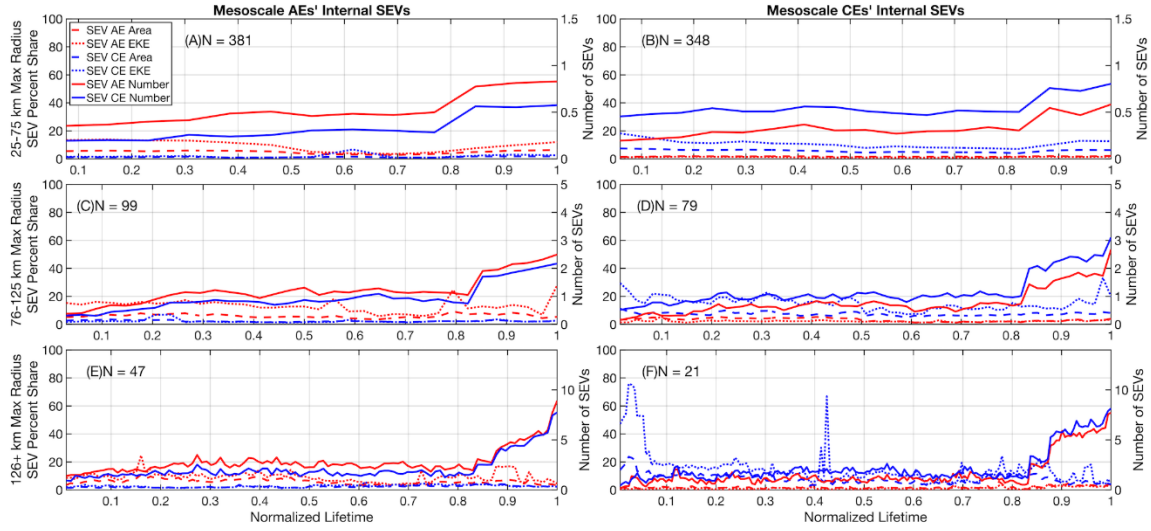


Figure 4.9. The numbers, fractions of parent eddy area, and fractions of parent eddy EKE taken up by internal SEVs over the normalized lifespan of their parent eddies. Number of parent eddies in each figure is shown. The left y-axes depict the percentage statistics, while the right y-axis depict the number of SEVs. (A) The statistics for parent AEs with a maximum trajectory radius of between 25 and 75 km. (B) As in (A) but for parent CEs. (C) As in (A) but for eddies whose maximum radius lies between 76 and 125 km. (D) As in (C) but for parent CEs. (E) As in (A) but for eddies whose maximum radius lies above 126 km. (F) As in (E) but for parent CEs.

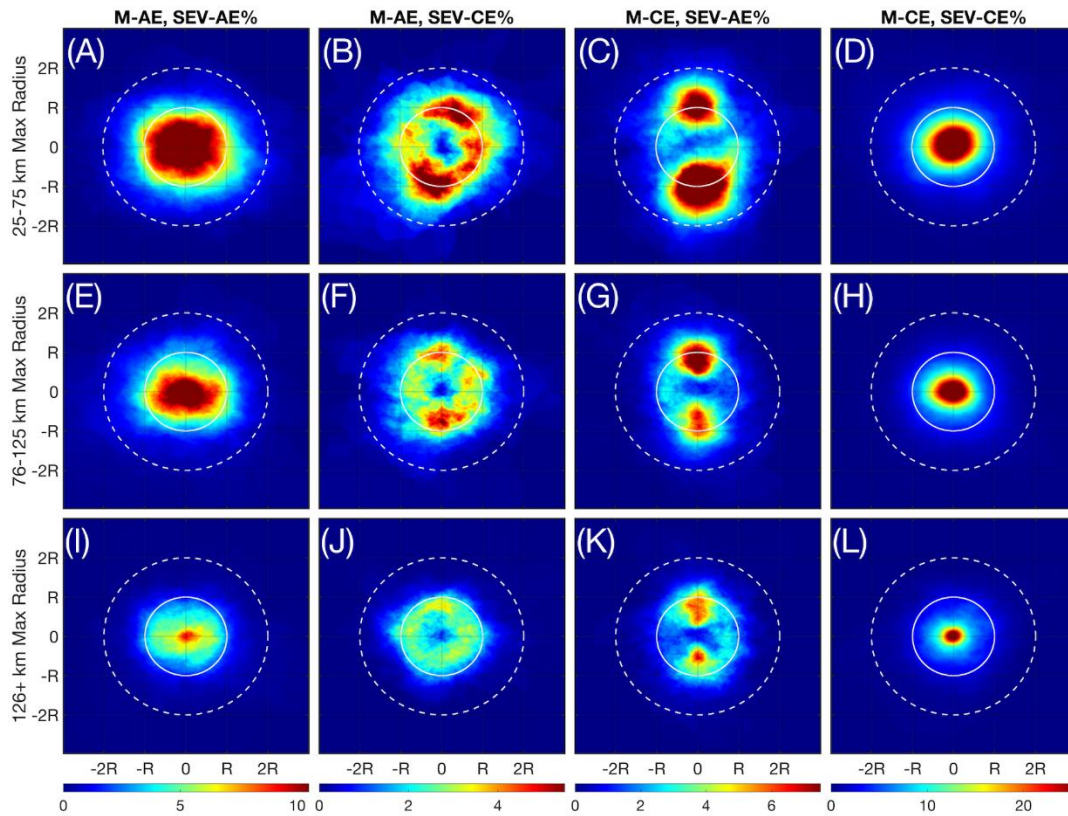


Figure 4.10. The locational composites for all instances of internal SEVs, showing the likelihood of a SEV covering a given pixel in a mesoscale eddy in percentage points for each type of internal SEV-outer mesoscale eddy combination pair. (A)-(D) The composites for eddies of maximum radius between 25 and 75 km. (E)-(H) As in (A)-(D) but for eddies of maximum radius between 76 and 125 km. (I)-(L) As in (A)-(D) but for eddies whose maximum radius lies above 126 km.

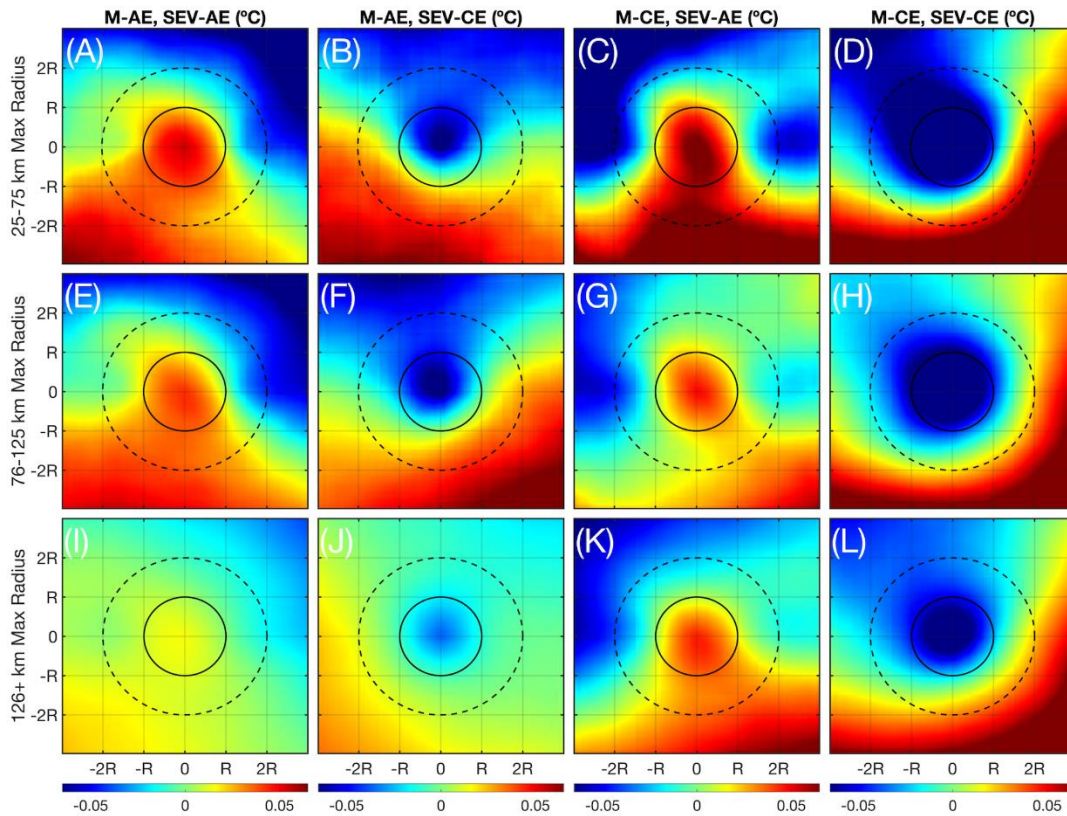


Figure 4.11. The composites for all SST anomalies ($^{\circ}\text{C}$) associated with internal SEVs (difference between center SEV temperature and mean temperature computed up to 3 radii) for each type of internal SEV-outer mesoscale eddy combination pair. (A)-(D) The composites for eddies of maximum radius between 25 and 75 km. (E)-(H) As in (A)-(D) but for eddies of maximum radius between 76 and 125 km. (I)-(L) As in (A)-(D) but for eddies whose maximum radius lies above 126 km.

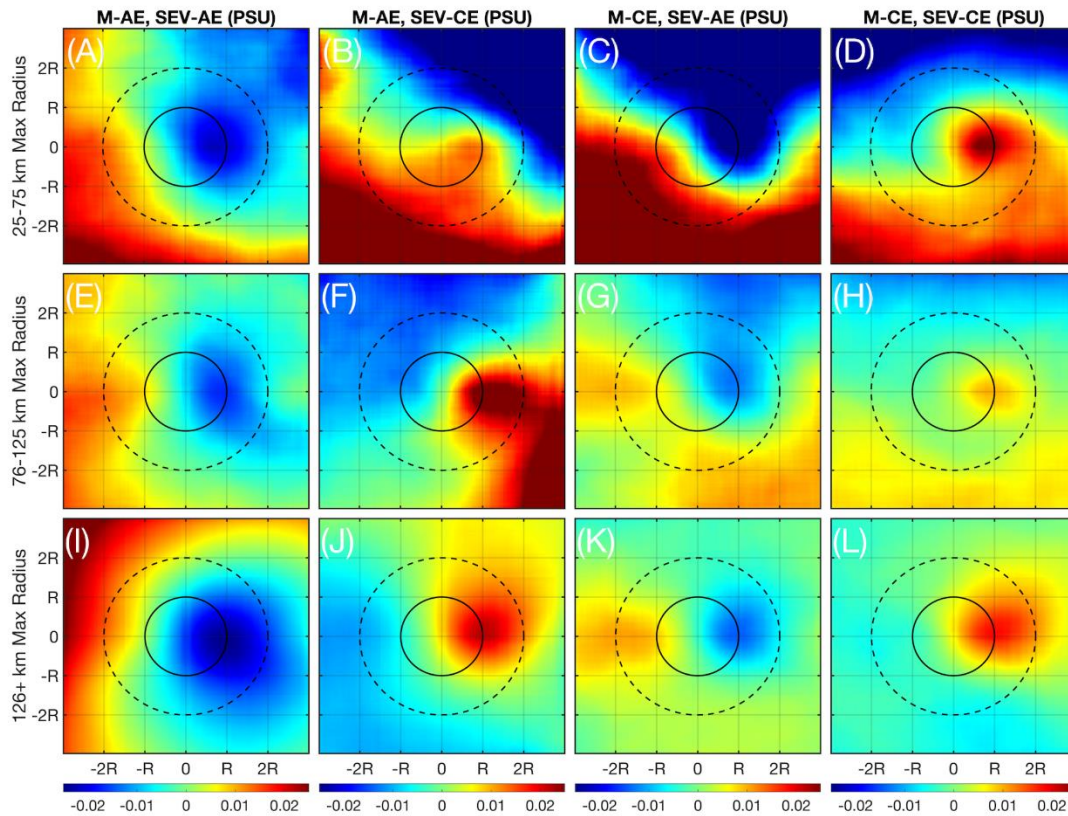


Figure 4.12. The composites for all SSS anomalies (PSU) associated with internal SEVs (difference between center SEV salinity and mean salinity computed up to 3 radii) for each type of internal SEV-outer mesoscale eddy combination pair. (A)-(D) The composites for eddies of maximum radius between 25 and 75 km. (E)-(H) As in (A)-(D) but for eddies of maximum radius between 76 and 125 km. (I)-(L) As in (A)-(D) but for eddies whose maximum radius lies above 126 km.

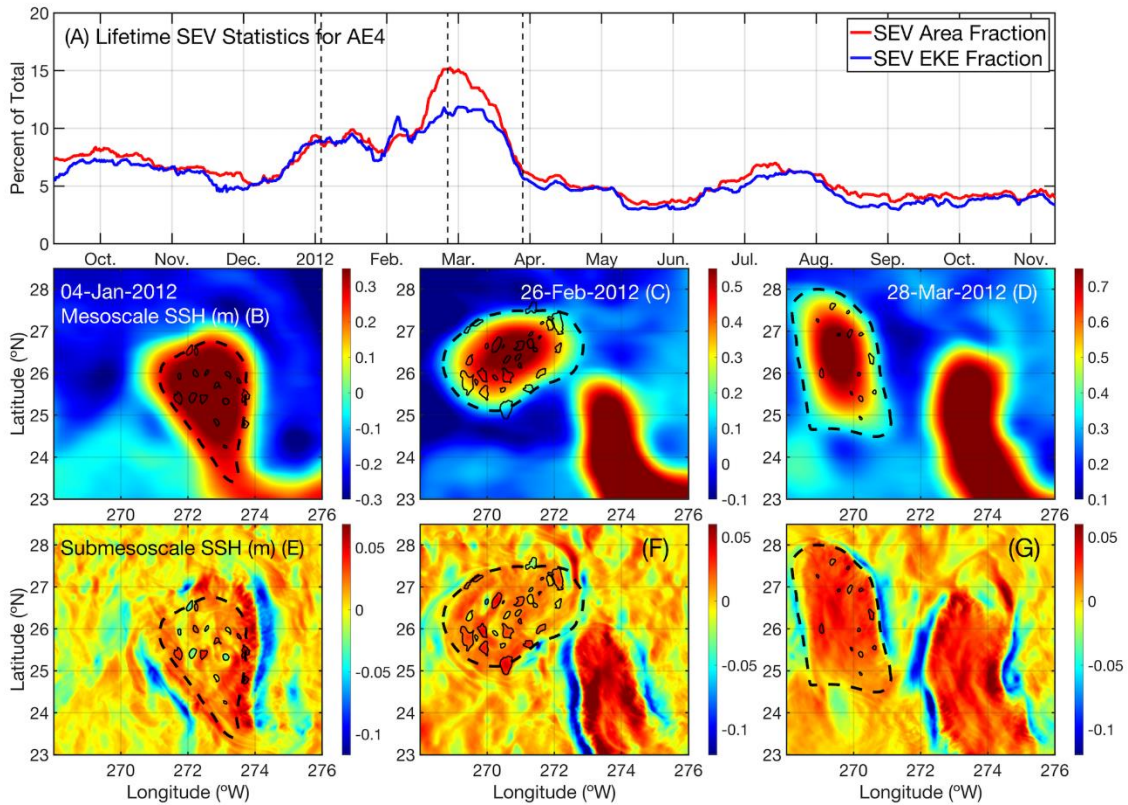


Figure 4.13. The separation of the Loop Current Eddy AE trajectory #4, or AE4. (A) The percent of AE4’s area and EKE taken up by SEVs over its lifespan, with black dashed lines showing the dates of the following snapshots. (B) The large-scale SSH (m) field associated with Jan. 4th, 2012 showing AE4 (dashed line) and its internal SEVs (solid lines). (C) As in (B) but for Feb. 26th, 2012. (D) As in (B) but for Mar. 28th, 2012. (E)-(G) As in (B)-(D) but showing the small-scale SSH (m) field instead.

CHAPTER 5

CONCLUSION

The study of eddies is crucial to understanding ocean circulation. Transporting as much water as the rest of the global ocean currents combined, eddies play major roles in the advection and mixing of biogeochemical components and physical properties (Zhang et al., 2014). Eddies are even more important in regions that are dominated by one or multiple large mesoscale surface eddies for months out of the year, such as the Somali Current and the Lakshadweep Sea in the Arabian Sea (AS) (Brokaw et al., 2020; Shankar & Shetye, 1997; Schott & McCreary, 2001). Such mesoscale eddies and eddy fields, typically studied via satellite altimetry, are often not fully described due to a lack of robust surface tracking, subsurface components, and submesoscale components. This work has focused on enhancing old methods and developing new techniques for studying eddy dynamics in these changing environments.

Chapter 2 of this dissertation focused on the Lakshadweep High (LH), a climatological anticyclonic eddy that forms in the Lakshadweep Sea every November-December and dominates the local circulation for several months. Building upon earlier low-resolution studies with newer high resolution composite data, the LH was tracked for the first time over 27 years of continuous observations. Using a rank-order method and a closed-contour tracking algorithm, the LH was found to have three distinct types of propagation, with the majority of years seeing the LH propagate across the entirety of the

AS upon a westward Rossby wave. This Rossby wave, spawned by a confluence of remote wind forcing and the second annual downwelling coastal Kelvin wave, carries the LH and sustains it; however, in some years, the wind forcing is insufficient for full or even partial propagation, as the LH fails to overcome the Lakshadweep Island barrier. Finally, after propagating, the LH merges with the Somali Current, inhibiting a local intense cyclonic eddy from forming around the Great Whirl. This chapter also highlights the importance of the LH as a spreading and mixing agent for Bay of Bengal low salinity waters across the AS. Such surface and middle water masses are seen to be modulated by the presence of the LH, with downwelled water disrupting the local stratification.

Next, Chapter 3 takes the concept of subsurface eddy components in the AS and asks the question: can *fully* subsurface eddies and their impacts on water mass circulation be robustly tracked? The answer is yes: using the rescaled Potential Vorticity (PV) for the first time in such a way, a novel eddy tracking algorithm tracks eddies within isopycnic layers delineating water masses. The rescaled PV algorithm is tested and optimized alongside several other popular methods, including the fundament of the popular Angular Momentum Eddy Detection and Tracking Algorithm (AMEDA), the Local Normalized Angular Momentum (LNAM) (Le Vu et al., 2018). In a final test of all optimized parameters, the PV algorithm is demonstrated to provide superior performance and tracking capabilities. Using a high-resolution NEMO model, the PV algorithm is tested on the intermediate water mass of the Red Sea Water, with subsurface eddy properties catalogued. Finally, using state-of-the-art Lagrangian particle tracking with the rescaled PV, the sources of PV that formed a major subsurface eddy near the Chagos Archipelago

are identified. The new algorithm is made available to the public for use in any future water mass or subsurface eddy studies.

Finally, Chapter 4 homes in on the submesoscale, using the Gulf of Mexico as a contrasting environment for study. In this part of the work, the submesoscale structures in the region were simulated using a $1/48^\circ$ ECCO model and isolated using a custom-designed Dolph-Chebyshev window-based spatial filtering process (Lynch, 1997). These small-scale structures were analyzed in the context of the overlying mesoscale eddy field, identifying the inner structures and instabilities that reside within mesoscale eddies. In this analysis, it is found that the presence and increased intensity of submesoscale eddy-like structures are indicative of mesoscale eddy dissipation and LCE separation. This is supported by parallels drawn with previous work that indicates the role of such instabilities in the forward and inverse energy cascades of the region (Yang et al., 2021; Yang et al., 2020). Lastly, it is shown that the submesoscale structures align with robust temperature and salinity anomalies at the surface, highlighting the role of such structures on vertical mixing in the upper layers of the ocean as well as the entrainment of edge waters into eddy cores.

Given the nature of the work completed in this dissertation, many paths forward are illuminated for future studies; indeed, it is the hope of the author that the tools and techniques developed here will inspire and catalyze future work. In the Arabian Sea, there are other major eddies, such as the Socotra Eddy and the South Arabian High that may play as important roles in the pre-monsoon circulation as the LH but have not been scrutinized using modern data and procedures (Prasad & Ikeda, 2001; Schott et al., 1997). When analyzed in the context of the monsoon onset vortex and the Arabian Sea Mini Warm Pool,

these formations, if analyzed in the way of the LH in this work, may provide new insights into the monsoon phenomena (Kurian & Vinayachandran, 2007). Furthermore, the subsurface components of these eddies and other eddies in the Arabian Sea and other regions around the world's oceans deserve more attention. Given the enhanced performance of the PV method in conjunction with high resolution models, subsurface water mass propagations and modulations by eddies might be traced to further illuminate their roles in the changing thermohaline circulation. Finally, with the advent of the Surface Water Ocean Topography (SWOT) mission, the conclusions of Chapter 4 might be examined and validated against observational data, with the possible application of such methods in other regions around the globe (Chelton et al., 2019). Overall, the advance of modern observation and modelling techniques will continue to advance in tandem with the methods and conclusions drawn from those methods; ultimately, this dissertation represents one step of this process, such that others might follow and build upon the work done here in the future.

REFERENCES

- Adcroft, A., Hill, C., Campin, J.-M., Marshall, J., & Heimbach, P. (2004). Overview of the formulation and numerics of the MIT GCM. *Proceedings of the ECMWF Seminar Series on Numerical Methods, Recent Developments in Numerical Methods for Atmosphere and Ocean Modeling*.
- Akuetevi, C. Q. C., Barnier, B., Verron, J., Molines, J.-M., & Lecointre, A. (2016). Interactions between the Somali Current eddies during the summer monsoon: insights from a numerical study. *Ocean Science*, *12*(1), 185–205. <https://doi.org/10.5194/os-12-185-2016>
- Al Saafani, M. A., & Shenoi, S. S. C. (2007). Water masses in the Gulf of Aden. *Journal of Oceanography*, *63*(1), 1–14. <https://doi.org/10.1007/s10872-007-0001-1>
- Amores, A., Jordà, G., Arsouze, T., & Sommer, J. L. (2018). Up to What Extent Can We Characterize Ocean Eddies Using Present-Day Gridded Altimetric Products? *Journal of Geophysical Research: Oceans*, *123*(10), 7220–7236. <https://doi.org/10.1029/2018JC014140>
- Arbic, B. K., Elipot, S., Brasch, J. M., Menemenlis, D., Ponte, A. L., Shriver, J. F., et al. (2022). Near-Surface Oceanic Kinetic Energy Distributions From Drifter Observations and Numerical Models. *Journal of Geophysical Research: Oceans*, *127*(10), e2022JC018551. <https://doi.org/10.1029/2022JC018551>
- Assassi, C., Morel, yves, Vandermeirsch, F., Chaigneau, A., Pegliasco, C., Morrow, R., et al. (2016). An Index to Distinguish Surface- and Subsurface-Intensified Vortices from Surface Observations. *Journal of Physical Oceanography*, *46*(8), 2529–2552. <https://doi.org/10.1175/JPO-D-15-0122.1>
- Assene, F., Morel, Y., Delpech, A., Aguedjou, M., Jouanno, J., Cravatte, S., et al. (2020). From Mixing to the Large Scale Circulation: How the Inverse Cascade Is Involved in the Formation of the Subsurface Currents in the Gulf of Guinea. *Fluids*, *5*(3), 147. <https://doi.org/10.3390/fluids5030147>
- Barkan, R., Molemaker, M. J., Srinivasan, K., McWilliams, J. C., & D'Asaro, E. A. (2019). The Role of Horizontal Divergence in Submesoscale Frontogenesis. *Journal*

of *Physical Oceanography*, 49(6), 1593–1618. <https://doi.org/10.1175/JPO-D-18-0162.1>

Beal, L. M., & Donohue, K. A. (2013). The Great Whirl: Observations of its seasonal development and interannual variability. *Journal of Geophysical Research: Oceans*, 118(1), 1–13. <https://doi.org/10.1029/2012JC008198>

Beal, L. M., Hormann, V., Lumpkin, R., & Foltz, G. R. (2013). The Response of the Surface Circulation of the Arabian Sea to Monsoonal Forcing. *Journal of Physical Oceanography*, 43(9), 2008–2022. <https://doi.org/10.1175/JPO-D-13-033.1>

Bracco, A., Liu, G., & Sun, D. (2019). Mesoscale-submesoscale interactions in the Gulf of Mexico: From oil dispersion to climate. *Chaos, Solitons & Fractals*, 119, 63–72. <https://doi.org/10.1016/j.chaos.2018.12.012>

Brandt, P., Stramma, L., Schott, F., Fischer, J., Dengler, M., & Quadfasel, D. (2002). Annual Rossby waves in the Arabian Sea from TOPEX/POSEIDON altimeter and in situ data. *Deep Sea Research Part II: Topical Studies in Oceanography*, 49(7), 1197–1210. [https://doi.org/10.1016/S0967-0645\(01\)00166-7](https://doi.org/10.1016/S0967-0645(01)00166-7)

Brannigan, L. (2016). Intense submesoscale upwelling in anticyclonic eddies. *Geophysical Research Letters*, 43(7), 3360–3369. <https://doi.org/10.1002/2016GL067926>

Brannigan, Liam, Marshall, D. P., Garabato, A. C. N., Nurser, A. J. G., & Kaiser, J. (2017). Submesoscale Instabilities in Mesoscale Eddies. *Journal of Physical Oceanography*, 47(12), 3061–3085. <https://doi.org/10.1175/JPO-D-16-0178.1>

Bretherton, F. P. (1966). Critical layer instability in baroclinic flows. *Quarterly Journal of the Royal Meteorological Society*, 92(393), 325–334. <https://doi.org/10.1002/qj.49709239302>

Brokaw, R. J., Subrahmanyam, B., Trott, C. B., & Chaigneau, A. (2020). Eddy Surface Characteristics and Vertical Structure in the Gulf of Mexico from Satellite Observations and Model Simulations. *Journal of Geophysical Research: Oceans*, 125(2), e2019JC015538. <https://doi.org/10.1029/2019JC015538>

Bruce, J. G. (1979). Eddies off the Somali Coast during the southwest monsoon. *Journal of Geophysical Research: Oceans*, 84(C12), 7742–7748. <https://doi.org/10.1029/JC084iC12p07742>

Bruce, J. G. (1983). The Wind Field in the Western Indian Ocean and the Related Ocean Circulation. *Monthly Weather Review*, 111(7), 1442–1452. [https://doi.org/10.1175/1520-0493\(1983\)111<1442:TWFITW>2.0.CO;2](https://doi.org/10.1175/1520-0493(1983)111<1442:TWFITW>2.0.CO;2)

- Bruce, J. G., Kindle, J. C., Kantha, L. H., Kerling, J. L., & Bailey, J. F. (1998). Recent observations and modeling in the Arabian Sea Laccadive High region. *Journal of Geophysical Research: Oceans*, 103(C4), 7593–7600. <https://doi.org/10.1029/97JC03219>
- Bruce, John G., Johnson, D. R., & Kindle, J. C. (1994). Evidence for eddy formation in the eastern Arabian Sea during the northeast monsoon. *Journal of Geophysical Research: Oceans*, 99(C4), 7651–7664. <https://doi.org/10.1029/94JC00035>
- Buckingham, C. E., Khaleel, Z., Lazar, A., Martin, A. P., Allen, J. T., Naveira Garabato, A. C., et al. (2017). Testing Munk’s hypothesis for submesoscale eddy generation using observations in the North Atlantic. *Journal of Geophysical Research: Oceans*, 122(8), 6725–6745. <https://doi.org/10.1002/2017JC012910>
- Calil, P. H. R., Richards, K. J., Jia, Y., & Bidigare, R. R. (2008). Eddy activity in the lee of the Hawaiian Islands. *Deep Sea Research Part II: Topical Studies in Oceanography*, 55(10), 1179–1194. <https://doi.org/10.1016/j.dsr2.2008.01.008>
- Callendar, W., Klymak, J. M., & Foreman, M. G. G. (2011). Tidal generation of large sub-mesoscale eddy dipoles. *Ocean Science*, 7(4), 487–502. <https://doi.org/10.5194/os-7-487-2011>
- Cao, H., Fox-Kemper, B., & Jing, Z. (2021). Submesoscale Eddies in the Upper Ocean of the Kuroshio Extension from High-Resolution Simulation: Energy Budget. *Journal of Physical Oceanography*, 51(7), 2181–2201. <https://doi.org/10.1175/JPO-D-20-0267.1>
- Cao, H., Fox-Kemper, B., Jing, Z., Song, X., & Liu, Y. (2023). Towards the Upper-Ocean Unbalanced Submesoscale Motions in the Oleander Observations. *Journal of Physical Oceanography*, 53(4), 1123–1138. <https://doi.org/10.1175/JPO-D-22-0134.1>
- Chaigneau, A., Gizolme, A., & Grados, C. (2008). Mesoscale eddies off Peru in altimeter records: Identification algorithms and eddy spatio-temporal patterns. *Progress in Oceanography*, 79(2), 106–119. <https://doi.org/10.1016/j.pocean.2008.10.013>
- Chaigneau, A., Eldin, G., & Dewitte, B. (2009). Eddy activity in the four major upwelling systems from satellite altimetry (1992–2007). *Progress in Oceanography*, 83(1), 117–123. <https://doi.org/10.1016/j.pocean.2009.07.012>
- Challenor, P. G., Cipollini, P., & Cromwell, D. (2001). Use of the 3D Radon Transform to Examine the Properties of Oceanic Rossby Waves. *Journal of Atmospheric and Oceanic Technology*, 18(9), 1558–1566. [https://doi.org/10.1175/1520-0426\(2001\)018<1558:UOTRTT>2.0.CO;2](https://doi.org/10.1175/1520-0426(2001)018<1558:UOTRTT>2.0.CO;2)

- Chaudhuri, A., Amol, P., Shankar, D., Mukhopadhyay, S., Aparna, S. G., Fernando, V., & Kankonkar, A. (2021). Observed variability of the West India Coastal Current on the continental shelf from 2010–2017. *Journal of Earth System Science*, *130*(2), 77. <https://doi.org/10.1007/s12040-021-01603-4>
- Chelton, D. B., deSzoeke, R. A., Schlax, M. G., Naggar, K. E., & Siwertz, N. (1998). Geographical Variability of the First Baroclinic Rossby Radius of Deformation. *Journal of Physical Oceanography*, *28*(3), 433–460. [https://doi.org/10.1175/1520-0485\(1998\)028<0433:GVOTFB>2.0.CO;2](https://doi.org/10.1175/1520-0485(1998)028<0433:GVOTFB>2.0.CO;2)
- Chelton, D. B., Schlax, M. G., & Samelson, R. M. (2011). Global observations of nonlinear mesoscale eddies. *Progress in Oceanography*, *91*(2), 167–216. <https://doi.org/10.1016/j.pocean.2011.01.002>
- Chelton, D. B., Schlax, M. G., Samelson, R. M., Farrar, J. T., Molemaker, M. J., McWilliams, J. C., & Gula, J. (2019). Prospects for future satellite estimation of small-scale variability of ocean surface velocity and vorticity. *Progress in Oceanography*, *173*, 256–350. <https://doi.org/10.1016/j.pocean.2018.10.012>
- Chelton, D. B., Samelson, R. M., & Farrar, J. T. (2022). The Effects of Uncorrelated Measurement Noise on SWOT Estimates of Sea Surface Height, Velocity, and Vorticity. *Journal of Atmospheric and Oceanic Technology*, *39*(7), 1053–1083. <https://doi.org/10.1175/JTECH-D-21-0167.1>
- Chereskin, T. K., Rocha, C. B., Gille, S. T., Menemenlis, D., & Passaro, M. (2019). Characterizing the Transition From Balanced to Unbalanced Motions in the Southern California Current. *Journal of Geophysical Research: Oceans*, *124*(3), 2088–2109. <https://doi.org/10.1029/2018JC014583>
- Cui, W., Wang, W., Zhang, J., & Yang, J. (2019). Multicore structures and the splitting and merging of eddies in global oceans from satellite altimeter data. *Ocean Science*, *15*(2), 413–430. <https://doi.org/10.5194/os-15-413-2019>
- D’Addezio, J. M., Jacobs, G. A., Yaremchuk, M., & Souopgui, I. (2020). Submesoscale Eddy Vertical Covariances and Dynamical Constraints from High-Resolution Numerical Simulations. *Journal of Physical Oceanography*, *50*(4), 1087–1115. <https://doi.org/10.1175/JPO-D-19-0100.1>
- Dai, A., Qian, T., Trenberth, K. E., & Milliman, J. D. (2009). Changes in Continental Freshwater Discharge from 1948 to 2004. *Journal of Climate*, *22*(10), 2773–2792. <https://doi.org/10.1175/2008JCLI2592.1>
- Deans, S. R. (2007). *The Radon Transform and Some of Its Applications*. Courier Corporation.

- Doglioli, A. M., Blanke, B., Speich, S., & Lapeyre, G. (2007). Tracking coherent structures in a regional ocean model with wavelet analysis: Application to Cape Basin eddies. *Journal of Geophysical Research: Oceans*, *112*(C5). <https://doi.org/10.1029/2006JC003952>
- Drushka, K., Asher, W. E., Sprintall, J., Gille, S. T., & Hoang, C. (2019). Global Patterns of Submesoscale Surface Salinity Variability. *Journal of Physical Oceanography*, *49*(7), 1669–1685. <https://doi.org/10.1175/JPO-D-19-0018.1>
- Ducet, N., Le Traon, P. Y., & Reverdin, G. (2000). Global high-resolution mapping of ocean circulation from TOPEX/Poseidon and ERS-1 and -2. *Journal of Geophysical Research: Oceans*, *105*(C8), 19477–19498. <https://doi.org/10.1029/2000JC900063>
- Durand, F., Shankar, D., Birol, F., & Shenoi, S. S. C. (2009). Spatiotemporal structure of the East India Coastal Current from satellite altimetry. *Journal of Geophysical Research: Oceans*, *114*(C2). <https://doi.org/10.1029/2008JC004807>
- Durand, M., Fu, L.-L., Lettenmaier, D. P., Alsdorf, D. E., Rodriguez, E., & Esteban-Fernandez, D. (2010). The Surface Water and Ocean Topography Mission: Observing Terrestrial Surface Water and Oceanic Submesoscale Eddies. *Proceedings of the IEEE*, *98*(5), 766–779. <https://doi.org/10.1109/JPROC.2010.2043031>
- Echols, R., & Riser, S. C. (2020). Spice and Barrier Layers: An Arabian Sea Case Study. *Journal of Physical Oceanography*, *50*(3), 695–714. <https://doi.org/10.1175/JPO-D-19-0215.1>
- El Aouni, A. (2021). A hybrid identification and tracking of Lagrangian mesoscale eddies. *Physics of Fluids*, *33*(3), 036604. <https://doi.org/10.1063/5.0038761>
- Ernst, P. A., Subrahmanyam, B., & Trott, C. B. (2022). Lakshadweep High Propagation and Impacts on the Somali Current and Eddies During the Southwest Monsoon. *Journal of Geophysical Research: Oceans*, *127*(3), e2021JC018089. <https://doi.org/10.1029/2021JC018089>
- Ernst, P. A., Subrahmanyam, B., Morel, Y., Trott, C. B., & Chaigneau, A. (2023). Subsurface Eddy Detection Optimized with Potential Vorticity from Models in the Arabian Sea. *Journal of Atmospheric and Oceanic Technology*, *1*(aop). <https://doi.org/10.1175/JTECH-D-22-0121.1>
- Faghmous, J. H., Frenger, I., Yao, Y., Warmka, R., Lindell, A., & Kumar, V. (2015). A daily global mesoscale ocean eddy dataset from satellite altimetry. *Scientific Data*, *2*. <https://doi.org/10.1038/sdata.2015.28>

- Findlater, J. (1969). A major low-level air current near the Indian Ocean during the northern summer. *Quarterly Journal of the Royal Meteorological Society*, 95(404), 362–380. <https://doi.org/10.1002/qj.49709540409>
- Fine, R. A. (1993). Circulation of Antarctic intermediate water in the South Indian Ocean. *Deep Sea Research Part I: Oceanographic Research Papers*, 40(10), 2021–2042. [https://doi.org/10.1016/0967-0637\(93\)90043-3](https://doi.org/10.1016/0967-0637(93)90043-3)
- Fischer, A. S., Weller, R. A., Rudnick, D. L., Eriksen, C. C., Lee, C. M., Brink, K. H., et al. (2002). Mesoscale eddies, coastal upwelling, and the upper-ocean heat budget in the Arabian Sea. *Deep Sea Research Part II: Topical Studies in Oceanography*, 49(12), 2231–2264. [https://doi.org/10.1016/S0967-0645\(02\)00036-X](https://doi.org/10.1016/S0967-0645(02)00036-X)
- Forget, G., Campin, J.-M., Heimbach, P., Hill, C. N., Ponte, R. M., & Wunsch, C. (2015). ECCO version 4: an integrated framework for non-linear inverse modeling and global ocean state estimation. *Geoscientific Model Development*, 8(10), 3071–3104. <https://doi.org/10.5194/gmd-8-3071-2015>
- Franz, K., Roscher, R., Milioto, A., Wenzel, S., & Kusche, J. (2018). Ocean Eddy Identification and Tracking using Neural Networks. *arXiv:1803.07436 [Cs]*. Retrieved from <http://arxiv.org/abs/1803.07436>
- Fu, L.-L., Christensen, E. J., Yamarone Jr., C. A., Lefebvre, M., Ménard, Y., Dorrer, M., & Escudier, P. (1994). TOPEX/POSEIDON mission overview. *Journal of Geophysical Research: Oceans*, 99(C12), 24369–24381. <https://doi.org/10.1029/94JC01761>
- Fu, L.-L., Chelton, D. B., Le Traon, P.-Y., & Morrow, R. (2010). Eddy Dynamics from Satellite Altimetry. *Oceanography*, 23(4), 14–25.
- Garabato, A. C. N., Yu, X., Callies, J., Barkan, R., Polzin, K. L., Frajka-Williams, E. E., et al. (2022). Kinetic Energy Transfers between Mesoscale and Submesoscale Motions in the Open Ocean's Upper Layers. *Journal of Physical Oceanography*, 52(1), 75–97. <https://doi.org/10.1175/JPO-D-21-0099.1>
- Greaser, S. R., Subrahmanyam, B., Trott, C. B., & Roman-Stork, H. L. (2020). Interactions Between Mesoscale Eddies and Synoptic Oscillations in the Bay of Bengal During the Strong Monsoon of 2019. *Journal of Geophysical Research: Oceans*, 125(10), e2020JC016772. <https://doi.org/10.1029/2020JC016772>
- Grinsted, A., Moore, J. C., & Jevrejeva, S. (2004). Application of the cross wavelet transform and wavelet coherence to geophysical time series. *Nonlinear Processes in Geophysics*, 11(5/6), 561–566. <https://doi.org/10.5194/npg-11-561-2004>

- Gula, J., Blacic, T. M., & Todd, R. E. (2019). Submesoscale Coherent Vortices in the Gulf Stream. *Geophysical Research Letters*, 46(5), 2704–2714. <https://doi.org/10.1029/2019GL081919>
- Haller, G., Hadjighasem, A., Farazmand, M., & Huhn, F. (2016). Defining coherent vortices objectively from the vorticity. *Journal of Fluid Mechanics*, 795, 136–173. <https://doi.org/10.1017/jfm.2016.151>
- Haza, A. C., Özgökmen, T. M., & Hogan, P. (2016). Impact of submesoscales on surface material distribution in a gulf of Mexico mesoscale eddy. *Ocean Modelling*, 107, 28–47. <https://doi.org/10.1016/j.ocemod.2016.10.002>
- Heffner, D. M., Subrahmanyam, B., & Shriver, J. F. (2008). Indian Ocean Rossby waves detected in HYCOM sea surface salinity. *Geophysical Research Letters*, 35(3). <https://doi.org/10.1029/2007GL032760>
- Henson, S. A., & Thomas, A. C. (2008). A census of oceanic anticyclonic eddies in the Gulf of Alaska. *Deep Sea Research Part I: Oceanographic Research Papers*, 55(2), 163–176. <https://doi.org/10.1016/j.dsr.2007.11.005>
- Isern-Fontanet, J., García-Ladona, E., & Font, J. (2003). Identification of Marine Eddies from Altimetric Maps. *Journal of Atmospheric and Oceanic Technology*, 20(5), 772–778. [https://doi.org/10.1175/1520-0426\(2003\)20<772:IOMEFA>2.0.CO;2](https://doi.org/10.1175/1520-0426(2003)20<772:IOMEFA>2.0.CO;2)
- Izumo, T., Montégut, C. B., Luo, J.-J., Behera, S. K., Masson, S., & Yamagata, T. (2008). The Role of the Western Arabian Sea Upwelling in Indian Monsoon Rainfall Variability. *Journal of Climate*, 21(21), 5603–5623. <https://doi.org/10.1175/2008JCLI2158.1>
- Izumo, T., Vialard, J., Lengaigne, M., de Boyer Montegut, C., Behera, S. K., Luo, J.-J., et al. (2010). Influence of the state of the Indian Ocean Dipole on the following year's El Niño. *Nature Geoscience*, 3(3), 168–172. <https://doi.org/10.1038/ngeo760>
- Jaimés, B., Shay, L. K., & Brewster, J. K. (2016). Observed air-sea interactions in tropical cyclone Isaac over Loop Current mesoscale eddy features. *Dynamics of Atmospheres and Oceans*, 76, 306–324. <https://doi.org/10.1016/j.dynatmoce.2016.03.001>
- Jensen, T. G. (2007). Wind-Driven Response of the Northern Indian Ocean to Climate Extremes. *Journal of Climate*, 20(13), 2978–2993. <https://doi.org/10.1175/JCLI4150.1>

- Kobashi, D., & Hetland, R. (2020). Reproducibility and variability of submesoscale frontal eddies on a broad, low-energy shelf of freshwater influence. *Ocean Dynamics*, 70(11), 1377–1395. <https://doi.org/10.1007/s10236-020-01401-4>
- Kurian, J., & Vinayachandran, P. N. (2007). Mechanisms of formation of the Arabian Sea mini warm pool in a high-resolution Ocean General Circulation Model. *Journal of Geophysical Research: Oceans*, 112(C5). <https://doi.org/10.1029/2006JC003631>
- Kurian, J., Colas, F., Capet, X., McWilliams, J. C., & Chelton, D. B. (2011). Eddy properties in the California Current System. *Journal of Geophysical Research: Oceans*, 116(C8). <https://doi.org/10.1029/2010JC006895>
- Lahaye, N., & Zeitlin, V. (2015). Centrifugal, barotropic and baroclinic instabilities of isolated ageostrophic anticyclones in the two-layer rotating shallow water model and their nonlinear saturation. *Journal of Fluid Mechanics*, 762, 5–34. <https://doi.org/10.1017/jfm.2014.631>
- Lapeyre, G., & Klein, P. (2006). Dynamics of the Upper Oceanic Layers in Terms of Surface Quasigeostrophy Theory. *Journal of Physical Oceanography*, 36(2), 165–176. <https://doi.org/10.1175/JPO2840.1>
- Lazaneo, C. Z., Calil, P. H. R., Tandon, A., & da Silveira, I. C. A. (2022). Submesoscale Coherent Vortices in the South Atlantic Ocean: A Pathway for Energy Dissipation. *Journal of Geophysical Research: Oceans*, 127(2), e2020JC017099. <https://doi.org/10.1029/2020JC017099>
- Le Traon, P. Y., Nadal, F., & Ducet, N. (1998). An Improved Mapping Method of Multisatellite Altimeter Data. *Journal of Atmospheric and Oceanic Technology*, 15(2), 522–534. [https://doi.org/10.1175/1520-0426\(1998\)015<0522:AIMMOM>2.0.CO;2](https://doi.org/10.1175/1520-0426(1998)015<0522:AIMMOM>2.0.CO;2)
- Le Vu, B., Stegner, A., & Arsouze, T. (2018). Angular Momentum Eddy Detection and Tracking Algorithm (AMEDA) and Its Application to Coastal Eddy Formation. *Journal of Atmospheric and Oceanic Technology*, 35(4), 739–762. <https://doi.org/10.1175/JTECH-D-17-0010.1>
- Leben, R. R., & Born, G. H. (1993). Tracking Loop Current eddies with satellite altimetry. *Advances in Space Research*, 13(11), 325–333. [https://doi.org/10.1016/0273-1177\(93\)90235-4](https://doi.org/10.1016/0273-1177(93)90235-4)
- Lellouche, J.-M., Le Galloudec, O., Greiner, E., Garric, G., Regnier, C., Drevillon, M., et al. (2018). The Copernicus Marine Environment Monitoring Service global ocean 1/12° physical reanalysis GLORYS12V1: description and quality assessment, 19806. Presented at the EGU General Assembly Conference Abstracts.

- L'Hégaret, P., Duarte, R., Carton, X., Vic, C., Ciani, D., Baraille, R., & Corréard, S. (2015). Mesoscale variability in the Arabian Sea from HYCOM model results and observations: impact on the Persian Gulf Water path. *Ocean Science*, *11*(5), 667–693. <https://doi.org/10.5194/os-11-667-2015>
- L'Hégaret, Pierre, Carton, X., Louazel, S., & Boutin, G. (2016). Mesoscale eddies and submesoscale structures of Persian Gulf Water off the Omani coast in spring 2011. *Ocean Science*, *12*(3), 687–701. <https://doi.org/10.5194/os-12-687-2016>
- L'Hégaret, Pierre, Marez, C. de, Morvan, M., Meunier, T., & Carton, X. (2021). Spreading and Vertical Structure of the Persian Gulf and Red Sea Outflows in the Northwestern Indian Ocean. *Journal of Geophysical Research: Oceans*, *126*(4), e2019JC015983. <https://doi.org/10.1029/2019JC015983>
- Lian, Z., Sun, B., Wei, Z., Wang, Y., & Wang, X. (2019). Comparison of Eight Detection Algorithms for the Quantification and Characterization of Mesoscale Eddies in the South China Sea. *Journal of Atmospheric and Oceanic Technology*, *36*(7), 1361–1380. <https://doi.org/10.1175/JTECH-D-18-0201.1>
- Liu, B., Wu, G., & Ren, R. (2015). Influences of ENSO on the vertical coupling of atmospheric circulation during the onset of South Asian summer monsoon. *Climate Dynamics*, *45*(7), 1859–1875. <https://doi.org/10.1007/s00382-014-2439-3>
- Liu, X., Wang, M., & Shi, W. (2009). A study of a Hurricane Katrina–induced phytoplankton bloom using satellite observations and model simulations. *Journal of Geophysical Research: Oceans*, *114*(C3). <https://doi.org/10.1029/2008JC004934>
- Liu, Y., Weisberg, R. H., Hu, C., Kovach, C., & Riethmüller, R. (2011). Evolution of the Loop Current System During the Deepwater Horizon Oil Spill Event as Observed With Drifters and Satellites. In Y. Liu, A. MacFadyen, Z.-G. Ji, & R. H. Weisberg (Eds.), *Geophysical Monograph Series* (Vol. 195, pp. 91–101). Washington, D. C.: American Geophysical Union. <https://doi.org/10.1029/2011GM001127>
- Lynch, P. (1997). The Dolph–Chebyshev Window: A Simple Optimal Filter. *Monthly Weather Review*, *125*(4), 655–660. [https://doi.org/10.1175/1520-0493\(1997\)125<0655:TDCWAS>2.0.CO;2](https://doi.org/10.1175/1520-0493(1997)125<0655:TDCWAS>2.0.CO;2)
- Ma, X., Jing, Z., Chang, P., Liu, X., Montuoro, R., Small, R. J., et al. (2016). Western boundary currents regulated by interaction between ocean eddies and the atmosphere. *Nature*, *535*(7613), 533–537. <https://doi.org/10.1038/nature18640>
- de Marez, C., L'Hégaret, P., Morvan, M., & Carton, X. (2019). On the 3D structure of eddies in the Arabian Sea. *Deep Sea Research Part I: Oceanographic Research Papers*, *150*, 103057. <https://doi.org/10.1016/j.dsr.2019.06.003>

- de Marez, C., Carton, X., Corréard, S., L'Hégaret, P., & Morvan, M. (2020). Observations of a Deep Submesoscale Cyclonic Vortex in the Arabian Sea. *Geophysical Research Letters*, 47(13). <https://doi.org/10.1029/2020GL087881>
- de Marez, C., Carton, X., L'Hégaret, P., Meunier, T., Stegner, A., Le Vu, B., & Morvan, M. (2020). Oceanic vortex mergers are not isolated but influenced by the β -effect and surrounding eddies. *Scientific Reports*, 10(1), 2897. <https://doi.org/10.1038/s41598-020-59800-y>
- de Marez, C., Meunier, T., Morvan, M., L'Hégaret, P., & Carton, X. (2020). Study of the stability of a large realistic cyclonic eddy. *Ocean Modelling*, 146, 101540. <https://doi.org/10.1016/j.ocemod.2019.101540>
- Marshall, J., Adcroft, A., Hill, C., Perelman, L., & Heisey, C. (1997). A finite-volume, incompressible Navier Stokes model for studies of the ocean on parallel computers. *Journal of Geophysical Research: Oceans*, 102(C3), 5753–5766. <https://doi.org/10.1029/96JC02775>
- McCreary, J. P., Kundu, P. K., & Molinari, R. L. (1993). A numerical investigation of dynamics, thermodynamics and mixed-layer processes in the Indian Ocean. *Progress in Oceanography*, 31(3), 181–244. [https://doi.org/10.1016/0079-6611\(93\)90002-U](https://doi.org/10.1016/0079-6611(93)90002-U)
- McDougall, T. J., & Krzysik, O. A. (2015). Spiciness. *Journal of Marine Research*, 73(5), 141–152. <https://doi.org/10.1357/002224015816665589>
- McDougall, T. J., Barker, P. M., & Stanley, G. J. (2021). Spice Variables and Their Use in Physical Oceanography. *Journal of Geophysical Research: Oceans*, 126(2), e2019JC015936. <https://doi.org/10.1029/2019JC015936>
- McKenna, S., Santoso, A., Gupta, A. S., Taschetto, A. S., & Cai, W. (2020). Indian Ocean Dipole in CMIP5 and CMIP6: characteristics, biases, and links to ENSO. *Scientific Reports*, 10(1), 11500. <https://doi.org/10.1038/s41598-020-68268-9>
- Melnichenko, O., Amores, A., Maximenko, N., Hacker, P., & Potemra, J. (2017). Signature of mesoscale eddies in satellite sea surface salinity data. *Journal of Geophysical Research: Oceans*, 122(2), 1416–1424. <https://doi.org/10.1002/2016JC012420>
- Melzer, B. A., Jensen, T. G., & Rydbeck, A. V. (2019). Evolution of the Great Whirl Using an Altimetry-Based Eddy Tracking Algorithm. *Geophysical Research Letters*, 46(8), 4378–4385. <https://doi.org/10.1029/2018GL081781>

- Menemenlis, D., Campin, J.-M., Heimbach, P., Hill, C., Lee, T., Nguyen, A., et al. (2008). ECCO2: High Resolution Global Ocean and Sea Ice Data Synthesis. *AGU Fall Meeting Abstracts*, 31.
- Meschanov, S. L., & Shapiro, G. I. (1998). A young lens of Red Sea Water in the Arabian Sea. *Deep Sea Research Part I: Oceanographic Research Papers*, 45(1), 1–13. [https://doi.org/10.1016/S0967-0637\(97\)00018-6](https://doi.org/10.1016/S0967-0637(97)00018-6)
- Meunier, T., Tenreiro, M., Pallàs-Sanz, E., Ochoa, J., Ruiz-Angulo, A., Portela, E., et al. (2018). Intrathermocline Eddies Embedded Within an Anticyclonic Vortex Ring. *Geophysical Research Letters*, 45(15), 7624–7633. <https://doi.org/10.1029/2018GL077527>
- Morel, Y., Gula, J., & Ponte, A. (2019). Potential vorticity diagnostics based on balances between volume integral and boundary conditions. *Ocean Modelling*, 138, 23–35. <https://doi.org/10.1016/j.ocemod.2019.04.004>
- Morrison, J. M., Codispoti, L. A., Gaurin, S., Jones, B., Manghnani, V., & Zheng, Z. (1998). Seasonal variation of hydrographic and nutrient fields during the US JGOFS Arabian Sea Process Study. *Deep Sea Research Part II: Topical Studies in Oceanography*, 45(10), 2053–2101. [https://doi.org/10.1016/S0967-0645\(98\)00063-0](https://doi.org/10.1016/S0967-0645(98)00063-0)
- Morvan, M., L'Hégaret, P., Carton, X., Gula, J., Vic, C., de Marez, C., et al. (2019). The life cycle of submesoscale eddies generated by topographic interactions. *Ocean Science*, 15(6), 1531–1543. <https://doi.org/10.5194/os-15-1531-2019>
- Morvan, M., Carton, X., L'Hégaret, P., de Marez, C., Corréard, S., & Louazel, S. (2020). On the dynamics of an idealised bottom density current overflowing in a semi-enclosed basin: mesoscale and submesoscale eddies generation. *Geophysical & Astrophysical Fluid Dynamics*, 114(4–5), 607–630. <https://doi.org/10.1080/03091929.2020.1747058>
- Morvan, M., Carton, X., Corréard, S., & Baraille, R. (2020). Submesoscale Dynamics in the Gulf of Aden and the Gulf of Oman. *Fluids*, 5(3), 146. <https://doi.org/10.3390/fluids5030146>
- Murtugudde, R., & Busalacchi, A. J. (1999). Interannual Variability of the Dynamics and Thermodynamics of the Tropical Indian Ocean. *Journal of Climate*, 12(8), 2300–2326. [https://doi.org/10.1175/1520-0442\(1999\)012<2300:IVOTDA>2.0.CO;2](https://doi.org/10.1175/1520-0442(1999)012<2300:IVOTDA>2.0.CO;2)
- Nakamura, T., Matthews, J. P., Awaji, T., & Mitsudera, H. (2012). Submesoscale eddies near the Kuril Straits: Asymmetric generation of clockwise and counterclockwise eddies by barotropic tidal flow. *Journal of Geophysical Research: Oceans*, 117(C12). <https://doi.org/10.1029/2011JC007754>

- Nencioli, F., Dong, C., Dickey, T., Washburn, L., & McWilliams, J. C. (2010). A Vector Geometry–Based Eddy Detection Algorithm and Its Application to a High-Resolution Numerical Model Product and High-Frequency Radar Surface Velocities in the Southern California Bight. *Journal of Atmospheric and Oceanic Technology*, 27(3), 564–579. <https://doi.org/10.1175/2009JTECHO725.1>
- Ni, Q., Zhai, X., Wilson, C., Chen, C., & Chen, D. (2021). Submesoscale Eddies in the South China Sea. *Geophysical Research Letters*, 48(6), e2020GL091555. <https://doi.org/10.1029/2020GL091555>
- Okubo, A. (1970). Horizontal dispersion of floatable particles in the vicinity of velocity singularities such as convergences. *Deep Sea Research and Oceanographic Abstracts*, 17(3), 445–454. [https://doi.org/10.1016/0011-7471\(70\)90059-8](https://doi.org/10.1016/0011-7471(70)90059-8)
- Özgökmen, T. M., Chassignet, E. P., Dawson, C. N., Dukhovskoy, D., Jacobs, G., Ledwell, J., et al. (2016). Over What Area Did the Oil and Gas Spread During the 2010 Deepwater Horizon Oil Spill? *Oceanography*, 29(3), 96–107.
- Pegliasco, C., Chaigneau, A., & Morrow, R. (2015). Main eddy vertical structures observed in the four major Eastern Boundary Upwelling Systems. *Journal of Geophysical Research: Oceans*, 120(9), 6008–6033. <https://doi.org/10.1002/2015JC010950>
- Pegliasco, C., Chaigneau, A., Morrow, R., & Dumas, F. (2021). Detection and tracking of mesoscale eddies in the Mediterranean Sea: A comparison between the Sea Level Anomaly and the Absolute Dynamic Topography fields. *Advances in Space Research*, 68(2), 401–419. <https://doi.org/10.1016/j.asr.2020.03.039>
- Pelland, N. A., Eriksen, C. C., & Lee, C. M. (2013). Subthermocline Eddies over the Washington Continental Slope as Observed by Seagliders, 2003–09. *Journal of Physical Oceanography*, 43(10), 2025–2053. <https://doi.org/10.1175/JPO-D-12-086.1>
- Petersen, M. R., Williams, S. J., Maltrud, M. E., Hecht, M. W., & Hamann, B. (2013). A three-dimensional eddy census of a high-resolution global ocean simulation. *Journal of Geophysical Research: Oceans*, 118(4), 1759–1774. <https://doi.org/10.1002/jgrc.20155>
- Polito, P. S., & Sato, O. T. (2015). Do eddies ride on Rossby waves? *Journal of Geophysical Research: Oceans*, 120(8), 5417–5435. <https://doi.org/10.1002/2015JC010737>

- Potter, H., Hsu, C.-Y., & DiMarco, S. F. (2021). Rapid dissipation of a Loop Current eddy due to interaction with a severe Gulf of Mexico hurricane. *Ocean Dynamics*, 71(9), 911–922. <https://doi.org/10.1007/s10236-021-01471-y>
- Prasad, T. G., & Ikeda, M. (2001). Spring evolution of Arabian Sea High in the Indian Ocean. *Journal of Geophysical Research: Oceans*, 106(C12), 31085–31098. <https://doi.org/10.1029/2000JC000314>
- Prasad, T. G., Ikeda, M., & Kumar, S. P. (2001). Seasonal spreading of the Persian Gulf Water mass in the Arabian Sea. *Journal of Geophysical Research: Oceans*, 106(C8), 17059–17071. <https://doi.org/10.1029/2000JC000480>
- Prasanna Kumar, S., & Prasad, T. G. (1999). Formation and spreading of Arabian Sea high-salinity water mass. *Journal of Geophysical Research: Oceans*, 104(C1), 1455–1464. <https://doi.org/10.1029/1998JC900022>
- Qiu, B., Chen, S., Klein, P., Wang, J., Torres, H., Fu, L.-L., & Menemenlis, D. (2018). Seasonality in Transition Scale from Balanced to Unbalanced Motions in the World Ocean. *Journal of Physical Oceanography*, 48(3), 591–605. <https://doi.org/10.1175/JPO-D-17-0169.1>
- Queste, B. Y., Vic, C., Heywood, K. J., & Piontkovski, S. A. (2018). Physical Controls on Oxygen Distribution and Denitrification Potential in the North West Arabian Sea. *Geophysical Research Letters*, 45(9), 4143–4152. <https://doi.org/10.1029/2017GL076666>
- Rabalais, N. N., Turner, R. E., & Wiseman, W. J. (2002). Gulf of Mexico Hypoxia, A.K.A. “The Dead Zone.” *Annual Review of Ecology and Systematics*, 33(1), 235–263. <https://doi.org/10.1146/annurev.ecolsys.33.010802.150513>
- Rai, S., Hecht, M., Maltrud, M., & Aluie, H. (2021). Scale of oceanic eddy killing by wind from global satellite observations. *Science Advances*, 7(28), eabf4920. <https://doi.org/10.1126/sciadv.abf4920>
- Rao, A. D., Joshi, M., & Ravichandran, M. (2008). Oceanic upwelling and downwelling processes in waters off the west coast of India. *Ocean Dynamics*, 58(3–4), 213–226. <https://doi.org/10.1007/s10236-008-0147-4>
- Rao, R. R., Girish Kumar, M. S., Ravichandran, M., Rao, A. R., Gopalakrishna, V. V., & Thadathil, P. (2010). Interannual variability of Kelvin wave propagation in the wave guides of the equatorial Indian Ocean, the coastal Bay of Bengal and the southeastern Arabian Sea during 1993–2006. *Deep Sea Research Part I: Oceanographic Research Papers*, 57(1), 1–13. <https://doi.org/10.1016/j.dsr.2009.10.008>

- Rocha, C. B., Gille, S. T., Chereskin, T. K., & Menemenlis, D. (2016). Seasonality of submesoscale dynamics in the Kuroshio Extension. *Geophysical Research Letters*, 43(21), 11,304–11,311. <https://doi.org/10.1002/2016GL071349>
- Roman-Stork, H. L., Byrne, D. A., & Leuliette, E. W. (2023). MESI: A Multiparameter Eddy Significance Index. *Earth and Space Science*, 10(2), e2022EA002583. <https://doi.org/10.1029/2022EA002583>
- Roman-Stork, Heather L., & Subrahmanyam, B. (2020). The Impact of the Madden–Julian Oscillation on Cyclone Amphan (2020) and Southwest Monsoon Onset. *Remote Sensing*, 12(18), 3011. <https://doi.org/10.3390/rs12183011>
- Roman-Stork, Heather L., Subrahmanyam, B., & Murty, V. S. N. (2020). The Role of Salinity in the Southeastern Arabian Sea in Determining Monsoon Onset and Strength. *Journal of Geophysical Research: Oceans*, 125(1), e2019JC015592. <https://doi.org/10.1029/2019JC015592>
- Roman-Stork, Heather L., Subrahmanyam, B., & Trott, C. B. (2021). Mesoscale eddy variability and its linkage to deep convection over the Bay of Bengal using satellite altimetric observations. *Advances in Space Research*, 68(2), 378–400. <https://doi.org/10.1016/j.asr.2019.09.054>
- Rosso, I., Hogg, A. McC., Kiss, A. E., & Gayen, B. (2015). Topographic influence on submesoscale dynamics in the Southern Ocean. *Geophysical Research Letters*, 42(4), 1139–1147. <https://doi.org/10.1002/2014GL062720>
- Sadarjoen, A. I., & Post, F. H. (2000). Detection, quantification, and tracking of vortices using streamline geometry. *Computers & Graphics*, 24(3), 333–341. [https://doi.org/10.1016/S0097-8493\(00\)00029-7](https://doi.org/10.1016/S0097-8493(00)00029-7)
- Schneider, T., Held, I. M., & Garner, S. T. (2003). Boundary Effects in Potential Vorticity Dynamics. *Journal of the Atmospheric Sciences*, 60(8), 1024–1040. [https://doi.org/10.1175/1520-0469\(2003\)60<1024:BEIPVD>2.0.CO;2](https://doi.org/10.1175/1520-0469(2003)60<1024:BEIPVD>2.0.CO;2)
- Schott, F., Reppin, J., Fischer, J., & Quadfasel, D. (1994). Currents and transports of the Monsoon Current south of Sri Lanka. *Journal of Geophysical Research: Oceans*, 99(C12), 25127–25141. <https://doi.org/10.1029/94JC02216>
- Schott, F. A., & McCreary, J. P. (2001). The monsoon circulation of the Indian Ocean. *Progress in Oceanography*, 51(1), 1–123. [https://doi.org/10.1016/S0079-6611\(01\)00083-0](https://doi.org/10.1016/S0079-6611(01)00083-0)

- Schott, Friedrich, Fischer, J., Gartnericht, U., & Quadfasel, D. (1997). Summer monsoon response of the Northern Somali Current, 1995. *Geophysical Research Letters*, 24(21), 2565–2568. <https://doi.org/10.1029/97GL00888>
- Seo, H. (2017). Distinct Influence of Air–Sea Interactions Mediated by Mesoscale Sea Surface Temperature and Surface Current in the Arabian Sea. *Journal of Climate*, 30(20), 8061–8080. <https://doi.org/10.1175/JCLI-D-16-0834.1>
- Shankar, D., & Shetye, S. R. (1997). On the dynamics of the Lakshadweep high and low in the southeastern Arabian Sea. *Journal of Geophysical Research: Oceans*, 102(C6), 12551–12562. <https://doi.org/10.1029/97JC00465>
- Shapiro, G., & Meschanov, S. L. (1991). Distribution and spreading of Red Sea Water and salt lens formation in the northwest Indian Ocean. *Deep Sea Research Part A. Oceanographic Research Papers*, 38, 21–34. [https://doi.org/10.1016/0198-0149\(91\)90052-H](https://doi.org/10.1016/0198-0149(91)90052-H)
- Shenoi, S. S. C., Shankar, D., Michael, G. S., Kurian, J., Varma, K. K., Kumar, M. R. R., et al. (2005). Hydrography and water masses in the southeastern Arabian Sea during March–June 2003. *Journal of Earth System Science*, 114(5), 475–491. <https://doi.org/10.1007/BF02702024>
- Shukla, J. (1975). Effect of Arabian Sea-Surface Temperature Anomaly on Indian Summer Monsoon: A Numerical Experiment with the GFDL Model. *Journal of the Atmospheric Sciences*, 32(3), 503–511. [https://doi.org/10.1175/1520-0469\(1975\)032<0503:EOASST>2.0.CO;2](https://doi.org/10.1175/1520-0469(1975)032<0503:EOASST>2.0.CO;2)
- Souza, J. M. a. C., de Boyer Montégut, C., & Le Traon, P. Y. (2011). Comparison between three implementations of automatic identification algorithms for the quantification and characterization of mesoscale eddies in the South Atlantic Ocean. *Ocean Science*, 7(3), 317–334. <https://doi.org/10.5194/os-7-317-2011>
- Spiro Jaeger, G., & Mahadevan, A. (2018). Submesoscale-selective compensation of fronts in a salinity-stratified ocean. *Science Advances*, 4(2), e1701504. <https://doi.org/10.1126/sciadv.1701504>
- Subrahmanyam, B., Robinson, I. S., Blundell, J. R., & Challenor, P. G. (2001). Indian Ocean Rossby waves observed in TOPEX/POSEIDON altimeter data and in model simulations. *International Journal of Remote Sensing*, 22(1), 141–167. <https://doi.org/10.1080/014311601750038893>
- Subrahmanyam, Bulusu, Heffner, D. M., Cromwell, D., & Shriver, J. F. (2009). Detection of Rossby waves in multi-parameters in multi-mission satellite

observations and HYCOM simulations in the Indian Ocean. *Remote Sensing of Environment*, 113(6), 1293–1303. <https://doi.org/10.1016/j.rse.2009.02.017>

Subrahmanyam, Bulusu, Roman-Stork, H. L., & Murty, V. S. N. (2020). Response of the Bay of Bengal to 3-7-Day Synoptic Oscillations During the Southwest Monsoon of 2019. *Journal of Geophysical Research: Oceans*, 125(6), e2020JC016200. <https://doi.org/10.1029/2020JC016200>

Sun, Z., Zhang, Z., Qiu, B., Zhou, C., Zhao, W., & Tian, J. (2022). Subsurface Mesoscale Eddies Observed in the Northeastern South China Sea: Dynamic Features and Water Mass Transport. *Journal of Physical Oceanography*, 52(5), 841–855. <https://doi.org/10.1175/JPO-D-21-0177.1>

Suresh, I., Vialard, J., Izumo, T., Lengaigne, M., Han, W., McCreary, J., & Muraleedharan, P. M. (2016). Dominant role of winds near Sri Lanka in driving seasonal sea level variations along the west coast of India. *Geophysical Research Letters*, 43(13), 7028–7035. <https://doi.org/10.1002/2016GL069976>

Tedesco, P., Gula, J., Ménesguen, C., Penven, P., & Krug, M. (2019). Generation of Submesoscale Frontal Eddies in the Agulhas Current. *Journal of Geophysical Research: Oceans*, 124(11), 7606–7625. <https://doi.org/10.1029/2019JC015229>

Tian, F., Li, Z., Yuan, Z., & Chen, G. (2021). EddyGraph: The Tracking of Mesoscale Eddy Splitting and Merging Events in the Northwest Pacific Ocean. *Remote Sensing*, 13(17), 3435. <https://doi.org/10.3390/rs13173435>

Toner, M., Kirwan Jr., A. D., Poje, A. C., Kantha, L. H., Müller-Karger, F. E., & Jones, C. K. R. T. (2003). Chlorophyll dispersal by eddy-eddy interactions in the Gulf of Mexico. *Journal of Geophysical Research: Oceans*, 108(C4). <https://doi.org/10.1029/2002JC001499>

Tozuka, T., Nagura, M., & Yamagata, T. (2014). Influence of the Reflected Rossby Waves on the Western Arabian Sea Upwelling Region. *Journal of Physical Oceanography*, 44(5), 1424–1438. <https://doi.org/10.1175/JPO-D-13-0127.1>

Trott, C. B., Subrahmanyam, B., & Murty, V. S. N. (2017). Variability of the Somali Current and eddies during the southwest monsoon regimes. *Dynamics of Atmospheres and Oceans*, 79, 43–55. <https://doi.org/10.1016/j.dynatmoce.2017.07.002>

Trott, C. B., Subrahmanyam, B., Chaigneau, A., & Delcroix, T. (2018). Eddy Tracking in the Northwestern Indian Ocean During Southwest Monsoon Regimes. *Geophysical Research Letters*, 45(13), 6594–6603. <https://doi.org/10.1029/2018GL078381>

- Trott, C. B., Subrahmanyam, B., Chaigneau, A., & Roman-Stork, H. L. (2019). Eddy-Induced Temperature and Salinity Variability in the Arabian Sea. *Geophysical Research Letters*, *46*(5), 2734–2742. <https://doi.org/10.1029/2018GL081605>
- Vecchi, G. A., Xie, S.-P., & Fischer, A. S. (2004). Ocean–Atmosphere Covariability in the Western Arabian Sea. *Journal of Climate*, *17*(6), 1213–1224. [https://doi.org/10.1175/1520-0442\(2004\)017<1213:OCITWA>2.0.CO;2](https://doi.org/10.1175/1520-0442(2004)017<1213:OCITWA>2.0.CO;2)
- Verezemskaya, P., Barnier, B., Gulev, S. K., Gladyshev, S., Molines, J.-M., Gladyshev, V., et al. (2021). Assessing Eddying (1/12°) Ocean Reanalysis GLORYS12 Using the 14-yr Instrumental Record From 59.5°N Section in the Atlantic. *Journal of Geophysical Research: Oceans*, *126*(6), e2020JC016317. <https://doi.org/10.1029/2020JC016317>
- Verma, V., Pham, H. T., & Sarkar, S. (2019). The submesoscale, the finescale and their interaction at a mixed layer front. *Ocean Modelling*, *140*, 101400. <https://doi.org/10.1016/j.ocemod.2019.05.004>
- Vic, C., Roullet, G., Carton, X., & Capet, X. (2014). Mesoscale dynamics in the Arabian Sea and a focus on the Great Whirl life cycle: A numerical investigation using ROMS. *Journal of Geophysical Research: Oceans*, *119*(9), 6422–6443. <https://doi.org/10.1002/2014JC009857>
- Vortmeyer-Kley, R., Gräwe, U., & Feudel, U. (2016). Detecting and tracking eddies in oceanic flow fields: a Lagrangian descriptor based on the modulus of vorticity. *Nonlinear Processes in Geophysics*, *23*(4), 159–173. <https://doi.org/10.5194/npg-23-159-2016>
- Vortmeyer-Kley, R., Holtermann, P., Feudel, U., & Gräwe, U. (2019). Comparing Eulerian and Lagrangian eddy census for a tide-less, semi-enclosed basin, the Baltic Sea. *Ocean Dynamics*, *69*(6), 701–717. <https://doi.org/10.1007/s10236-019-01269-z>
- Wang, H., McClean, J. L., & Talley, L. D. (2021). Full Vorticity Budget of the Arabian Sea from a 0.1° Ocean Model: Sverdrup Dynamics, Rossby Waves, and Nonlinear Eddy Effects. *Journal of Physical Oceanography*, *51*(12), 3589–3607. <https://doi.org/10.1175/JPO-D-20-0223.1>
- Wang, J. L., Zhuang, H., Chérubin, L. M., Ibrahim, A. K., & Muhamed Ali, A. (2019). Medium-Term Forecasting of Loop Current Eddy Cameron and Eddy Darwin Formation in the Gulf of Mexico With a Divide-and-Conquer Machine Learning Approach. *Journal of Geophysical Research: Oceans*, *124*(8), 5586–5606. <https://doi.org/10.1029/2019JC015172>

- Wang, Q., Dong, C., Dong, J., Zhang, H., & Yang, J. (2022). Submesoscale processes-induced vertical heat transport modulated by oceanic mesoscale eddies. *Deep Sea Research Part II: Topical Studies in Oceanography*, 202, 105138. <https://doi.org/10.1016/j.dsr2.2022.105138>
- Wang, S., Zhu, W., Ma, J., Ji, J., Yang, J., & Dong, C. (2019). Variability of the Great Whirl and Its Impacts on Atmospheric Processes. *Remote Sensing*, 11(3), 322. <https://doi.org/10.3390/rs11030322>
- Weiss, J. (1991). The dynamics of enstrophy transfer in two-dimensional hydrodynamics. *Physica D: Nonlinear Phenomena*, 48(2), 273–294. [https://doi.org/10.1016/0167-2789\(91\)90088-Q](https://doi.org/10.1016/0167-2789(91)90088-Q)
- Williams, S., Petersen, M., Bremer, P.-T., Hecht, M., Pascucci, V., Ahrens, J., et al. (2011). Adaptive Extraction and Quantification of Geophysical Vortices. *IEEE Transactions on Visualization and Computer Graphics*, 17(12), 2088–2095. <https://doi.org/10.1109/TVCG.2011.162>
- Xia, Q., Li, G., & Dong, C. (2022). Global Oceanic Mass Transport by Coherent Eddies. *Journal of Physical Oceanography*, 52. <https://doi.org/10.1175/JPO-D-21-0103.1>
- Xu, A., Yu, F., & Nan, F. (2019). Study of subsurface eddy properties in northwestern Pacific Ocean based on an eddy-resolving OGCM. *Ocean Dynamics*, 69(4), 463–474. <https://doi.org/10.1007/s10236-019-01255-5>
- Xu, C., Zhai, X., & Shang, X.-D. (2016). Work done by atmospheric winds on mesoscale ocean eddies. *Geophysical Research Letters*, 43(23), 12,174-12,180. <https://doi.org/10.1002/2016GL071275>
- Yang, Y., Weisberg, R. H., Liu, Y., & Liang, X. S. (2020). Instabilities and Multiscale Interactions Underlying the Loop Current Eddy Shedding in the Gulf of Mexico. *Journal of Physical Oceanography*, 50(5), 1289–1317. <https://doi.org/10.1175/JPO-D-19-0202.1>
- Yang, Y., McWilliams, J. C., Liang, X. S., Zhang, H., Weisberg, R. H., Liu, Y., & Menemenlis, D. (2021). Spatial and Temporal Characteristics of the Submesoscale Energetics in the Gulf of Mexico. *Journal of Physical Oceanography*, 51(2), 475–489. <https://doi.org/10.1175/JPO-D-20-0247.1>
- Yao, W., Teng, Z., Tang, Q., & Zuo, P. (2014). Adaptive Dolph–Chebyshev window-based S transform in time-frequency analysis. *IET Signal Processing*, 8(9), 927–937. <https://doi.org/10.1049/iet-spr.2013.0400>

- You, Y. (1998). Intermediate water circulation and ventilation of the Indian Ocean derived from water-mass contributions. *Journal of Marine Research*, 56(5), 1029–1067. <https://doi.org/10.1357/002224098765173455>
- Yuan, Y., Yang, H., Zhou, W., & Li, C. (2008). Influences of the Indian Ocean Dipole on the Asian summer monsoon in the following year. *International Journal of Climatology*, 28, 1849–1859. <https://doi.org/10.1002/joc.1678>
- Zachariah, J., Babu, C. A., & Varikoden, H. (2019). Dynamics of westward propagation and intensification of Lakshadweep low in the southern Arabian Sea. *Ocean Dynamics*, 69(5), 519–528. <https://doi.org/10.1007/s10236-019-01263-5>
- Zamuda, A., Hernández Sosa, J. D., & Adler, L. (2016). Constrained differential evolution optimization for underwater glider path planning in sub-mesoscale eddy sampling. *Applied Soft Computing*, 42, 93–118. <https://doi.org/10.1016/j.asoc.2016.01.038>
- Zhan, P., Guo, D., & Hoteit, I. (2020). Eddy-Induced Transport and Kinetic Energy Budget in the Arabian Sea. *Geophysical Research Letters*, 47(23), e2020GL090490. <https://doi.org/10.1029/2020GL090490>
- Zhang, H.-M., Bates, J. J., & Reynolds, R. W. (2006). Assessment of composite global sampling: Sea surface wind speed. *Geophysical Research Letters*, 33(17). <https://doi.org/10.1029/2006GL027086>
- Zhang, X., Dai, H., Zhao, J., & Yin, H. (2019). Generation mechanism of an observed submesoscale eddy in the Chukchi Sea. *Deep Sea Research Part I: Oceanographic Research Papers*, 148, 80–87. <https://doi.org/10.1016/j.dsr.2019.04.015>
- Zhang, Y., Hu, C., Liu, Y., Weisberg, R. H., & Kourafalou, V. H. (2019). Submesoscale and Mesoscale Eddies in the Florida Straits: Observations from Satellite Ocean Color Measurements. *Geophysical Research Letters*, 46(22), 13262–13270. <https://doi.org/10.1029/2019GL083999>
- Zhang, Zhengguang, & Qiu, B. (2018). Evolution of Submesoscale Ageostrophic Motions Through the Life Cycle of Oceanic Mesoscale Eddies. *Geophysical Research Letters*, 45(21), 11,847–11,855. <https://doi.org/10.1029/2018GL080399>
- Zhang, Zhengguang, Wang, W., & Qiu, B. (2014). Oceanic mass transport by mesoscale eddies. *Science*, 345(6194), 322–324. <https://doi.org/10.1126/science.1252418>
- Zhang, Zhiwei, Zhao, W., Qiu, B., & Tian, J. (2017). Anticyclonic Eddy Sheddings from Kuroshio Loop and the Accompanying Cyclonic Eddy in the Northeastern South

China Sea. *Journal of Physical Oceanography*, 47(6), 1243–1259.
<https://doi.org/10.1175/JPO-D-16-0185.1>

APPENDIX A

COPYRIGHT PERMISSIONS

A.1 CHAPTER 2 COPYRIGHT PERMISSIONS

JGR Oceans

Research Article | [Open Access](#) | 

Lakshadweep High Propagation and Impacts on the Somali Current and Eddies During the Southwest Monsoon

Paul A. Ernst  Bulusu Subrahmanyam, Corinne B. Trott

First published: 10 March 2022 | <https://doi.org/10.1029/2021JC018089> | Citations: 2

SECTIONS

 PDF  TOOLS  SHARE

Abstract

Climatological eddies in the Arabian Sea (AS), including the Lakshadweep High (LH) and the Great Whirl (GW), play major roles in the regional fluxes of upper ocean properties. For the first time, we apply an eddy tracking algorithm to the LH using altimetric sea surface height observations from 1993 through 2019. We additionally analyze the LH's water mass composition throughout its life cycle using the 1/12° Global eddy resolving physical ocean and sea ice reanalysis (GLORYS12). We observe that the second annual downwelling coastal Kelvin wave's (CKW) arrival during the winter monsoon is primarily responsible for generating the LH. In March, Rossby waves propagate along 8°N at the same speed of that of the LH. In 17 of 27 years, the LH maintains coherence across the AS. The LH sustains a shallow lens of lower salinity Bay of Bengal water up to 68°E in these years. In the remaining 10 years, the LH dissipates between 60°E and 70°E or fails to propagate beyond the southwest Indian coast. We attribute the differences between propagation types to fluctuations in the CKW strength, differences in wind stress between the southern tip of India and Sri Lanka, and the variable distribution of wind stress curl around the LH. We also find that longer propagating LH types negatively correlate with the eddy kinetic energy of the Somali Current region during the summer monsoon. We conclude that, upon its arrival in late July, the LH either merges with or replaces the GW, disrupting the cyclone that normally orbits the GW.



Volume 127, Issue 3
March 2022
e2021JC018089

 Figures  References  Related  Information

Metrics

Citations: 2
Full text views: 355 

Details

© 2022 The Authors.

This is an open access article under the terms of the [Creative Commons Attribution-NonCommercial License](#), which permits use, distribution and reproduction in any medium, provided the original work is properly cited and is not used for commercial purposes.

 Check for updates

Research Funding

DOD | US Navy | Office of Naval Research (ONR). Grant Number: N00014-20-1-2742

Keywords

A.2 CHAPTER 3 COPYRIGHT PERMISSIONS

Re: Permission Request Form [#2179] External Inbox x ✕

 **Gumbel, Erin** <egumbel@ametsoc.org>
to me, permissions 2:38 PM (39 minutes ago) ☆

Dear Mx. Ernst,

Thank you for your email. This signed message constitutes permission to use the material requested below.

You may include your 2023 JTECH article in your University of South Carolina dissertation, *NEW TECHNIQUES FOR STUDYING OCEAN EDDY DYNAMICS IN THE ARABIAN SEA AND THE GULF OF MEXICO*, with the following conditions:

1. Include the complete bibliographic citation of the original source.
2. Include the following statement with that citation: © American Meteorological Society. Used with permission.

Congratulations on completing your dissertation! If you have any questions or need additional information, please feel free to contact me.

Best,



Ms. Erin Gumbel, she/her/hers
Senior Peer Review Support Associate
Senior Permissions Specialist
egumbel@ametsoc.org
617-226-3926

A.3 CHAPTER 4 COPYRIGHT PERMISSIONS

Citation: Ernst PA, Subrahmanyam B, Trott CB and Chaigneau A (2023) Characteristics of submesoscale eddy structures within mesoscale eddies in the Gulf of Mexico from 1/48° ECCO estimates. *Front. Mar. Sci.* 10:1181676. doi: 10.3389/fmars.2023.1181676

Received: 07 March 2023; **Accepted:** 17 May 2023;
Published: 31 May 2023.

Edited by:
[Steven L. Morey](#), Florida Agricultural and Mechanical University, United States

Reviewed by:
[Wei Huang](#), Oak Ridge National Laboratory (DOE), United States
[Charly De Marez](#), California Institute of Technology, United States

Copyright © 2023 Ernst, Subrahmanyam, Trott and Chaigneau. This is an open-access article distributed under the terms of the [Creative Commons Attribution License \(CC BY\)](#). The use, distribution or reproduction in other forums is permitted, provided the original author(s) and the copyright owner(s) are credited and that the original publication in this journal is cited, in accordance with accepted academic practice. No use, distribution or reproduction is permitted which does not comply with these terms.

***Correspondence:** Paul A. Ernst, pernst@seoe.sc.edu

Disclaimer: All claims expressed in this article are solely those of the authors and do not necessarily represent those of their affiliated organizations, or those of the publisher, the editors and the reviewers. Any product that may be evaluated in this article or claim that may be made by its manufacturer is not guaranteed or endorsed by the publisher.

APPENDIX B

B. 1 CALCULATION OF AVERAGED PV IN THE SURFACE LAYER

As explained above (see Morel et al, 2019), the generalized PV is closely linked to the quasigeostrophic PV and its vertical integration in a layer bounded by two isopycnals ρ_1 and ρ_2 is representative of the average dynamics (vorticity and velocity fields). In this case, the mean –generalized- PV representative of the dynamics is given by

$$\overline{\text{PV}}_{\text{rescaled}} = \frac{1}{h_{\rho_1}^{\rho_2}} \int_{z_{\rho_1}}^{z_{\rho_2}} \text{PV}_{\text{rescaled}} dz$$

where $h_{\rho_1}^{\rho_2}$ is the layer depth and $\text{PV}_{\text{rescaled}}$ is given by equation (6).

The sea surface is a material surface in adiabatic conditions, but it is generally not an isopycnic surface. However, previous studies have shown that the vertical average of PV is still representative of the dynamics in the surface layer (that is a layer bounded by the sea surface at the top and a chosen isopycnic surface at depth), provided an additional term, associated with density variations at the surface, is added. Indeed, density variation along the surface is equivalent to a Dirac delta sheet of PV that is to be taken into account. Following Schneider et al (2003) and Morel et al (2019) it can be shown that in this case the proper calculation for the equivalent integrated rescaled PV is

$$\overline{\text{PV}}_{\text{rescaled}} = \frac{1}{h_{\rho_1}^{\rho_2}} \left[\int_{z_{\rho_1}}^{z=0} \text{PV}_{\text{rescaled}} dz - (\nabla \times U_{z=0} + f) Z(\rho_{z=0}) \right]$$

Where the additional term is calculated from velocity and density fields at the surface ($z=0$). We also recall that $Z(\rho)$ is the depth at density ρ but associated with a reference profile, representative of the fluid at rest.

This additional term has been proven to be very important for the understanding of the dynamics. Initially Bretherton (1966) discussed it for quasigeostrophic dynamics,

which has led to the development of the surface quasigeostrophic theory and models (see Lapeyre et al, 2006 and references therein). Schneider et al (2003) extended the concept to the general case.